Development of Alternating Amphiphilic Copolymers for Targeted Delivery Applications in Cancer

by

Kevin P. Brower

M.S., Chemical Engineering Practice
Massachusetts Institute of Technology, 2006

B.S., Chemical Engineering
Yale University, 2004

MASSACHUSETTS INSTITUTE OF TECHNOLOGY
FEB 09 2011
LIBRARIES

ARCHIVES

Submitted to the Department of Chemical Engineering
in partial fulfillment of the requirements for the degree of

DOCTOR OF PHILOSOPHY IN CHEMICAL ENGINEERING

at the

MASSACHUSETTS INSTITUTE OF TECHNOLOGY

January 2011
[February 2011]

© Massachusetts Institute of Technology 2011
All Rights Reserved

Signature of Author: _____
Department of Chemical Engineering
January 27th, 2011

Certified by: _____
Clark K. Colton
Professor of Chemical Engineering
Thesis Supervisor

Accepted by: _____
William M. Deen
Professor of Chemical Engineering
Chairman, Committee for Graduate Students

Development of Alternating Amphiphilic Copolymers for Targeted Delivery Applications in Cancer

by

Kevin Brower

Submitted to the Department of Chemical Engineering on January 27th, 2011
in partial fulfillment of the requirements for the degree of Doctor of Philosophy in Chemical Engineering

Abstract

According to the American Cancer Society, approximately 1,479,000 new cases of cancer were expected to be diagnosed, while 562,340 Americans were expected to die from cancer in 2009 alone. Even though advances in early diagnosis and therapy over the past few decades have led to continual decreases in incidence and mortality, cancer remains the second leading cause of death among all Americans. Consequently, further technological development in all areas of cancer detection and treatment are still of great importance not only to the scientific community, but to society itself.

To address the shortcomings in current cancer diagnosis and treatment, a novel, highly adaptable, targeted nanoparticle system based on alternating amphiphilic copolymers has been developed having a variety of potential clinical applications. These polymers consist of an alternating copolymer backbone composed of hydrophilic polyethylene glycol-900 (PEG900) and dimethyl 5-hydroxyisophthalate (linker) monomer units. The linker within the backbone polymer has a free hydroxyl group to which a variety of sidechains can be attached, including hydrophobic groups to impart amphiphilicity, targeting ligands, as well as contrast agents for imaging applications. Three major areas of investigation were addressed to develop and evaluate the performance of the proposed amphiphilic alternating copolymers: (1) backbone polymer synthesis, (2) attachment of radioiodine, and (3) targeted delivery *in vitro* and *in vivo*.

The first step in the production of the alternating amphiphilic copolymers is a chemo-enzymatic condensation polymerization of polyethylene glycol (PEG) and dimethyl 5-hydroxyisophthalate (linker) to produce backbone polymer. Because of their generally low equilibrium constants, condensation polymerizations require effective removal of the condensation byproduct (in this case, methanol) in order to achieve significant increases in molecular weight. The increased viscosities at higher molecular weights not only increase the difficulty of byproduct removal, but may also affect the mixing characteristics as well as the mass transfer of other species in the reaction.

The enzymatic polymerization was investigated using both predictive modeling and experiment. The ultimate goal was to increase the molecular weight of the synthesized polymer to allow for increased substitution of the polymer backbone. Key experimental variables were tested in glass flasks typically used in organic synthesis. In these reactions, 4Å molecular sieves had the greatest affect on the backbone polymer

molecular weight. In particular, addition of sieves, which can act as sinks for both water and methanol, led to a twofold increase in weight-average molecular weight above that observed previously for the enzymatic polymerization. The Protherm, a novel, thin-film reactor was employed in order to improve methanol mass transfer and mixing within the polymer melt. Three separate reactions in the Protherm produced the highest M_w backbone polymer (approximately 20 kDa). A blade speed of 500 rpm with molecular sieves present was able to achieve this M_w in 48 hr.

Two separate models were proposed to describe the polymerization, including a homogeneous kinetic model and a Fick's Law mass transfer model. Significant differences were observed between the experimental results and the predictions of the homogeneous model. The mass transfer modeling, which estimated the increase in reactant and methanol surface concentration relative to the concentration in the bulk, was unable to bridge the gap between experiment and model results. Limited knowledge of key model parameters, including the equilibrium constant and methanol solubility, was one proposed explanation for the observed discrepancy.

In order to assess the performance of a nanoparticle delivery system in biological applications, a label that is detectable under a wide range of conditions and concentrations must be present within the molecule. Radioiodine was selected because of its multiple potential applications depending on the selected isotope, including ^{124}I for positron emission tomography, ^{131}I for radiotherapy, and ^{125}I for inexpensive, quantitative research applications.

A standard protein-labeling technique was adapted for application to the copolymers in this work. The successful adaptation of this procedure for use with our polymers represented the first demonstration in the field of a nanoparticle-forming polymer that was directly labeled with radioiodine without any additional chemical-alterations or intermediate reactions. The process was characterized using a variety of chromatographic techniques and radiometric measurements to confirmed covalent, stable attachment of iodine in a product with high radiochemical purity.

The alternating amphiphilic copolymers were combined with an engineered peptide having an extremely high binding affinity for the epidermal growth factor receptor (EGFR), a biomarker prevalent in a variety of human cancers. This high-affinity binder, the EI3.4.3 peptide, was developed by collaborator Dr. Benjamin Hackel under the guidance of Professor K. Dane Wittrup. A number of polymer design variables were considered, including the targeting ligand density, identity of the hydrophobic sidechain, polymer molecular weight, and length of the spacer connecting the peptide to the backbone. The ligand density and hydrophobic sidechain identity were chosen for study.

Initial studies demonstrated selective uptake of EI3.4.3-conjugated polymers into a target-bearing, EGFR-positive human cancer cell line relative to untargeted controls. Preparative gel permeation chromatography (GPC) was used to create high molecular weight, low polydispersity fractions of backbone polymer. Polymers synthesized from these fractions achieved the greatest increase in selective uptake *in vitro* with a four- to

sixfold increase in uptake for EI3.4.3-conjugated polymers relative to untargeted controls. Animal studies measured the biodistribution, blood circulation, and tumoral accumulation of various polymer formulations. Statistically significant selective tumor accumulation was observed for two different targeted polymers, each having different targeting ligand density and different hydrophobic sidechains.

The EI3.4.3-polymers have proven a rich platform for study. Their demonstrated ability to selectively accumulate in targeted tumors combined with their potential use in diagnostic and/or therapeutic clinical applications makes them an attractive option for intensified investigation.

Thesis Supervisor: Clark K. Colton
Title: Professor of Chemical Engineering

Acknowledgements

The execution of the work described in this thesis was supported by innumerable people, both inside and outside of the M.I.T. community. First and foremost, I would like to express my sincerest gratitude to Prof. Clark K. Colton for his guidance throughout my graduate career. I would like to thank Clark for sharing his unbridled excitement for challenging scientific problems and for providing me with the critical eye required to interpret and present results meeting a high standard of excellence. I must also thank Prof. Arthur Watterson, my committee member and our close collaborator, for his continued support of my research and his continued willingness to educate a chemical engineer with a proclivity for organic chemistry. Thank you, as well, to Professor Dane Wittrup for his support and focused direction, Professor Robert Fisher for our many long chats and shared experiences at the General Mills Practice School station, and to Professor Anna Moore for providing the biological insight and guidance that was integral to this work.

During this research, I had the greatest fortune to collaborate heavily with Dr. Michelle Miller, a previous graduate of the Colton Lab. I credit much of my growth as a scientist and scientific thinker to my daily interactions with Michelle during our period of overlap on the project. I would like to thank her for always listening to my ideas, no matter how far-fetched, and for never hesitating to engage me in scientific debate. Most importantly, much of the success described in this thesis would not have been realizable without the knowledge gained and experimental techniques developed during Michelle's doctoral thesis. I would also like to thank my fellow Colton Lab colleagues, especially Jeff Millman and Jit Hin Tan, for their unbelievable support, both scientific and otherwise, over the course of our time together in 66-457.

I would like to thank the entire lab of Prof Arthur Watterson at the University of Massachusetts – Lowell, particularly Drs. Bhavna Gupta, Vijayendra Kumar, and Mukesh Pandey, for developing and executing the synthetic techniques required to produce material for these studies. Their skill and dedication enabled our collaboration to study nearly all of the polymers we could conceive. Special thanks are owed to Dr. Benjamin Hackel, whose superbinding EI3.4.3 peptide was responsible for fulfilling perhaps the most important word in the title of this thesis, 'targeted.' I am extremely grateful for his willingness to share his discovery for our research and for his continued collaborative spirit.

I would also like to thank the students, as well as Prof. William Dalzell, from the 2007 and 2009 10.26 course at MIT, who share in the achievements realized for the backbone polymerization. The students included Nathalie Pinkerton (who was also a UROP), Julie Shi, Drew Cameron, Greg Johnson, Anisa McCree, and Jose Sepulveda. Thank you, also, to James Steeves and Artisan Industries for their design and loan of the Protherm thin-film reactor. I would like to thank Dr. Mikhail Papisov for his extreme generosity in completing our PET imaging and, most significantly, for his willingness to devote many hours of personal discussion to a student with no official affiliation with his lab, department, or institution.

The majority of this research was funded by Axle International (The Hague, Netherlands) through a research grant sponsored by Dr. Eric Aiazian. In addition to my sincere gratitude for the financial support, I would also like to thank Dr. Aiazian for his participation as a scientific collaborator in addition to his role as sponsor. His clinical perspective was extremely valuable to the project and his focus on product commercialization was exciting for me for its potential applicability in my scientific career.

Finally, I would like to thank all of my family and friends for their unwavering support throughout my studies. To my MIT classmates, who know who they are, thank you for being fantastic friends first, and impressive colleagues second. To my mother, father, and sister, Katie, thank you for your love, support, patience, and understanding when my research or schoolwork precluded me from being the best son or brother that I should have been. To Jenny, thank you for always being there with universal love and support, both on days of triumph and frustration. Thank you for always sticking up for me, especially when I was unable to do so myself. And thank you, most of all, for popping your head in the circular window of my lab door or for tapping on the glass from the sidewalk outside of Building 66.

I would like to dedicate this thesis to my grandparents (Opa, Oma, and Grandma) and to someone I look forward to meeting very soon.

TABLE OF CONTENTS

1. Introduction 11
   1.1. Cancer 11
   1.2. A novel amphiphilic alternating copolymer 13
   1.3. Tumor Targeting by Passive and Active Mechanisms 15
   1.4. Summary of the Research 17
   1.5. References 18
2. Chemical Synthesis of Amphiphilic Alternating Copolymers 21
   2.1. Polymer synthetic scheme 21
   2.2. Peptide production 26
   2.3. References 27
3. Reaction Engineering of an Enzymatically Catalyzed Polymerization 28
   3.1. Background 28
      3.1.1. Enzymatic polymerization 28
      3.1.2. Reactor design for mass transfer limited processes 32
      3.1.3. Backbone Polymer Molecular Weight and Targeted Delivery 38
   3.2. Materials and Methods 40
      3.2.1. Materials 40
      3.2.2. Polymerization procedure in flasks 40
      3.2.3. Polymerization procedure in the Protherm 42
      3.2.4. Flow visualization 45
      3.2.5. Comminution of Novozym435 45
      3.2.6. Effect of Molecular Sieves on the Polymerization 46
      3.2.7. Forward Rate Constant Determination 46
      3.2.8. Residual Water Content after Drying 49
      3.2.9. Molecular Weight Determination by GPC 50
   3.3. Homogeneous model formulation 51
      3.3.1. Overall Strategy for Homogeneous Model Simulations 52
      3.3.2. Kinetic Model Overview – System of Reactions 52
      3.3.3. From concentration to molecular weight 57
      3.3.4. Determination of Model Parameters 60
   3.4. Fickian diffusion model formulation 63
   3.5. Results 70
      3.5.1. Conversion between PM and CM 70
      3.5.2. Forward Rate Constant Determination 75
      3.5.3. Residual Water after Drying 78
      3.5.4. Kinetic Modeling: Molecular Weight versus Time 79
      3.5.5. Equilibrium Modeling: Molecular Weight as a Function of PM 83
      3.5.6. Methanol Mass Transfer Modeling: Analytical Solutions 87
      3.5.7. Mass Transfer Modeling: Model Results 89
      3.5.8. Evaluating Polymer Molecular Weight by GPC 97
      3.5.9. Experimental Evaluation of Key Variables in Flasks 100
      3.5.10. Polymerization with the Addition of 4Å Molecular Sieves 105
      3.5.11. Backbone Polymerization in the Protherm 108
      3.5.12. Comparison of Results in the Flask and the Protherm 113
      3.5.13. Comparison of Experimental Results and Model Predictions 116

3.6. Discussion 120
3.7. Conclusion 127
3.8. References 128
4. Radioiodination method development for quantitative analysis 131
4.1. Introduction 131
4.2. Materials and Methods 138
4.2.1. Materials 138
4.2.2. Iodine attachment 139
4.2.3. Separation of Labeled Product and Free Iodine 140
4.2.4. Characterization of Labeled Materials – Analytical Tools 142
4.2.5. Confirmation of Covalent Attachment Using Sephadex 145
4.2.6. Confirmation of Covalent Attachment Using Radio-HPLC 147
4.2.7. Effect of the Iodination on Chemical Structure 147
4.2.8. GPC Analysis of Void Volume Fraction 149
4.2.9. Elution Profile of Free Iodine-125 149
4.2.10. Elution Profile of Post-Reaction Mixtures 150
4.2.11. Fractional Recovery for Purification with and without BSA 150
4.2.12. Labeling yield 152
4.2.13. Radiolabel stability 152
4.3. Results 153
4.3.1. Confirmation of Covalent Attachment Using Sephadex 153
4.3.2. Confirmation of Covalent Attachment Using Radio-HPLC 156
4.3.3. Effect of Iodination on Chemical Structure 159
4.3.4. Effect of the Iodination on Older Polymer Samples 163
4.3.5. GPC Analysis of Void Volume Fractions 165
4.3.6. Elution Profile of Free Iodine-125 166
4.3.7. Elution Profile of Post-Reaction Mixtures 169
4.3.8. Fractional Recovery for Purification with and without BSA 172
4.3.9. Labeling Yield 173
4.3.10. Labeling Yield for Ornamented Polymers 177
4.3.11. Radiolabel Stability 178
4.3.12. Radiolabeling High Molecular Weight Backbone 179
4.4. Discussion 183
4.5. Conclusion 194
4.6. References 196
5. Physico-chemical and Biological Evaluation of EI3.4.3-Conjugated Polymers 199
5.1. Introduction 199
5.1.1. Polymeric micelles 201
5.1.2. Targeted Delivery with the Alternating Amphiphilic Copolymers 204
5.1.3. The EI3.4.3 Peptide Targeting Ligand 205
5.2. Design of targeted polymers 206
5.2.1. Targeting Density and Molecular Weight 207
5.2.2. Hydrophobic Sidechain Identity 210
5.2.3. Spacer length 211
5.2.4. Experimental strategy 211
5.3. Materials and Methods 212

5.3.1. Materials 212
5.3.2. Backbone Polymer Fractionation by Preparative SEC 213
5.3.3. Evaluation of Preparative GPC for Fractionation 214
5.3.4. Development of a High-Throughput Fractionation Process 214
5.3.5. Dynamic Light Scattering 215
5.3.6. Cell Culture, Lines and Media 216
5.3.7. Cellular Uptake Measurement with [125I]-polymer 216
5.3.8. Cell Counting 218
5.3.9. Biodistribution and Blood Circulation in a Mouse Model 218
5.3.10. Comparison of in vivo Results to Model Predictions 220
5.4. Results 223
5.4.1. Polymer naming convention 223
5.4.2. In vitro Targeting with EI3.4.3-Polymers – Initial Study 224
5.4.3. Evaluation of Preparative GPC for Polymer Fractionation 228
5.4.4. Development of a High-Throughput Fractionation Process 232
5.4.5. Size Measurements of EI3.4.3-Conjugated Polymers 234
5.4.6. In vitro Uptake of Free EI3.4.3 Peptide 240
5.4.7. In vitro Uptake of EI3.4.3-Conjugated Polymers 241
5.4.8. Uptake Measurements in EGFR-positive and negative Cell Lines 246
5.4.9. Analysis of Uptake Normalized by Initial Peptide Concentration 249
5.4.10. Biodistribution and Blood Circulation in a Mouse Model 252
5.4.11. Tumor Targeting Compartmental Model Predictions 256
5.5. Discussion 259
5.6. Conclusion 268
5.7. References 269

Appendix A. Molecular weight calculation and Chromatogram Manipulation 274
Appendix B. MATLAB Codes for Kinetic and Mass Transfer Modeling 279
Appendix C. Model Parameter Calculations 285
Appendix D: Viscosity Measurements of PEG and Catalyst 288
Appendix E. Effect of Iodination: Recovery and Chromatogram Adjustments 293
Appendix F. Unicorn Method for Backbone Polymer Fractionation 295
Appendix G: Additional Representations of the Cellular Uptake Results 297
Appendix H: Positron Emission Tomography (PET) of ^{124}I-labeled polymers 300

1. Introduction

1.1 Cancer

According to data compiled by the American Cancer Society available publicly on their website, approximately 1,479,000 new cases of cancer were expected to be diagnosed while 562,340 Americans were expected to die from cancer in 2009 alone. The lifetime probability of developing cancer is 43.9% for men and 37.4% for women. Even though advances in early diagnosis and therapy over the past few decades have led to continual decreases in cancer incidence and mortality, cancer remains the second leading cause of death among all Americans trailing only heart disease [1]. It is therefore apparent that further technological development in all areas of cancer detection and treatment are still of great importance not only to the scientific community, but to society itself.

In the field of cancer imaging, moderate progress has been achieved in increasing the speed and resolution of computed tomography (CT) and magnetic resonance (MR) imaging. The primary shortcoming of these 'traditional' imaging methods is their inability to detect tumors smaller than 2 mm in width (containing fewer than 500,000 cells). A significant consequence of this detection limit is the resulting underdiagnosis of metastatic disease, [2] which is significant because occurrence of metastases drastically reduce patient survival rates. Finally, the response to therapeutic treatment is also unsatisfactorily monitored by current imaging techniques. To most effectively overcome these shortcomings, the ability of a tumor to differentially scatter, absorb, or emit radiation must be maximized using new imaging techniques, novel imaging agents, or a combination of both.

In the area of cancer treatment, advances in chemotherapy and radioimmunotherapy, in conjunction with the progress in cancer diagnosis, have led to a decrease in cancer incidence and mortality rates. However, the *in vitro* potency of therapeutics rarely translates directly when administered to patients. A successful therapeutic must not only be effective in the solid tumor microenvironment, but must also reach the target in sufficient quantities and with minimal toxicity to normal tissues [3, 4]. Although it would be ideal to build pharmacological features such as solubility, stability, permeability, and targeting into the bioactive agent itself, it is more reasonable to build such features into a delivery system that enhances the drug function [5].

1.2 A novel amphiphilic alternating copolymer

The group of Arthur Watterson at the University of Massachusetts Lowell has developed an alternating amphiphilic chemo-enzymatically synthesized copolymer that forms micelles with a highly adaptable chemistry with potential application as a carrier of imaging agents or therapeutics [6]. These micelles, which have been observed to have hydrodynamic diameters between 10-100 nm, will be referred to as nanoparticles.

The alternating amphiphilic copolymers are produced by a well-developed synthetic scheme (FIGURE 1.1A). A trifunctional diester linker molecule (shown schematically in purple) is copolymerized with the hydrophilic diol, poly(ethylene glycol) (PEG, in green), in an enzymatically catalyzed condensation reaction to form a polyester designated the 'backbone polymer.' A hydrophobic sidechain is then attached to the backbone via the remaining functional group on the linker molecule. Under the proper aqueous conditions, the resulting alternating amphiphilic polymer chains

spontaneously self-assemble to form nano-sized micelles, or nanoparticles. The organic chemistry of the required reaction scheme is described in the second chapter: Synthesis.

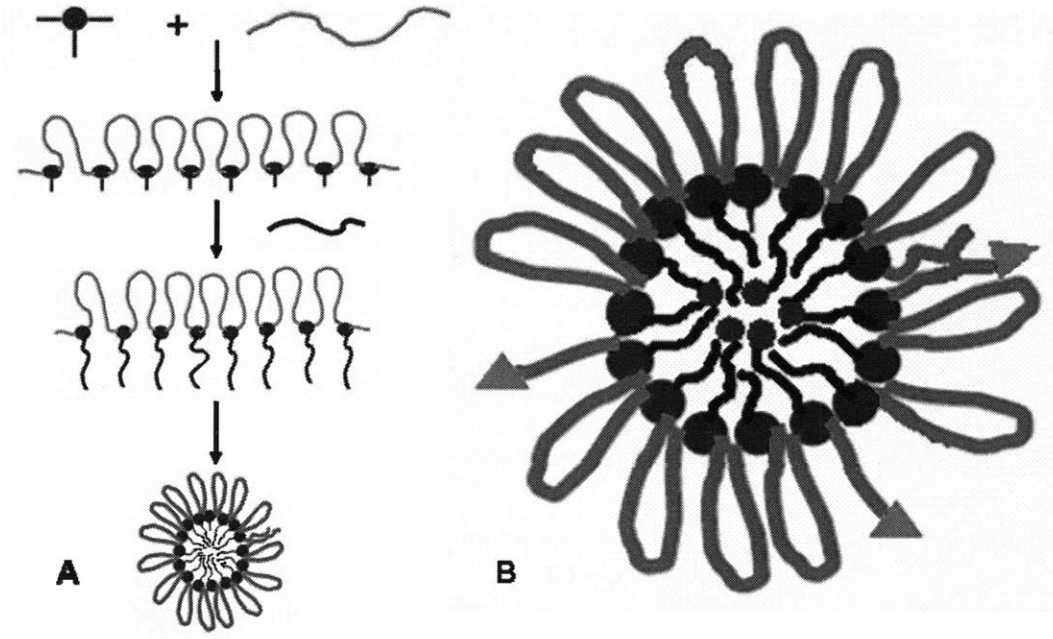

Figure 1.1. Schematic diagram of the (A) chemo-enzymatic synthesis of the amphiphilic alternating copolymers, and (B) the resulting nanoparticles modified for targeted delivery applications.

To address the challenges in cancer diagnosis and therapy outlined above, additional synthetic methods have been developed at UML and at MIT to incorporate contrast and therapeutic agents, as well as targeting moieties, into the nanoparticles via either direct chemical conjugation or encapsulation. Examples of these modifications are shown schematically in FIGURE 1.1B. Targeting ligands (red triangles) can be attached to the polymer via hydrophilic PEG spacer groups (green). These ligands are attached to direct the nanoparticles to target-bearing cells, *in vitro* and, ultimately, *in vivo*. Selection of agents for active targeting of human cancer cell lines is discussed in the subsequent section.

Contrast agents for enhanced imaging techniques have also been attached directly to or encapsulated by the nanoparticles. Examples of these applications include the

attachment and encapsulation of perfluorocarbon chains that are responsive in ^{19}F magnetic resonance imaging applications. Interestingly, the perfluorocarbon chains attached as sidechains contribute to the final application not only as a potential contrast agent, but as the hydrophobic sidechain required to impart the amphiphilicity required in the final polymer for spontaneous self-assembly. The study of perfluorinated polymers was a significant portion of a previous thesis in the Colton lab completed by Dr. Jin Zhou Dawson [7].

The alternating amphiphilic copolymers have also been used to encapsulated chemotherapeutic and therapeutic agents, such as doxorubicin, paclitaxel [8], and aspirin [9]. This application is shown schematically in FIGURE 1.1A by the blue circles. Encapsulation of chemotherapeutics is an attractive application for our polymer system and others like for two reasons: (1) chemotherapeutics typically have large, hydrophobic structures that make them poorly soluble in water or the bloodstream and (2) the hydrophobic interior of polymeric micelle nanoparticles contains a microenvironment in which chemotherapeutics have significant solubility. Encapsulation of chemotherapeutic agents can also increase the stability of the micelle, which may also be a desirable advantage. Previous work in the Colton lab by Dr. Michelle Miller investigated our polymer system for its potential use in targeted therapeutic applications [8].

The flexibility of the chemical structure used to create the nanoparticles described above provided even more options beyond those studied in the theses of Drs. Dawson and Miller. For this work, attachment of radiolabels, specifically radioisotopes of iodine, was chosen as the focus. The unique chemical structure of the polymer system allowed for direct attachment of radioiodine using methods originally developed for radiolabeling of

small proteins and antibodies. Radioiodine was also an attractive option due to its use in a wide array of clinical application depending on the selected isotope. For example, ^{124}I is a positron emitting isotope that can be used in positron emission tomography (PET), ^{125}I and ^{123}I are gamma emitting isotope used in single photon emission computed tomography (SPECT) and nuclear scintigraphy, while ^{131}I is a strong gamma emitting isotope used commonly in clinical radioimmunotherapy. For the purposes of this research, ^{125}I was chosen as the primary isotope due to its comparatively low cost and ease of detection using standard gamma counting techniques.

In addition to those previously described, synthetic schemes have also been developed to attach fluorescent dyes, including Cy5.5 and FITC for near infrared fluorescence (NIRF) and optical imaging applications, respectively.

1.3 Tumor Targeting by Passive and Active Mechanisms

Targeting is required to increase the delivery of an intended agent to a tumor *in vivo*. An effective targeting technique will be highly specific for the targeted tumor in order to minimize the accumulation in untargeted, normal tissues in the body. By minimizing non-specific accumulation, the toxic side-effects of chemo- and radiotherapeutic agents can be significantly reduced while the efficacy of the administered dose is maintained by effective targeting.

Tumor targeting can be achieved through two distinct mechanisms in cancer applications: (1) passive or (2) active. These two mechanisms are not necessarily mutually exclusive and can therefore both be exploited for maximum targeting efficiency. In passive tumor targeting, macromolecules take advantage of the "leaky vasculature" commonly observed in tumors *in vivo*. This increased passive uptake by tumors, which

was originally described by Maeda, is known as the enhance permeability and retention (EPR) effect [10-12]. According to the EPR effect theory, tumors grow so rapidly that they are unable to develop fully functional vascularization or effective lymphatic drainage systems. These vascular and lymphatic defects allow macromolecular particles, typically between 5 and 200 nm in hydrodynamic diameter [13-16], to preferentially accumulate in tumors by completely passive, mass transfer-related mechanisms.

Tumor targeting can also be achieved through active mechanisms, specifically the through targeting of a receptor present on the cell surface of a cancerous cell in a tumor. This targeting is achieved by attaching a targeting ligand to a circulating delivery system, such as a nanoparticle, that has a high affinity and specificity to the targeted cell surface receptor. There is a wide array of targeting pairs under investigation in the literature. The most common of these is folate used to target the folate receptor [17-21]. Other targeting pairs include epidermal growth factor (EGF) and the epidermal growth factor receptor (EGFR) [22], anti-carcinoembryonic antigen (CEA) antibody and CEA [23], and telomerase inhibitor and telomerase [24].

For this research, the epidermal growth factor receptor (EGFR), the overexpression of which is associated with reduced survival in 70% in a variety of human carcinomas [25], was chosen as the target antigen due to the availability of an extremely high affinity (low dissociation constant) targeting ligand by means of a collaboration with a colleague in the Department of Chemical Engineering at MIT, Dr. Benjamin Hackel. The pertinent details for the high affinity binder, which was given the designation EI3.4.3 by its inventor, are presented in the introduction to Chapter 5.

1.4 Summary of the Research

The overall goal of this project was the development and biological evaluation of a novel, highly adaptable, targeted nanoparticle system for potential imaging and radioimmunotherapeutic applications in the diagnosis and treatment of cancer. The three major areas of investigation were (1) nanoparticle synthesis, (2) radiolabeling with isotopes of iodine, and (3) biological evaluation both *in vitro* and *in vivo*.

The nanoparticle synthesis involved the investigation and development of a chemo-enzymatic polymerization reaction to produce significant quantities of high molecular weight backbone polymer for use as the starting material in the synthesis of the targeted alternating amphiphilic copolymers. To accomplish this, the polymerization was studied as it was originally developed – in flasks. These initial studies, together with theoretical kinetic and mass transfer modeling, were used to develop improvements to the polymerization. These improvements included both improved reaction conditions and reactor configurations aimed at reducing mass transfer limitations. A novel, continuous thin-film evaporator prototype developed by our industrial collaborators at Artisan Industries (Waltham, MA) was adapted for use as a thin-film batch reactor. These advances in backbone polymer molecular weight sought to improve the biological performance of the resulting targeted nanoparticles.

The area of polymer radiolabeling focused on the adaptation and implementation of a procedure commonly used to radioiodinate proteins for use with our polymer system. Successful radiolabeling with radioiodine provided two important benefits. In the near term, labeling with iodine-125 enabled quantitative analysis of the performance of the labeled polymers in *in vitro* and *in vivo* experimentation. In the long term, this developed

method could be used with different isotopes of iodine for a variety of imaging and therapeutic applications in either research or clinical settings. A number of characterization tests were performed to validate the successful adaptation of the iodination method, including measurements of the structure and stability of the labeled polymer. Additional studies sought to determine the reaction and purification conditions required to maximize reaction yield and product recovery while minimizing radiochemical impurities.

Finally, the biological characterization investigated the nanoparticles in *in vitro* cellular uptake studies to determine whether the presence of the targeting ligand could increase uptake relative to that measured for untargeted control polymers. Any increase in uptake due to targeting would represent selectivity for the targeted antigen on the cell surface. The nanoparticles tested *in vitro* would also be tested in *in vivo* biodistribution and blood circulation studies to determine their tumor targeting efficacy. These biological studies were also supported by particle size distribution measurements by dynamic light scattering.

1.5 References

1. *Greenlee, R.T., Hill-Harmon, M. Murray, T., Thun, M., Cancer Statistics, 2001. CA: A Cancer J for Clinicians, 2006.* ***51****: p. 15-36.*
2. *Benaron, D.A., The future of cancer imaging. Cancer and Metastasis Rev, 2002.* ***21****: p. 45-78.*
3. *Jain, R.K., Delivery of molecular medicine to solid tumors. Science, 1996.* ***271****: p. 1079-1080.*
4. *Jain, R.K., The next frontier of molecular medicine: Delivery of therapeutics. Nature Medicine, 1998.* ***4****(6): p. 655-657.*
5. *Hubbell, J.A., Enhancing drug function. Science, 2003.* ***300****: p. 595-596.*
6. *Kumar, R., Shakil, N. A., Chen, M-H., Parmar, V. S., Samuelson, L. A., Kumar, J., Watterson, A. C., Chemo-enzymatic synthesis and characterization of novel functionalized amphiphilic polymers. J Macromolecular Science, 2002.* ***A39****(10): p. 1137-1149.*

7. *Dawson, J.Z., Physicochemical characterization of PEG-based comb-like amphiphilic copolymer structures for possible imaging and therapeutic applications, in Chemical Engineering. 2008, MIT: Cambridge.*
8. *Miller, M.T., In vitro evaluation of cytotoxicity and cellular uptake of alternating copolymers for use as drug delivery vehicles, in Chemical Engineering. 2009, MIT: Cambridge.*
9. *Sharma, S.K., Kumar, R., Kumar, S., Mosurkal, R., Parmar, V. S., Samuelson, L. A. Watterson, A. C., Kumar, J., Influence of EDA-pi interactions in drug encapsulation using nanospheres. Chem Comm, 2004: p. 2689-2691.*
10. *Maeda, H., The enhanced permeability and retention (EPR) effect in tumor vasculature: The key role of tumor-selective macromolecular drug targeting. Advan Enzyme Regul, 2001. **41**: p. 189-207.*
11. *Maeda, H., Wu, J., Sawa, T., Matsumura, Y., Hori, K., Tumor vascular permeability and the EPR effect in macromolecular therapeutics: A review. J Controlled Release, 2000. **65**: p. 271-284.*
12. *Noguchi, Y., Wu, J., Duncan, R., Strohalm, J., Ulbrich, K., Akaike, T., Maeda, H., Early phase tumor accumulation of macromolecules: A great difference in clearance rate between tumor and normal tissues. Jpn J Cancer Res, 1998. **89**(307-314).*
13. *Gref, R., Domb, A., Quellec, P., Blunk, T., Muller, R. H., Verbavatz, J. M., Langer, R., The controlled intravenous delivery of drugs using PEG-coated sterically stabilized nanospheres. Adv Drug Delivery Rev, 1995. **16**: p. 215-233.*
14. *Hobbs, S.K., Monsky, W. L., Yuan, F., Roberts, W. G., Griffith, L., Torchilin, V. P., Jain, R. K., Regulation of transport pathways in tumor veseels: Role of tumor type and microenvironment. PNAS, 1998. **95**: p. 4607-4612.*
15. *Yuan, F., Dellian, M., Fukumura, D., Leunig, M., Berk, D. A., Torchilin, V. P., Jain, R. K., Vascular permeability in a human tumour xenograft: Molecular size dependence and cutoff size. Cancer Research, 1995. **55**(3752-3756).*
16. *Wu, N.Z., Da, D., Rudoll, T. L., Needham, D., Whorton, A. R., Dewhirts, M. W., Increased microvascular permeability contributes to preferential accumulation of stealth liposomes in tumor tissue. Cancer Research, 1993. **53**: p. 3765-3770.*
17. *Rossin, R., Pan, D., Qi, K., Turner, J. L., Sun, X., Wooley, K. L., Welch, M. J., 64Cu-labeled folate-conjugated shell cross-linked nanoparticles for tumor imaging and radiotherapy: Synthesis, radiolabeling, and biologic evaluation. J Nucl Med, 2005. **46**(7): p. 1210-1218.*
18. *Low, P., Antony, A. C., Folate receptor-targeted drugs for cancer and inflammatory diseases. Adv Drug Delivery Rev, 2004. **56**(8): p. 1055-1058.*
19. *Lu, Y., Low, P. S., Immunotherapy of folate receptor-expressing tumors: Review of recent advances and future prospects. J Controlled Release, 2003. **91**(1-2): p. 17-29.*
20. *Hong, S., Leroueil, P. R., Majoros, I. J., Orr, B. G., Baker, Jr., J. R., Holl, M. M. B., The binding avidity of a nanoparticle-based multivalent targeted drug delivery platform. Chemistry & Biology, 2007. **14**: p. 107-115.*
21. *Kukowska-Latallo, J.F., Candido, K. A., Cao, Z., Nigavekar, S. S., Majoros, I. J., Thomas, T. P., Balogh, L. P., Khan, M. K., Baker, Jr., J. R., Nanoparticle*

targeting of anticancer drug improves therapeutic response in animal model of human epithelial cancer. Cancer Research, 2005. ***65****(12): p. 5317-5324.*

22. *Hackel, B.J., Fibronectin Domain Engineering, in Chemical Engineering. 2009, M.I.T.*
23. *Williams, L.E., Beatty, B. G., Shively, J. E., Beatty, J. D., Accumulation of radiolabeled anti-CEA antibody in the case of multiple LS174T tumors in a nude mouse model. Cancer Biotherapy and Radiopharmaceuticals, 2001.* ***16****(2): p. 147-157.*
24. *Matera, L., The choice of the antigen in the dendritic cell-based vaccine therapy for prostate cancer. Cancer Treatment Rev, 2010.* ***36****(2): p. 131-141.*
25. *Nicholson, R.I., Gee, J. M., Harper, M. E., EGFR and cancer prognosis. European J Cancer, 2001.* ***37 Sup 4****: p. S9-S15.*

2. Chemical Synthesis of Amphiphilic Alternating Copolymers

2.1 Polymer Synthetic Scheme

A number of synthetic schemes have been investigated to produce amphiphilic alternating copolymers conjugated to a variety of sidegroups, including hydrophobic chains, hydrophilic (PEG) chains, targeting peptides, fluorescent dyes, and other organic molecules [1-6]. The majority of this work has been performed, under the guidance of Professor Arthur C. Watterson (UMass-Lowell), by Rajesh Kumar, Rahul Tyagi, Mukesh Pandey, Vijayendra Kumar, and Bhavna Gupta, in collaboration with Clark Colton *et al.* The different reactants, intermediates, and reaction conditions were studied for their effect on yield, purity, cross-linking, polymer aggregation, and cytotoxicity. Based on these studies and the specific requirements of the proposed work, the following synthetic scheme has been developed, characterized, and implemented to supply the radiochemical, physico-chemical, *in vitro* and *in vivo* experiments described in subsequent chapters.

The first step in the synthesis is the chemo-enzymatic polymerization reaction to form the alternating copolymer designated as 'backbone polymer.' The chemical structure for this step is presented in FIGURE 2.1.

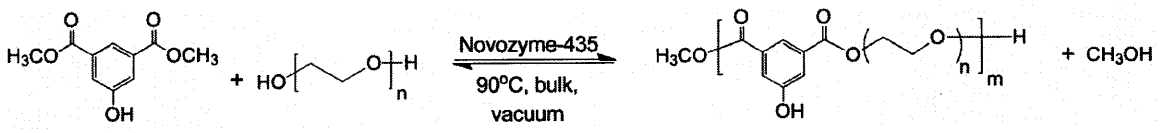

Figure 2.1. Enzymatically catalyzed polymerization to synthesize the alternating copolymer backbone.

In this reaction, dimethyl 5-hydroxyisophthalate, which will be referred to as the linker, reacts with PEG (MW = 900 or 1000 Da) to produce the alternating copolymer backbone and the methanol byproduct. This reaction is catalyzed by Novozym435, a lipase derived from *Candida antarctica* immobilized on an acrylic resin, and is typically

performed under bulk, solvent-free conditions. The backbone polymer product contains free aromatic hydroxyl groups available for reaction to attach the various sidechains listed above. Before any further attachments occur, activation reactions are performed to prepare the intended sidechains, including the PEG spacer as well as the hydrocarbon and perfluorocarbon hydrophobic chains, for reaction with the linker hydroxyls (FIGURE 2.2).

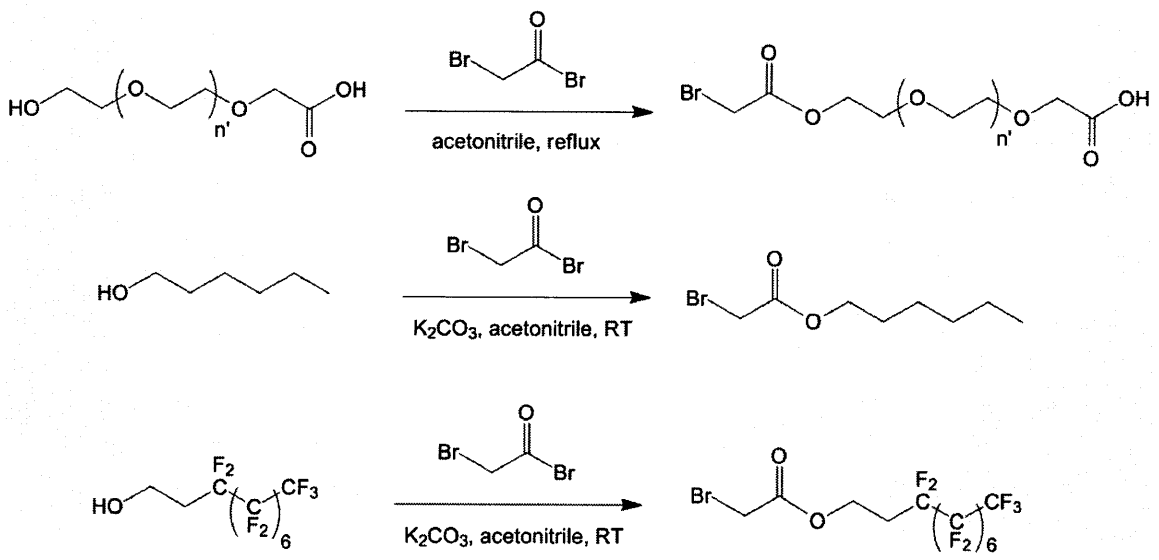

Figure 2.2. Intended sidechains are activated through reaction with bromoacetyl bromide.

All three sidechains are reacted with bromoacetyl bromide to produce the activated form of the sidechain that is terminated with the bromoester. Activation in this manner provides a strong leaving group that is highly reactive with the linker hydroxyls. Although a PEG of unspecified length is represented in the scheme, this reaction has been successfully performed with PEG 900, 1500, and 3400, along with triethylene glycol (TEG). All three unactivated sidechains are commercially available; however, the bifunctional high MW PEG molecules are a specialty chemical available from Lysan Bio (Arab, AL). The bifunctional PEG, with its carboxylate and hydroxyl endgroups can be used to synthesize PEGs with a single activated site. Use of the bifunctional PEG

therefore mitigates potential cross-linking that would occur for a dually activated PEG diol.

The activated PEG (or TEG) spacer molecule is attached to the backbone polymer according to the scheme depicted in FIGURE 2.3. Because of the high reactivity of the bromoester, the reaction between the activated PEG and backbone polymer goes to completion. Consequently, the percent substitution of the PEG spacer, X, could be varied by adjusting the amount of activated PEG added to the reaction. The reaction is performed in acetonitrile in the presence of the base, potassium carbonate, at room temperature (RT).

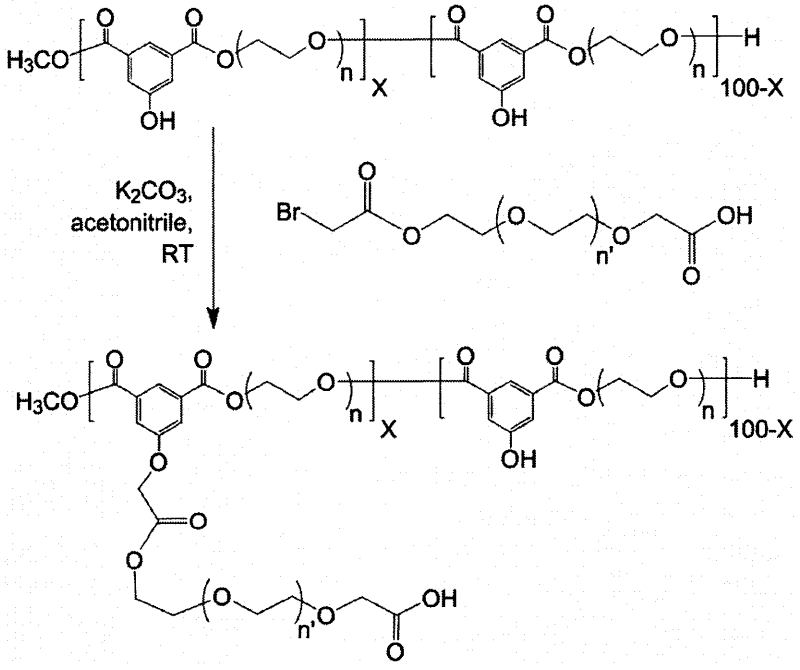

Figure 2.3. Attachment of the activated PEG spacer to the backbone polymer via the linker hydroxyl. The activated spacer is added according to the desired percent substitution, X.

The hydrophobic sidechains are added by the same reaction, including the same reaction conditions, as that for the PEG spacer (FIGURE 2.4). Either hydrocarbon or perfluorocarbon chains can be attached by this method.

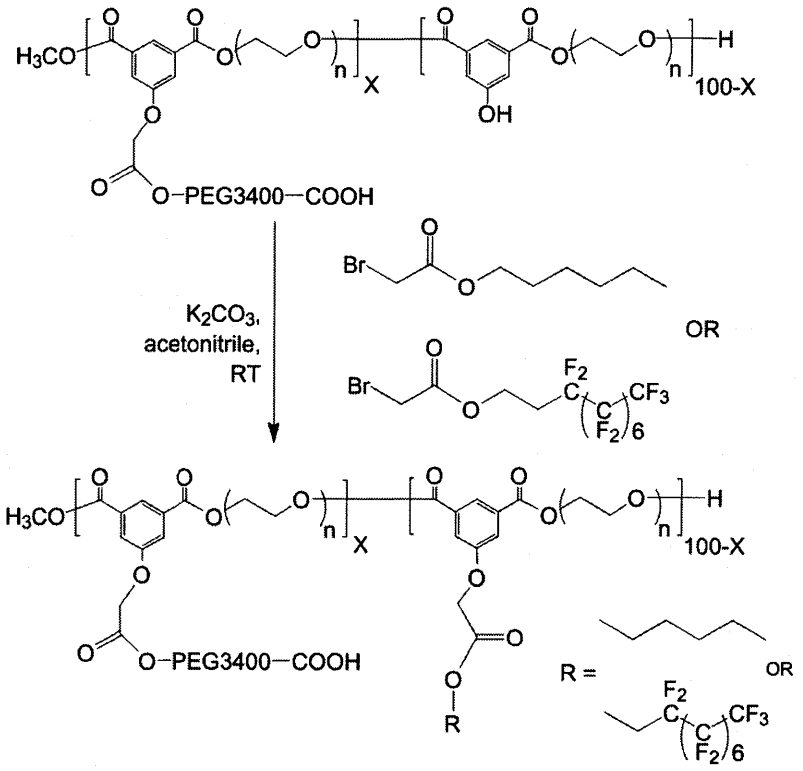

Figure 2.4. Attachment of the activated hydrophobic sidechain, either hydrocarbon or perfluorocarbon, to the backbone polymer via the remaining linker hydroxyls.

If the targeting peptide is to be attached, the terminal hydroxyl on the PEG spacer is activated using N-hydroxysuccinimide (NHS) in the presence of dicyclohexylcarbodiimide (DCC) in acetonitrile at room temperature. This reaction (FIGURE 2.5) produces an activated NHS-ester that reacts readily with amino groups, such as the lysine residues or N-terminal amines present in proteins. The acetonitrile is allowed to evaporate in a fume hood and the polymer is resuspended in a phosphate buffered saline (PBS) solution containing the EI3.4.3 peptide. The peptide is added stoichiometrically with respect to the activated ester groups on the PEG spacer. The product of this reaction is dialyzed for 24 hr using a dialysis bag with a MWCO of 10 kDa ($M_{EI3.4.3}$ = 12.5 kDa). The final result is an amphiphilic alternating copolymer conjugated to the EI3.4.3 targeting peptide.

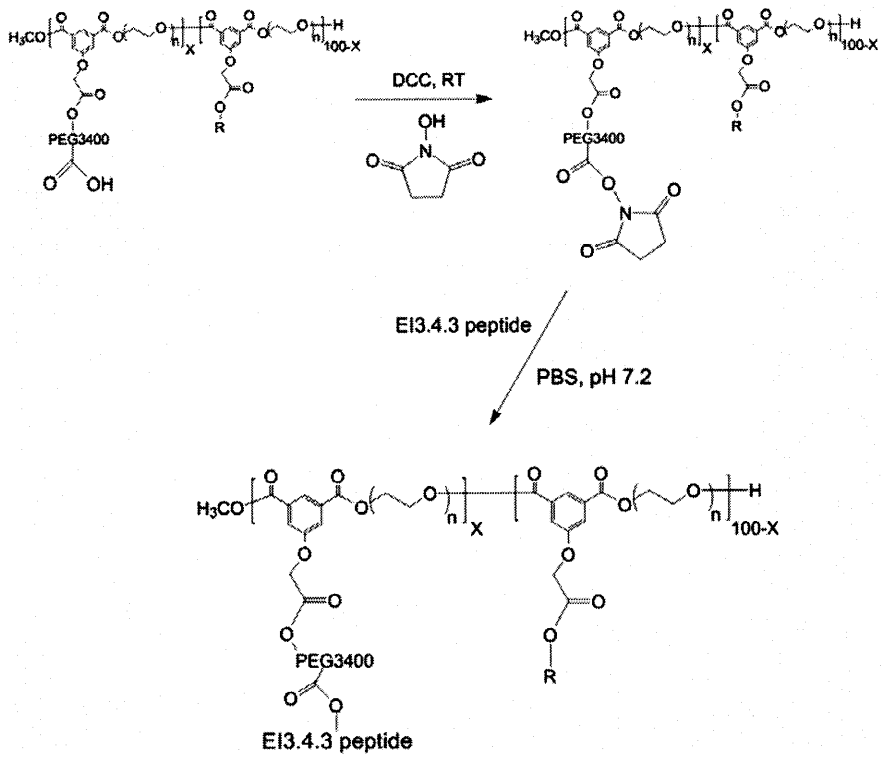

Figure 2.5. Activation of the terminal PEG carboxylate to an NHS-ester and subsequent reaction with EI3.4.3 peptide to produce the targeted amphiphilic alternating copolymer.

Product characterization was performed primarily by nuclear magnetic resonance (NMR) spectroscopy. The synthesis of model compounds was performed as necessary to simplify the spectra in order to more easily identify the peaks and peak shifts that are representative of the anticipated reaction. For example, an arginine-glycine-aspartic acid (RGD) tripeptide was used as a surrogate for the much more complicated EI3.4.3 peptide. Although thorough analysis and characterization of the synthesized polymers were integral to the successful execution of the research, it is beyond the scope and intent of this document to faithfully reproduce our collaborator's synthetic chemical analyses.

2.2 Peptide Production

The EI3.4.3 peptide is produced by standard bacterial fermentation procedures [7] using *Escherichia coli* as the recombinant host cell. Briefly, Rosetta(DE3) cells (EMD Chemicals, Gibbstown, NJ) are transformed by heat shock in order to insert the appropriate EI3.4.3-expressing, kanamycin-resistant plasmid. A starter colony is grown on a yeast extract peptone (YEPD) plate in the presence of kanamycin. A large culture is induced from the starter colony and isopropyl β-D-1-thiogalactopyranoside (ITPG) is added to stimulate transcription. This culture is incubated in a shake flask until reaching an optical density of approximately 1.

At this point, cells are centrifuged, separated from supernatant, and lysed with lysis buffer (50 mM phosphates, pH 8.0, 0.5M NaCl, 5% glycerol, 5 mM CHAPS, 25 mM imidazole). The lysed cells are filtered and subsequently purified using TALON metal-affinity chromatographic resin according to the manufacturer's protocol. The TALON resin is designed to selectively bind the six-histidine tag engineered into the N-terminus of the EI3.4.3 peptide. Multiple small-scale (1L shake flask) peptide production and purifications were kindly performed by Dr. Benjamin Hackel.

To supply the expanded *in vitro* and *in vivo* studies with EI3.4.3-conjugated polymer, large-scale peptide production was implemented in a 5 L bioreactor by Professor Carl Lawton at UMass-Lowell. The protocol for these productions was identical to that described for the small-scale with two exceptions. The expanded culture from a 1 L shake flask was transferred into the 5 L bioreactor and diluted with fresh media. As before, the cells were lysed upon achieving an optical density of

approximately one. The large-volume cell lysis was performed using a microfluidizer (Microfluidics Corp., Newton, MA).

2.3 References

1. Miller, M.T., *In vitro evaluation of cytotoxicity and cellular uptake of alternating copolymers for use as drug delivery vehicles*, in *Chemical Engineering*. 2009, MIT: Cambridge.
2. Dawson, J.Z., *Physicochemical characterization of PEG-based comb-like amphiphilic copolymer structures for possible imaging and therapeutic applications*, in *Chemical Engineering*. 2008, MIT: Cambridge.
3. Kumar, R., Tyagi, R., Parmar, V. S., Watterson, A. C., Kumar, J., Zhou, J., Hardiman, M., Fisher, R., Colton, C. K., *Perfluorinated amphiphilic polymers as nano probes for imaging and delivery of therapeutics for cancer.* Polymer Preprints, 2005.
4. Kumar, R., Chen, M-H., Parmar, V. S., Samuelson, L. A., Kumar, J., Nicolosi, R., Yoganathan, S., Watterson, A. C., *Supramolecular assemblies based on copolymers of PEG600 and functionalized aromatic diesters for drug delivery.* JACS, 2004. **126**: p. 10640-10644.
5. Kumar, R., Tyagi, R., Parmar, V. S., Samuelson, L. A., Watterson, A. C., Kumar, J., *Candida antarctica Lipase B catalyzed copolymerizations of non-proteinogenic amino acids and poly(ethylene glycol) to generate novel functionalized polyesters.* J Macromolecular Science, 2003. **A40**(12): p. 1283-1293.
6. Kumar, R., Shakil, N. A., Chen, M-H., Parmar, V. S., Samuelson, L. A., Kumar, J., Watterson, A. C., *Chemo-enzymatic synthesis and characterization of novel functionalized amphiphilic polymers.* J Macromolecular Science, 2002. **A39**(10): p. 1137-1149.
7. Hackel, B.J., *Fibronectin Domain Engineering*, in *Chemical Engineering*. 2009, M.I.T.

Reaction Engineering of an Enzymatically Catalyzed Condensation Polymerization[1]

3.1 Background

3.1.1 Enzymatic polymerization

Recent investigation has demonstrated the utility of employing enzymes to perform traditional chemical polymerizations in a more efficient and selective manner [1, 2]. In particular, *Candida antarctica* Lipase B immobilized on acrylic resin beads, which was developed and is marketed as Novozyme-435 by Novozymes A/S (Copenhagen, Denmark), overcomes a number of problems traditionally encountered in polyester chemistry. The high enantio- and regiospecificity of the enzyme in the condensation reaction of diacids/diesters with diols to form polyesters is desirable since protection and deprotection steps may be avoided while attaining a high molecular weight linear polymerization product with very little branching. These benefits are even more pronounced as the size and complexity of selected monomers increases. Because of the solubility of many diacids and diesters in diols, condensation polymerizations have often been performed in solvent-free, bulk conditions. Lipase immobilization maintains the enzymatic activity across a broad range of temperatures, up to at least 90°C and solvents, including polymer melts [3]. The polymerization, therefore, is an example of a 'green chemistry' [4].

Novozyme-435 has been used in various polyesterifications, including the polymerization of adipic acid and butane-1,4-diol to form a polyester (FIGURE 1). Use of the immobilized enzyme allows for mild reaction conditions, 40-60 °C, compared to

[1] Major portions of the work presented in this chapter were completed during 10.26 projects sponsored by the author in 2007 and 2009. Team members included Nathalie Pinkerton, Julie Shi, Drew Cameron, Greg Johnson, Anisa McCree, and Jose Sepulveda, as well as faculty advisor, William Dalzell.

those used in typical industrial production processes, >150 °C, while still achieving comparably high molecular weights [5] (FIGURE 3.1). In both cases, strong vacuum must be applied to remove the condensation byproduct.

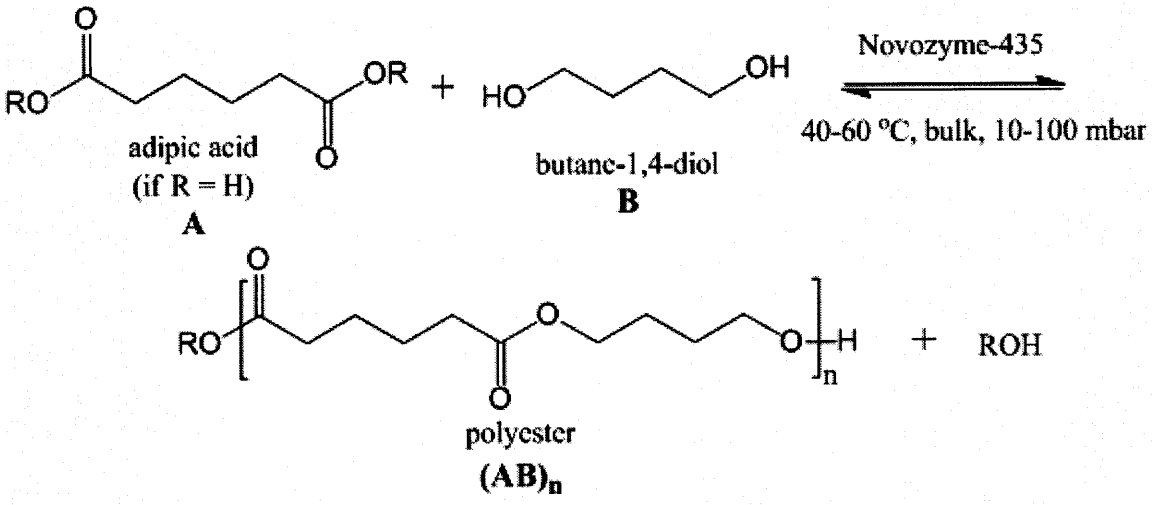

Figure 3.1. Examples of bulk polyesterification of a diester with diol using Novozyme-435 under mild reaction conditions, where R = H [6], -CH=CH$_2$ [5].

A critical factor in achieving a high molecular weight product is the removal of the condensation byproduct, ROH, such as water or methanol, or in the case of the work of Chaudhary [5], the tautomerization of the vinyl alcohol byproduct to form acetaldehyde (CH_3CHO). Continual removal of the condensation byproduct shifts the equilibrium towards the polymer product.

The mechanism for the polymerization by Novozyme-435 has been investigated by Binns et. al. by performing GPC analysis of the oligomers present during the reaction using synthesized low molecular weight intermediates for comparison [6]. In the proposed mechanism (FIGURE 3.2), the enzyme forms an active complex by acylating the diacid (or diester), **A**, forming **A-Enz**. This activated complex then reacts with the diol, **B**, to form the single polymer repeat unit, **AB**. The step is repeated for each subsequent chain extension, which leads to the eventual formation of the **B(AB)**$_n$

oligomer presented in FIGURE 1. In the acylation step, the enzyme attaches itself to the oligomer via a 'pseudo-ester bond' forming a highly reactive intermediate where the enzyme itself is the leaving group in the subsequent reaction. This step-wise mechanism was also reported by Okumura during investigation of polyesterification using Aspergillus niger lipase [7].

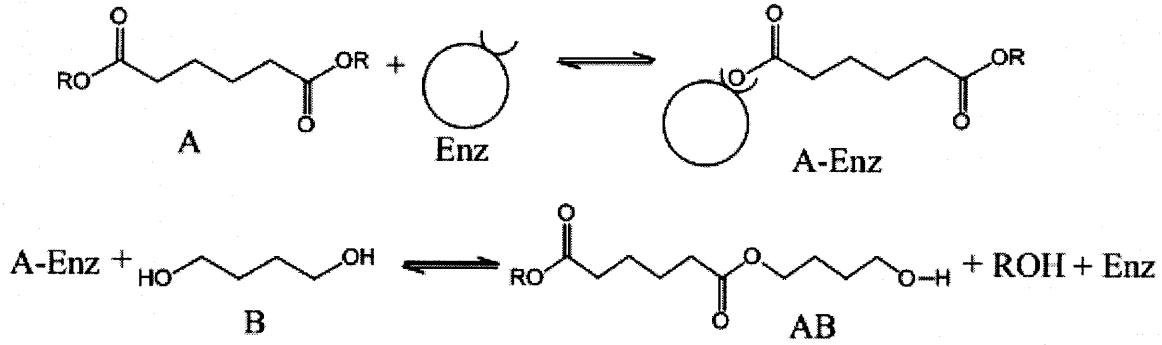

Figure 3.2. Chemical structural representation of the proposed mechanism for lipase-catalyzed polyesterifications. The reaction of adipic acid (A) with butane-1,4-diol to form a single polymer repeat unit is presented as an example.

A reaction scheme has been developed by Watterson and colleagues [4, 8-10] that utilizes Novozyme-435 to synthesize a novel alternating copolymer (FIGURE 3.3).

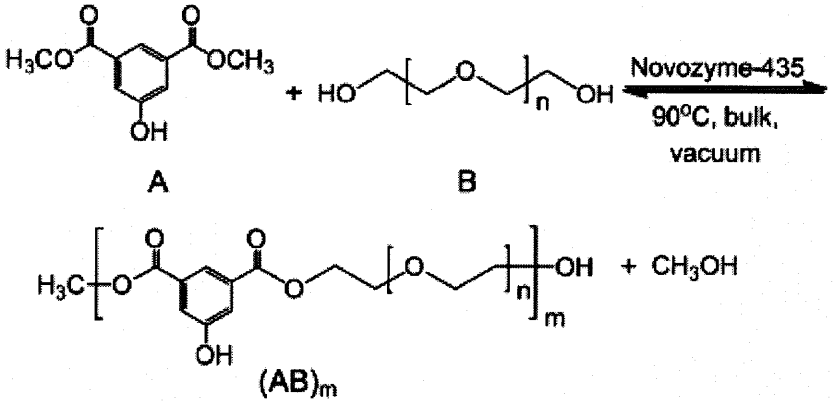

Figure 3.3. Enzymatic condensation using Novozyme-435 of a diester and diol to form a polyester.

For this reaction, dimethyl 5-hydroxyisophthalate (**A**) participates as the diester while poly(ethylene glycol-900) (**B**) is the diol. The product is the polyester poly[poly(oxyethylene-900)-oxy-5-hydroxyisophthaloyl] ($(\mathbf{AB})_m$) The condensation byproduct, methanol, is removed from the reacting mixture by vacuum applied to the

vapor phase. The condensation product, **3**, is henceforth referred to as the 'backbone polymer.' Application of a suitably low vacuum removing the methanol is necessary to shift the equilibrium towards the polymer product since the reaction energetics alone are not favorable enough to achieve sufficiently high molecular weights. In fact, the equilibrium constant for transesterifications is in the range of 0.1-1 (while that for polyesterifications is 1-10 and polyamidations 100-1000) [11]. Therefore, all polymer chain extension is driven by the removal of the transesterification byproduct, either methanol or water.

The backbone polymer is a precursor in the synthesis of polymers intended for targeted delivery applications in cancer. As originally developed (FIGURE 3.3) by our collaborator, Dr. Arthur Watterson, the polymerization was performed at low pressure (< 1 mm Hg) using either magnetic or mechanical stirring. Reactions performed at these conditions, as well as in similar set-ups constructed at MIT, produced low molecular weight product having typically ≤ 4 repeat units (M_n = 3 kDa, M_w = 5 kDa) with little or no progression in molecular weight observed after 48 hours, which suggested that steady-state had been reached. Moreover, the key variables affecting the backbone polymerization were poorly understood. Therefore, an experimental and theoretical reaction engineering study was performed to identify and determine the relative contribution of these key variables in the synthesis of the backbone polymer.

It was also proposed that increasing molecular weight would improve the biological performance of the polymer by potentially increasing particle size as well as the number of targeting ligands that could be linked to a single polymer chain.

3.1.2 Reactor design for mass transfer limited processes

The first reaction configuration employed a round-bottom flask with a magnetic stirring bar for mixing. The schematic diagram in FIGURE 3.4 represents a typical progression of the polymerization reaction as originally developed.

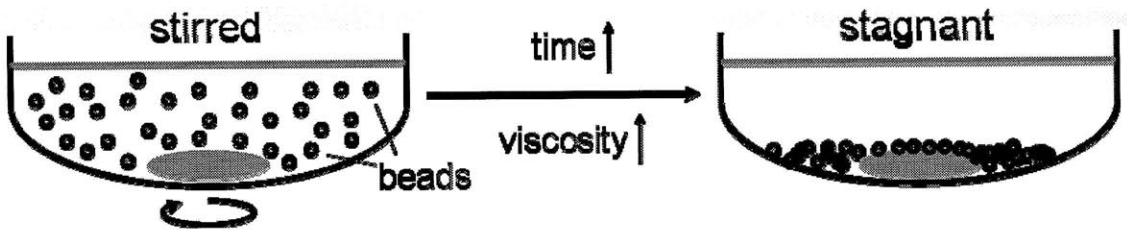

Figure 3.4. Typical progression of polymerization reaction in round-bottom flasks with magnetic stirring. Reaction mixture is well-stirred initially, but as the reaction proceeds and higher MW is achieved, the corresponding increase in viscosity leads to a cessation in stirring and stagnation of the melt.

Initially, the reaction is well-stirred by the magnetic stirring bar and the catalyst beads are dispersed throughout the melt. As the reaction proceeds and molecular weight increases, the viscosity of the melt increases such that the stirring bar becomes decoupled from the magnetic drive. Soon after, the reaction mixture is stagnant and unmixed and the catalyst beads settle to the flask bottom by gravity. A stagnant polymer melt is undesirable, not only for promoting efficient methanol removal, but for increasing the collision frequency of individual reactants and the enzyme. FIGURE 3.5 presents a qualitative representation of the various mass transfer limitations that may play a role in the process, both in the stirred and stagnant cases.

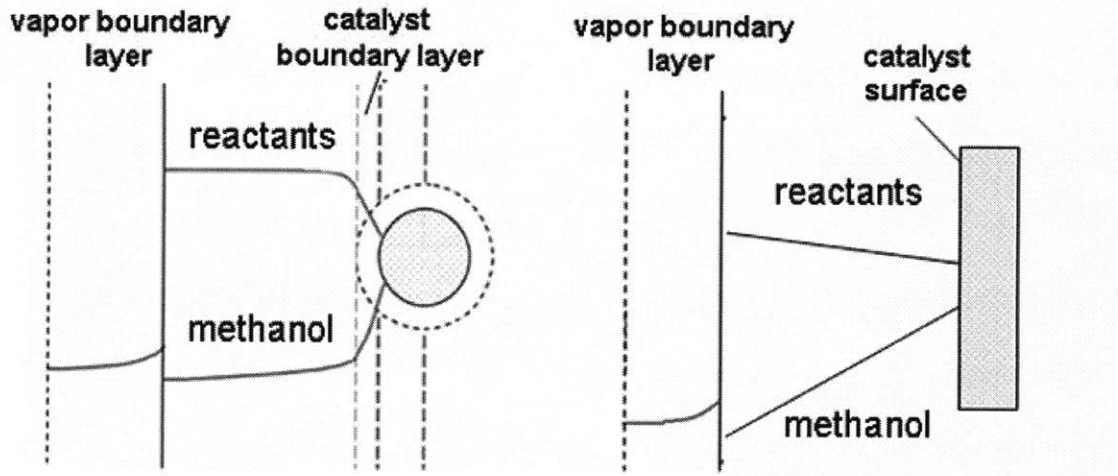

Figure 3.5. Qualitative representation of the condensation profiles describing the potential mass transfer limitations in the backbone condensation polymerization. The diagram on the left represents a well-mixed reaction mixture in the bulk with a mass transfer boundary layer around each bead through which reactants and products, including methanol, diffuse. The diagram on the right represents a stagnant reaction mixture in which diffusion of reactants and products occurs throughout the stagnant layer between the catalyst beads and the vapor-liquid interface.

In the single-bead case, the primary mass transfer limitation is the movement of reactants and products to and from the catalyst surface across the mass transfer boundary layer around the bead. The methanol and reactant concentrations are constant throughout the homogeneous melt. In the stagnant case, the mass transfer of both reactants and methanol is limited primarily by rates of diffusion from the settled catalyst beads to the vapor-liquid interface, which results in the linear concentration profiles within the melt. In both cases, the removal of methanol from the reaction mixture into the evacuated headspace occurs at the vapor-liquid interface, where the methanol concentration in the reaction melt is related to its partial pressure in the vapor by an equilibrium partition coefficient.

The problem of achieving high molecular weight polymers by sequential condensation reactions is not a new one. Industrial production of nylon 6,6, a polyamide, combining adipic acid and hexane-1,6-diamine (FIGURE 3.6), requires special reactor design to achieve high molecular weights. For example, molecular weights of 10 kDa can

be readily achieved in a CSTR [12, 13]. However, the diffusivity of water, the condensation byproduct for nylon 6,6, is significantly lowered at molecular weights exceeding 10 kDa due to the high viscosity of the polymer melt. As a result, diffusion of water to the vapor-liquid interface is extremely slow such that the byproduct can no longer be removed to shift the equilibrium towards the condensation product [14]. Considering the observations previously described (FIGURE 3.4), it was hypothesized that the low molecular weights achieved in the first setup were due to mass transfer limitations similar to those observed industrially for similar reactions.

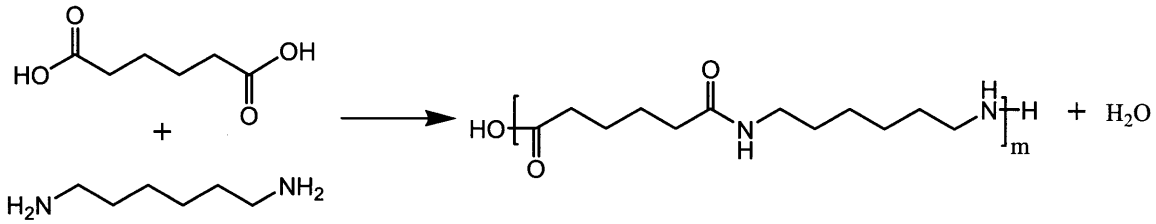

Figure 3.6. Chemical structure representation the polymerization reaction to produce nylon 6,6, the most common industrial polyamide.

A number of 'thin film' reactor designs have been employed to address the issue of poor byproduct mass transfer. These reactors fall into several categories, including wiped film and falling film reactors [15], representations for which are shown in FIGURE 3.7. In the wiped film reactor shown in FIGURE 3.7A, the reacting polymer is deposited along the edges of a tubular reactor by rotating blades [14]. The blades, which are pitched to move the polymer melt through the continuous reactor (direction of motion into the page), continually remove and deposit the polymer film repeatedly exposing the surface to high vacuum (shown in white). In FIGURE 3.7B, a cylinder rotating in the polymer bulk creates a thin polymer film that is exposed to high vacuum. The bulk polymer mixture moves through the reactor (into the page) [16], while the effectiveness of this design depends heavily on minimizing the bulk volume through the introduction

of a large diameter cylinder. In FIGURE 3.7C, a polymer film falls along a heated corrugated wall allowing for vacuum removal of the byproduct. The film thickness is determined primarily by the polymer inlet flow rate and the nature of the interactions between the polymer and the wall.

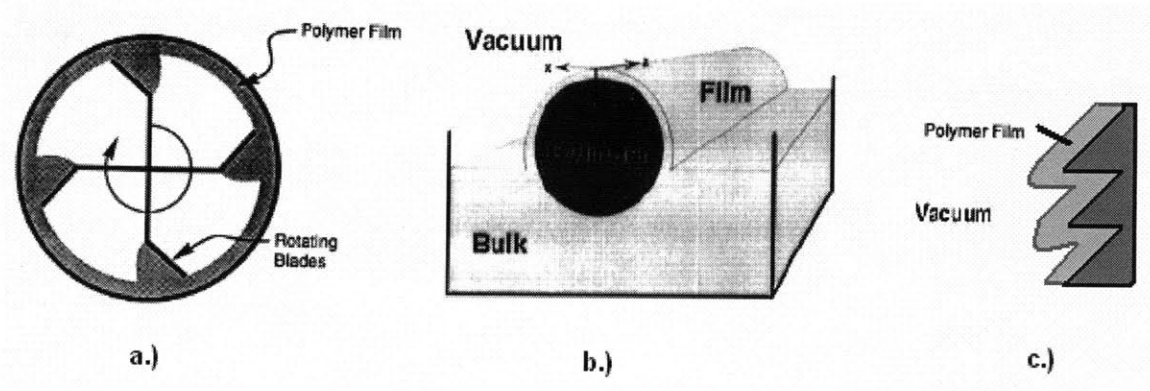

Figure 3.7. Schematic diagrams of different 'thin film' reactors. a.) and b.) Wiped-film reactors [14, 16]. c.) Corrugated falling film reactor.

These designs attempt to maximize the ratio of surface area-to-volume for the polymer reaction mixture. By maximizing this ratio, the area over which byproduct is transferred from the bulk is greatly increased while the byproduct diffusion length is reduced. Continuing the example from above, the 10,000 Da nylon 6,6 polymer produced in a CSTR is oftentimes transferred to a thin film reactor as a 'finishing stage' where molecular weights up to 20,000 Da can be achieved. It would not be possible to achieve a polymer of this molecular weight without using one of these specially designed reactors [14].

The Protherm reactor (shown schematically in FIGURE 8), which is an example of a thin-film evaporator, was manufactured by our industrial collaborator, Artisan Industries (Waltham, MA). The manner in which the Protherm was employed in experimentation is described in the Methods. The device is a scaled-down prototype of

larger equipment, marketed under the brand name Rototherm™, developed for continuous processing of liquids. In the Protherm, liquid is spread into a thin-film by rotating blades having a 1.5 mm clearance between the blade tips and cylinder wall. If desired, vacuum can be applied to increase the stripping of undesired species within the thin-film, such as the methanol reaction byproduct. The rotor speed and wall temperature are controlled by external controllers.

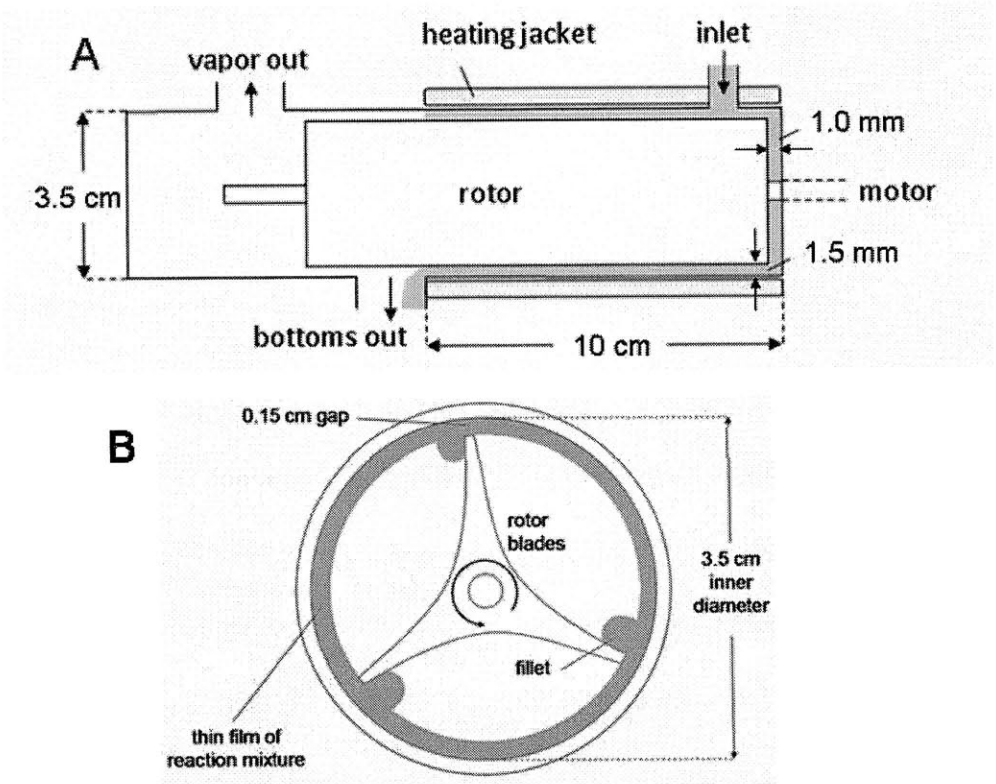

Figure 3.8. (A) Side view: Operation of the Protherm, as originally designed, in a continuous process with an inlet at the top right and an outlet toward the bottom left. In this research, the Protherm was modified to operate in batch mode (see FIGURE XXX). (B) Front view: The Protherm blades rotate counter-clockwise to produce fillets on the advancing edge. Fluid flow within the fillets occurs in the clockwise direction.

The blade rotation in the Protherm, which creates the thin film, also creates a secondary fluid element that has been observed previously in similar processes [17]. This so-called fillet, which is a buildup of fluid in front of the rotating blade, occurs once thresholds for fluid viscosity and blade rotational speed are met [17]. Theory and

experiment have shown that significant mixing may occur within fillets due to the rotational motion of fluids with the fillet [17, 18]. Transfer of fluid between the thin film and rotating fillet due to hydraulic jump may further promote mixing, particularly at lower viscosities [18]. The intermixing between the film and fillet becomes less prominent at higher viscosities where hydraulic jump is likely no longer encountered. The improved mass transfer and mixing characteristics in the Protherm when compared to round-bottom flasks make the Protherm a potentially powerful tool in the effort to increase the extent of reaction for the polymerization and, consequently increase the backbone polymer molecular weight.

Although previous studies have focused on the fillet as the primary location for mixing in a horizontal thin film reactor, mixing may also occur due to other instabilities in the thin film. In particular, the repeated formation and destruction of Pearson instabilities [19], ridges that form when a high viscosity fluid passes through a small gap while being spread into a thin film, was also considered as another possible source of mixing.

Researchers have also proposed theoretical models that represent the reaction kinetics and transport phenomena present in these thin film reactors [14-16, 20]. The theoretical models generally yield two key dimensionless groups, the Damköhler number of the first kind (*Da I*), which represents the ratio of characteristic residence and reaction times, and the Damköhler number of the second kind (*Da II*), which represents the ratio of characteristic reaction and diffusion times. The models rely heavily on system-specific, temperature-dependent parameters including rate and equilibrium constants. These parameters were determined, with significant effort, for the widely studied nylon

6,6 polymerization. Because no such library of data exists for the backbone polymerization in this study, system-specific parameters were either measured or assumed and subsequently tested for their sensitivity.

3.1.3 The Relevance of Backbone Polymer Molecular Weight to Targeted Delivery

The backbone polymer is the precursor to a class of amphiphilic alternating copolymers used in targeted delivery applications in cancer. In subsequent synthetic steps developed in the laboratory of Arthur Watterson at UMass Lowell [8, 10, 21], sidechains are attached for a variety of purposes by means of the free hydroxyl group on the isophthalate linker within the backbone polymer. Hydrophobic chains can be attached to impart amphiphilicity such that the polymers self-assemble to form nanoparticle micelles that exhibit desirable behavior *in vivo* [22], while targeting ligands attached directly or by a spacer promote cancer cell-specific targeting [23]. These modifications to the backbone polymer are shown schematically in FIGURE 3.9.

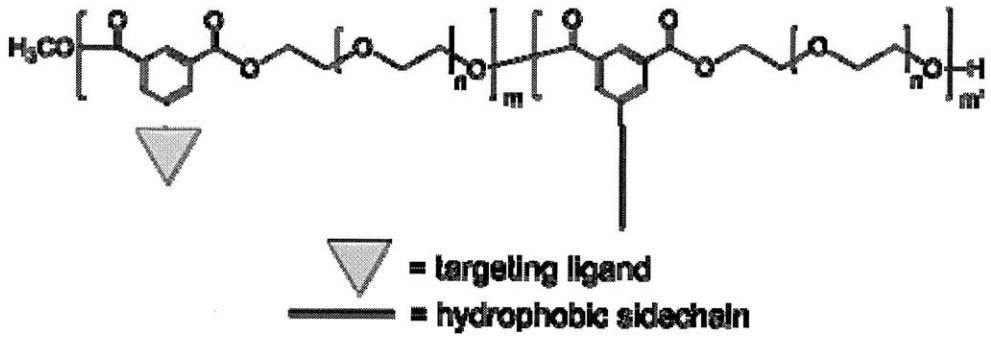

Figure 3.9. Chemical structure of backbone polymer substituted with representations of various sidechains, including targeting ligands and hydrophobic sidechains.

Recently, there has been increasing evidence that polyvalency, which refers to single molecules or particles that have multiple targeting ligands, is essential for successful targeting of cell-surface receptors [24, 25]. Theoretical models developed to described the phenomenon have shown that polyvalency improves the avidity of a

targeted delivery system by increasing the local concentration of targeting ligand once a receptor-ligand interaction occurs [24, 26]. The potential to improve the performance of our targeted polymers using polyvalency has been studied in detail by applying the cited theoretical models [27].

The diagram in FIGURE 3.10 illustrates an important consideration when increasing the targeting ligand polyvalency along the backbone polymer. A single backbone polymer chain has a finite number of reactive sites for the addition of sidechains; consequently, increasing the fractional substitution of targeting ligand reduces that for hydrophobic sidechains. In order to increase the number of targeting ligands per chain while maintaining the ability to form micelles, the backbone polymer molecular weight must be increased. In practice, appropriate physico-chemical characterization techniques, such as dynamic light scattering or surface tension measurements, must be used to determine the relative levels of substitution required for micelle formation.

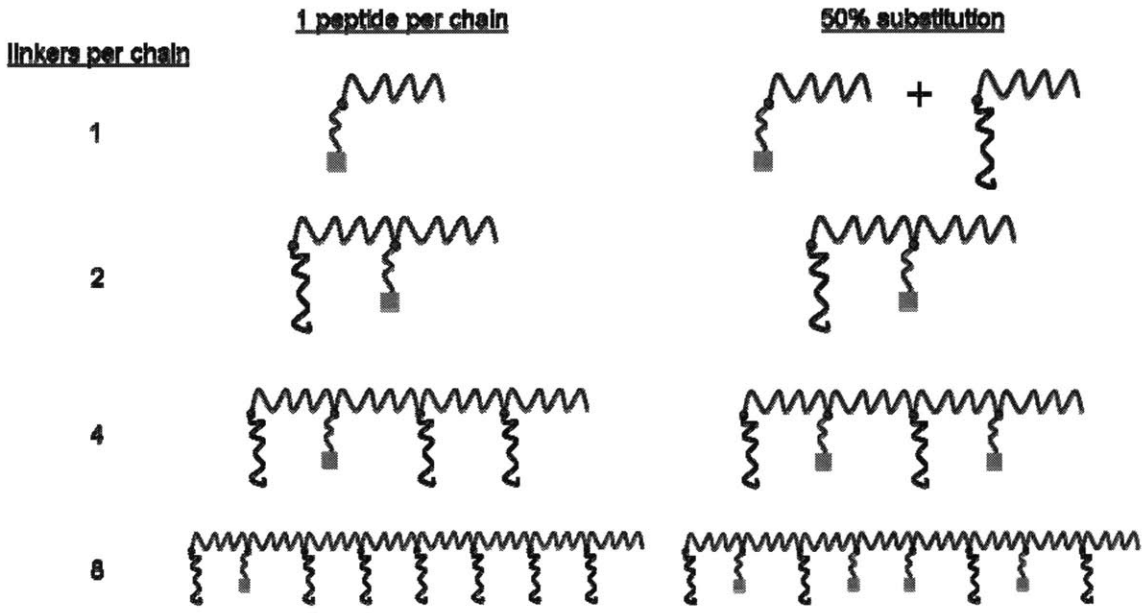

Figure 3.10. Schematic diagram illustrating the trade-off between the number of targeting ligands per polymer chain and the ability to form targeted micelles. The impact of increasing ligand substitution and polymer molecular weight on micelle formation, particle size, and biological function is uncertain.

Increasing the number of targeting ligands per polymer chain by increasing backbone polymer weight does not guarantee a greater density of targeting ligands in the final nanoparticle. This is because the aggregation number as well as the particle size may be affected by differences in molecular weight. Nonetheless, the ability to increase molecular weight beyond that previously attained increases the design space for the targeted polymers. Molecular weight could also potentially be adjusted to control properties of the targeted polymers both in terms of their physico-chemical properties like particle size and critical micelle concentration, as well as their biological function in targeted delivery applications.

3.2 Materials and Methods

3.2.1 Materials

All chemicals were purchased from Sigma-Aldrich (St. Louis, MO) unless otherwise noted. Glassware was purchased from Chemglass (Vineland, NJ) and Kimble-Kontes (Vineland, NJ). Heavy wall flasks, adapters, and manifolds were selected to withstand high vacuum conditions.

3.2.2 Polymerization Procedure in Flasks

The experimental setup for the flask polymerizations is shown in FIGURE 11. Flasks were immersed in a silicon oil bath that was maintained at 90 °C by an immersion circulator (Cole-Parmer, Vernon Hills, IL). Vacuum was applied by means of a vacuum hose connection to a glass adapter (not shown) and any volatilized material was captured by means of a dry ice cold trap. Polymerizations were stirred mechanically in three-neck round-bottom flasks using a variable speed Servodyne motorized electronic mixing

system (Cole-Parmer, Vernon Hills, IL). The drive motor rotated a glass stirring blade that was fitted at the end of a glass shaft (both from Chemglass, Vineland, NJ). Polymerizations were stirred magnetically in single-neck flat-bottom flasks using one-inch stirring bars driven by magnetic stirring plates located beneath the silicon oil bath. For the magnetic apparatus, the flask was placed as close to the stirring plate in order to maximize the magnetic coupling. Sampling was performed via the sample ports by depressurizing the system and removing the stopper.

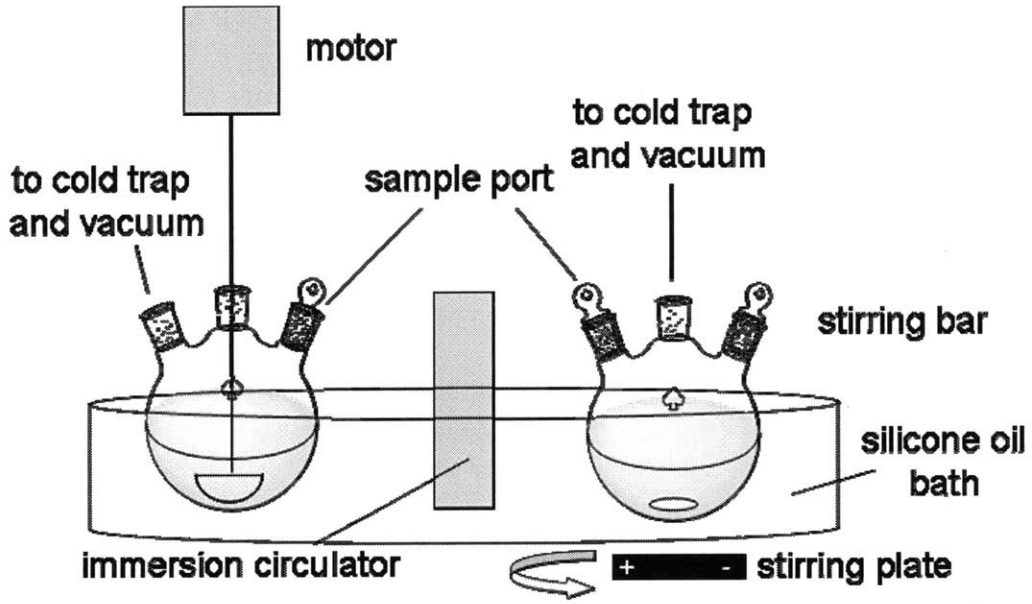

Figure 3.11. Schematic diagram of the experimental setup for flask polymerizations using either mechanical or magnetic stirring. Multiple reactions could be run simultaneously using a large heating bath and multiple vacuum manifolds.

Polyethylene glycol (PEG) was added to a 250 mL flat-bottom flask and dried for at least 1 hr at 90°C under high vacuum (10-100 μm Hg) using a rotary vane direct drive vacuum pump (Labconco, Kansas City, MO); and pressure was measured using a analog vacuum gage (Chemglass, Vineland, NJ). The flask was removed from vacuum, and the dried PEG was reweighed before addition of dimethyl 5-hydroxyisophthalate (linker) and

Novozym435 (See also [28], Sigma catalog number L4777[2]). Linker was added in an equimolar amount to the dried PEG and Novozym435 was added at 10 wt% (w/w) of the total combined mass of PEG and linker. Care was taken to add the reactants quickly in order to minimize the readsorption of water into the PEG. A representative starting mixture for flask reactions presented in the following includes 9 g of dried PEG900, 2.1 g of linker, and 1.1 g of Novozym435.

The mixture was heated to 90°C, and vacuum was applied after the linker was dissolved and Novozym435 was dispersed throughout the PEG melt by either magnetic or mechanical stirring (usually <1 min). Samples (less than 20 mg) were taken at specified times for subsequent analysis by gel permeation chromatography (GPC) using a metal spatula. The vacuum was reapplied after sampling, which typically required about 1-2 min to restabilize. At the end of the reaction period 100 mL of deionized water was added. Novozym435 beads were removed from the resulting slurry by vacuum filtration using qualitative filter paper (Whatman LTD, Piscataway, NJ). The filtrate was then frozen (-4°C) and placed on a freeze dryer (VirTis, Gardiner, NY) under 10 μm Hg vacuum to isolate final polymer product in solid form.

3.2.3 Polymerization Procedure in the Protherm

The Protherm was originally designed to be used as a continuous, flow-through evaporator (FIGURE 3.12A).In continuous mode, fluid enters through the inlet (top right) and is immediately spread into a thin film by the rotating blades. Addition of more fluid

[2] There are a number of immobilized *Candida antarctica* lipase B products commercially available. They vary in activity, original enzyme expression system, support material, and cost. All data presented were generated using Novozym435 that was manufactured by Novozymes and distributed by Sigma-Aldrich (Cat# L4777). Our collaborators at UML used Novozym435 received from Novozymes as a gift. Novozyme435 is *Candida antarctica* Lipase B expressed in *Aspergillus niger,* immobilized on a macroporous acrylic resin (Lewatit VP OC 1600, Bayer) with an activity of >10,000 U/mg.

creates flow through the reactor (right-to-left) and fluid exits the cylinder through the outlet (bottom left) by gravity. Modifications were made in order to use the Protherm as a batch reactor. Due to restrictions imposed by our industrial collaborator, the inlet and bottoms outlet could not be removed to create a sealed reaction zone (shaded region in FIGURE 3.12B). Instead, only modifications to the Protherm orientation could be made to prevent leakage of the polymer melt. To minimize loss of the reaction mixture to the bottoms outlet, the Protherm was rotated 90° axially and elevated 1° above horizontal (FIGURE 3.12B). Rotating the bottoms outlet (and inlet) to horizontal positions minimized loss due to gravity, while the slight elevation further reduced the loss through the bottoms outlet.

Polyethylene glycol drying and subsequent linker and Novozym435 mixing were performed as described above using the magnetic stirring setup. Once the linker and Novozym435 were dissolved and dispersed in the dried PEG, the entire reaction mixture was poured through the opening on the left end of the Protherm ('cap'), which had been pre-heated by setting the temperature controlled heating jacket to 90 °C. To add the reaction mixture, the cap was opened and the Protherm was temporarily elevated to 45° above horizontal such that the mixture quickly entered the heated reaction zone to minimize loss due to solidification.

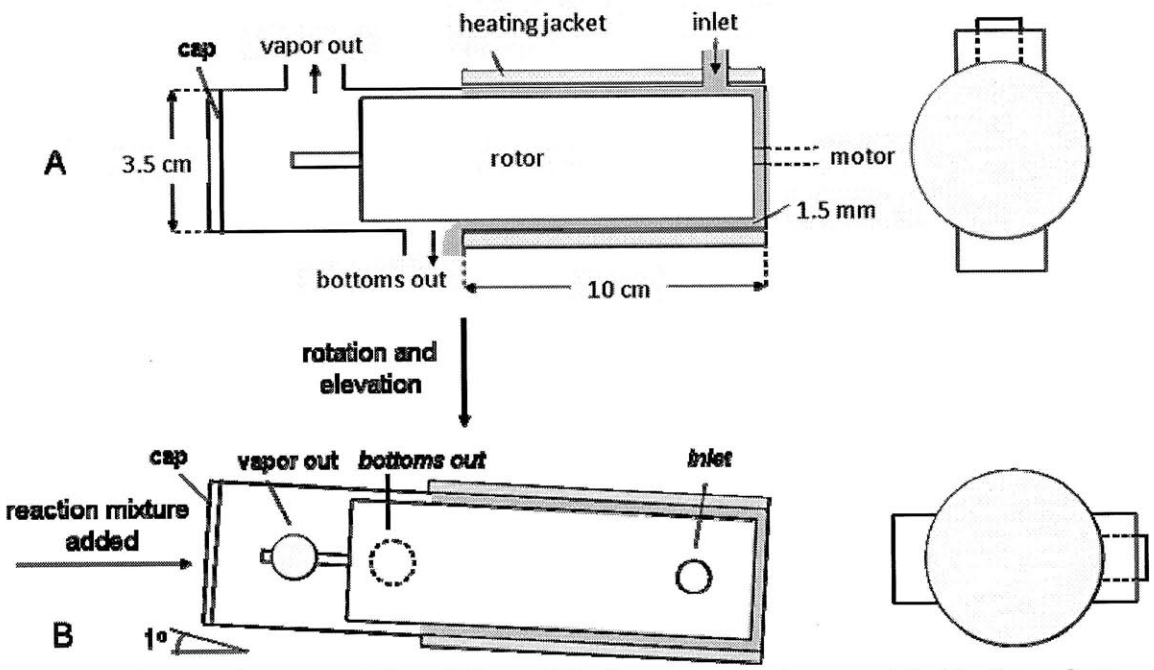

Figure 3.12. Schematic representation of the modifications necessary to convert the Protherm from (A) continuous to (B) batch operation mode. The Protherm is depicted in the transverse (left) and axial (right) directions. The reaction mixture is poured by opening the cap indicated on the leftmost side of the schematic. The bottoms out and inlet are labeled for completeness in (B) – they are not used in batch mode (indicated by italics).

Vacuum was applied via the 'vapor out' port and pressure of approximately 100 μm Hg was measured using an inline analog vacuum gage (Chemglass, Vineland, NJ). Temperature was maintained at 90°C by means of a temperature controller and a thermocouple placed between the heating jacket and the wall of the Protherm. The blade speed was set to 2000 rpm unless otherwise specified. The time of simultaneous application of vacuum and initiation of blade rotation was designated t=0 for the Protherm reactions.

Samples for subsequent GPC analysis were taken at various time points by reopening the cap through which the reaction mixture was originally added. A metal spatula was used to take approximately 20 mg samples at various locations throughout the reaction zone (FIGURE 3.13).

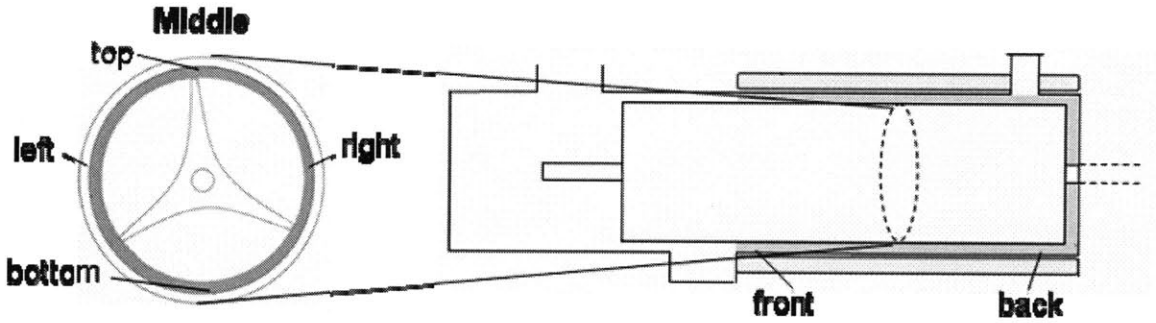

Figure 3.13. Schematic diagram of circumferential and axial views showing the various sampling locations within the Protherm. Samples were taken from the front, middle, and back, including four circumferential locations at the middle.

The starting reaction mixture for the Protherm was twice as large as that used in the flask reactions; the total volume of this doubled mixture (18 g PEG900, 4.2 g linker, 2.2 g Novozym435) was approximately 20 mL. At this batch size, only about 1 mL of the reaction mixture leaked out of the bottoms outlet. There was no benefit to increasing the batch size further because any additional reaction mixture charged to the Protherm leaked out the bottoms outlet when blade rotation was initiated.

3.2.4 Flow Visualizations

Flow visualizations were performed to better understand the fluid mechanics extant in the Protherm. In these experiments, 20 ml of PEG 1000 or PEG 4600 at 90°C were added to the Protherm, which was then set to rotor speeds of 500, 1200 and 2000 rpm. The flow within the Protherm was observed by removing the end cap and illuminating the cylinder with a strobe light set to three times the blade rpm. Qualitative observations of the extent of thin film development and the physical characteristics of the fillet were recorded and are presented in the Results.

3.2.5 Comminution of Novozym435

Because of the high shear created by the rapidly rotating blades in the Protherm and the low mechanical strength of the acrylic catalyst beads upon which the enzyme is

immobilized, Novozym435 was ground before use in the Protherm and occasionally before addition to flask reactions as well. Crushed beads were prepared by grinding the beads to a powder with a mortar and pestle for approximately 5 min until the originally 0.3-1 mm beads had become a fine powder. Additional details concerning the bead size, porosity, and enzyme localization have been determined previously by others [28].

3.2.6 Effect of Molecular Sieves on the Polymerization

Certain experiments investigated the effect of molecular sieves, a drying agent capable of sequestering polar molecules such as methanol or water from fluids, on the polymerization reaction. Powdered 4Å molecular sieves were obtained from Sigma-Aldrich (P/N 69836, St. Louis, MO) and activated in a vacuum oven (P_{abs} = 1 mm Hg) at 250°C for at least 8hr. Activated sieves were weighed and added, where indicated, to the reaction mixture along with the linker and Novozym435. Sieves were added at 10 wt% of the PEG and linker combined mass. Care was taken to minimize the exposure of the sieves to ambient conditions in order to maximize their capacity.

3.2.7 Forward Rate Constant Determination

The forward rate constant was measured experimentally for use in the theoretical kinetic modeling by reacting 1.05 g of linker (**A**) with 7.5 g of mono-methoxy PEG750 (**B'**) in the magnetic stirring setup. These masses of reactants create a 2:1 stoichiometric ratio of PEG to linker; however, since the linker is bifunctional and the PEG is monofunctional, the stoichiometric ratio of hydroxyl and ester groups in the mixture is 1:1. Mono-methoxyPEG750 was used because no PEG900 equivalent was commercially available. Novozym435 (whole beads) was added at 10 wt% (w/w) of the total combined mass of PEG and linker. A structural representation of the overall reaction, as well as the

forward and reverse elementary reactions for the two potential reaction steps, is provided (FIGURE 3.14).

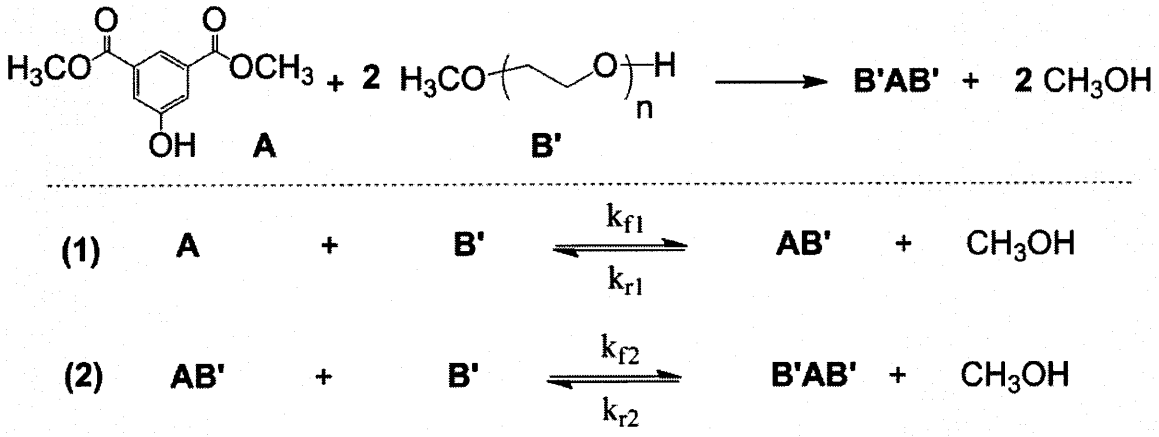

Figure 3.14. Scheme presenting the overall reaction of two equivalents of mono-methoxy PEG750 (A') and with one equivalent of dimethyl 5-hydroxyisophthalate linker (B) to form B'A'B. The two elementary reaction steps are also presented.

Samples were taken as described above. The concentration of the linker in each sample, which was assumed to be representative of the concentration of linker in the reaction melt, was determined using the GPC system. Because the linker peak in the GPC chromatogram was completely resolved from those for PEG750 and any higher molecular weight species, any decrease in the height of the linker peak corresponded directly to reaction of linker with PEG.

The GPC refractive index detector response was calibrated for linker concentration according to the following method. Standard solutions of linker dissolved in THF at four different concentrations were measured by GPC. The heights of the linker peak in the resulting chromatograms were used to construct a calibration curve. The resulting calibration, which was linear over the range of concentrations measured, was used to determine the concentration of linker present in a particular GPC vial, C_L^{GPC}:

$$C_L^{GPC} = \eta H_{peak} \quad (1)$$

where η is the refractive index calibration constant, and H_{peak} is the height of the linker peak in the chromatogram.

Again, assuming that the concentration of linker in the reaction sample, C_L^{sample}, is equal to that in the reaction melt, C_L^{melt}, the definitions in EQUATIONS 2 and 3 were used to convert from C_L^{GPC} to C_L^{melt},:

$$C_L^{GPC} = \frac{m_L^{sample}}{V_{THF}} \tag{2}$$

$$C_L^{melt} = C_L^{sample} = \frac{m_L^{sample}}{V_{sample}} \tag{3}$$

where m_L^{sample} is the mass of linker in the sample, V_{THF} is the volume of THF added to dissolve the sample, and V_{sample} is the volume of the sample taken from the reaction melt. Combining EQUATIONS 2 and 3 yields:

$$C_L^{melt} = C_L^{GPC} \frac{V_{THF}}{V_{sample}}. \tag{4}$$

V_{sample} was determined by:

$$V_{sample} = \frac{m_{sample}}{\rho_{melt}} \tag{5}$$

where m_{sample} was the mass of the sample and ρ_{melt} was the density of the reaction melt, which was determined to be 1.1 g/mL by measuring the weight and volume of the reaction melt, including the catalyst beads.

Combining EQUATIONS 1, 4, and 5 yields:

$$C_L^{melt} = \left(\eta H_{peak}\right) \frac{V_{THF}\rho_{melt}}{m_{sample}}, \tag{6}$$

which was used to calculate the concentration of linker in the reaction melt at various times[3]. A second-order kinetic reaction model was developed (see MODEL FORMULATION section) to estimate the effective forward rate constant for reaction between linker and PEG.

3.2.8 Residual Water Content after Drying

PEG900 was dried under 100 μm Hg at 90°C in a two-neck round bottom flask where one neck was used to apply vacuum and the second neck was sealed with a rubber septum. After designated periods of time, flasks were returned to atmospheric pressure with ultra high purity nitrogen (Airgas, Salem, NH). Samples were withdrawn using a syringe equipped with a long needle, transferred to a dried glass scintillation vial, and dissolved in 100 μL of anhydrous chloroform (Sigma-Aldrich, St. Louis, MO). Vials were purged and sealed under ultra high purity nitrogen (Airgas, Salem, NH). Some samples were withdrawn and exposed to ambient conditions in open vials for recorded times before being sealed. Samples of the PEG prior to the drying were taken as a control. The residual water content present in dried PEG was measured using a V30 Compact Volumetric Karl-Fischer titrator manufactured by Mettler Toledo (Columbus, OH) following the protocol provided along with the equipment. In this method, trace water reacts with a mixture of chemicals to produce iodine from iodide in a controlled reaction. This reaction is monitored by potentiometric measurements and the water content is calculated based on known electrochemical properties of iodine and iodide [29].

[3] This analysis assumes that V_{THF} and the total volume of the dissolved sample are equal. It also assumes that the density of the reaction melt is constant throughout the period of sampling.

3.2.9 Molecular Weight Determination by Gel Permeation Chromatography (GPC)

To prepare the samples for GPC analysis, chromatography grade tetrahydrofuran (THF, Sigma-Aldrich, St. Louis, MO) was added to the collected samples until fully dissolved. Typically, one milliliter of THF was added to approximately 10-20 mg of sample. The dissolved samples were then filtered with a 0.45 micron PTFE Acrodisc syringe filter (Pall Corporation, Port Washington, NY) to remove the catalyst beads and other particulates that may have been present. The filtered samples were then added to sample vials and analyzed on a Breeze 2 HPLC system (Waters, Milford, MA) equipped with an auto-sampler, UV/Vis detector (λ = 250 nm), and refractive index detectors. The column bank consisted of three Styragel® high resolution GPC columns connected in series (HR1, HR3, and HR4, Waters, Milford, MA). The mobile phase was THF and the flow rate was 1 ml/min. The standard method involved a 60-min column preparation stage to equilibrate the columns and purge the detectors, a 36-min run time for each sample, and a 15-min elution to restore the columns to their resting state.

Chromatograms obtained from the GPC system were analyzed with the Breeze software package (Waters, Milford, MA), which was used to calculate the product number average ($\bar{M}_n$) and weight average ($\bar{M}_w$) molecular weight based on a calibration curve established using a kit of poly(methyl methacrylate) (PMMA) standards (Waters, Milford, MA). The results of a study of the calculation of molecular weight from the raw data measured by the detectors are presented in APPENDIX A. The definitions of $\bar{M}_n$, $\bar{M}_w$, and the polydispersity index (PDI) are presented in EQUATION 12:

$$\bar{M}_n = \sum \frac{N_x M_x}{N_x} \qquad \bar{M}_w = \sum w_x M_x = \sum \frac{N_x{}^2 M_x}{N_x M_x} \qquad PDI = \frac{\bar{M}_w}{\bar{M}_n} \tag{7}$$

where N_x is the number of moles whose weight is M_x and w_x is the weight fraction of molecules who weight is M_x [11].

3.3 Homogeneous Model Formulation

Theoretical models were developed to determine under what conditions the backbone polymer molecular weight could be increased. The models were also used to quantify the extent to which molecular weight could be increased by improving the reaction conditions. An ideal homogeneous reaction model was chosen as the base system for the evaluation. In this ideal system, the reaction mixture is perfectly mixed and the methanol concentration in solution is related to the vapor pressure in the vapor space above the reaction mixture according to Raoult's law. Measured and/or estimated rate and equilibrium constants were used with the model to predict the ideal molecular weight progression for the system.

Considering the low backbone polymer molecular weight achieved previously, as well as the prevalence of literature devoted to byproduct removal in condensation polymerizations [11, 15, 16, 30], the potential contributions of excess methanol in the reaction mixture to reduce molecular weight were of primary interest. This potential mechanism was studied by varying the methanol concentration specified in the model. Even though methanol partial pressure in the vapor space was kept very low experimentally, elevated methanol concentrations can exist in the melt because of the mass transfer limitations described qualitatively in FIGURE 3.5. This is important because the *liquid*-phase methanol concentration is the key driving force of the reverse reaction that inhibits the production of higher molecular weight polymer. The molecular

weight predictions at these elevated methanol concentrations will serve as a basis against which experimental results will be assessed.

3.3.1 Overall Strategy for Homogeneous Model Simulations

The homogeneous model was used to simulated the theoretical backbone polymer molecular weight as a function of time given a constant bulk methanol concentration, C_M. Multiple simulations were performed, each having a different specified value of C_M, and the time-dependent molecular weight progressions were recorded and plotted for inspection. C_M was varied over eight orders of magnitude to simulate the effect of severely elevated (or depressed) methanol concentrations. These methanol concentrations represented the deviations from ideality in a real, non-homogeneous mixture.

The same model was also used to simulate the equilibrium molecular weight as a function of bulk methanol concentration. To generate these results, the model was solved for a range of C_M and the equilibrium molecular weight was recorded for each simulation. The simulation time span was set high enough to ensure that the simulated reaction system had reached equilibrium.

3.3.2 Kinetic Model Overview – System of Reactions

As described in the Introduction, the reaction of interest involves the transesterification of polyethylene glycol (PEG) and dimethyl 5-hydroxyisophthalate (linker) to form a chain-extended polyester and methanol byproduct. A second order kinetic model was used to study this reaction; however, modifications to the classical application of the second order model were required. Specifically, in the classical example of A + B → C, an individual reaction between A and B consumes the two reactants. Conversely, for the polymerization reaction in question, reaction between

bifunctional monomers does not consume the reactants in the classical sense because the second ester and hydroxyl present in the bifunctional linker and PEG remain and can participate in further reaction. To account for the bifunctionality of the linker and PEG monomers, the reaction model was formulated in terms of reactive endgroups and not in terms of individual molecules [11].

In the primary chain-extension reaction (FIGURE 3.15a), a linker methyl ester endgroup, **A**, reacts with a PEG hydroxyl endgroup, **B**, to form the chain extending ester bond, **L**, and methanol, **M**. Two side-reactions were also included in the model description to assess how residual water in the melt might affect molecular weight. In the hydrolysis reaction (FIGURE 3.15b), a linker methyl ester, **A**, is hydrolyzed by a water molecule, **W**, to form a carboxylic acid, **C**. This side reaction reduces the concentration of methyl esters in solution, which, in turn, can affect the stoichiometric balance between hydroxyl and methyl ester endgroups. Disruption of this balance, which is essential to maximize extent of polymerization, may reduce the final molecular weight. In the proposed model, the carboxylic acid hydrolysis product is allowed to react with PEG in a chain extension reaction (FIGURE 15c) to produce a chain extending ester bond, **L**, and methanol, **M**. Although the chain extension product, **L**, is represented in FIGURE 3.15 in a molecule having only one repeat unit, any reaction between **A** and **B** or **C** and **B** will lead to a chain extension and a corresponding increase in the average molecular weight of the mixture. For all three reactions, the reverse reaction was also possible. For example, methanol, **M**, could react with **L** to regenerate the linker methyl ester and PEG hydroxyl. This reverse reaction would lead to a corresponding decrease in polymer molecular weight.

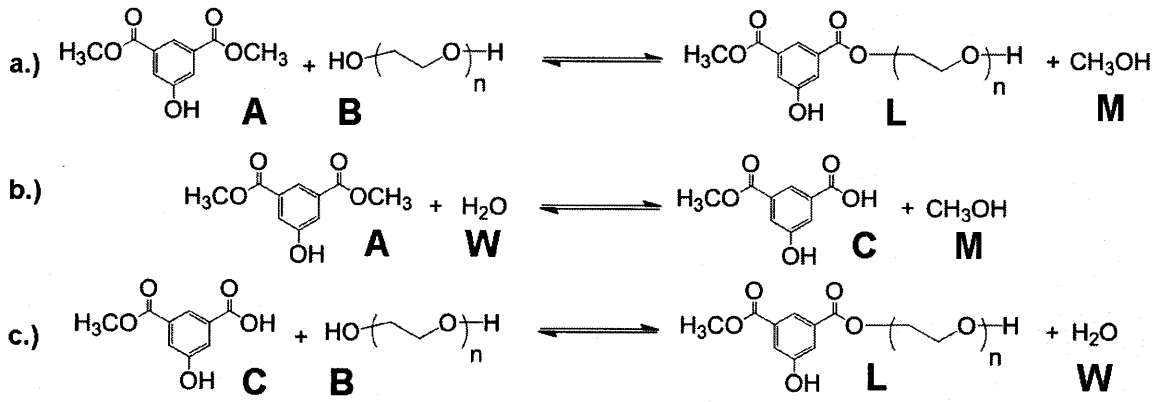

Figure 3.15. Model formulation: Polymerization reaction with side reactions represented by reactive endgroups, which are labeled in the chemical structure representations of the proposed reactions.

The chemical kinetics and equilibria for these three reactions were modeled assuming that all forward and reverse reactions were second order with respect the reactive endgroups. The forward and reverse rate constants are k_i for the transesterification (FIGURE 3.15a), k_i^h for the hydrolysis of the linker ester (3.15b), and k_i^c for the carboxylic acid-mediated polymer chain extension (3.15c), where the subscript *f* refers to the forward reaction and *r* refers to the reverse reaction.

The system of equations for these reactions, again assuming second order kinetics, is as follows:

$$
\begin{aligned}
&\text{a.)}\ \frac{dC_A}{dt} = -R - R_C \\
&\text{b.)}\ \frac{dC_B}{dt} = -R - R_H \\
&\text{c.)}\ \frac{dC_L}{dt} = R + R_C \\
&\text{d.)}\ \frac{dC_M}{dt} = R + R_C \\
&\text{e.)}\ \frac{dC_W}{dt} = -R_H + R_C \\
&\text{f.)}\ \frac{dC_C}{dt} = R_H - R_C
\end{aligned}
\qquad (8)
$$

where,

$$\begin{aligned} &\text{a.)} \quad R = k_f C_A C_B - k_r C_L C_M \\ &\text{b.)} \quad R_H = k_f^H C_B C_W + k_r^H C_C C_M \\ &\text{c.)} \quad R_C = k_f^C C_A C_C + k_r^C C_L C_W \end{aligned} \tag{9}$$

For this model, k_i^j are the effective homogeneous rate constants, which are lumped representations of system-specific characteristics according to:

$$k_f = \frac{\kappa_f \sigma_{enz} A_{cat} N_{cat}}{V_{melt}} \tag{10}$$

where κ_f is the intrinsic forward rate constant, σ_{enz} is the enzyme surface density, A_{cat} is the surface area per catalyst bead, N_{cat} is the number of catalyst beads present, and V_{melt} is the volume of the reaction melt.

The time-dependent initial conditions for A and B are known according to experimental conditions and are C_A^o, C_B^o, respectively. These two initial conditions are equal because the linker and PEG are added stoichiometrically and both monomers are bifunctional. The initial conditions for L and C, which are not present at the beginning of the reaction, are all equal to zero.

The initial concentration for water requires additional discussion because the modeled system is not a closed system, but an open, driven system due to the vacuum pump. In the experimental system, the initial concentration of water is equal to the residual water present in the system after drying and subsequent addition of solids. For the proposed model, it was assumed that the residual water present after drying represented the minimum amount of water that could be removed from the melt given the temperature, pressure, and configuration of the experimental system. As a result, the system was considered closed with respect to water. Karl Fischer titration measurements were performed to determine the approximate order-of-magnitude of the residual water

present after drying. The initial water concentration was varied during the simulation study in order to better understand the potential role of water on the polymerization.

While the other system components could be determined or estimated experimentally, no inline measurement of liquid phase methanol or of the flux of methanol from the reaction system was available due to instrumentation limitations. Therefore, the only inline measurement available that related to methanol concentration was the pressure measured in the vapor space above the melt, P^{exp}. The partial pressures of all other components in the system, including water and linker (dimethyl 5-hydroxyisophthalate) were assumed to be equal to zero. This assumption is safe for linker, which exerts very little vapor pressure due to its high molecular weight (210 Da) and will exert no vapor pressure once it becomes attached to PEG. The assumption is less straightforward for water, although its pure component vapor pressure is more than four times lower than that for methanol at 90 °C [31]fh. Therefore, the system pressure was equal to the vapor-phase methanol pressure, p_M. The bulk liquid phase methanol concentration, C_M, was then calculated from the system vapor pressure according to a vapor-liquid equilibrium relationship, such as Henry's Law:

$$P_M^{exp} = K_H C_M^{exp} \tag{11}$$

where K_H is the Henry's Law constant and P_M^{exp} and C_M^{exp} are the experimental partial pressure and bulk concentration of methanol, respectively.

Because the measured pressure was constant throughout the reaction (after a brief initial depressurization period of less than 5 min), the liquid phase, bulk methanol concentration was assumed to be constant for all times in each particular simulation. This assumption, which was applied even during the initial stages of the polymerization, led to

a physically unrealistic, non-zero value of C_M^o for the early times in the simulation. This choice, which greatly facilitated program development, was not expected to have a significant effect on the results due to the comparatively small concentrations of **L** and **M** at the beginning of the reaction relative to those for **A** and **B,** even at the highest simulated methanol concentrations ($< 10^{-2}$ M versus 1M, respectively).

3.3.3 From concentration to molecular weight

The system of differential equations and associated initial conditions was implemented and solved in MATLAB using the ODE solving routine, 'ode15s.' The MATLAB code can be found in APPENDIX B. The differential and algebraic equation solver yields the concentration of each species as a function of time. These concentrations can be translated into molecular weight using the following definitions and manipulations. First, let $\overline{P}_n$, the number average degree of polymerization be defined as follows:

$$\overline{P}_n(t) = \frac{\text{total initial no. monomer units}}{\text{no. molecules remaining}} = \frac{N(t=0)}{N(t)} \tag{12}$$

where N(t = 0) is the initial number of monomer units present and N(t) is the total number of molecules remaining at time, *t*. According to [11], the degree of polymerization is related to the fractional conversion by the following:

$$\overline{P}_n(t) = \frac{1+r}{1 - 2r\pi_i(t) + r} \tag{13}$$

where π_i is the fractional conversion of either reactive endgroup (A or B) and *r* is the stoichiometric ratio, which are defined as:

$$\pi_i(t) = \frac{N_i^o - N_i(t)}{N_i^o} \tag{14}$$

$$r = \frac{N_B^o}{N_A^o} \tag{15}$$

where N_i^o is the number of reactive endgroups of species *i* present initially. By definition, the stoichiometric ratio always contains the minority species in the numerator. When the monomers are added stoichiometrically, as is the case for the polymerization in question, *r* is equal to unity and EQUATION 14 reduces to:

$$\overline{P}_n(t) = \frac{1}{1-\pi_i(t)} \tag{16}$$

While the subscripts A and B can be used interchangeably in EQUATIONS 13, 14, and 16 because any reaction of A must be accompanied by equal reaction of B, this is not the case for a system in which side reactions can occur. In the proposed model, conversion of linker methyl esters (A) does not necessarily indicate polymer chain extension. On the other hand, all fractional conversion of PEG hydroxyls (B) leads to polymer chain extension (FIGURE 3.15a and c). Therefore, for the proposed system of reactions, the polymerization number could be calculated according to:

$$\overline{P}_n(t) = \frac{1}{1-\pi_B(t)} \tag{17}$$

The output of the MATLAB program, the time-dependent concentrations of the various components in the reaction system, can be converted to time-dependent fractional conversions using the following relationship:

$$\pi_i(t) = 1 - \frac{C_i(t)}{C_i^o} \tag{18}$$

where $C_i(t)$ is the concentration of species *i* at a given time and C_i^o is the initial concentration of species *i*. In order for this relationship to be valid, it must be assumed

that the volume of the reaction mixture is constant throughout the polymerization. This assumption is likely valid because (1) the density of PEG is very weakly dependent on molecular weight [32] and the relative mass of the condensation byproduct (methanol) that may be removed during the course of the reaction is < 3% (assuming stoichiometric reactants: 32/(210+900) = 0.03). The solution to the system of differential equations (EQUATION 9), therefore, provides all of the information required to determine the degree of polymerization as a function of time according to EQUATIONS 17 and 18.

The final step, then, is to convert degree of polymerization to either a number-average or weight-average molecular weight. According to [11], the number-average molecular weight, $\bar{M}_n$, is related to the degree of polymerization by the relationship

$$\bar{M}_n = \frac{M_{repeat}}{2}\bar{P}_n + M_{eg} \tag{19}$$

where M_{repeat} is the molecular weight of the polymer repeat unit and M_{eg} is the molecular weight of the monomer endgroups, which becomes negligible as $\bar{P}_n$ increases. For the case of the polymerization of PEG900 and linker, a single polymer repeat unit is PEG900 connected to linker by an ester bond (FIGURE 3.16).

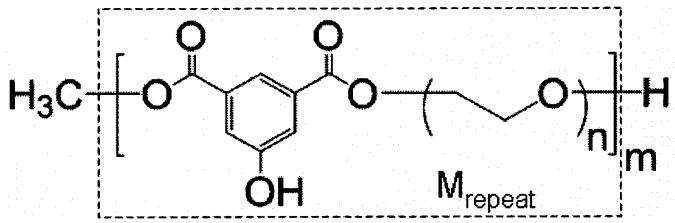

Figure 3.16. The parts of the backbone polymer chemical structure that comprise a single repeat unit.

The actual value of M_{repeat} was calculated:

$$M_{repeat} = M_{PEG} + M_{linker} - 2M_{methanol} = 900 + 210 - 2(32) = 1046 \text{ Da} \tag{20}$$

where the M_i are the molecular weight of PEG900, linker, and methanol, respectively. The two equivalents of methanol are subtracted because one molecule of methanol is not present in the repeat unit (outside the dotted line in FIGURE 3.16) while a second molecule of methanol is the condensation byproduct. It follows that the endgroup molecular weight M_{eg} is 32 Da.

The weight average molecular weight can be calculated from the fractional conversion of PEG using the following formula [11]:

$$\bar{M}_W = \left(\frac{M_{repeat}}{2}\right)\frac{1+\pi_B}{1-\pi_B}. \tag{21}$$

Combining EQUATIONS 17 and 21 yields a relationship between the weight-average molecular weight and degree of polymerization:

$$\bar{M}_W = \frac{M_{repeat}}{2}\left(2\bar{P}_n - 1\right). \tag{22}$$

Therefore the number- and weight-average polymer molecular weight can be modeled for the backbone polymerization MATLAB program using a differential algebraic equation solver (see APPENDIX B for code) and the preceding definitions and derivations.

3.3.4 Determination of Model Parameters

In order to solve this system of differential equations, a number of parameters are necessary, including the six kinetic rate constants and initial concentrations of the reactive species.

a.) Effective forward rate constant

The experimentally measured linker concentrations were used to estimate the effective forward rate constant according to the experimental procedure described in the

Methods and the system of reactions presented in FIGURE 3.14. If samples are taken at early times and $C_{AB'} << C_A$ and $C_{B'}$, only the first forward elementary reaction will occurs (all other reactions will be negligible). The polymerization can be modeled using the same reactive endgroup strategy exploited during the formulation of the kinetic model for the complete reaction system. The reaction between linker and mono-methoxyPEG750 can be described by the second-order rate equation:

$$-\frac{dC_A}{dt} = k_f C_A C_{B'} \tag{23}$$

where k_f is the effective forward rate constant and C_A and $C_{B'}$ are the volumetric concentration of linker methyl esters and monomethoxy-PEG750 hydroxyls, respectively. At $t = 0$, C_A is equal to C_A^o. Because the monofunctional PEG was added in a 2:1 molar ratio to the bifunctional linker molecule, C_A and $C_{B'}$ are equal and EQUATION 23 becomes:

$$-\frac{dC_A}{dt} = k_f C_A^{\,2} \tag{24}$$

The analytical solution to EQUATION 24 in linearized form is:

$$\frac{1}{C_A(t)} = k_f t + \frac{1}{C_A^o} \tag{25}$$

If the model assumptions are valid (i.e. $C_{AB'} << C_A, C_{B'}$), then a plot of the left-hand-side of EQUATION 25 versus reaction time, *t*, should yield a straight line, the slope of which is equal to the effective forward rate constant, k_f. However, if the resulting plot is non-linear, that would likely indicate that the other proposed elementary reactions were contributing significantly to the time-dependent progression of the linker concentration, C_A. This empirically determined rate constant was assumed to apply for all steps in the

polymerization, an assumption which is commonly made for tractability [11, 30]. The reverse rate constant was calculated according to the selected value for the equilibrium constant, K_{eq}, according to:

$$K_{eq} = \frac{k_f}{k_r} \tag{26}$$

The exact equilibrium constant for the reaction was unknown and was therefore treated as a variable during the execution of the simulations. Recall that the equilibrium constant for transesterification reactions is typically 0.1-1 [11]. Finally, because no data were available for the remaining two reactions (FIGURE 15b and c), the remaining forward and reverse rate constants, for hydrolysis (H) and carboxylic acid-mediated chain-extension (C), were also unknown and were assumed to be equivalent to k_f as an approximation.

b.) Initial Concentrations

The initial concentrations of the various reactive endgroups were determined experimentally by measuring the volume of a stoichiometric mixture of 9 g of PEG900 and 2.1 g linker. The mixture volume was 10.0 mL. Because the number of moles of each reactant was known (0.01 mol), the initial concentrations of the monomer species were 0.01 mol/10.0 mL, or 1M. However, because there are two reactive endgroups for each monomer, the initial concentrations of, C_A^o and C_B^o, were 2.0 M. Detailed results for the model parameters that were determined experimentally are presented in the subsequent results section.

3.4 Fickian Diffusion Model Formulation

The homogeneous kinetic model was used to determine the predicted molecular weight for a variety of bulk methanol concentrations, not just for that which corresponded to the experimentally measured vapor-phase pressure (according to EQUATION 11). These C_M values, most of which were greater than that measured experimentally, were intended to account for mass transfer limitations not addressed by the homogeneous assumption. The results of the model at these various concentrations represent the expected molecular weight that might be observed as a result of limitations in mass transfer from the bulk to the catalytic surface. To supplement the kinetic model, a model that incorporated Fickian diffusion across a stagnant film of thickness δ was developed and applied to several different situations. The goal of this model was to (1) quantitatively predict the increase in the concentration of methanol participating in the reverse reaction as a function of position relative to the bulk methanol concentration, and (2) to use this information to estimate the effect on polymer molecular weight. The model incorporates the physical properties of the system, including diffusivities, rate constants, and length scales, for two different limiting cases: (1) a well-stirred solution with a stagnant boundary layer around each individual bead, and (2) a completely stagnant system in which the catalyst particles have settled to form a monolayer at the bottom of the reaction vessel. A cartoon representation of the physical state in the flask reaction was depicted earlier in FIGURE 3.4. The model framework for these two cases is shown schematically in FIGURE 3.17. In order to describe the two cases by the same physical model, curvature effects have been neglected for the boundary layer around the catalyst bead. The height of the boundary layer, δ, is equal to (1) the radius of the catalyst bead

for the single-bead case (for the worst-case scenario for which the Sherwood number is equal to 2) and (2) the height of the polymer melt for the stagnant case.

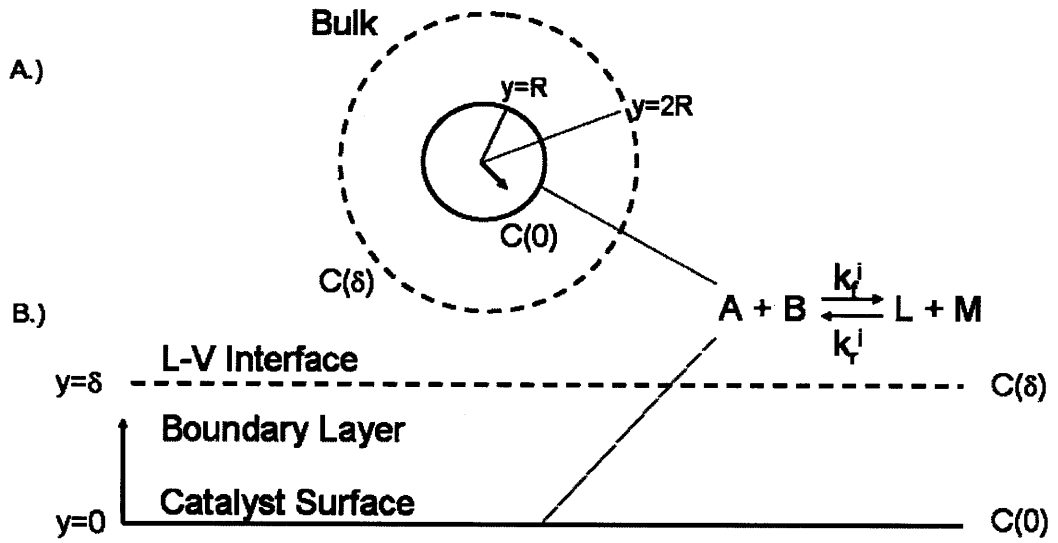

Figure 3.17. Schematic representation of the Fickian mass transfer model proposed to describe mass transfer limitations in the flask polymerization for the (A) single-bead and (B) stagnant cases. The height of the boundary layer, δ, is equal to (1) the diameter of the catalyst bead for the single-bead case and (2) the height of the polymer melt for the stagnant case.

In the proposed one-dimensional model the chain-extending chemical reaction occurs at the catalyst surface at a position of y = 0. Potential reactions with water were not included in this model formulation to simplify the analysis. The surface reaction is governed by the effective forward and reverse rate constants, k_f^i and k_r^i, where *i* can represent either the single-bead or the stagnant case. The effective rate constants for the two cases are related to the intrinsic rate constant by:

$$k_f^{\,bead} = \kappa_f \sigma_{enz} \tag{27}$$

$$k_f^{\,stagnant} = \frac{\kappa_f \sigma_{enz} \left[f A_{cat} N_{cat} \right]}{A_{flask}} \tag{28}$$

where A_{flask} is the surface area of the bottom of the flask and f is the efficiency of the catalyst area, which is required because a portion of the settled beads cannot catalyze the reaction. The remaining terms are defined as in EQUATION 10.

EQUATION 10 was rearranged to separate the known and unknown system parameters:

$$\kappa_f \sigma_{enz} = \frac{k_f V_{melt}}{A_{cat} N_{cat}} \tag{29}$$

The Fick's Law diffusion model was used to perform individual analyses of the mass transfer limitation of the methanol byproduct, **M**, and the reactive endgroups, **A** and **B**. After the initial stages of the polymerization, all of the reactive endgroups are present as terminal groups on a polymer chain. Because of this, together with the 1:1 stoichiometry of the reaction, it was assumed that the mass transfer behaviors of **A** and **B** were identical. Diffusion from the catalyst surface was assumed to be governed by Fick's Law. In the single-bead case, diffusion occurs across a boundary layer into the homogeneous liquid bulk, while in the stagnant case, diffusion occurs through a stagnant region equal to the height of the entire liquid, which is bounded by the liquid-vapor interface. Two assumptions were made: (1) the system was assumed to be at quasi-steady state so that time derivate for Fick's Law is equal to zero. In order for this assumption to be valid, the Fourier number (Fo), which relates the diffusive time scale to the characteristic timescale of a system, must be O(1) or greater. (2) When modeling the mass transfer of a particular species, the concentration of all other species were assumed to be constant in space. For example, when modeling the methanol mass transfer limitations, **A**, **B**, and **L** were all held constant with respect to space.

Based on these assumptions, the one-dimensional governing equation for diffusion of methanol across the boundary layer (EQUATION 30A) and two associated boundary conditions for the single-bead (EQUATION 30A-C) and stagnant cases (EQUATION 30D-F) become:

a.) $\nabla^2 C_M = \frac{1}{y^2}\frac{d}{dy}\left(y^2 \frac{dC_M}{dy}\right) = 0$ d.) $\nabla^2 C_M = \frac{d^2 C_M}{dy^2} = 0$

b.) $C_M\big|_{y=3R} = C_M(2R)$ e.) $C_M\big|_{y=\delta} = C_M(\delta)$ (30)

c.) $-D_M \frac{dC_M}{dy}\bigg|_{y=R} = k_f{}^i C_A C_B - k_r{}^i C_L C_M(R)$ f.) $-D_M \frac{dC_M}{dy}\bigg|_{y=0} = k_f{}^i C_A C_B - k_r{}^i C_L C_M(0)$

The first boundary condition states that the concentration of methanol at the edge of the boundary layer is known. For both cases, this methanol concentration is the bulk concentration that was used as the input in the homogeneous reaction model. The second boundary condition equates the rates of diffusion and reaction at the catalyst surface. The superscript *i* indicates that different effective rate constants are required for both the single-bead and stagnant cases. EQUATION 30 can be rewritten for other species, such as the reactive endgroups, by selecting the corresponding reaction rate equation for the right-hand-side of the second boundary condition.

The preceding model equations for methanol were non-dimensionalized according to the following:

$$\theta_M = \frac{C_M(\eta)}{C_M(\delta)}; \quad \eta = \frac{y}{R} \text{ or } \eta = \frac{y}{\delta} \tag{31}$$

where the characteristic length was either the radius of the bead, R, or the melt height, δ, and EQUATION 30 becomes:

a.) $\frac{1}{\eta^2}\frac{d}{d\eta}\left(\eta^2 \frac{d\theta_M}{d\eta}\right) = 0$ d.) $\frac{d^2\theta_M}{d\eta^2} = 0$

b.) $\theta_M\big|_{\eta=3} = 1$ e.) $\theta_M\big|_{\eta=1} = 1$ (32)

c.) $\frac{d\theta_M}{d\eta}\bigg|_{\eta=1} = Da_{f,M}^{bead} - Da_{r,M}^{bead}\theta_M(1)$ f.) $\frac{d\theta_M}{d\eta}\bigg|_{\eta=0} = Da_{f,M}^{film} - Da_{r,M}^{film}\theta_M(0)$

where,

$$Da_{f,M}^{bead} = \frac{k_f^{bead} R}{D_M}\left(\frac{C_A C_B}{C_M(R)}\right); \quad Da_{r,M}^{bead} = \frac{k_f^{bead} R}{D_M K_{eq}}(C_L)$$
$$Da_{f,M}^{film} = \frac{k_f^{film} \delta}{D_M}\left(\frac{C_A C_B}{C_M(\delta)}\right); \quad Da_{r,M}^{film} = \frac{k_f^{film} \delta}{D_M K_{eq}}(C_L) \tag{33}$$

$Da_{f,M}^{i}$ and $Da_{r,M}^{i}$ are the respective forward and reverse Damköhler numbers for the methanol mass transfer model for the *i*th case.

Based on the previously described assumptions, as well as the assumption that C_A is equal to C_B because of the stoichiometry of the reaction, a similar model was proposed for the mass transfer of **A**, the methyl ester reactive endgroup:

$$\text{a.)}\ \frac{1}{\eta^2}\frac{d}{d\eta}\left(\eta^2 \frac{d\theta_A}{d\eta}\right) = 0 \qquad \text{d.)}\ \frac{d^2\theta_A}{d\eta^2} = 0$$
$$\text{b.)}\ \theta_A\big|_{\eta=2} = 1 \qquad \text{e.)}\ \theta_A\big|_{\eta=1} = 1 \tag{34}$$
$$\text{c.)}\ \left.\frac{d\theta_A}{d\eta}\right|_{\eta=1} = Da_{f,M}^{bead}\theta_A(1)^2 - Da_{r,M}^{bead} \qquad \text{f.)}\ \left.\frac{d\theta_A}{d\eta}\right|_{\eta=0} = Da_{f,M}^{film}\theta_A(0)^2 - Da_{r,M}^{film}$$

where the non-dimensionalized concentration and positions were defined as in EQUATION 31 and,

$$Da_{f,A}^{bead} = \frac{k_f^{bead} R C_A(R)}{D_A}; \quad Da_{r,A}^{bead} = \frac{k_f^{bead} R}{D_A K_{eq}}\left(\frac{C_L C_M}{C_A(R)}\right)$$
$$Da_{f,A}^{film} = \frac{k_f^{film} \delta C_A(\delta)}{D_A}; \quad Da_{r,A}^{film} = \frac{k_f^{film} \delta}{D_A K_{eq}}\left(\frac{C_L C_M}{C_A(\delta)}\right) \tag{35}$$

A methanol mass transfer model was also proposed for the Protherm (FIGURE 3.18). In this model, the polymerization reaction is assumed to occur homogeneously through the polymer thin-film in the Protherm. There is a no-flux boundary condition at the wall.

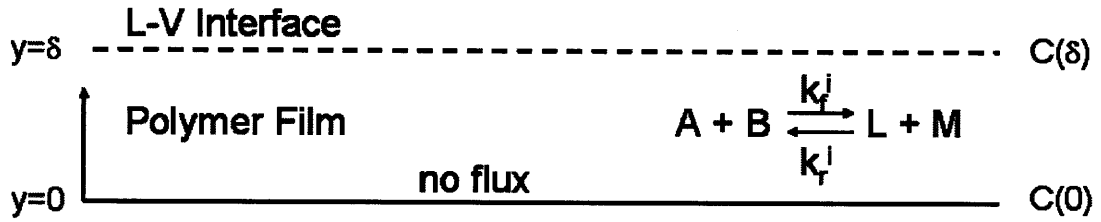

Figure 3.18. Schematic representation of the Fickian mass transfer model proposed to describe mass transfer limitations in the Protherm. δ is the thickness of the thin polymer film in which the reaction occurs homogeneously.

For the Protherm mass transfer model, it was assumed that the time-dependent term in the Fick's law mass balance was equal to zero. In order for this assumption to be true, the characteristic relaxation time of the diffusion profile must be shorter than the characteristic reaction time (i.e. how quickly the reaction affects a change in C_M). Curvature effects were neglected allowing for the mass transfer model to be written in rectangular rather than cylindrical coordinates (necessary for an analytical solution). Under these assumptions, the mass balance becomes:

$$\begin{aligned} -D_M \frac{d^2C_M}{dy^2} &= k_f^{PT} C_A C_B - k_r^{PT} C_L C_M \\ C_M(\delta) & \\ \frac{dC_M}{dy} &= 0 \end{aligned} \tag{36}$$

Applying the same non-dimensionalization strategy as above, where concentration is normalized by the C(δ) and position is normalized by δ, yields:

$$\begin{aligned} \frac{d^2\theta_M}{d\eta^2} &= -Da_f^{PT} + Da_r^{PT}\theta_M \\ \theta(1) &= 1 \\ \frac{d\theta_M}{d\eta} &= 0 \end{aligned} \tag{37}$$

where,

$$Da_f^{PT} = \frac{k_f^{PT}\delta^2}{D_M}\left(\frac{C_A C_B}{C_M(\delta)}\right); \qquad Da_r^{PT} = \frac{k_r^{PT}\delta^2}{D_M K_{eq}}(C_L) \tag{38}$$

In this case for which reaction occurs homogeneously, the characteristic height is squared in the two Damköhler numbers and the effective forward rate constant for the Protherm mass transfer model, k_f^{PT}, is:

$$k_f^{PT} = \frac{\kappa_f \sigma_{enz} A_{cat} N_{cat}}{V_{melt,PT}} \tag{39}$$

where $V_{melt,PT}$ is the volume of the polymer melt in the Protherm.

Whenever possible, the model parameters were estimated experimentally. In lieu of experimental values, empirical formulae were used to determine the necessary parameters, such as the diffusion constant for methanol in PEG, D_M, which was calculated using the Wilke-Chang correlation:

$$D_M = 1.173 \times 10^{-16}(\varphi M_{BP})^{1/2} \frac{T}{\mu_{BP} V_M^{0.6}} \tag{40}$$

where D_M is the diffusion coefficient of methanol in backbone polymer (BP) in units of m^2/s, φ is the solvent association parameter (assumed to be equal to 1), M_{BP} is the molecular weight, T is temperature in Kelvin (363 K), μ_{MP} is the viscosity in Pa-s, and V_M is the molar volume of methanol in kg/m^3. The methanol partial molar volume was estimated to be 0.72 g/mL according to a physical property table [33].

The diffusivity of A, D_A, was assumed to be equal to the self-diffusivity of PEG because the methyl ester groups become the terminal groups of the backbone polymer early in the polymerization. The self-diffusivity and viscosity of PEG, both of which were assumed to be representative of corresponding properties of the backbone polymer,

were estimated from the literature as a function of molecular weight and are presented in the Results [31, 34].

3.5 Results

3.5.1 Conversion between P_M and C_M

As previously discussed, the bulk methanol concentration was the primary variable of interest during the simulations performed according to the proposed theoretical models. Ideally, measurement of bulk methanol concentration during each experimental polymerization would have been available in order to make direct comparisons between experiment and theory. Due to limitations in instrumentation, bulk methanol concentration measurement was not possible in our experimental system. The only measurement available was the pressure in the vapor-phase headspace above the reaction mixture. This experimental pressure data can be used to estimate the liquid-phase methanol concentration by means of a relationship describing the vapor-liquid equilibrium behavior of methanol solute and the bulk polymer solvent.

This vapor-liquid equilibrium approach has been used previously in mass transfer modeling of byproduct removal-limited condensation polymerizations to convert from vapor-phase pressure to bulk concentration [14-16, 35]. In the cited literature, well-established empirical vapor-liquid equilibrium models were available for the simulated systems, which included nylon-6,6 and poly(ethylene terephthalate). Unfortunately, for our system of interest, methanol dissolved in either PEG or backbone polymer oligomers, which are primarily comprised of PEG, no experimental information was available.

Consequently, the vapor-liquid behavior had to be approximated using simple models informed by relevant solubility data from the literature.

For simplicity, it was assumed that methanol was the only species in the vapor phase. As a result, the vapor pressures of all other system components, including water and linker, were set equal to zero. This assumption is likely valid because the PEG is dried before addition of linker and enzyme and the fact that the vapor pressure of methanol is significantly greater than that for water at 90 °C (2000 vs. 500 mm Hg, respectively). Given this assumption, $P_{sys} = p_M$, where P_{sys} is the experimental pressure measured in the system and p_M is the partial pressure of methanol.

Two classical descriptions of vapor-liquid equilibria were considered: (1) Raoult's Law and (2) Henry's Law. If the solute and solvent interact ideally, Raoult's Law can be used to describe the vapor-liquid equilibrium behavior at all solute mole fractions:

$$p_M = p_M^{\circ} x_M \tag{43}$$

where, p_M° is the pure component vapor pressure of methanol.

If the interactions are non-ideal, the solubility may vary as a function of the solute mole fraction. For small solute mole fractions, the non-ideal solubility approaches linearity and is typically described by Henry's Law:

$$p_M = K_H C_M \tag{44}$$

where K_H is the Henry's Law constant. A qualitative representation of typical ideal and non-ideal solubility behaviors is shown in FIGURE 3.19.

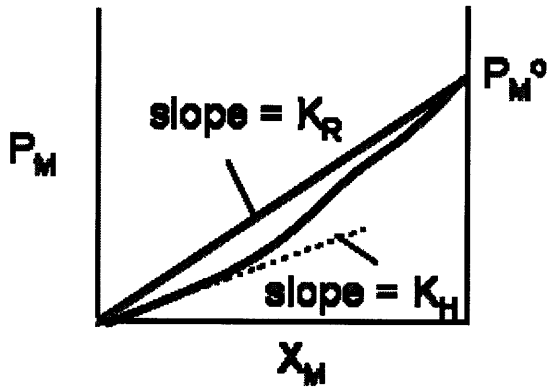

Figure 3.19. Qualitative representation of the ideal and non-ideal solubility behaviors of methanol in polyethylene glycol as a function of methanol mole fraction.

Depending on the nature of the interactions between solute and solvent, the Henry's Law constant may deviate positively or negatively from the slope of the Raoult's Law description of vapor-liquid equilibrium. The extent to which the two slopes differ also depends on the solute-solvent interactions. If the solute and solvent molecule interactions do not deviate from ideality by a significant amount, then the solubility calculated according to Raoult's Law can be used as an approximation of the Henry's Law constant. To estimate the extent of these deviations for our system of interest, Hildebrand solubility and polymer-liquid interaction (Flory-Huggins χ) parameter data that was available for methanol, PEG, and methanol in PEG in the literature [36, 37] were examined.

The Hildebrand solubility parameter for individual components in a mixture, δ, can be used to predict the nature of the interactions between multiple components upon mixture in solution. In particular, materials with similar Hildebrand solubility parameters are likely to be miscible. The Hildebrand solubility parameters for several relevant molecules are presented in TABLE 3.1. The values for methanol and polyethylene glycols of various molecular weights are 29.7 and approximately 20 $MPa^{1/2}$, respectively

[36]. From these data it was inferred that methanol and polyethylene glycol are somewhat, but not completely, miscible with one another.

Table 3.1. Hildebrand solubility parameters, δ, for selected molecules, including an approximate value for polyethylene glycol molecules of various molecular weights [36].

Molecule	δ $[MPa]^{1/2}$
PEG (various MW)	20 (approx.)
Methanol	29.7
Ethylene glycol	34.9
Water	48.0

The polymer-liquid interaction (Flory-Huggins χ) parameter for methanol in PEG was also used to determine the miscibility of the two compounds. In particular, χ parameters indicate the extent to which solute-polymer interactions deviate from ideality. In an ideal solute-polymer mixture the χ parameter is equal to zero, while a χ parameter less than 0.5 corresponds to complete miscibility of two compounds [38]. The χ parameter for methanol in poly(ethylene oxide) was measured between 90-110 °C and determined to be 1.3 $MPa^{1/2}$ [37, 39] after extrapolation to the reference temperature of 25 °C. Because the corresponding χ parameter was approximately 1 $MPa^{1/2}$, this datum provided further evidence that methanol and PEG are somewhat miscible and only interact weakly with one another [38]. Previous studies have suggested that the electron pairs of the PEG hydroxyl groups and the proton of the methanol hydroxyl form weak hydrogen bonds [40, 41]. These weak bonds are responsible for the weakly interactive, somewhat miscible solubility behavior implied by the solubility parameter data.

From the preceding analysis, it was inferred that the solubility of methanol in PEG900 determined according to Raoult's Law would be a reasonable approximation of the Henry's Law constant for the same mixture; i.e. the slopes represented schematically

in FIGURE 19 would not differ substantially. A relationship describing the Raoult's Law solubility, K_R, as a function of known system-specific parameters was derived using EQUATION 43 and the following definition:

$$x_M = \frac{C_M}{\sum_i C_i} = \frac{C_M}{C_{total}} \tag{44}$$

where the denominator is the total molar density of the solution, C_{total}, which includes the concentration of A, B, C, L, M, and W. A similar strategy has been used by others to describe vapor-liquid equilibria in similar reaction systems [14, 16, 30].

Removal of methanol throughout the course of the polymerization can lead to a nearly twofold decrease in C_{total}, assuming the volume of the polymer melt is constant. The potential error introduced by the decrease in C_{total} was ignored because the accuracy of the solubility estimate was not considered to be sufficiently high to warrant a corresponding adjustment. Combining EQUATIONS 43 and 44 yields,

$$p_M = p_M^o \frac{C_M}{C_{total}} \tag{45}$$

Therefore, the Henry's Law constant for methanol in the reaction mixture, which was approximated by the slope of the Raoult's Law solubility relationship, is described by:

$$K_H \approx K_R = \frac{p_M^o}{C_{total}} \tag{46}$$

A physical property table [33] was used to determine that p_M^o at 90 °C was 2000 mmHg, while C_{total}, which was assumed to be equal to $C_{total,initial}$, was 4.0 M. Therefore, K_H was equal to 500 mmHg/M.

As previously described, the bulk methanol concentration, C_M, was treated as a variable during the kinetic and equilibrium modeling of the homogeneously catalyzed

polymerization. The methanol partial pressures that correspond to methanol concentrations of interest are summarized in TABLE 3.2. The experimentally measured headspace vapor pressure is also included. The pressure was maintained at $5x10^{-2}$ mmHg throughout the course of all experimental polymerizations with the exception of initial depressurization periods that lasted less than 5 min.

Table3. 2. Specific bulk methanol concentrations and their corresponding methanol partial pressures used during the theoretical modeling. The experimentally measured headspace vapor pressure is indicated by asterisks.

C_M (mol/L)	P_M (mm Hg)
$1x10^{-8}$	$5x10^{-8}$
$1x10^{-6}$	$5x10^{-4}$
$1x10^{-4}$ ***	$5x10^{-2}$ ***
$1x10^{-2}$	5
1	$5x10^{2}$

3.5.2 Forward Rate Constant Determination

A calibration curve for linker was constructed using the GPC (FIGURE 3.20). Solutions with known concentrations of linker were dissolved in THF and their chromatograms were recorded by GPC. The height of the GPC chromatogram peak (RI response) was directly proportional to the linker concentration in the GPC sample vial.

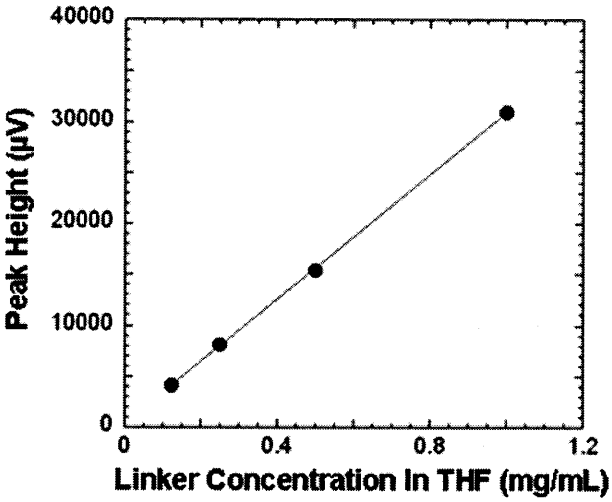

Figure 3,20. Calibration curve relating the height of the linker peak in the GPC chromatogram for various concentrations of linker dissolved in known volumes of THF.

Samples were taken from the reaction between mono-methoxy PEG750 and linker at various time points. The samples were weighed and the masses were adjusted to account for the mass of the Novozym435 beads. Samples were dissolved in known volumes of THF (typically 1 mL) and chromatograms were recorded on the GPC system. The concentration of linker in each sample, C_A, was calculated using the sample weight, THF volume, and calibration curve presented in FIGURE 3.20 according to EQUATION 6.

The resulting concentration was assumed to be representative of the entire reaction mixture. The inverse linker concentration was plotted against reaction time (FIGURE 3.21) and the effective homogeneous forward rate constant, k_f, was determined by regression according to EQUATION 25

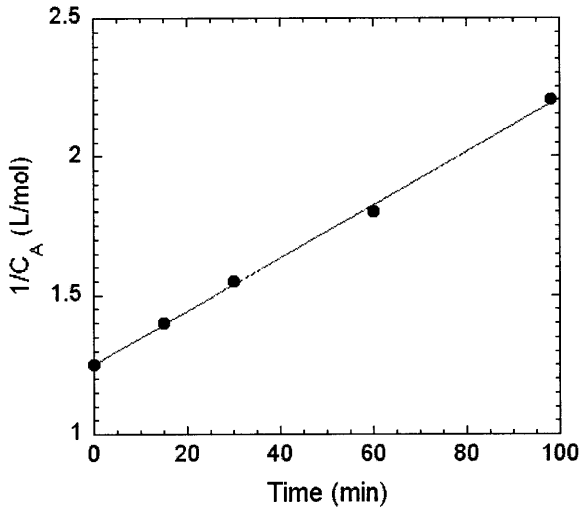

Figure 3.21. Plot of the inverse of the experimentally determined linker concentration, C_A, versus reaction time for the reaction between mono-methoxyPEG750 and linker. The slope of the linear regression is equal to the forward rate constant for the reaction.

The slope of the linear least-squares fit in FIGURE 3.21 was $9.0 \times 10^{-3} \pm M^{-1}min^{-1}$. with a standard error of 0.4×10^{-3} $M^{-1}min^{-1}$, which is equal to the effective forward rate constant for the model reaction. The resulting regression line did not significantly diverge from the experimental data, implying that the initial rate of reaction was observed through the final datum at t = 96 min.

The resulting effective forward rate constant, together with EQUATION 29, was used to calculate the product $\kappa_f \sigma_{enz}$. The system-specific parameters for intact beads were required for the calculation were determined according to the following. The surface area of a catalyst bead was calculated assuming a bead diameter of 1 mm for an intact bead (according to manufacturer specifications). A melt volume of 8.3 mL was measured experimentally during the rate constant determination experiment. Finally, the number of catalyst beads was determined as follows. One-hundred intact beads were counted and weighed to determine the number density of the beads (beads/gram). This measurement was repeated in triplicate. The measured number density (4300 beads/gram) was used to determine the number of beads added during the rate constant determination experiment.

Together, these known values were used to calculate the product of $\kappa_f\sigma_{enz}$, which was subsequently used to calculate the effective forward rate constants for the single-bead and stagnant cases according to EQUATIONS 27 and 28. For the latter, three system-specific parameters were required: (1) N_{cat}, which was determined from the number density, (2) A_{flask}, which was calculated based on a measured flask diameter of 5 mm, and (3) f, which was assumed to be 0.5.

This product, which was used to calculate the effective forward rate constant for the other geometries studied throughout this work, was determined to be $1.1x10^{-10}$ m^4/mol-s (in SI units).

3.5.3 Residual Water after Drying

Karl-Fischer titration experiments were performed to determine the residual water remaining in the PEG900 after various periods of drying. The amount of water present after various periods of drying of PEG900 is presented in TABLE 3. The water contents for the PEG900 samples were not adjusted for the contribution due to water in the chloroform since it was extremely low. These values were converted into concentrations for use in the model as C_w^o. The average value for the 1 and 2 hour drying times, $2.4x10^{-2}$ mol H_2O/mol PEG900, was converted into a molar volumetric concentration. The resulting value, 1.5 mM, was used as C_w^o in the subsequent simulations, as indicated.

Table 3.3. Water content measured by Karl-Fischer titration. The data are presented as moles of water per moles of analyzed sample.

Sample	Drying Time (hr)	Water Content (mol H_2O/mol sample)
Anhydrous Chloroform	N/A	$3.3x10^{-4}$
PEG900	None	$2.2x10^{0}$
	1	$2.6x10^{-2}$
	2	$2.2x10^{-2}$
	24	$8.8x10^{-3}$

The dried PEG900 was also exposed to the atmospheric humidity in the laboratory to determine the rate of water readsorption (FIGURE 3.22). This exposure simulated the conditions in a typical reaction preparation during which the dried PEG is exposed to the laboratory atmosphere while linker and enzyme are added.

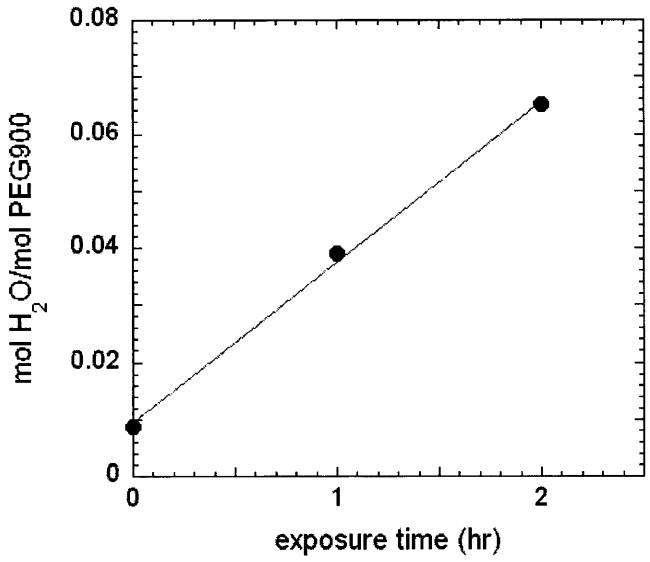

Figure 3.22. The water content measured by Karl-Fischer titration for PEG900 after 24 hr of drying and subsequent exposure to atmospheric conditions. The rate of water adsorption was approximately 0.028 mol H_2O/hour.

The rate of water readsorption into the dried PEG900 was 0.028 mol H_2O/mol PEG900 per hr. Normalizing this rate to the initial concentration of water in undried PEG (2.2 mol H_2O/mol PEG) yields an initial readsorption rate of 1.3% of water removed per hour. Because the maximum exposure time of PEG to atmospheric conditions was approximately 30 min, with most exposures occurring for less than 10 min, the change in the residual water present at the beginning of each polymerization due to water readsorption was quite small.

3.5.4 Kinetic Modeling: Molecular Weight versus Time

The theoretical model proposed in the Model Formulation Section was implemented and solved in MATLAB. The weight-average molecular weight, M_w, was

determined as a function of time (0-20,000 hr) at five different bulk methanol concentrations from 10^{-8} to 1M (FIGURE 3.23). The equilibrium constant, K_{eq}, was set equal to 1 for these simulations.

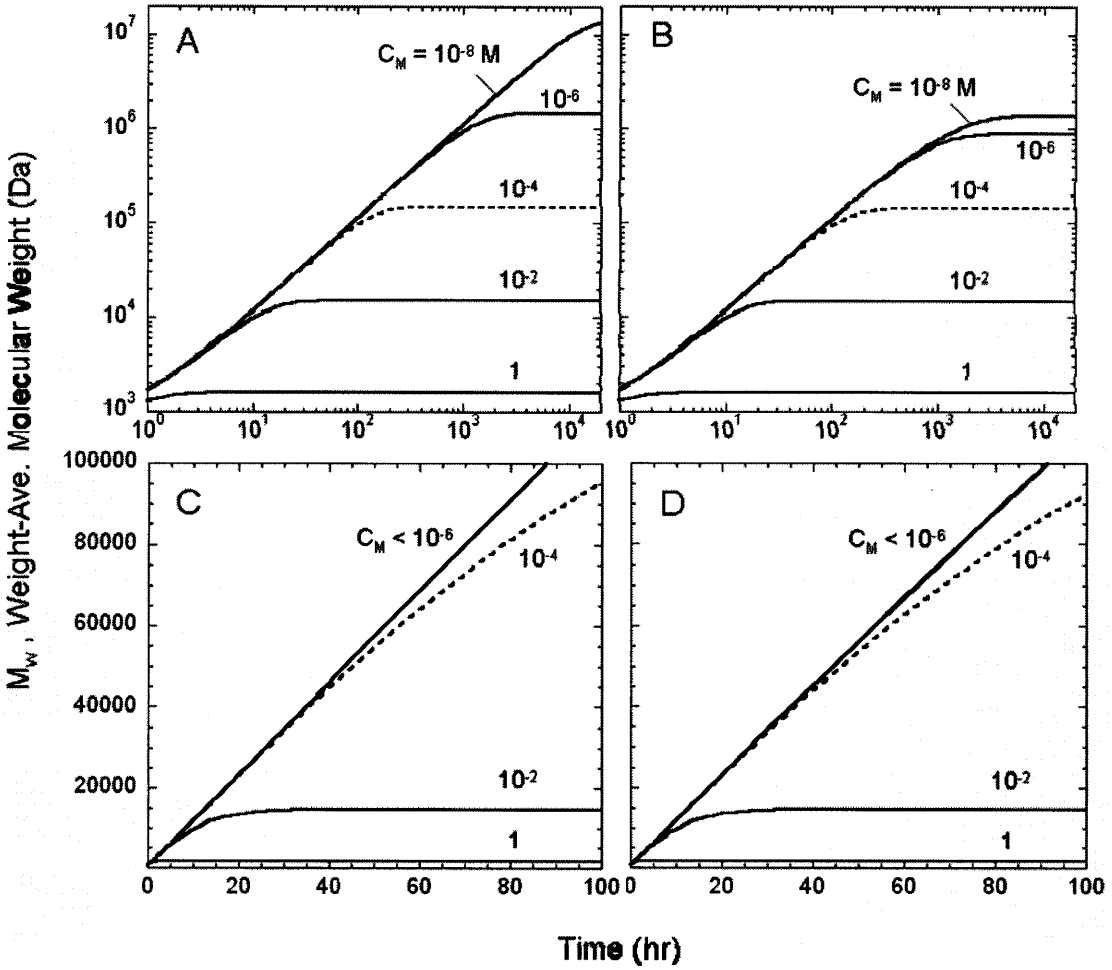

Figure 3.23. Simulated M_w as a function of time at various bulk concentrations of methanol. The experimentally measured pressure in the reaction system was $5x10^{-2}$ mm Hg, which corresponds to a methanol concentration of 10^{-4} M (dotted lines). The results of the entire simulation results are plotted logarithmically (A) without ($C_w^o = 0$) and (B) with ($C_w^o = 1.5$ mM) water present; subsets at short times are plotted linearly both without (C) and with (D) water present. Reaction times between 0 and 100 hr are similar to those the typically encountered experimentally.

The experimentally measured pressure achieved by the vacuum system with the glass reaction vessels was $5x10^{-2}$ mm Hg, which corresponds to a bulk methanol concentration of $1x10^{-4}$ M. The results at this concentration are represented by dotted lines in FIGURE 3.23. In all simulations, the vapor-phase pressure was assumed to be

due entirely to methanol vapor. In simulations with water present, the initial water concentration, C_W^o, was set at 1.5 mM, according to the results of the Karl-Fischer titration measurements.

These results demonstrate the importance of decreasing methanol partial pressure in order to substantially increase the weight-average molecular weight, particularly considering the estimated equilibrium constant ($K_{eq} = 1$) characteristic of similar polyesterification reactions [11]. The simulated M_W increased as a function of time along identical reaction trajectories for all values of C_M and departed from the shared trajectory when the back-reaction (in which methanol reacts with esters within the backbone polymer to reduce the chain length) became appreciable. At that point, the molecular weight progression slowly leveled off until eventually reaching the equilibrium value in all simulated cases except the lowest C_M (10^{-8} M).

At $C_M = 1x10^{-4}$ M, which corresponds to a p_M of $5x10^{-2}$ mm Hg according to the Raoult's Law description of the vapor-liquid equilibrium, the weight-average molecular weight increased linearly until the rate of reaction began to decrease at approximately 200 hr and ultimately reached an equilibrium value of 182 kDa after 1000 hr. At high degrees of polymerization, the predicted value of M_w approached twice that of M_n, which was expected according to EQUATIONS 19 and 22. Therefore, the equilibrium M_w can be converted to M_n by dividing the simulation results by two. At all times, the exact theoretical relationship between M_n and M_w applies.

The simulated reaction times required to substantially increase molecular weight and ultimately reach equilibrium, especially at the lower partial pressures, were quite

long. The time required to reach 95% of the equilibrium M_w, t_{eq}, was calculated in the model system both with and without residual water present (TABLE 3.4).

Table 3.4. Predicted time for the simulated M_w to reach 95% of the equilibrium M_w in the model system both with and without residual water present.

C_M (M)	t_{eq}, $C_w^o = 0$ (hr)	t_{eq}, $C_w^o = 1.5$ μM (hr)
10^{-8}	7000	1050
10^{-6}	950	720
10^{-4}	105	95
10^{-2}	27	23
10^{0}	3	3

The simulation was also performed with residual water present after drying, C_w^o = 1.5 mM. As was observed for the water-free case, the results of the simulations (FIGURE 3.23B and 3.23D) follow identical trajectories until finally leveling off to their equilibrium values at long reaction times. The time to reach equilibrium (TABLE 3.4) decreases with the inclusion of residual water in the model at all simulated methanol partial pressures. Therefore, the presence of water not only reduces the final molecular weight, but also decreases the total reaction time until equilibrium.

The presence of water had the greatest effect on molecular weight at the lowest methanol partial pressures. At the higher partial pressures, the increasingly prevalent back reaction overshadowed any effect that the simulated concentration of water may have had on decreasing molecular weight. For the estimated experimental concentration ($1x10^{-4}$ M), the final weight-average molecular weight was 140 kDa with the residual water and 147 kDa without, a reduction of about 5%. The time to reach equilibrium was 95 hr with residual water present and 105 hr without the water. The differences were much less pronounced at elevated levels of methanol.

The weight-average molecular weight was simulated as a function of time at the estimated experimental C_M at three different equilibrium constants to assess the sensitivity of the results to the uncertainty in that particular variable. The molecular weight progressions are identical for all three K_{eq} until M_w begins to level off due to increases in the reverse reaction. The equilibrium M_w was 48, 147, and 490 kDa for K_{eq} of 0.1, 1, and 10, respectively.

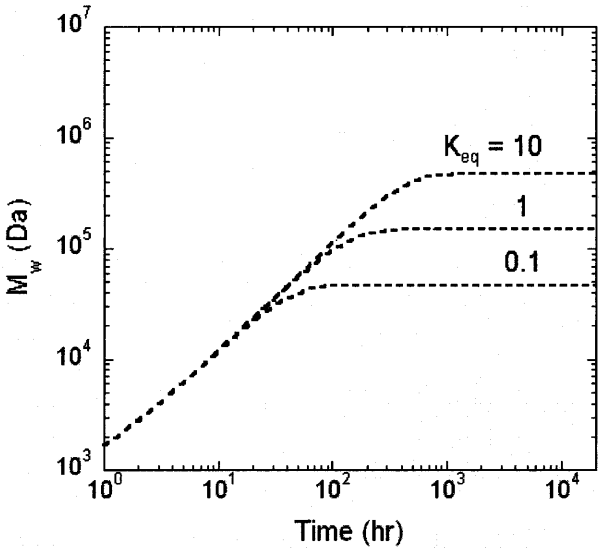

Figure 3.24. Weight-average molecular weight, M_w, as a function of time at three different values of the equilibrium constant, K_{eq}. Simulations were performed at a bulk methanol concentration of $1x10^{-4}$ M, which corresponds to the experimentally measured pressure of $5x10^{-2}$ mm Hg, with no water present.

3.5.5 Equilibrium Modeling: Molecular Weight as a Function of P_M

The equilibrium weight-average molecular weight was simulated as a function of methanol partial pressure to supplement the results of the time-dependent kinetic model. The equilibrium weight-average molecular weight was determined as a function of methanol partial pressure, P_M, at various K_{eq} (0.1, 1, and 10), both with and without residual water present after drying, C_w^o = 0 or 1.5 mM (FIGURE 3.25). The secondary x-axis represents the methanol partial pressure, p_M, that corresponds to each bulk methanol concentration, C_M, using the Raoult's Law vapor-liquid equilibrium description.

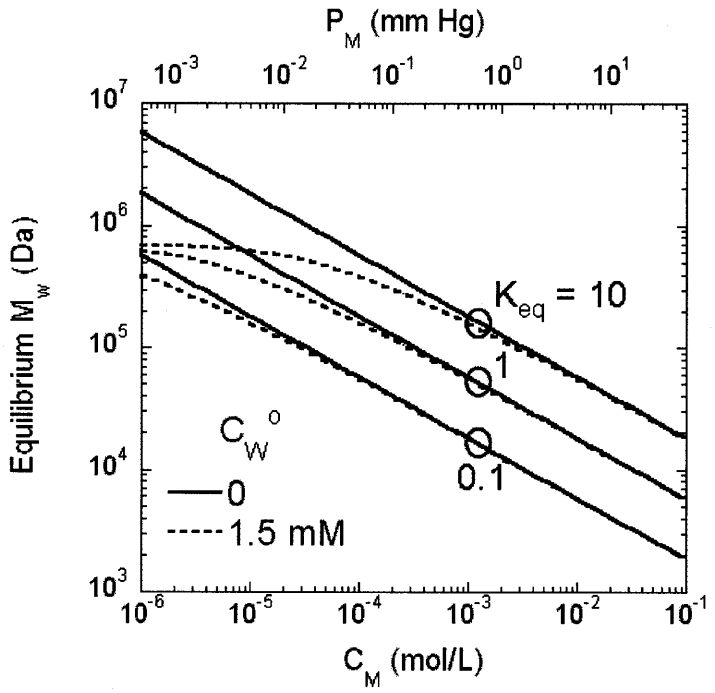

Figure 3.25. Equilibrium weight-average molecular weight as a function of P_M at various K_{eq} with (solid lines) and without (dashed lines) the presence of residual water after drying. The experimental pressure was measured as $5x10^{-2}$ mm Hg.

The equilibrium simulation results demonstrated the significance of both C_M and K_{eq} on the equilibrium weight-average molecular weight. For the water-free case, the equilibrium M_w increased logarithmically over the entire range of simulated methanol concentrations. The simulation was sensitive to the selected K_{eq}; increasing K_{eq} by a factor of 10 resulted in an increase in the theoretical equilibrium M_w by a factor of approximately 3.2 for simulations without water present – the results were almost exactly parallel when plotted logarithmically.

The effect of water was greatest at the lowest C_M and highest K_{eq}. Interestingly, if C_M is set equal to zero, the equilibrium M_w at the three simulated K_{eq} converged to 692 kDa for 1.5 mM water. This suggested that a point could be reached experimentally where methanol removal would provide little benefit due to the limit imposed by the minimum in the residual water under the driest possible conditions. The resulting

disruption of the endgroup stoichiometry by the side-reaction, even in a small amount, reduced the maximum achievable molecular weight.

The Karl-Fischer titration experiments demonstrated that exposed PEG readsorbs water. To investigate the role of water in reducing equilibrium molecular weight, additional values of C_w° (3, 7.5 and 15 mM) were examined over a range of K_{eq} values, 0.1, 1, and 10 (FIGURE 3.26). As before, the secondary x-axis for p_M was calculated assuming Raoult's Law. In these simulations, increasing C_w° had the greatest effect on equilibrium M_w for $K_{eq} = 10$ (FIGURE 3.26A) and little to no effect, except at very the lowest simulated methanol partial pressures, for $K_{eq} = 0.1$ (FIGURE 3.26C).

The increased C_w° had little effect on equilibrium M_w at high C_M at all simulated K_{eq}. This implied that the presence of residual water at the simulated levels would have no effect on equilibrium M_w until a C_M of approximately 10 mM can be achieved. It was evident from the presented results that maximal reduction in both C_M and C_w° both contributed to maximizing equilibrium molecular weight.

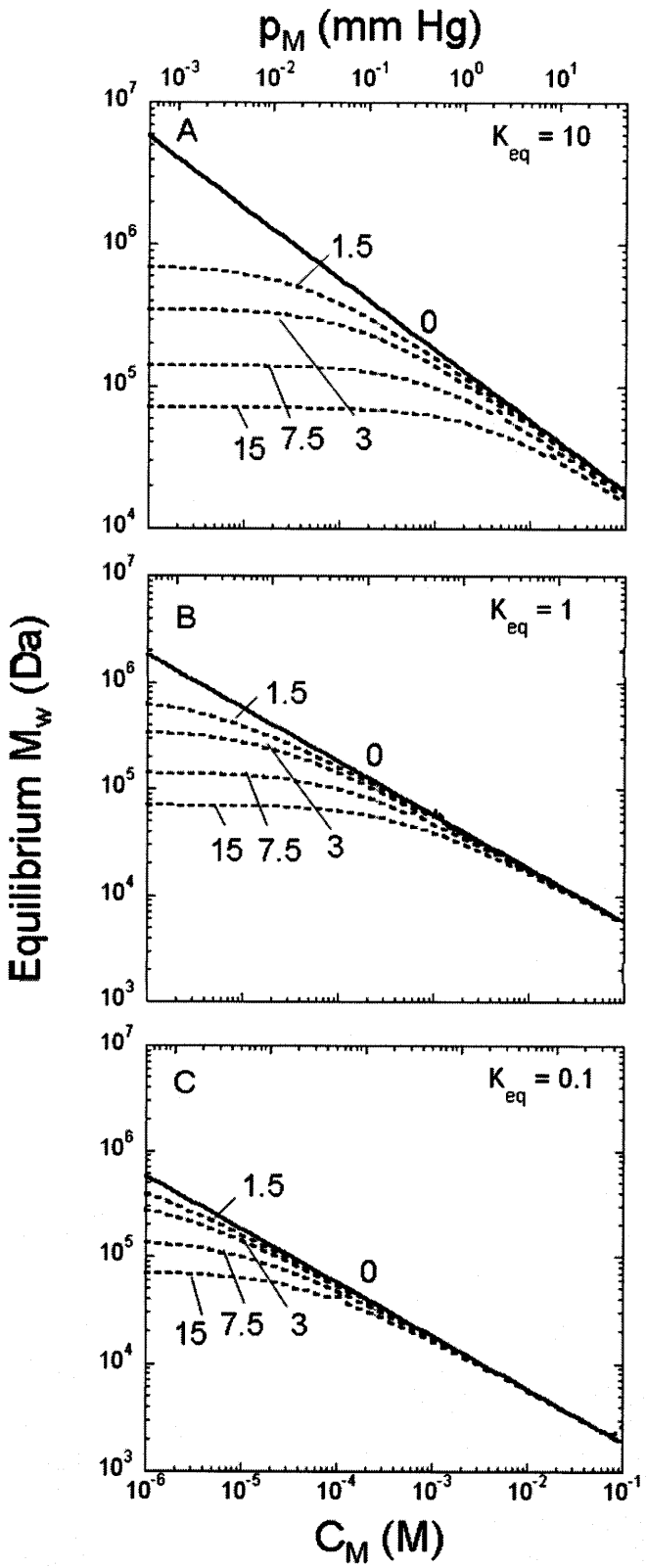

Figure 3.26. Equilibrium M_w as a function of P_M at various C_w^o and three different K_{eq} values, (A) 10, (B) 1, and (C) 0.1. Dotted lines correspond to various C_w^o in units of mM, while solid lines correspond to a water-free system. The secondary x-axis, p_M, was calculated assuming Raoult's Law.

3.5.6 Methanol Mass Transfer Modeling: Analytical Solutions

A Fickian diffusion model was developed to determine the extent to which mass transfer limitations could affect the results of the homogenous kinetic model. The quasi-steady state, one-dimensional model was used to analyze the concentration of either methanol or reactive endgroups as a function of the distance from the catalyst surface. The model was solved for three cases: (1) a well-stirred bulk for which diffusion was modeled in the boundary layer surrounding the catalyst bead, (2) a stagnant bulk where catalyst beads have settled to the bottom of the flask, and (3) the thin film in the Protherm in which the catalyst beads were homogeneously dispersed.

For the well-stirred bulk and the stagnant film cases, the polymerization reaction is heterogeneous, and the solutions to the non-dimensionalized differential equation and associated boundary conditions (EQUATION 32) for mass transfer of methanol in the single-bead and stagnant cases are:

$$\theta_M(\eta) = \left[Da_{f,M}^{bead} - Da_{r,M}^{bead}\theta_M(1)\right]\left(\frac{1}{2} - \frac{1}{\eta}\right) + 1 \qquad (47A)$$

$$\theta_M(\eta) = \left[Da_{f,M}^{film} - Da_{r,M}^{film}\theta_M(0)\right](1 - \eta) + 1 \qquad (47B)$$

The effective forward rate constants for the single-bead and stagnant cases are described by EQUATIONS 27 and 28, respectively. Solving EQUATIONS 47A and B for $\theta_M(1)$ and $\theta_M(0)$, respectively, yields:

$$\theta_M(0) = \frac{2 + Da_{f,M}^{bead}}{2 + Da_{r,M}^{bead}} \qquad (48A)$$

$$\theta_M(0) = \frac{1 + Da_{f,M}^{film}}{1 + Da_{r,M}^{film}} \tag{48B}$$

Both EQUATIONS 48A and B provide the ratio of the methanol concentration at the surface to that in the bulk. It represents the increase in the effective methanol concentration at the catalyst surface due to mass transfer limitations.

For the Protherm case with homogeneous reaction, for which the effective forward rate constant was defined in EQUATION 39, the solution is:

$$\theta_M(\eta) = \left(1 - \frac{Da_{f,M}^{PT}}{Da_{r,M}^{PT}}\right)\frac{\cosh\left(\eta\sqrt{Da_{r,M}^{PT}}\right)}{\cosh\left(\delta\sqrt{Da_{r,M}^{PT}}\right)} + \frac{Da_{f,M}^{PT}}{Da_{r,M}^{PT}} \tag{49}$$

The solution to EQUATION 49 for $\theta_M(0)$ is:

$$\theta_M(0) = \frac{\left(1 - \frac{Da_{f,M}^{PT}}{Da_{r,M}^{PT}}\right)}{\cosh\left(\delta\sqrt{Da_{r,M}^{PT}}\right)} + \frac{Da_{f,M}^{PT}}{Da_{r,M}^{PT}} \tag{50}$$

An analytical solution was also determined for the mass transfer model for the linker methyl ester reactive endgroup (EQUATION 34):

$$\theta_A(\eta) = \left[Da_{r,A}^{bead} - Da_{f,A}^{bead}\theta_A(1)^2\right]\left(\frac{1}{2} - \frac{1}{\eta}\right) + 1 \tag{51}$$

$$\theta_A(\eta) = \left[Da_{r,A}^{film} - Da_{f,A}^{film}\theta_A(0)^2\right](\eta - 1) + 1 \tag{52}$$

For $\eta = 1$ (single-bead) and $\eta = 0$ (stagnant), the term within the parentheses in EQUATIONS 51 and 52 becomes (-1/2) and (-1), respectively. The (-2/3) factor was approximated as (-1) and the quadratic equation was used to solve for $\theta_A(1)$ and $\theta_A(0)$.

$$\theta_A(1) \text{ or } \theta_A(0) = \frac{1 \pm \sqrt{1 - 4Da^i_{f,A} + 4Da^i_{f,A}Da^i_{r,A}}}{2Da^i_{f,A}} \quad (53)$$

where *i* is 'bead' for $\theta_A(1)$ and 'film' for $\theta_A(0)$. The quadratic formula solution presented in EQUATION 53 leads to two difficulties – multiple roots and a square root term. With respect to the former, there is no way to *a priori* choose the correct root unless the negative root provides a physically unrealistic, negative result. Similarly, because imaginary solutions are unrealistic, as well, any results for which the determinant is negative will be ignored.

3.5.7 Mass Transfer Modeling: Model Results

The solutions to the various mass transfer models were studied across a broad range of molecular weights, up to 10^6 Da. The forward and reverse Damköhler numbers and the value of θ_i, the ratio of concentration of species *i* at the surface to either that in the bulk or at the liquid-vapor interface, were calculated as a function of backbone polymer molecular weight for each case. Some terms in these relationships varied with molecular weight, while others were constant and specific to the geometry for the respective case. The concentrations of the non-methanol species (A, B, and L) were determined as a function of backbone polymer molecular weight according to EQUATIONS 17, 18 and 19. For the methanol mass transfer modeling, these species were assumed to be constant in space. For the endgroup modeling, the concentration of A and B, as a function of molecular weight, was set as the bulk/liquid-vapor interface concentration. The geometry-specific terms for each case are summarized in TABLE 3.5. The bulk methanol concentration was set according to the experimentally measured partial pressure assuming Raoult's law.

Table3. 5. Summary of estimates for various inputs into the Fickian methanol mass transfer model for the stirred and stagnant cases. Parameters were tabulated using SI units for consistency.

	Well-Stirred	Stagnant	PT	Units
δ or R	5.0×10^{-4}	1×10^{-2}	1×10^{-3}	m
N_{bead}		3800	7600	beads
A_{flask}		2.6×10^{-3}		m^2
A_{bead}		3.1×10^{-6}	3.1×10^{-6}	m^2
f		0.5		dimensionless
V_{PT}			1.5×10^{-5}	m^3
$K_f\sigma_{enz}$		1.1×10^{-10}		$m^4/(mol\text{-}s)$
$C_M(\delta)$		1×10^{-7} (exp)		mol/m^3
K_{eq}		1		dimensionless

Finally, the diffusion coefficient of methanol in PEG was calculated using the Wilke-Chang correlation (EQUATION 40) at 90°C. This calculation required the solvent viscosity as a function of molecular weight, which was estimated according to the literature [31] as follows. It is well-established [34] that the viscosity of low molecular weight polymers is directly proportional to molecular weight. Once the molecular weight is increased such that the polymers become entangled upon reaching the so-called critical chain length, viscosity is approximately proportional to molecular weight raised to the 3.4 power. According to the tabulated data in the literature [31], which include entries for PEG with M_n of 500, 1000, 3350, and 8000 Da, the critical chain length for PEG is between 3350 and 8000 Da. The PEG viscosity was modeled in three segments: (1) $M_n <$ 3350: a linear regression of the data for which viscosity α M_n^1, (2) $3350 < M_n < 8000$: a straight line between the data points at either limit, and (3) $M_n > 8000$: an extrapolation from the datum at $M_n = 8000$ Da following the 3.4 power rule. The resulting PEG

viscosity as a function of molecular weight (FIGURE 3.27) was used to calculate the methanol diffusivity (FIGURE 3.28).

A sample calculation of the forward and reverse Damköhler numbers for the single bead, methanol mass transfer case are presented in APPENDIX C. These calculations are representative of those performed for the other species and other geometric cases according to thee relevant equations detailed above (Equations 47-53).

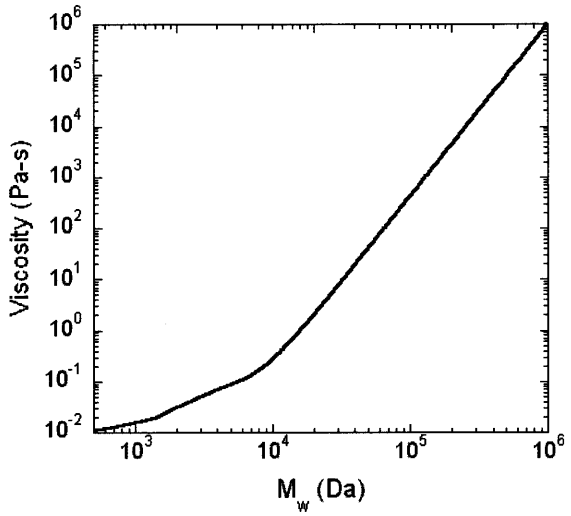

Figure 3.27. Viscosity of PEG presented as a function of weight-average molecular weight. The viscosity was modeled according to literature data and polymer entanglement theory.

The self-diffusivity of PEG, which was assumed to be representative of the diffusivity of the reactive endgroups, was modeled according to literature data [34]. According to the authors, the self-diffusivity of entangled polymers follows a minus-2 power law rule ($D \alpha M^{-2}$). The literature data were extrapolated according to this rule to estimate the PEG self-diffusivity as a function of molecular weight (FIGURE 3.28).

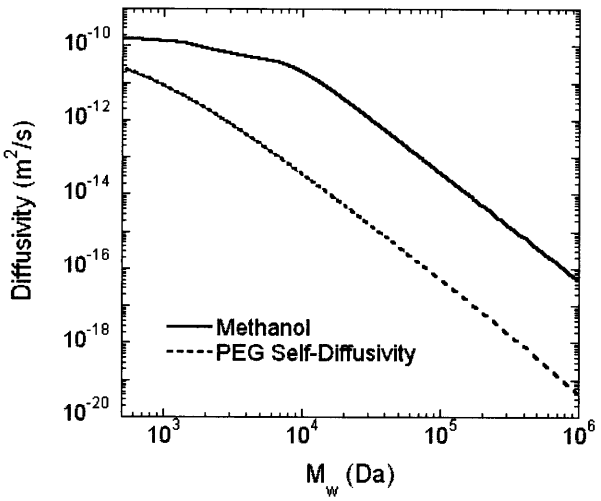

Figure 3.28. Diffusivity of methanol in PEG and the self-diffusivity of PEG presented as a function of weight-average molecular weight. The diffusivities were modeled according to the Wilke-Chang correlation, literature data, and appropriate power law rules for entangled polymers.

The geometric parameters in TABLE 3.5, the diffusivities in FIGURE 3.28, and the corresponding equations from the Model Formulation section were used to calculate the forward and reverse Damköhler numbers for the methanol and reactive endgroup mass transfer models (FIGURE 3.29). In all cases the Damköhler number represents the ratio of the rate of reaction to the rate of diffusion; for Damköhler numbers much greater than one, the rate of reaction is much greater than the rate of diffusion and the modeled process is diffusion-limited. Conversely, when the Damköhler number is much less than one, diffusion occurs more rapidly than reaction and the process in question is reaction-limited.

For the methanol models, Da was the highest for the stagnant film and the lowest for the bead within the well-stirred bulk. This result was a direct consequence of differences in the diffusion length and the effective forward rate constant for these two cases. The results for Da_i^{PT} were at an intermediate level. The forward Damköhler numbers all followed the same trend, decreasing initially at lower molecular weights before reaching a minimum at approximately 10 kDa. The initial decrease was due to a

decrease in the reaction rate associated with consumption of reactants, while the ensuing increase was caused by the decreasing diffusivity of methanol, which decreased at a faster rate than did the forward reaction rate. The minimum occurs soon after the critical entanglement molecular weight (i.e. when viscosity shifts from the M_n^1 rule to the $M_n^{3.4}$ rule).

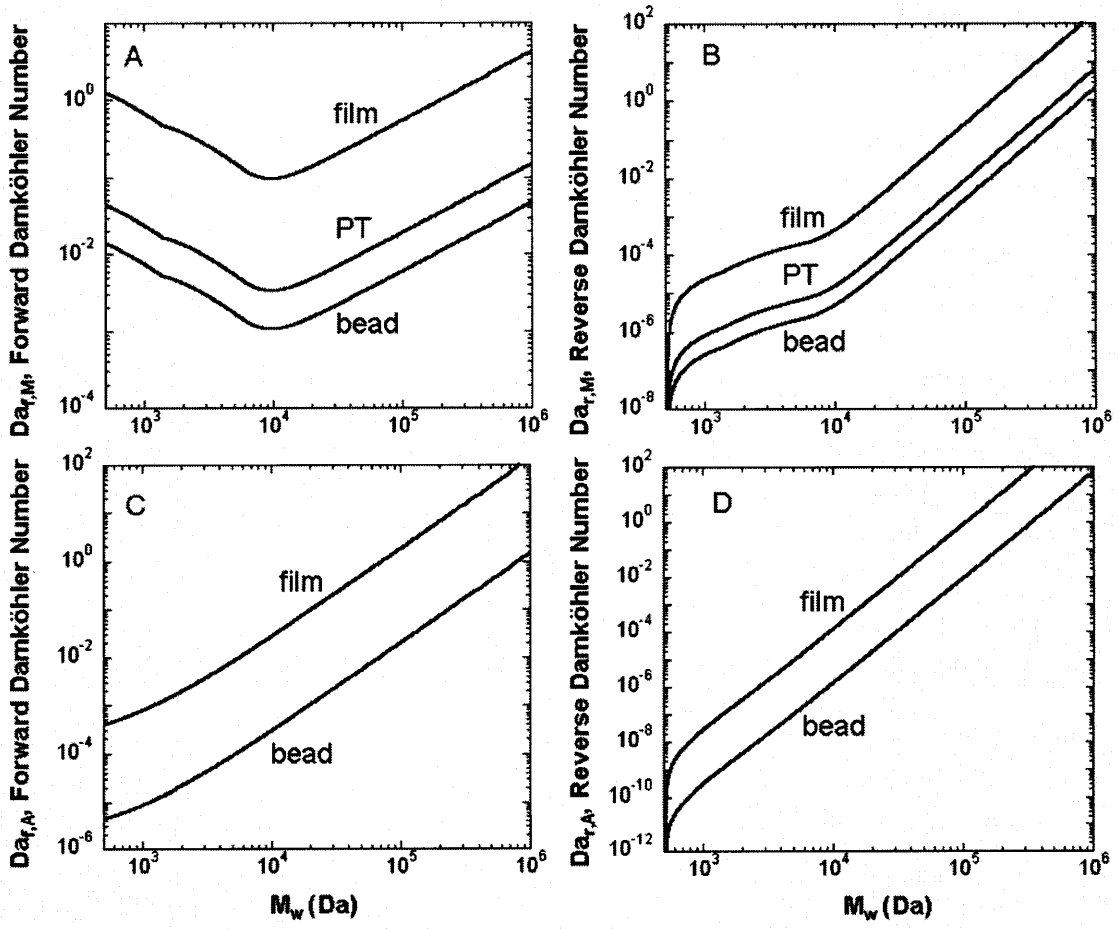

Figure 3.29. Forward and reverse Damköhler numbers for the methanol (A and B) and reactive endgroup (C and D) mass transfer models estimated for the three different cases: a stagnant film, a well-stirred bulk surround a catalyst bead, and the Protherm.

The reverse Damköhler numbers were monotonically increasing across all of the simulated molecular weights for all three cases. The magnitude of Da_r is initially quite small because there are minimal linker groups available to participate in the reverse reaction. As before, the inflection point near 10 kDa coincides with the shift to an

entangled polymer model for the PEG viscosity. The reverse Damköhler number increases at a greater rate than the forward Damköhler number because the reverse reaction is relatively more significant than the forward at the increased molecular weights. The fact that both the forward and reverse Damköhler numbers are, with a few exceptions, less than one, suggested that, although the predicted rate of diffusion may have been slow due to the increased polymer viscosity, the rate of reaction was even slower for the most part.

The ratio of the methanol concentration at the catalyst surface to that at the bulk (bead) or liquid-vapor interface (film and PT) was calculated according to EQUATIONS 48A, 48B, and 50 (FIGURE 3.30A). For the film model, the methanol ratio begins at approximately 2 at low molecular weights, reaches a local minimum at 10 kDa and a local maximum of approximately 1.5 at 80 kDa before eventually decreasing below one. The brief increase in the methanol ratio between 10 and 80 kDa suggested some, albeit relatively small, accumulation of methanol at the catalyst surface because of mass transfer limitations. A methanol ratio O(<1) is not physically realistic because it implies that methanol is somehow being added to the system at the interface. In fact, the methanol ratio for the film model is equal to one at a M_w of 147 kDa, which is exactly equal to the equilibrium molecular weight predicted in the homogeneous modeling.

The methanol ratios for the bead and Protherm cases were approximately unity for nearly all of the simulated molecular weights. This suggested that there would be no methanol accumulation at the catalyst surface (bead) or reactor wall (PT) due to methanol mass transfer limitations.

Because one of the goals of the mass transfer modeling was to determine whether methanol accumulation occurred at the catalyst surface, it is instructive to determine under which conditions significant methanol accumulation would occur by inspection of the analytical solution. To increase the methanol ratio two conditions must be satisfied: the forward Damköhler number must be greater than (1) one and (2) the reverse Damköhler number. Because terms in the forward and reverse Damköhler numbers are both shared (D_M, effective k_f) and interrelated (C_i), there are limited conditions for which these requirements are satisfied. Specifically, the following ratio must be large:

$$\frac{C_A C_B}{C_L C_M (R \text{ or } \delta)} \tag{54}$$

Again, because the concentrations of A, B, and L are related to one another by stoichiometry, this ratio can be large in only two situations: (1) early in the reaction when C_L is comparatively small or (2) when the bulk methanol concentration is further reduced. The first case makes sense because there are few linkage groups available early in the reaction to react with methanol in the reverse reaction. Overall, this analysis suggested that methanol mass transfer limitations were not significant at the bulk methanol concentration estimated for the experimental set-up.

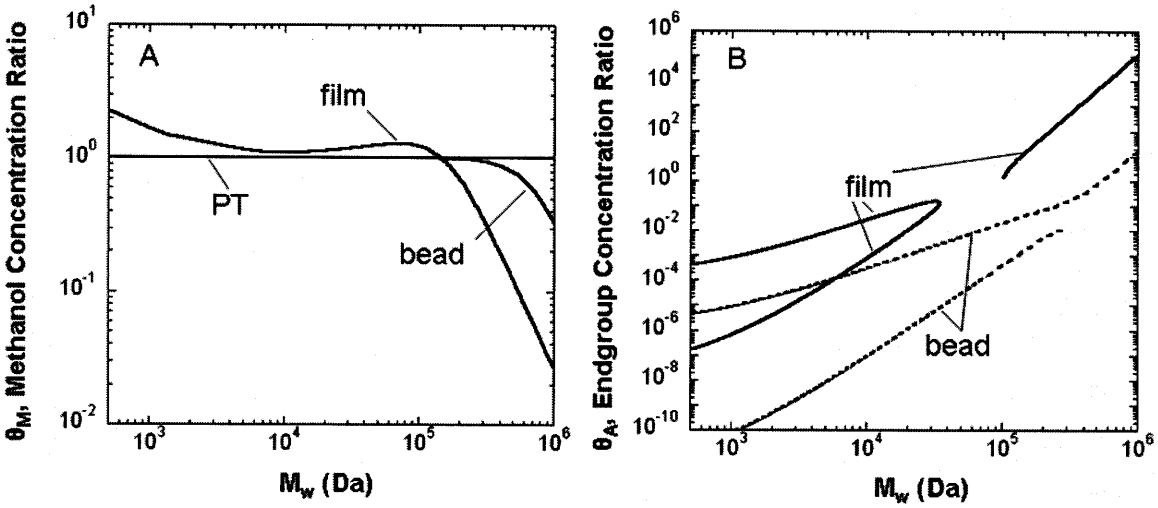

Figure 3.30. Ratios of concentration at the surface to that at the bulk or liquid-vapor interface for the single-bead and stagnant cases, respectively. The concentration ratio, θ_i, was determined for the (A) methanol and (B) reactive endgroup models.

The forward and reverse Damköhler numbers for the reactive endgroup mass transfer model were also calculated (FIGURE 3.29C and D). Unlike the results for $Da_{f,M}$, the $Da_{f,A}$ were monotonically increasing. This was due to two factors: the reactive endgroups (1) could only exist at the end of the same polymer chain and (2) were added stoichiometrically. Therefore, the boundary condition at the catalyst surface contained a squared variable term, which led to a different formula for the Damköhler numbers. These factors also caused the $Da_{i,A}$ results to cover a much broader range of orders-of-magnitude than were observed for $Da_{f,M}$.

The endgroup concentration ratios were calculated according to EQUATION 53 (FIGURE 3.30B). The presented results omit any solutions for which the determinant in the quadratic formula was negative, which was the case for the film model for molecular weights between 30 and 100 kDa, as well as any negative values for the concentration ratio, θ_A. Unfortunately, there was no way to distinguish between the positive and negative roots that gave physically realizable results.

The concentration ratio at low molecular weight was less than O(1), which means that the surface concentration of the reactive endgroups was less than that at the interface. This implied that limitations in the transfer of reactive endgroups to the catalyst may inhibit the reaction rate at low molecular weights. At higher molecular weights, the ratio increased to a value greater than O(1) possibly suggesting regeneration of reactive endgroups due to significant back reaction, which is an unlikely scenario in a real system.

3.5.8 Evaluating Polymer Molecular Weight by Gel Permeation Chromatography

Gel permeation chromatography (GPC), a type of size exclusion chromatography (SEC) was used to evaluate the molecular weight of unknown polymer samples. GPC can be used to make qualitative molecular weight comparisons between samples based on their respective elution volumes. In SEC, higher molecular weight species elute at shorter elution times than do lower molecular weight species because low molecular weight polymers can enter the porous media thereby increasing their effective path length within the column bank.

The GPC column bank was calibrated using a kit of narrow PMMA standards of known molecular weights. Because retention time is related not only to polymer molecular weight but to differences in hydrodynamic radius and non-specific interactions with the packing media, as well, it was necessary to convert from PMMA molecular weight to that of the backbone polymer. This conversion was performed using an empirical relationship proposed by Mori [42, 43]:

$$(M_{backbone})_i = s(M_{PMMA})_i^t \tag{54}$$

where $(M_j)_i$ is the molecular weight of species j eluting at an elution volume, i, and s and t are regressed empirical parameters. Application of this methodology to the GPC system and PMMA standards is represented in FIGURE 3.31.

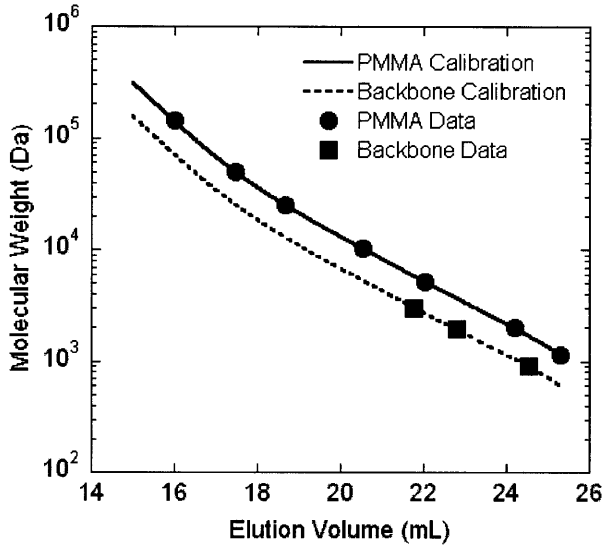

Figure 3.31. Elution volumes for PMMA standards (•) were fit to a fifth order polynomial (solid line). Elution volumes for known backbone polymer samples (■) and the and empirical relationship of Mori [42, 43] were used to calibrate the GPC system for backbone polymer molecular weight.

The first step in the calibration was to determine the elution volumes for low polydispersity PMMA standards of known molecular weights as represented by the circles in FIGURE 3.31. A PMMA calibration curve was constructed by fitting the individual PMMA data to a fifth-order polynomial (represented by the solid line).

The number of backbone polymer samples was limited because backbone polymer standards could not be synthesized and were not commercially available[4]. Consequently, the elution volumes for PEG900 and short backbone polymer oligomers were estimated from experimental data (FIGURE 3.32). The elution volume of PEG900 was determined for a sample containing only PEG900 dissolved in THF. A sample from

[4] Monodisperse standards are usually synthesized by ionic or free-radical polymerization. Backbone polymer can only be produced by condensation reaction. Moreover, although PEG standards were available, their limited solubility in THF prohibited their use in the calibration.

an early time point in the polymerization (t = 30 min) is shown in FIGURE 3.32. The three discernible peaks observed in the chromatogram were attributed to a mixture of PEG900 and PEG900-linker (BA), BAB, and $(BA)_2B$. The BAB and $(BA)_2B$ peaks likely contain a mixture of BAB + BABA and $(BA)_2B$ + $(BA)_3$, respectively. Unfortunately, the column bank was unable to resolve higher molecular weight backbone polymer into individual peaks. The solid squares in FIGURE 3.31 were determined according to the elution volumes of the peaks and corresponding molecular weights in FIGURE 3.32.

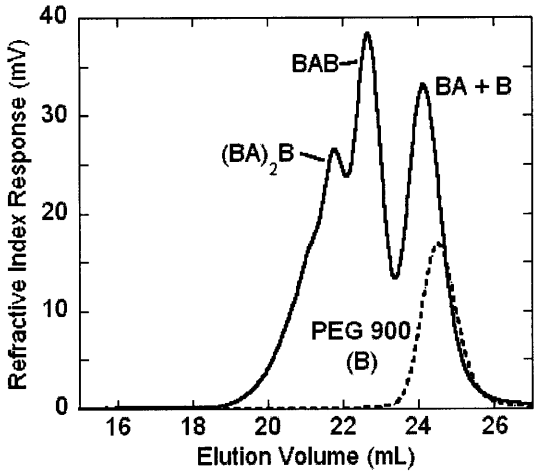

Figure 3.32. Chromatograms used to determine the elution volume for PEG900 and backbone polymer oligomers of known molecular weights.

A least-squares regression was performed using the PMMA calibration and the backbone polymer data according to the empirical relationship in EQUATON 54 (the corresponding MATLAB code is included in APPENDIX B). The empirical parameters, *s* and *t*, were determined to be 0.5 and 0.96, respectively. The dotted line in FIGURE 3.31 represents the backbone polymer calibration curve that results by transforming the PMMA calibration according to the regressed parameters. The relationship of this dotted line to the backbone polymer individual data points also represents the fit of the least-squares regression used to determine *s* and *t*.

Samples were taken from the polymerization throughout the experimental study of the backbone polymerization and analyzed by GPC. These measurements yielded a chromatogram representing the molecular weight profile of the sample. Because it is not possible to present and compare chromatograms for all time points in all of the completed reactions, the information in a given chromatogram was reduced to representative values, including M_n, M_w, and the polydispersity index, in order to compare results across a large number of samples (see APPENDIX A for more information on these calculations). The weight-averaged molecular weight, M_w, was chosen for the analysis because it best represented the differences in the chromatograms observed throughout the study. Entire chromatograms for specific samples will be presented and compared, as necessary.

3.5.9 Experimental Evaluation of Key Variables in Flasks

Backbone polymerizations were performed according to the procedure described in Methods. All initial experiments were performed in glass flasks under a variety of experimental conditions. Sixteen different reactions or sets of reactions were performed during the polymerization studies. The conditions for these reactions were tabulated and numbered for reference during the presentation of the results.

Table 3.6. Summary of reaction conditions investigated during the polymerization studies. The reactor, stirring, and presences of molecular sieves are listed for each reaction. The comment column indicates other deviations from the standard reaction conditions, including those for reactions investigating the effect of vapor-phase pressure, solvent weight percentage and the length of PEG drying.

Reaction	Reactor	Stirring	Sieves	Comment
1	Flask	Magnetic	No	n = 5
2	Flask	Magnetic	No	P = 380 mm Hg, n = 2
3	Flask	Mechanical	No	
4	Flask	Mechanical	No	UML
5	Flask	None	No	
6	Flask	Mechanical	No	25 wt% solvent
7	Flask	Mechanical	No	50 wt% solvent
8	Flask	Mechanical	Yes	
9	Flask	Mechanical	Yes	10 min drying
10	Flask	Mechanical	Yes	No drying
11	Protherm	2000 rpm	Yes	
12	Protherm	2000 rpm	No	
13	Protherm	2000 rpm	No	25 wt% solvent
14	Protherm	2000 rpm	Yes	Double catalyst
15	Protherm	500 rpm	Yes	1st run
16	Protherm	500 rpm	Yes	Repeat of 15

The effect of vapor-phase pressure above the reaction melt was assessed in flasks with magnetic stirring of the reaction mixture (FIGURE 3.33). The vapor-phase pressure, which was assumed to be directly related to methanol concentration in solution, was varied using two different vacuum pumps. A diaphragm pump was used to maintain the vapor-phase pressure above the reaction melt at 380 mm Hg. Under this condition, the reaction was only modest with M_w = 3 kDa achieved after more than 50 hr. On the other hand, a significant increase in M_w was observed when an oil-driven pump was used to maintain a vapor-phase pressure of 0.05 mm Hg. The results for these high vacuum polymerizations were quite variable, particularly at 48 hr; however, these results were produced by a variety of experimentalists (including two 10.26 projects) over a range of more than 3 years. Unfortunately, no further refinement in the polymerization behavior as

a function of vapor-phase pressure was obtainable due to the inability to regulate the system to intermediate pressure levels.

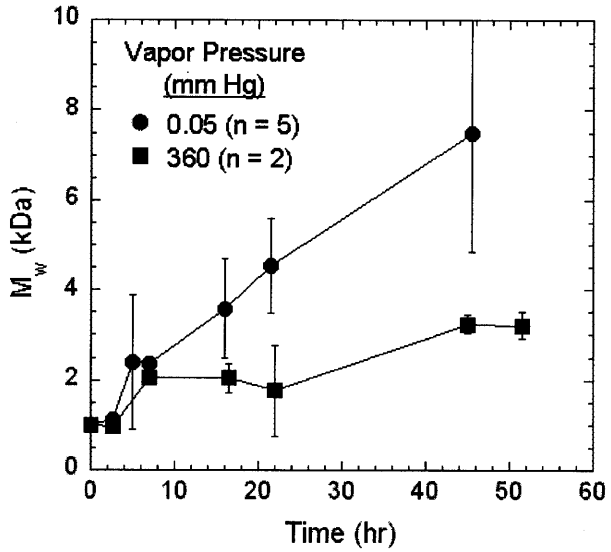

Figure 3.33. Backbone polymer M_w versus time at two different vapor-phase pressures above the reaction mixture. Flasks were magnetically stirred and total vapor pressure was controlled by an oil-driven or diaphragm pump at low and high pressures, respectively. (Reactions 1 and 2)

The magnetic stirring bar stopped at reaction times corresponding to an approximate M_w of 4-5 kDa in the five reactions at 0.05 mm Hg presented in FIGURE 3.33. With the exception of one reaction in which M_w continued to increase to 11 kDa at 48 hr, the rate of M_w increase was drastically reduced once the stirring bar stopped. This exception was the primary cause in the variability at 48 hr.

The effect of different methods of stirring the reaction mixture was investigated, both at MIT and by our collaborators at UMass Lowell (FIGURE 3.34).

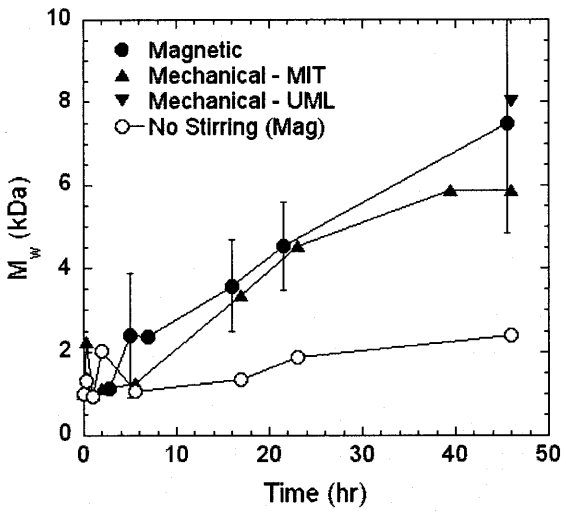

Figure 3.34. Backbone polymer M_w versus time under various stirring conditions. A stationary magnetic stirring bar was placed in the reaction melt for the 'no stirring' case. Mechanical stirring reactions were performed by different researchers at both MIT and UML. (Reactions 1, 3-5)

Two different stirring set-ups, magnetic and mechanical, were investigated at MIT for polymerizations in flasks. The progression of the backbone polymer M_w in these two different set-ups was nearly identical. Moreover, reactions in an identical mechanically stirred flask set-up at UMass Lowell produced backbone polymer product very similar in M_w (only final product was available for analysis – no intermediate time points were sampled). The negligible differences between the two stirring methods was unexpected because the mechanically driven blades were able to rotate for the duration of the polymerization while the magnetic stirring bar typically stopped at a M_w of approximately 4-5 kDa. The intact or crushed Novozym435 beads acted as tracers in the mixture for visualizations of the mechanically stirred reactions. At early reaction times ($t < 12$ hr), the reaction mixture was thrown up the sides of the flask with each rotation of the mechanically driven blades. Under these conditions, mixing was achieved through the combination of rotational and radial motion, the latter of which was caused by the spreading and falling of the polymer melt along the flask wall. At longer reaction times ($t > 18$ hr), the more viscous polymer melt accumulated in front of the blades to a height of

approximately 2-3 cm. The rotating blades pushed the accumulated polymer in a circle. The accumulated polymer did not appear to rotate or churn, remaining stationary relative to the frame of reference of the rotating blade.

Figure 3.35. Schematic representation of the mechanically stirred polymerization in the flask. At early times (A), the reaction is well-stirred, with the polymer melt spread repeatedly along the sides of the flasks with each blade rotation. At late times (B), the polymer melt accumulates in front of the blade and pushed around the flask with minimal mixing.

The reaction with no stirring used the magnetic set-up with a stationary stirring bar. In this reaction, there was very little increase in M_w. In fact, even though a low system pressure was maintained (0.05 mm Hg) for this experiment, the M_w for this unstirred reaction was less than that for the stirred reaction at 360 mm Hg. This result suggested that effective stirring was more important than methanol removal at the initial stages in the reaction.

Polyethylene glycol-250 dimethyl ether, a non-reactive, negligible vapor pressure solvent, was investigated to determine whether addition of a solvent could extend the time that mechanical stirring could mix the polymer melt. The solvent was added at varying weight percentages to reactions performed in the mechanical stirring set-up (FIGURE 3.36).

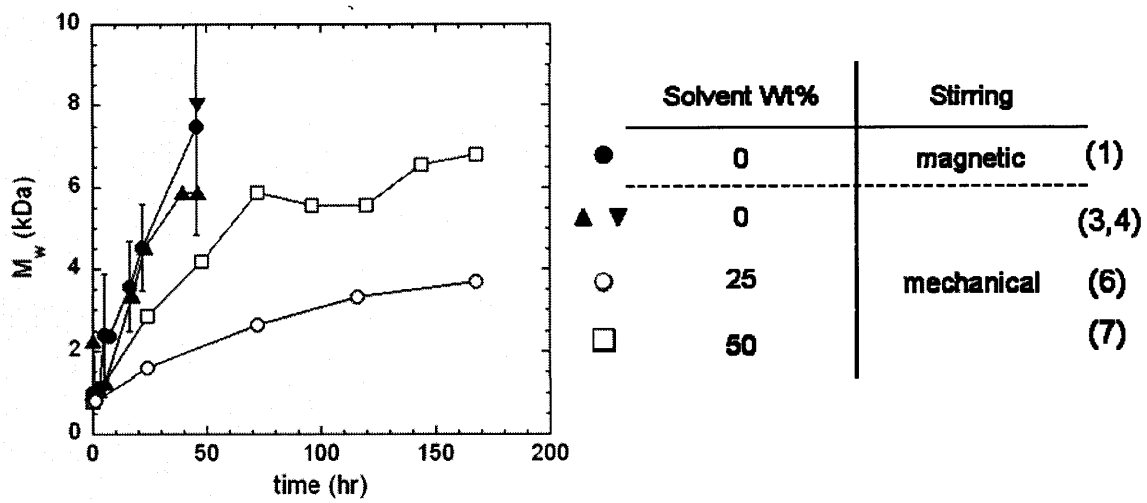

Figure 3.36. Backbone polymer M_w versus time at various solvent weight percentages. PEG250 dimethyl ether was chosen as the solvent due to its non-reactivity and negligible vapor pressure. (Reactions 1, 3, 4, 6, 7)

The M_w for both polymerizations with solvent added (25 and 50 wt%) were lower than that for the bulk polymerizations. Although the addition of solvent likely improved the mixing conditions in the reaction, any related benefits were offset by the reductions in reactive endgroup concentrations. These concentration considerations were one of the key motivations behind performing polymerizations in bulk. The solvent addition also has competing effects with respect to the methanol removal. While the solvent may reduce diffusion limitations by decreasing the viscosity of the reaction mixture, it also increases the methanol diffusion length due to the increased volume.

3.5.10 Polymerization with the Addition of 4Å Molecular Sieves

Activated powdered 4Å molecular sieves were added to the reaction mixture as a potential scavenger of small polar molecules. Although sieves are traditionally used as a drying agent, 4Å sieves have the capacity, in theory, to trap both residual or reabsorbed water and the methanol byproduct. The sieves were added at 10 wt% of the total mixture.

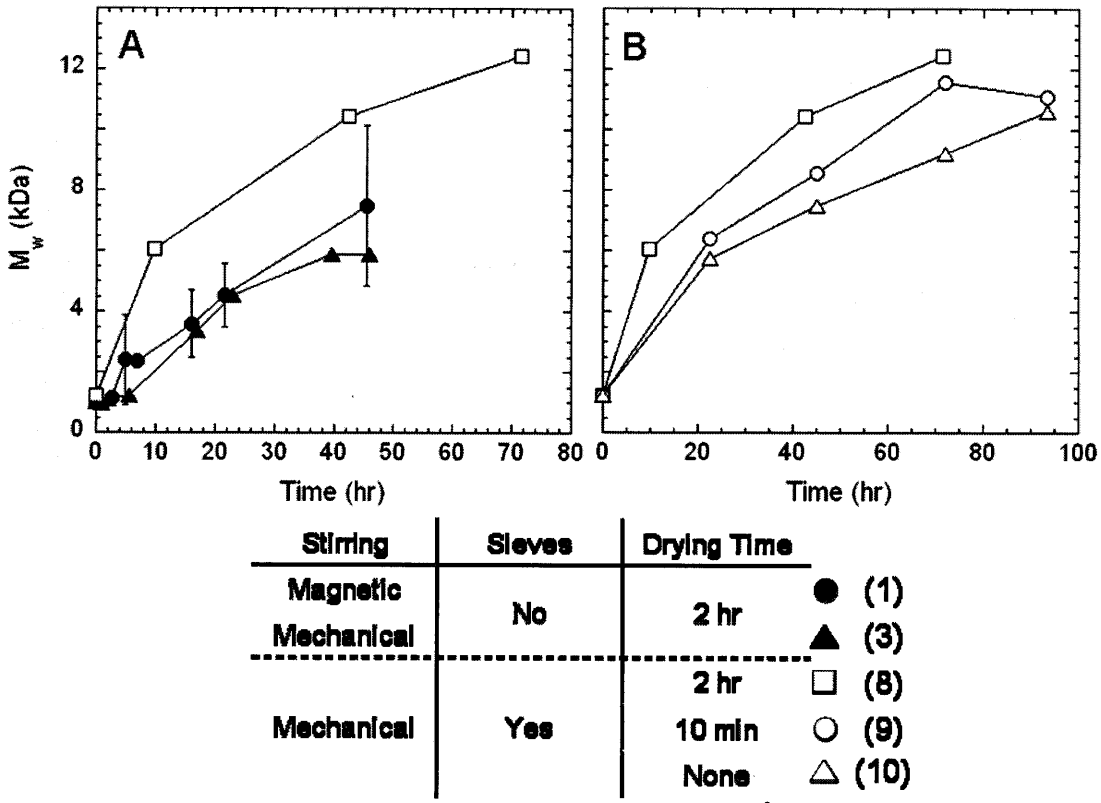

Figure 3.37. Backbone polymer M_w versus time in the presence of 4Å molecular sieves compared to reactions (A) with no sieves present and (B) under varying lengths of PEG drying. The typical drying period was 2 hr. The data without sieves were reproduced from FIGURE 34.

The polymerization with molecular sieves added was compared to polymerizations without sieves added (FIGURE 3.37A). Mechanical stirring was used for the reaction with sieves. The results presented previously in FIGURE 3.34 were reproduced for the reactions without sieves. Addition of molecular sieves led to a significant increase in molecular weight compared to reactions without sieves added. The increased molecular weight was observed at all times measured, which suggested that the sieves increased both the initial rate of reaction as well as the maximum achievable steady-state molecular weight. The molecular weight observed with the molecular sieves added was the highest ever achieved for the backbone polymer. The molecular weight also continued to increase even though poor mixing like that described in FIGURE 3.35 was observed after for time points greater than approximately 12 hr. Considering that

they are designed to trap polar molecules smaller than 4Å, it is possible that the sieves were scavenging the methanol byproduct, essentially acting as small localized vacuums within the melt.

Experiments were also performed with molecular sieves where the drying conditions were varied (FIGURE 3.37B). In these experiments, the drying time was either decreased to 10 min or completely omitted. The molecular weight still increased substantially, reaching weight-average values of 10.5 kDa for both limited drying cases. These molecular weights were also higher than that achieved in any previous experiments without molecular sieves added, despite the fact that either no or minimal water was removed from the hygroscopic PEG. The primary difference between the experiment with complete drying (open squares) and those with incomplete drying (open circles and triangles) was a slight delay in the molecular weight progression. Because the PEG was not dry at the beginning of the reaction, the first part of the polymerization period may have been devoted to PEG drying instead of chain extension. During this period, water was likely removed both in the vapor headspace and by the molecular sieves.

During the course of the study, a number of polymerizations failed to achieve any significant increase in molecular weight and were deemed failures, often for unknown reasons. The cumulative failure rates for all reactions in both the flasks and Protherm, either with or without molecular sieves present, were compiled (TABLE 3.7). A reaction was designated as failed if the weight-average molecular weight was less than 4 kDa after 48 hours. Reactions without stirring or at high pressure were not included in this analysis.

Table 3.7. Effect of 4Å molecular sieves on the historical failure rate of backbone polymerization in flasks and the Protherm.

Sieves?	no. rxns	Failure Rate
No	32	38%
Yes	12	0%

During the course of the study and particularly before the introduction of molecular sieves, a significant number of reactions (38%) failed for unknown reasons. However, not a single reaction out of the 12 in which molecular sieves were added failed. This observation, together with the molecular weight increases achieved in the polymerization (FIGURE 3.37), demonstrate the absolute necessity of adding molecular sieves to improve the performance and reliability of the backbone polymerization.

3.5.11 Backbone Polymerization in the Protherm

The results of the polymerization study in the flask set-up were used to guide experimental condition selection for reactions in the Protherm. The reaction conditions investigated included the original reaction mixture ('no additives'), as well as reaction with molecular sieves, 25 wt% PEG250 dimethyl ether solvent, or double catalyst loading (FIGURE 3.38). The reaction times for the Protherm polymerizations were longer than those for the flask reactions.

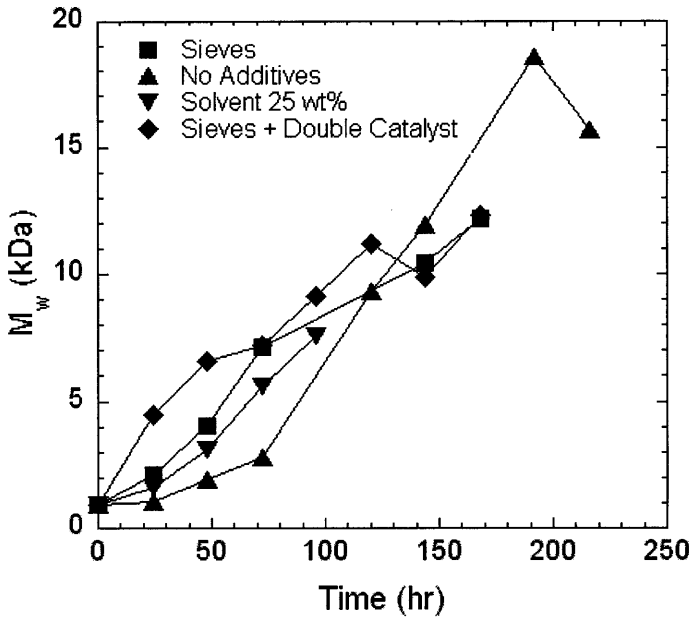

Figure 3.38. Backbone polymer M_w versus time in the Protherm under various experimental conditions, including sieves, solvent, and double catalyst loading. The blade speed was 2000 rpm. Samples were taken from the middle of the reaction zone. (Reactions 11-14)

In contrast to the flask polymerization study, a smaller total number of reactions were performed because only a single reactor was available. The blade speed was set to 2000 rpm for all the polymerization data in FIGURE 3.38. This blade speed, which was the maximum achievable by the Protherm drive motor, was chosen because it was hypothesized that increasing the rotational speed would improve the mixing in the system. Reaction in the Protherm produced significantly higher molecular weight product in all cases compared to that observed in the flasks. Most importantly, the M_w for the 'no additives' reaction at 196 hr represented the highest backbone polymer M_w ever achieved. The Protherm produced higher M_w backbone polymer for the reaction with PEG250 dimethyl ether solvent (25% w/w), even though addition of the solvent significantly reduced M_w in the flask set-up (FIGURE 3.36).

With the exception of the reaction with double catalyst (20 wt%), all M_w profiles were concave upwards at early reaction times. This behavior is inconsistent with the

concave downward reaction profile typically observed for condensation polymerizations, The typical concave downward trend was restored by the addition of double catalyst, which significantly increased the initial reaction rate. The M_w for the double catalyst reaction converged with that for the other reaction conditions, which suggested that the kinetic limitations may have been superseded by mass transfer limitations.

Based on the interesting concavity trends observed during the initial Protherm reactions, a study was performed to better understand the fluid dynamics in the reactor, specifically focusing on the characteristics of the thin film and fillet (TABLE 3.8). In these studies, two different PEG molecules were used to simulate lower and higher viscosities. The blade speeds were varied from 500 to 2000 rpm to simulate different possible fluid mechanical regimes.

Table 3.8. Flow visualizations of the fillet and thin film in the Protherm for different PEG molecules at three different blade speeds. Blade rotation is in the counter-clockwise direction.

PEG M_n (Da)	Speed (rpm)	Observations
1000	500	Observable fillet from bottom to right, thinner at top, and not noticeable on left. Film thinner at top than at bottom, significant pooling.
	1200	Fillet observed at lower right with small fillet elsewhere. Thin film is still noticeably thinner on the top with some pooling.
	2000	Fillet largest on right side and nearly disappears at the top. Thin film appears to be approximately the same over entire circumference.
4600	500	Film appears completely uniform. Fillet the same size at all circumferential positions.
	1200	Uniform thin film. Fillet nearly uniform but significantly smaller than seen at 500 rpm (about 1mm size).
	2000	Uniform thin film. Fillet is uniform and about the same size as at 1200 rpm.

Significant differences in the extent of fillet development and fillet thickness were observed during the Protherm fluid visualizations. At the lowest blade speeds and melt viscosities, the fillet did not formed over the entire circumference of the reactor. Consequently, the thin film was thinner at the top of the reactor and significant pooling was observed at the bottom of the reactor. Under these conditions, the fluid viscosity and blade speed were unable to overcome the force of gravity. For the low viscosity PEG at the highest blade speed, 2000 rpm, which is close to the conditions in the reactor for the polymerization results in FIGURE 3.38, the fillet exists throughout the circumference of the reactor, albeit to a small extent at the top of the Protherm.

For the higher molecular weight PEG (M_n = 4600 Da), a uniform thin film and complete fillet were observed over the entire reactor circumference at both 1200 and 2000 rpm. This result suggested that complete thin-film and fillet development likely occurred between PEG molecular weights of 1000 and 4600 Da. The result for PEG should be a reasonable proxy for the backbone polymer, which is composed primarily of PEG900 monomer units.

During the Protherm reaction with molecular sieves added, samples were taken from six locations throughout the reaction zone (FIGURE 3.39), including the front, back, and four equidistant circumferential positions in the middle as detailed in the Methods. There were no differences among circumferential samples taken at the middle of the reaction zone. However, at the front and back of the reactor the backbone polymer M_w did not increase beyond 5-6 kDa.

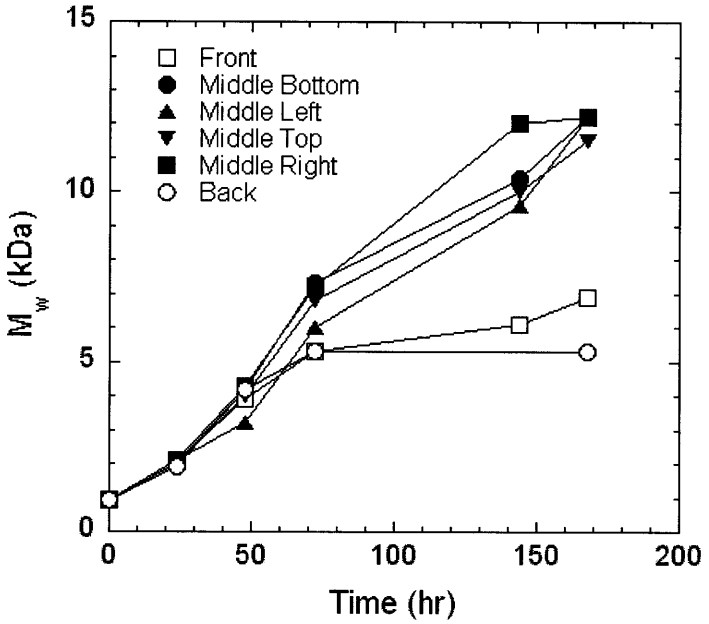

Figure 3.39. Backbone polymer M_w versus time at various positions within the Protherm reaction zone. The reaction included 10 wt% molecular sieves. (Reaction 11)

The blades were set at 2000 rpm, the maximum attainable speed for the prototype drive motor, in all of the Protherm results presented thus far. Two polymerizations, both with 10 wt% molecular sieves, were performed at 500 rpm to assess Protherm performance at a lower rotational speed. The M_w as a function of time for these polymerizations are plotted along with the average M_w data for the 2000 rpm polymerizations (FIGURE 3.40).

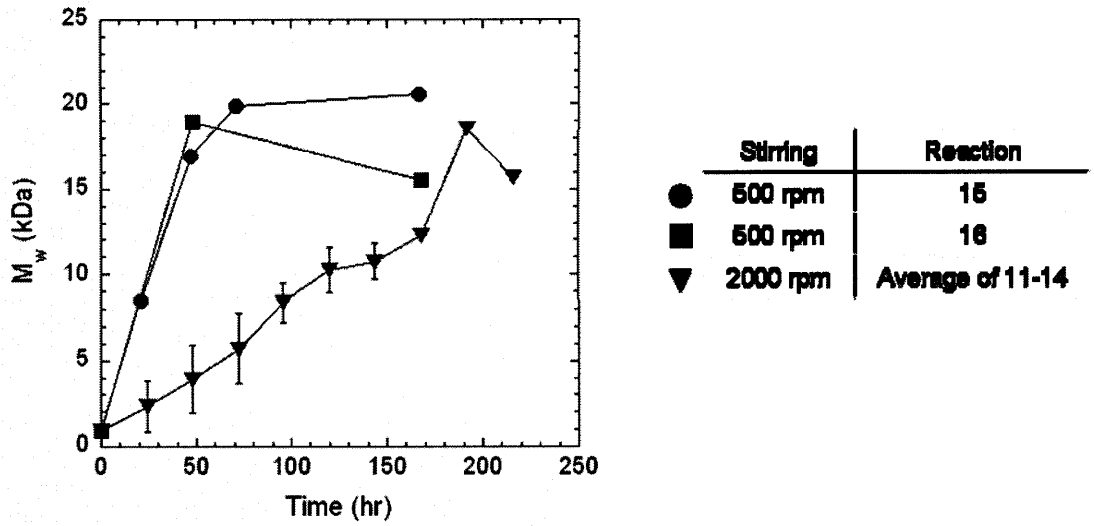

Figure 3.40. Backbone polymer M_w versus time for two different Protherm blade speeds. Two polymerizations were performed at 500 rpm, both with 10 wt% molecular sieves. The data from FIGURE 38 (Reactions 11-14) were averaged to produce the 2000 rpm curve for comparison.

In both of the experiments at the decreased blade speed of 500 rpm, the backbone polymer M_w was 17 and 19 kDa after only 48 hr. This M_w was comparable in magnitude to the highest previously attained M_w in approximately only one-fourth of the reaction time. In both reactions, more than 75% of the mass of the initial reactants charged to the reactor was observed to have been transferred from the walls to the blades, becoming completely solidified on the unheated blade surfaces as a result. In both reactions, this transfer occurred after the 48 hr time point and before the next sampling time. This transfer of the melt out of the heated reaction zone and onto the blades likely prohibited any further increases in M_w.

3.5.12 Comparison of Results in the Flask and the Protherm

Results for polymerizations in both the flasks and Protherm were selected for comparison (FIGURE 41). Some reactions were omitted to avoid further complicating the resulting plot.

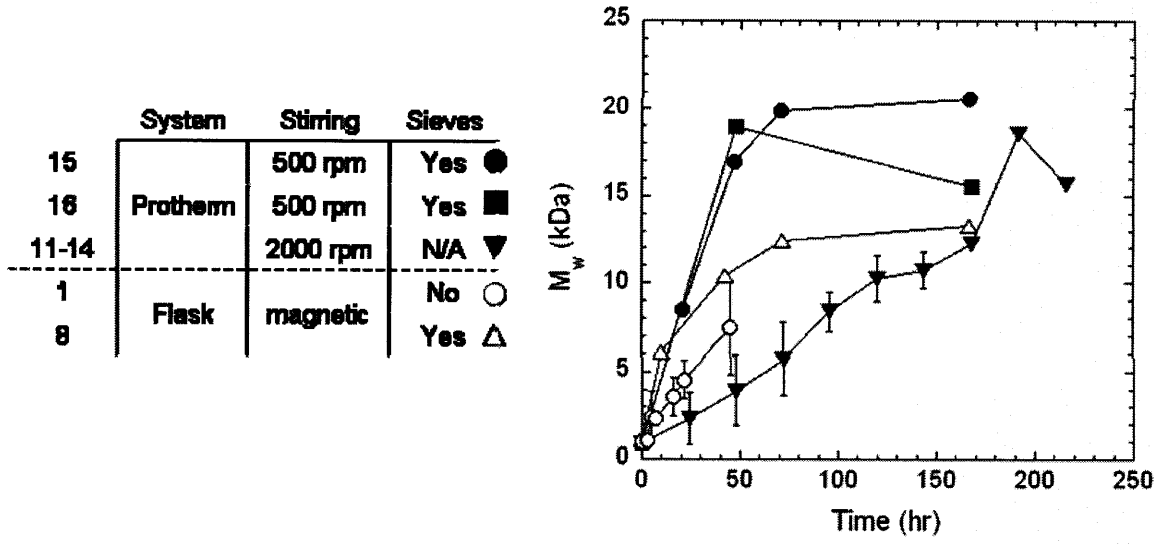

Figure 3.41. Comparison of backbone polymerizations performed in different experimental set-ups and reaction conditions.

This direct comparison demonstrated that the combination of the Protherm thin-film reactor at 500 rpm and the methanol and water scavenging capability of the molecular sieves produced backbone polymer with the highest M_w. The Protherm reactions at 2000 rpm proceeded more slowly than even the magnetically stirred flask reactions without sieves added. However, all of the 2000 rpm Protherm reactions, regardless of the addition of solvent, sieves, or double catalyst, ultimately reached or were on a trajectory to reach M_w comparable to the M_w for the best recorded flask reaction (magnetic stirring and molecular sieves, #8).

Three chromatograms were selected for closer analysis: (1) the flask reaction with magnetic stirring at 48 hr (one of the five runs from which the average for reaction condition 1 was determined), (2) the 144 hr time point from the 2000 rpm Protherm reaction with sieves added (reaction condition 11), and (3) the 48 hr sample from the 500 rpm Protherm reaction with sieves added (reaction condition 15). The chromatograms were processed to represent the absolute mass of species measured at the various molecular weights by the procedure described in Appendix A, multiplying the relative

mass by the total initial mass charged to the system in the form of PEG and linker (mass losses due to methanol removal were ignored). This normalization technique accounted for differences in the sample mass, allowing for direct comparison of the mass of backbone polymer at each molecular weight.

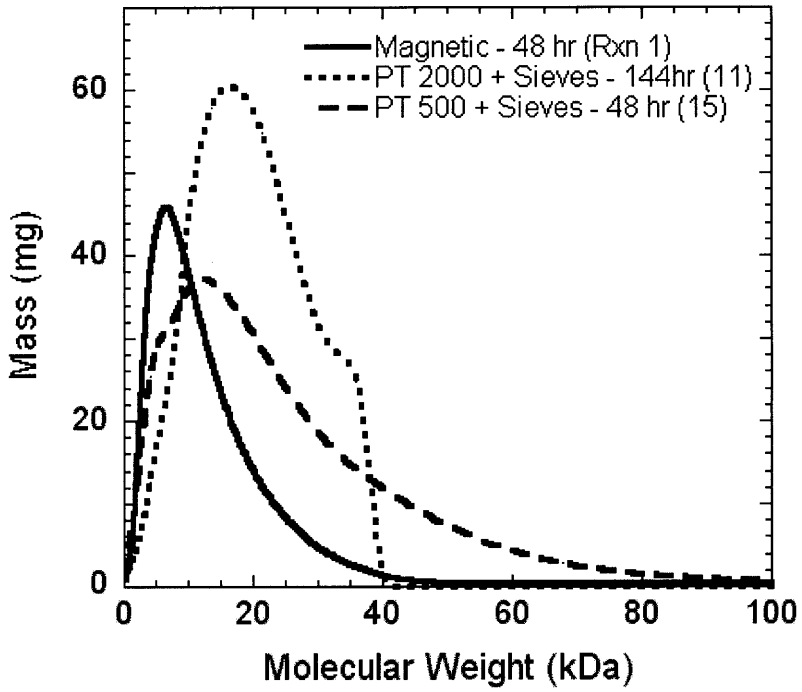

Figure 3.42. Chromatograms for specific time points from select polymerizations. Data are presented as the relative mass of backbone polymer at particular molecular weights

In addition to producing polymer with the highest M_w, the 500 rpm Protherm reaction with sieves was the only chromatogram to produce any polymer species having molecular weight greater than 40 kDa. Inspection of the shape of the chromatograms provided additional insight. In particular, the sharp edge at 40 kDa for the 2000 rpm Protherm reaction may have indicated that transesterification reactions were rearranging any polymer chains greater than 40 kDa in length. This behavior is a characteristic trait in condensation polymerizations as they approach or reach quasi-steady state [11]. There was some moderate increase in molecular weight observed for this reaction beyond the

144 hr time point (FIGURE 38, squares); however, the shape of the chromatogram was unlikely to have been artifact. Moreover, transesterifications do not necessarily preclude further increases in molecular weight – recall that the molecular weights are calculated as averages of a distribution. Conversely, this phenomenon was not observed for the 500 rpm Protherm 48 hr time point. In this chromatogram, the diffuse right shoulder suggested that the reaction had not yet reached quasi-steady state, providing further evidence that the cessation of the molecular weight progression was caused by transfer of the reaction mixture onto the unheated blades.

3.5.13 Comparison of Experimental Results and Model Predictions

Different models have been proposed and investigated to different extents. The results of the homogeneous kinetic model were compared to experimental results for four selected polymerizations (FIGURE 3.45). The experimental bulk methanol concentration was estimated to be $1x10^{-4}$ M according to the Raoult's Law assumption. The model predictions for this concentration (the steep solid line) were higher than the experimentally measured weight-average molecular weights at all reaction times. The experimental results were actually most comparable to the homogeneous model predictions for a bulk methanol concentration of $1x10^{-2}$ M. This was particular true for the 500 rpm Protherm reaction and mechanically stirred flask reactions, both with molecular sieves added. The difference between the experimental results and the predictions for the estimated experimental bulk methanol concentration ($1x10^{-4}$ M) suggested that the homogeneous kinetic model over-predicted the concentration of methanol present in the reaction mixture by 2 orders-of magnitude or more. This

discrepant prediction could be caused by insufficiencies in the homogeneous description of the reaction mixture as well as uncertainties in the various model parameters.

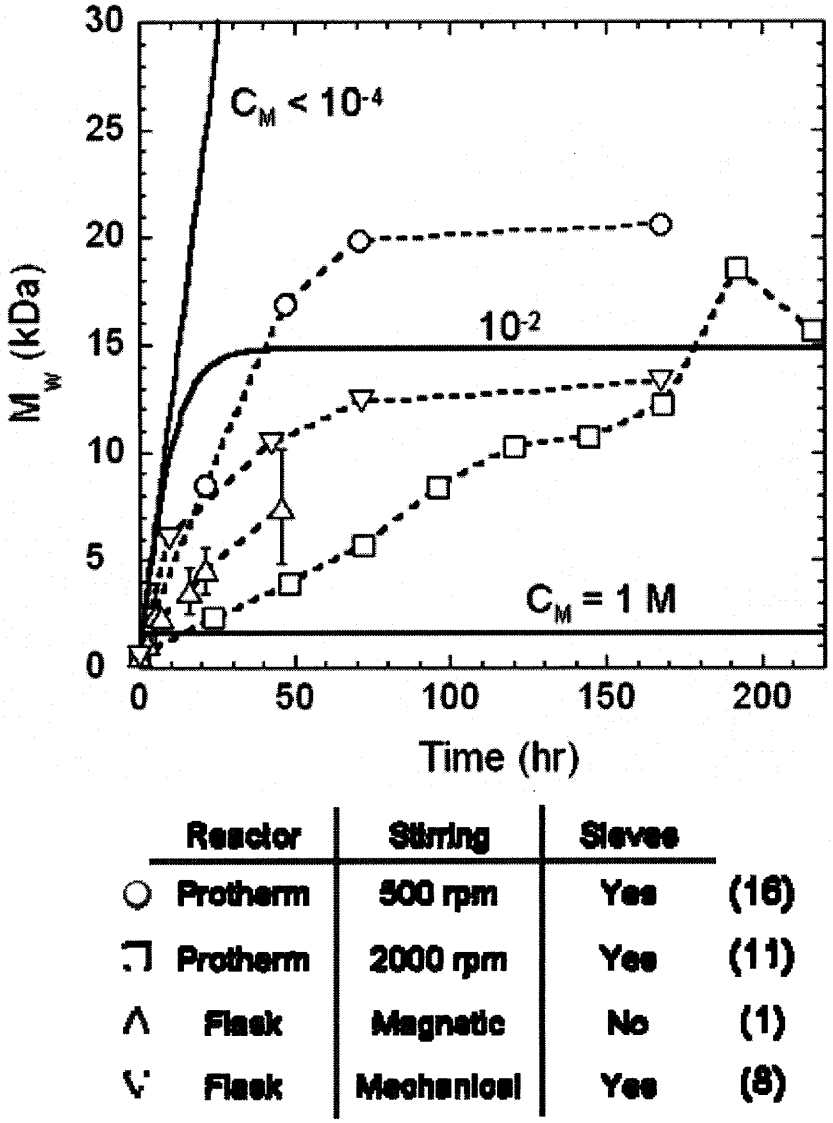

Figure 3.43. Comparison of various experimental polymerizations with kinetic modeling results. The experimental bulk methanol concentration was $1x10^{-4}$M.

Although K_{eq} for similar reactions are typically O(1) [11], the inability to experimentally determine the K_{eq} for the backbone polymerization created additional parameter uncertainty. To address this uncertainty, the homogeneous model predictions at equilibrium were also compared with selected experimental results (FIGURE 3.46). The experimental data did not intersect the model predictions at any of the simulated K_{eq}

(between 0.1 and 10) in either a water-free or dried PEG system (C_w^o = 0 and 1.5 mM, respectively).

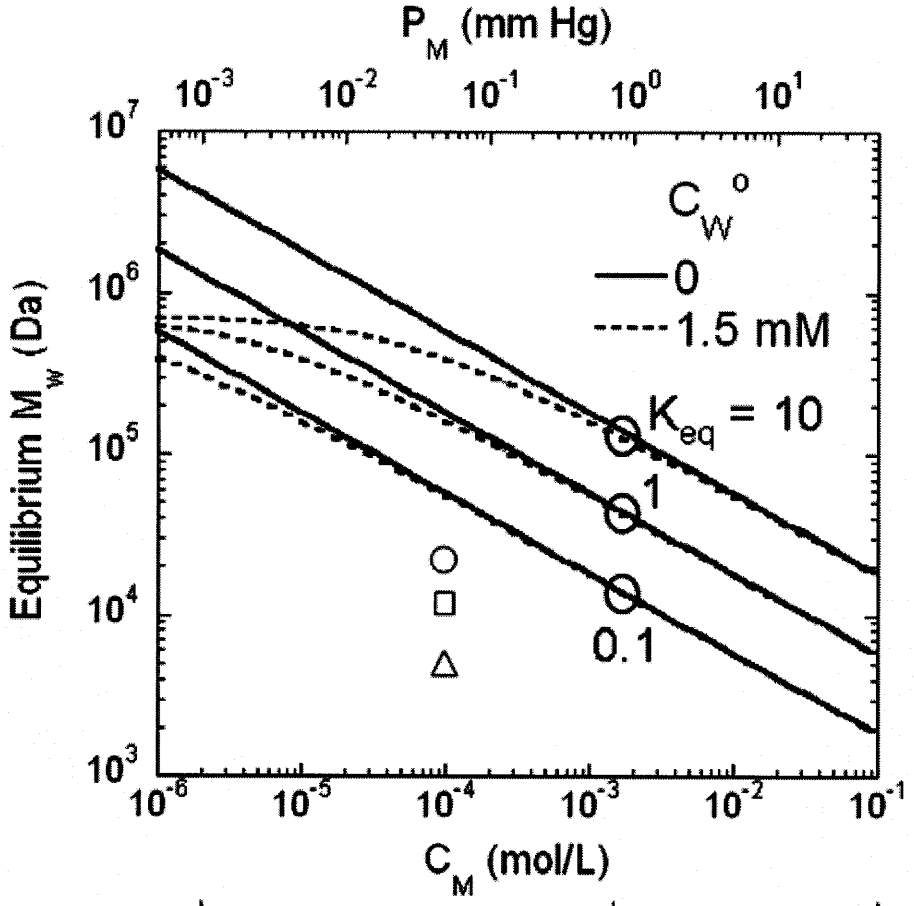

	Reactor	Stirring	Sieves	Rxn
○	Protherm	500 rpm	Yes	16
□	Flask	Mechanical	Yes	8
△	Flask	Magnetic	No	1

Figure 3.44. Comparison of three experimental polymerizations with equilibrium modeling predictions.

To try and identify the source(s) of the differences between the model predictions and experimental results, two possible strategies could be invoked to explain the aforementioned discrepancies: (1) decrease the equilibrium molecular weight predicted by the model (i.e. shift the solid and/or dashed lines down) or (2) increase the methanol

concentration corresponding to the experimental data (i.e. shift the open symbols to the right).

The mass transfer modeling was completed, in part, to estimate the actual concentration of methanol participating in the reverse polymerization reaction. The proposed diffusion limitations would increase the concentration of methanol beyond that designated in the bulk by the vapor-liquid equilibrium. Although the results of the mass transfer modeling did predict some increase in methanol concentration due to these mass transfer limitations (FIGURE 3.30), the predicted increase was uniformly less than a factor of two. This predicted factor of two (or less) would not be sufficient to shift the experimental data enough to align with the experimental results.

Inaccuracies in model parameters could also account for the observed differences. In particular, if the initial water concentration in the system was much higher than that measured by Karl-Fischer titration, then the resulting stoichiometric imbalance could significantly reduce the predicted equilibrium molecular weight. Because there is no experimental data for the equilibrium constant, it is also possible that the lowest equilibrium constant simulated was not low enough. Both of these inaccuracies could shift the model predictions downward and therefore closer to the experimental results.

3.6 Discussion

Overall, the solubility data in the literature, in the form of Hildebrand solubility and Flory-Huggins chi parameters, suggested that the Raoult's Law description was a reasonable estimate of the vapor-liquid equilibrium behavior of methanol in PEG (or the backbone polymer). Although some hydrogen bonding is clearly possible, particularly between the free hydroxyl groups at the terminus of the PEG and the methanol in solution, the other groups within the PEG, both the CH_2 and weak electron pairs of the ether oxygen, would be minimally interactive with molecules the methanol.

Application of the Raoult's Law assumption also required that any effect of the increase in moles in the polymer melt over the course of the reaction were essentially ignored. That is, the Raoult's Law solubility was calculated at the very beginning of the reaction and assumed to be equivalent to the Henry's Law constant, which is applied independently of the number of moles in a particular solvent. If this assumption was invalid, the estimated bulk methanol concentration could be considerably underpredicted. However, Henry's Law should be the most appropriate description of the vapor-liquid equilibrium in the system considering the high pure component vapor pressure of methanol at 90 ^{0}C and the low level of vapor-phase pressure maintained in the reaction system.

The importance of minimizing the bulk methanol concentration was emphasized by the predictions for the homogeneous kinetic model. The model results also provided an upper bound for the molecular weight that could be achieved under ideal experimental conditions at the bulk methanol estimated according to the Raoult's Law solubility. This upper bound of approximately 150 kDa was fifty times higher than any weight-average

molecular weights achieved experimentally before initiation of the research described herein.

The effect of residual water after drying was also investigated with the kinetic homogeneous model. Using the amount of residual water measured by Karl-Fischer titration experiments, as well as initial water concentrations up to 10 times higher, molecular weight predictions were affected minimally at high C_M and moderately at low C_M. There is opportunity to adjust the system of reactions to include a stronger effect of water on the stoichiometric ratio, r, and, therefore, a stronger influence in reducing the predicted molecular weight. In the current model, the forward and reverse rate constants for the hydrolysis reaction were set equal to those for the chain-extension reaction. One could propose a system of reactions where the reverse rate constant for the hydrolysis reaction was set equal to zero.

Interestingly, some researchers have observed deleterious effects on the catalytic ability of immobilized lipases due to reduced water content in reaction mixtures [3]. These researchers proposed that some level of water was required to hydrate the enzyme to promote binding and catalysis of the esterification reaction.

The model non-dimensionalization and resulting analytical solutions provided insight into the mass transfer dynamics within the polymer melt in multiple geometries. Damköhler numbers, which relate the rate of reaction to the rate of diffusion, were the result of the non-dimensionalization for all models studied. In addition to determining the length of the mass transfer boundary layer, the system geometry was responsible for two contributions to the model through (1) the calculation of the effective rate forward constant according to the distribution and availability of enzyme sites in the polymer melt

and (2) the coordinates applied when solving Fick's Law. For the single-bead model, spherical coordinates led to a 2 instead of a 1 (for rectangular coordinates) as part of the sum in both the numerator and denominator of the solution (see Equation 48A).

The analytical solution for the reactive endgroup species led to imaginary results for some of the backbone polymer molecular weights evaluated. These imaginary results (negative determinants) indicate a physically unrealizable state in the reaction mixture for molecular weights between 20 and 90 kDa. This is due to a combination of two effects: (1) the second order consumption of the reactive endgroups and (2) diffusion limitations that reduce mass transport of the reactive endgroups to the catalyst surface. Although the model continues to predict a reactive endgroup concentration ratio (θ_A) beyond 90 kDa, this point cannot be reached in a real experimental system due to the imaginary solutions beginning at approximately 20 kDa. The analytical solution for the reactive endgroups for the well-stirred bead also required application of the quadratic equation; however, the determinant for this case was never less than zero and, therefore, no imaginary solutions were encountered. The determinant was only very narrowly positive and it is possible that an imaginary solution was within the uncertainty of the model parameters.

The inability of the mass transfer modeling to account for the difference between the homogeneous model predictions and the experimentally observed results was surprising, particularly with respect to methanol mass transfer limitations, considering the breadth of experience in both the literature and industry with byproduct removal-limited polycondensation reactions. The primary difference between the system studied in this work and those studied in the literature, most notably the polyamidation reaction for the production of nylon 6,6, was the enzyme catalysis. It is well known that enzymatically

catalyzed reactions oftentimes do not follow elementary kinetics such as the second order kinetic rate equation assumed for the mass transfer analysis. Models, such as Michaelis-Menten, have much more complicated dependences on the reactant concentration. Although an analytical solution would likely not exist for the mass transfer cases studied, a more complex rate equation may have yielded different results.

A second difference between the backbone polymerization system and nylon 6,6 was the relatively large size of the monomer units, particularly PEG900. The primary effect of this difference is that backbone polymer viscosity increases much more significantly with polymerization number than does that for nylon 6,6. This means that, holding all else equal, for a given molecular weight and associated viscosity and diffusion coefficient, the concentrations for the reactive endgroups will be lower for a polymer having higher molecular weight monomer subunits. According to the analytical solutions (Equations 48A and B), this could contribute to a corresponding decrease in the result for $\theta_M(0)$, which suggests that some correction or adjustment to the model development may be necessary to account for the large molecular weight of the PEG and linker monomers.

A wide range of variables were studied during the polymerization experiments. Decreasing the vapor-phase pressure by nearly four orders-of-magnitude (from 360 to 0.05 mm Hg) only led to a modest, fivefold increase in polymer molecular weight. This was in contrast to the homogeneous model, which would have predicted an approximately two order-of-magnitude increase in molecular weight with such a drastic change in vapor-phase pressure (and the corresponding decrease in bulk methanol concentration). This first result was an early indication that significant non-idealities, in particular, deviations from homogeneity, were present in the reaction system. The results

for the stirring experiment (FIGURE 3.34) demonstrated that some fluid motion was necessary to promote the reaction, which was likely related to the need for a multi-body collision or sequence of collisions required to generate a chain extending ester bond. The stirring would be necessary not only to homogenize the bulk but to increase the collision frequency of reactants, as well.

The addition of molecular sieves was the key improvement to the experimental conditions during the studies in flasks. The 4Å molecular sieves were able to act as scavengers for either water or methanol (or both). The addition of sieves improved the absolute molecular weights achieved in the flasks and the reliability of the flask reactions. In the experiments where either minimal or no PEG drying was performed, M_w greater than those previously measured without sieves were still realized even though significant water was present in the system upon initiation of the polymerization. The fact that the molecular weight progressions were delayed in these incompletely dried experiments was tangible evidence of water inhibiting the polymer chain extension most likely via its side reaction with linker. The fact that the high molecular weight was still achieved suggested that any hydrolysis reaction that had occurred was reversible to a certain extent.

The significant improvements in backbone polymer molecular weight achieved by addition of sieves were surpassed by adapting the Protherm thin-film evaporator for use as a batch thin-film reactor. With the exception of the reaction with double catalyst loading, the initial reaction rate in the Protherm at 2000 rpm was slower than that observed in the flasks. Flow visualizations were performed to try and develop an explanation for this observed trend. For PEG1000 at 2000 rpm, a thin film was completely developed, but fillet formation was incomplete. Conversely, a rapid increase

in molecular weight was observed for the same reaction conditions with a blade speed of 500 rpm. Flow visualizations of PEG1000 at 500 rpm showed significant pooling and minimal fillet formation. It is unclear, *a priori*, whether the observed fluid dynamics were causative or correlative.

Fluid dynamic modeling in the literature provides relevant information [17]. In his work, Komori models the fluid dynamics in a falling thin-film evaporator. Although the model results predict significant rotational fluid velocity within a fillet, very little mixing is predicted either within the fillet or between the fillet and thin film. This would be even more pronounced for fluids having viscosities greater than water. Because the reaction mixture is more readily distributed into fillets and a thin film at the higher blade speed and because minimal mixing occurs within fillets, limited mixing may cause the decreased initial reaction rate at 2000 rpm. At 500 rpm, the centripetal forces are unable to overcome gravity and the reaction mixture remains predominantly in a pool at the bottom of the cylinder. In this situation, one could liken the mixing of the polymer melt by the rotating Protherm blades to the motion in a conventional front-loading washing machine. The minimal mixing predicted in the fillet does raise some concern for the later stages of reaction, even for the 500 rpm case, where the fillets and thin films are well-developed. However, given the correspondingly higher viscosities at the later stages in the reaction[5], it is unlikely that significant mixing, in either the laminar or turbulent sense, could be achieved by any means, mechanical or otherwise.

For the 500 rpm Protherm reaction, further increases in molecular weight were not realized because the polymer was transferred to the unheated blades from the reaction

[5] Viscometry measurements were performed for three PEG MWs at various added solvent wt%, with and without catalyst beads present. This study, which was performed by Nathalie Pinkerton as part of the UROP program, is presented in detail in APPENDIX D.

zone. This could be potentially avoided by heating the blades, which was not possible in the prototype model used in these studies. It is possible that even higher M_w could be achieved if such an improvement was implemented in the Protherm. Beyond the heated blades, additional experiments at other blade speeds to determine a potential optimum are recommended, as well. Further study of the polymerization in a scaled-up thin-film reactor (larger bore cylinders are commonly manufactured by our industrial collaborator, Artisan Industries) would also be interesting to investigate the scalability of the process.

The results from modeling and experiment were compared to assess the validity of the various model assumptions and the accuracy of the model inputs. The methanol mass transfer modeling, which only predicted a very minimal increase in the surface methanol concentration due to mass transfer limitations, was unable to account for the observed differences. The mass transfer modeling for the reactive endgroups did suggest a possible explanation for the lower molecular weights achieved; however, the fact that molecular weight increases were observed when molecular sieves were added strongly suggested that the presence of either water or methanol played some role in inhibiting molecular weight progression.

3.7 Conclusion

The enzymatic polymerization of PEG and dimethyl 5-hydroxyisophthalate (linker) to produce backbone polymer was investigated using both predictive modeling and experiment. The production of high molecular weight backbone polymer was desirable both as a reaction engineering problem as well as for the intended application for the resulting backbone polymer. As described in Chapter 5, the production of high weight polymer increased the design space over which the final synthetic product, the targeted nanoparticle micelles, could be investigated.

Key experimental variables were tested, including vapor-phase pressure, stirring, and PEG water content. Once suitable vacuum was applied, addition of molecular sieves, which could participate by scavenging either residual water or methanol byproduct, was the greatest factor in increasing M_w (12 kDa at 70 hr) in reactions performed in flasks. The Protherm, which was modified to operate as a batch thin-film reactor, was employed in order to improve methanol mass transfer and mixing within the polymer melt. Three separate reactions in the Protherm produced the highest M_w backbone polymer (approximately 20 kDa). A blade speed of 500 rpm with molecular sieves present was able to achieve this M_w in 48 hr.

3.8 References

1. Roberts, S.M., *Preparative biotransformations.* J Chem Soc, Perkin Trans 1, 2001: p. 1475-1499.
2. Kobayashi, S., Uyama, H., Kimura, S., *Enzymatic Polymerization.* Chem Rev, 2001. **101**: p. 3793-3818.
3. Arroyo, M., Sanchez-Montero, J. M., Sinisterra, J. V., *Thermal stabilization of immobilized lipase B from Candida antarctica on different supports: Effect of water activity on enzymatic activity in organic media.* Enzyme and Microbial Technology, 1999. **24**: p. 3-12.
4. Kumar, R., Chen, M-H., Parmar, V. S., Samuelson, L. A., Kumar, J., Nicolosi, R., Yoganathan, S., Watterson, A. C., *Supramolecular assemblies based on copolymers of PEG600 and functionalized aromatic diesters for drug delivery applications.* JACS, 2004. **126**: p. 10640-10644.
5. Chaudhary, A.K., Lopez, J., Beckman, E. J., Russell, A. J., *Biocatalytic solvent-free polymerization to produce high molecular weight polyesters.* Biotechnol Prog, 1997. **13**: p. 318-325.
6. Binns, F., Harffey, P., Roberts, S. M., Taylor, A., *Studies of lipase-catalyzed polyesterification of an unactivated diacid/diol system.* J Polymer Science: Part A: Polymer Chemistry, 1998. **36**: p. 2069-2080.
7. Okumura, S., Iwai, M., Tominaga, Y., Agric Biol Chem, 1994. **48**: p. 2805.
8. Kumar, R., Shakil, N. A., Chen, M-H., Parmar, V. S., Samuelson, L. A., Kumar, J., Watterson, A. C., *Chemo-enzymatic synthesis and characterization of novel functionalized amphiphilic polymers.* J Macromolecular Science, 2002. **A39**(10): p. 1137-1149.
9. Sharma, S.K., Sharma, A. K., Kumar, R., Parmar, V. S., Samuelson, L. A., Kumar, J., Watterson, A. C., *Synthesis of amino functionalized amphiphilic copolymers as potential gene delivery carriers.* Polymer Preprints, 2003. **44**(2): p. 791-792.
10. Kumar, R., Tyagi, R., Parmar, V. S., Samuelson, L. A., Watterson, A. C., Kumar, J., *Candida antarctica Lipase B catalyzed copolymerizations of non-proteinogenic amino acids and poly(ethylene glycol) to generate novel functionalized polyesters.* J Macromolecular Science, 2003. **A40**(12): p. 1283-1293.
11. Odian, G., *Principles of Polymerization, 4th edition.* 4th ed. 2004, Hoboken, NJ: John Wiley & Sons, Inc.
12. Steppan, D.D., Doherty, M. F., Malone, M. F., *A kinetic and equilibrium model for nylon 6,6 polymerization.* J Appl Polymer Sci, 1987. **33**: p. 2333-2344.
13. Steppan, D.D., Doherty, M. F., Malone, M. F., *A simplified degradation model for nylon 6,6 polymerization.* J Appl Polymer Sci, 1991. **42**: p. 1009-1021.
14. Steppan, D.D., Doherty, M. F., Malone, M. F., *Wiped film reactor model for nylon 6,6 polymerization.* Ind Eng Chem Res, 1990. **29**: p. 2012-2020.
15. Nisoli, A., Dohery, M. F., Malone, M. F., *Feasible regions for step-growth melt polycondensation systems.* Ind Eng Chem Res, 2004. **43**: p. 428-440.
16. Choi, B.R., Lee, H. H., *Transient and steady-state behavior of wiped-film reactors for reversible condensation polymerization.* Ind Eng Chem Res, 1996. **35**: p. 1550-1555.

17. Komori, S., Takata, K., Murakami, Y., *Flow structure and mixing mechanism in an agitated thin-film evaporator.* J Chem Eng Japan, 1987. **21**(6): p. 639-644.
18. Watanabe, T., Toyama, M., Nakamura, K., *Fundamental investigation of the flow in an agitated thin film evaporator.* Bulletin of the JSME, 1976. **19**(135): p. 1047-1053.
19. Pearson, J.R.A., *The instability of uniform viscous flow under rollers and spreaders.* J Fluid Mech, 1960. **7**: p. 481-500.
20. Bhaskar, V., Gupta, S. K., Ray, A. K., *Multiobjective optimization of an industrial wped film poly(ethylene terephthalate) reactor: some further insights.* Computers and Chem Eng, 2001. **25**: p. 391-407.
21. Kumar, R., Tyagi, R., Parmar, V. S., Watterson, A. C., Kumar, J., Zhou, J., Hardiman, M., Fisher, R., Colton, C. K., *Perfluorinated amphiphilic polymers as nano probes for imaging and delivery of therapeutics for cancer.* Polymer Preprints, 2005.
22. Maeda, H., Wu, J., Sawa, T., Matsumura, Y., Hori, K., *Tumor vascular permeability and the EPR effect in macromolecular therapeutics: A review.* J Controlled Release, 2000. **65**: p. 271-284.
23. Pirollo, K.F., Chang, E. H., *Does a targeting ligand influence nanoparticle tumor localization or uptake?* Trends in Biotechnology, 2008. **26**(10): p. 552-558.
24. Hong, S., Leroueil, P. R., Majoros, I. J., Orr, B. G., Baker, Jr., J. R., Holl, M. M. B., *The binding avidity of a nanoparticle-based multivalent targeted drug delivery platform.* Chemistry & Biology, 2007. **14**: p. 107-115.
25. Rai, P., Padala, C., Poon, V., Saraph, A., Basha, S., Kate, S., Tao, K., Mogridge, J., Kane, R. S., *Statistical pattern matching facilitates the design of polyvalent inhibitors of anthrax and cholera toxins.* Nature Biotechnology, 2006. **24**(5): p. 582-586.
26. Gargano, J.M., Ngo, T., Kim, J. Y., Acheson, D. W. K., Lees, W. J., *Multivalent inhibition of AB5 toxins.* JACS, 2001. **123**: p. 12909-12910.
27. Miller, M.T., *In vitro evaluation of cytotoxicity and cellular uptake of alternating copolymers for use as drug delivery vehicles*, in *Chemical Engineering.* 2009, MIT: Cambridge.
28. Mei, Y., Miller, L., Gao, W., Gross, R. A., *Imaging the distribution and secondary structure of immobilized enzymes using infrared microspectroscopy.* Biomacromolecules, 2003. **4**: p. 70-74.
29. Cedergren, A., Luan, L. W., *Potentiometric determination of water using spent imidazole-buffered Karl Fischer reagents.* Analytical Chem, 1998. **70**(10): p. 2174-2180.
30. Steppan, D.D., Doherty, M. F., Malone, M. F., *A kinetic and equilibrium model for nylon 6,6 polymerization.* J Applied Polymer Sci, 1987. **33**: p. 2333-2344.
31. O'Neil, M.J., Smith, A., Heckelman, P. E., Budavari, S., *Merck Index.* 2007, Whitehouse Station, NJ: Merck.
32. Dee, G.T., Ougizawa, T., Walsh, D. J., *The pressure volume temperature properties of polyethylene, poly(dimethyl siloxane), poly(ethylene glycol) and poly(propylene glycol) as a function of molecular-weight.* Polymer, 1992. **33**(16): p. 3462-3469.

33. Flick, E.W., *Industrial Solvents Handbook (5th Edition)*. 1998: William Andrew Publishing/Noyes.
34. Hong, B., Escobedo, F., Panagiotopoulos, *Diffusivities and viscosities of poly(ethylene oxide) oligomers.* J Chem Eng Data, 2010. **55**: p. 4273-4280.
35. Bhaskar, V., Gupta, S. K., Ray, A. K., *Multiobjective optimization of an industrial wiped film poly(ethylene terephthalate) reactor: Some further insights.* Computers and Chem Eng, 2001. **25**: p. 391-407.
36. Barton, A.F.M., *CRC Handbook of solubility parameters and other cohesion parameters, 2nd Edition.* 1991, Boca Raton, FL: CRC Press LLC.
37. Barton, A.F.M., *CRC Handbook of Polymer-Liquid Interaction Parameters and Solubility Parameters*. 1983: CRC Press.
38. Milczewska, K., Voelkel, A., *The use of Flory-Huggins parameters in characterization of polymer-filler compositions.* Material Science Forum, 2008. **587-588**: p. 667-671.
39. Elorza, J.M., Fernandez-Berridi, M. J., Iruin, J. J., Guzman, G. M., *The interaction parameters of a PEO/PVA blend by inverse gas chromatography.* Proc 28th IUPAC Macromol Symp, 1982: p. 683.
40. Juan, J.C., Daud, J. M., Yarmo, M. A., *A new reversed phase HPLC method for separation of PEG600 on C8 column coupled with evaporative light scattering detector.* Malaysian J Chem, 2007. **9**(1): p. 060-066.
41. Kawakami, M., Egashira, M., Kagawa, S., *Measurements of the interactions between polyethylene glycol and organic compounds by gas chromatographic technique.* Bulletin of the Chemical Society of Japan, 1976. **49**(12): p. 3449-3453.
42. Mori, S., *Calibration of size exclusion chromatography columns for molecular weight determination of poly(acrylonitrile) and poly(vinylpyrrolidone) in N,N-dimethylformamide.* Anal Chem, 1983. **55**: p. 2414-2416.
43. Mori, S., *Conversion factors for polystyrene molecular weight into molecular weights of polymethacrylates in size exclusion chromatography.* J Liquid Chromatography, 1990. **13**(9): p. 1719-1729.

Radioiodination Method Development for Quantitative Analysis *in vitro* and *in vivo*

4.1 Introduction

In order to assess the performance of a nanoparticle delivery system in biological applications, a label that is detectable under a wide range of conditions and concentrations must be present within the molecule. Spectrophotometric measurements of aromatic groups within a structure, such as tyrosine residues within a peptide, are a straightforward example. In fact, one of the primary benefits of magnetic nanoparticles, such as cross-linked iron oxide [1], or quantum dot based nanoparticles [2] is their inherent measurability. However, for organic delivery system, such as polymeric micelles, dendrimers, and liposomes, straightforward measurement techniques prove insufficient as the introduction of cellular or even tissue components from biological systems significantly increase the complexity of experimental conditions; consequently, some exogenous label must be introduced to facilitate detection of the delivery system.

An ideal label will have the following properties: (1) high sensitivity to allow for *quantitative* measurement across a broad concentration range, (2) negligible effect on particle properties due to minimal interactivity and/or size, (3) straightforward chemical reaction for simple introduction into the chemical structure, and (4) broad applicability in a variety of analytical techniques.

Various fluorescent and radioactive labels have been developed that meet some, but not all, of the above requirements. In particular, fluorescent dyes can be conjugated to structures with well-established synthetic techniques. Unfortunately, commonly employed dyes like those of the Cy or Alexa fluor® families, though unquestionably effective for a variety of microscopy studies [3], are large, hydrophobic structures. As a

result, fluorescent dyes fail to meet the second criterion of minimal size and interactivity with the particulate delivery vehicle. For the case of the polymeric micelles studied in our research, the addition of highly hydrophobic moieties can disrupt the micellization putting any subsequent analysis into question. A second major drawback of fluorescent techniques is the short penetration depth of light within the body (typically ≤ 50 mm), which limits the use of fluorescent dyes in imaging of near-surface phenomena [4].

Radioactive isotopes are particularly attractive because they can be quantifiably detected across a broad range of concentrations, are small, and broadly applicable. There are some potential drawbacks, which include the occupational and waste disposal hazards inherent to work with radioactivity, limited commercial availability and corresponding high costs of certain isotopes, and comparatively difficult synthetic steps for conjugation.

Researchers, including those studying circulating delivery systems [5, 6], have frequently used the β-emitting isotope tritium [^{3}H]. Due to the weakness of the β decay, sample activity is determined indirectly by measurement of ionizing radiation-induced phosphorescence using a liquid scintillation cocktail. Accurate quantification requires careful calibration as well as additional preparation steps to remove any photoactivity that might obscure spectrophotometric measurements by the scintillation counter. The fact that β emissions cannot penetrate the skin eliminates tritium as an option in live animal imaging applications.

In response to the demands of the field, many researchers have conjugated high energy-emitting isotopes, such as γ and positron emitters, to their structures. Examples used in the field include ^{64}Cu [7], ^{67}Ga [8], ^{99m}Tc [9], ^{111}In [10], ^{125}I [11], and ^{131}I [12]. Radiolabels and relevant experimental procedures for use in nanoparticle research have

been reviewed [13]. Due to their high penetration length and ease of detection via gamma counting, these strong-emitting isotopes all satisfy the first criterion for an effective label – straightforward quantification across a broad range of concentration – and, in terms of research application, are excellent labels for *in vitro* and *ex vivo* biodistribution studies [14]. Moreover, when compared to the large, hydrophobic structures of fluorescent dyes, strong-emitting radioisotopes are small and should, in general, have minimal effect on physical properties upon conjugation. This is also the case, but most likely less so, for metallic isotopes, such as ^{64}Cu, which are conjugated via small macrocyclic chelators like DOTA.

In imaging, gamma emitting isotopes found early use in nuclear imaging applications using planar gamma cameras. This technology has been surpassed by subsequent nuclear imaging techniques, including single photon emission computed tomography (SPECT) and positron emission tomography (PET), which provide increased resolution and richer spatial information [4, 14].

There are many isotopes from which to choose to meet the four requirements for an ideal label, and both the particular delivery system and intended application will influence this choice. However, with respect to the fourth criterion, the various isotopes of iodine provide many potential applications for an iodine-conjugated particle. Specifically, ^{124}I is a positron emitter for use in PET [15], ^{123}I and ^{131}I can both be used in SPECT [4], and ^{125}I, as previously described, can be used in research applications and gamma imaging. Beyond the previously described imaging applications, an isotope of iodine, ^{131}I, has been used clinically for radioimmunotherapy of various cancers since 1943 [16].

Although stability must be considered for all radiolabeled compounds and is of particular concern for metal chelators such as those used for ^{64}Cu [17], the relative lability of the carbon-iodine bond, particularly when exposed to a class of enzymes in the body known broadly as 'deiodinases,' must be considered when using radioiodine for *in vivo* applications. Previous research suggests that deiodination occurs to a much greater extent for iodine bound directly to proteins than for iodine bound to non-proteinaceous compounds [18, 19]. Therefore, stability can be improved by incorporating non-protein based carbon-iodine bonds into a delivery system.

There are a number of methods by which iodine is chemically conjugated to organic molecules [20], including isotopic exchange, electrophilic substitution, nucleophilic substitution, or replacement of an activated group, such as a trialkyl stannane [21]. Electrophilic substitution of a hydrogen atom on an activated aromatic ring is the most common method. This is accomplished by adding an oxidizing agent, such as chloramine-T (FIGURE 4.1A) [20] to a solution of sodium iodide to generate oxidative reactive iodine species. After addition of the material to be labeled, the reactive species replaces a hydrogen atom in the position ortho (immediately adjacent) to an electron-withdrawing group to produce the radiolabeled product (see structures in FIGURE 4.2, [20]). The presence of this electron-withdrawing group at the ortho position creates a partial positive charge that makes the carbon-hydrogen bond more susceptible to oxidative substitution by the activated iodine species. Increasingly strong electron-withdrawing neighbors impart greater reactivity. The electron-withdrawing group typically does not affect carbon-hydrogen bonds at the meta or para positions, which are further removed than ortho.

Products, such as Pierce Chemical's Pierce Iodination beads (formerly IODObeads) and Iodogen (FIGURE 4.1B and 1C, respectively), have been developed to reduce sample damage caused by excessively oxidative conditions as well as to facilitate the separation of oxidizing material from the labeled sample [22]. Pierce Iodination beads are chloramine-T immobilized on a neutral bead, whereas Iodogen, which has very minimal solubility in water, is used by coating glass reaction tubes with the chemical.

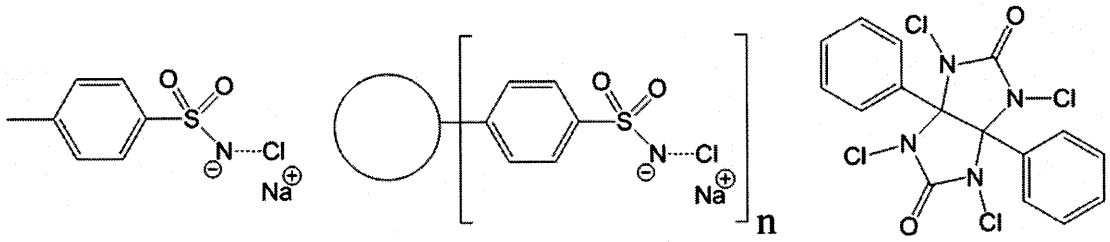

Figure 4.1. Chemical structure representations of chloramine-T (A), Pierce iodination beads (B), and the Iodogen reagent (C).

The previously described techniques, though well-characterized and in common use for decades, require the presence of an activated aromatic group, that is, an aromatic substituted with some strongly electron-withdrawing group. Iodination of proteins and antibodies has been the most common application of the technique due to the phenol group within tyrosine moieties (FIGURE 4.2C). In fact, Iodogen has been used to label proteins in a microfluidic device [23].

However, activated aromatic groups are not nearly as common in the circulating delivery field as in protein biology. The straightforward conjugation of radioiodine using materials like Pierce Iodination Beads has inspired researchers to modify their chemical structures to introduce tyrosine-like groups. In particular, tyramine [24] (FIGURE 4.2D), tyrosinamide [25, 26], or other tyrosine-like groups [27] have been incorporated into block copolymer structures in small quantities to allow for iodination. The Bolton and

Hunter reagent (FIGURE 4.2E), which can be used to attach a tyrosine-like residue to primary amines, has also been used to modify structures of a delivery system for easy iodination [28].

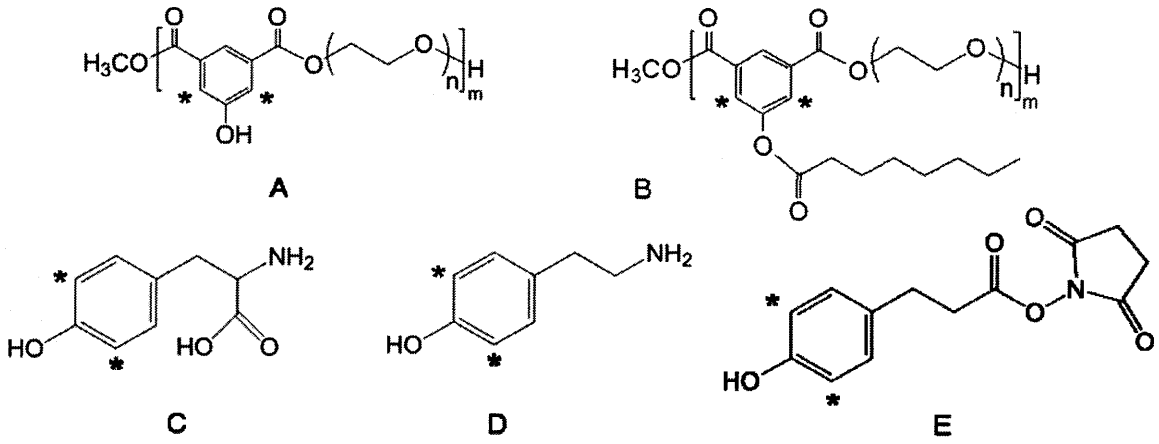

Figure 4.2. Chemical structures of various molecules designed for iodination by the reagents in FIGURE 1, including (A) our alternating copolymer backbone polymer, (B) the backbone polymer substituted with 100% hydrocarbon sidechains via an ester linkage (polymer 027), (C) tyrosine, (D) tyramine, and (E) the Bolton and Hunter reagent. Asterisks indicate sites for iodination, which are at the position ortho to aromatic electron-withdrawing groups.

Although these techniques are straightforward, the modifications introduce additional synthetic steps and potentially obfuscate results by altering the system of interest. Though instances of circulating delivery systems iodinated without modification are few, two specific examples were identified: directly-labeled iron oxide magnetic particles [12] and single-wall carbon nanotubes [29]. While these two examples are interesting, they are separate from the polymeric micelle family of delivery systems. The unique structure of our alternating copolymer [30-32] (FIGURE 4.2A), the hydroxyisophthalate linker in particular, provides an intrinsic iodination target within the structural design. Substituting the polymer backbone with hydrophobic groups to produce an amphiphilic molecule transforms the aromatic hydroxyls into ethers or esters (FIGURE 4.2B). The carbon hydrogen bonds in positions ortho to aromatic ethers and esters, which are comparatively weaker electron-withdrawing groups, will likely have a

lower reactivity relative to that for aromatic hydroxyls. However, in contrast to proteins, which may only have a few surface-exposed tyrosine residues available for labeling, every repeat unit in our polymer contains two potential iodination sites.

Polymer 027 (FIGURE 4.2B), which is the backbone polymer fully substituted with hydrocarbon sidechains via an ester linkage, was the primary polymer formulation studied, (1) because it was synthesized in sufficient quantity to supply the breadth of the desired studies; and, (2) like many of the polymers investigated in this work, polymer 027 contains a tyrosine-like group with an activated aromatic group that is sufficiently chemically different from tyrosine such that successful labeling was not assured. In fact, the ester sidechain linkage was the weakest electron-withdrawing group present in any of the linkages studied (The electron-withdrawing capacity of the linkage groups studied were: hydroxyl < ether < ester).

Though much research has carefully characterized iodination of small aromatic compounds with a variety of techniques [33-35], we are aware of no investigation into the direct iodination of macromolecules similar to our copolymer system. In this work, we demonstrate successful attachment of radioiodine to our copolymer system by adapting a standard method used to label tyrosine residues in proteins. This method was adapted and directly applied to our novel alternating amphiphilic copolymer without any additional modifications to the chemical structure of the target molecule because of the tyrosine-like groups present within its repeating backbone structure. This adapted procedure produced highly pure, stably radiolabeled polymer with high overall product recovery. Radiolabeling yield was sufficient to supply radiolabeled product for use in a variety of research applications, including quantitative cellular uptake and biodistribution

studies using iodine-125, as well as positron emission tomographic imaging (PET) of both mice and rats with iodine-124.

4.2 Materials and Methods

4.2.1 Materials

All polymers were synthesized by collaborators in the lab of Professor Arthur Watterson at the University of Massachusetts at Lowell (UML) as described in Chapter 2. Unless otherwise indicated, the backbone polymer starting material for all samples in this study had a number average molecular weight (M_n) of 3 kDa with a polydispersity of about 1.75 using measurement and data analysis techniques described in Section 3.2. The molecular weight of the final polymer differed depending on the nature of the attached sidechains. Aqueous solutions of known concentrations were created by weighing and dissolving the solid polymer as received. The EI3.4.3 targeting peptide was produced via bacterial fermentation of Rosetta (DE3) cells (P/N 70954, Novagen, Madison, WI) in a 20 L bioreactor by Professor Carl Lawton at UML as previously described [36, 37]. All other materials and reagents were obtained from commercial sources. Polyethylene glycol (PEG-1000), dimethyl 5-hydroxyisophthalate, sodium metabisulfite ($Na_2S_2O_5$), bovine serum albumin (BSA), tetrahydrofuran (THF) Trizma HCL, Trizma base, sodium iodide, potassium iodide (KI), sodium azide, hydrochloric acid, and sodium hydroxide were purchased from Sigma-Aldrich (St. Louis, MO). Phosphate buffered saline (PBS, 10x) was purchased from VWR International (West Chester, PA) and diluted in deionized water. Pierce Iodination Beads (formerly IODObeads) were purchased from Thermo Fisher Scientific (Rockford, IL). Various Sephadex media, including G10, G15, G25 ('Medium' particle size), and DEAE (diethylaminoethyl) Sephadex, were purchased

from both Sigma-Aldrich and GE Healthcare (Piscataway, NJ). PD-10 desalting columns, which are pre-packed with Sephadex G25, were purchased from GE Healthcare. Disposaflex disposable columns were purchased from Kimble Chase (Vineland, NJ). Finally, carrier-free sodium [^{125}I]iodide (specific activity: 17 Ci (629 GBq)/mg, radioactive concentration: 100 mCi/mL in 10^{-5} M NaOH, concentration: 5.88 μg/mL) was purchased from PerkinElmer (Waltham, MA).

Preparation of Radioiodinated Product

A standard protocol was used for iodine attachment. Experimental conditions were varied from this standard procedure depending on the requirements of the particular experiment. For example, reaction time was varied to determine conditions for optimal yield or concentrations were increased to provide sufficient material for certain assays. All reaction conditions were as described in this standard protocol unless otherwise specified.

4.2.2 Iodine Attachment

One iodination bead was washed with 1 mL of PBS, dried, and transferred to a 2-mL conical-bottom microcentrifuge tube (Sarstedt, Newton, NC) before addition of 100 μL Tris buffer. Sodium [^{125}I]iodide solution (1 mCi total activity, 10 μL/mCi) was added to the tube and allowed to activate for 5 min with occasional mixing by tapping the tube. A 100-μL volume of sample solution (1 mg/mL) was added to the activated [^{125}I]iodide and reaction was allowed to proceed for 5 min with occasional mixing. After reaction, the product solution was removed from the iodination bead with a pipette. For procedures labeling only protein (i.e. samples without polymer), the remaining bead was washed

twice with 60 μL of BSA chase solution (5 mg/mL BSA, 1 mM KI) to promote protein desorption. For procedures with the polymer, BSA was deemed unnecessary due to the low non-specific adsorption of the highly PEGylated polymer, and BSA chase solution was replaced by an identical volume of PBS. Residual oxidizing species were inactivated by addition of 60 μL sodium metabisulfite solution (12 mg/mL in PBS). The bead and inactivation washes were combined with the product solution.

4.2.3 Separation of Labeled Product and Free Iodine

Unreacted, free ^{125}I was separated from the labeled sample using Sephadex separation media with either manually-packed Disposaflex columns (Kimble-Chase, Vineland, NJ) or pre-packed PD-10 columns (with Sephadex G25, GE Healthcare, Piscataway, NJ). The dimensions of the Disposaflex columns and PD-10 columns are summarized in TABLE 4.1. For the manually-prepared columns, Sephadex media, including G10, G15, G25, DEAE-Sephadex (diethyl aminoethyl), were swelled in PBS (with 0.02% w/v sodium azide) for at least 1 day at room temperature.

All operations in both the Disposaflex and PD-10 columns, including packing (where relevant), equilibration, and separation, were performed by gravity flow. Sufficient buffer was maintained in the reservoirs above each media at all times to ensure that air did not contact the resin bed. The approximate flow rate was 0.4 mL/min for all operations. Columns were packed by adding the Sephadex slurry to the Disposaflex columns and allowing the resin to settle. PBS was added as necessary during the settling period to maintain the flow rate and avoid airing out the resin. After the Disposaflex column was filled with approximately 1 column volume (10 mL) of media, the Sephadex was then washed and equilibrated by flowing approximately 3 column volumes (30 mL)

of PBS through the settled resin bed. For purifications of labeled protein, 1-2 mL of BSA chase solution was added in between the second and third column volumes of PBS in order to reduce non-specific protein adsorption on the Sephadex. Columns were washed with an additional 5 mL of PBS, again by gravity flow, and stored overnight at 4 °C.

On the day of the iodination, manually-packed columns were washed by flowing 1 additional column volume of PBS through the resin bed. The product solution (210 μL), which was combined with the bead and inactivation washes (180 μL) to yield a total volume of 380 μL, was gently added directly to the top of the column by a P1000 pipette to avoid disturbing the resin. After the entirety of this solution entered the resin, PBS was gently poured and replenished as necessary into the cone feeding the column inlet to maintain flow and to avoid drying of the packed resin. At least 4-5 mL was maintained in the reservoir at all times. A volume of PBS equal to that collected at the column outlet was added over the course of the separation. The total amount varied depending on the total elution time investigated for a particular experiment.

Fractions were collected in 2 mL microcentrifuge tubes, typically at 1-2 minute intervals, and assayed for radioactivity using a QC2000 'table top' gamma counter (Bioscan, Washington, DC). The total volume in each fraction was typically 150-300 μL. The QC2000, which provided a crude measure of sample activity in less than 10 s, was used to quickly screen the collected fractions in the iodination room to determine the highest-activity fractions. The rapid screening of the fractions was necessary because of the hazards associated with the labeling procedure, specifically, the volatility of free radioiodine. The highest-activity fractions, which corresponded to labeled sample, were pooled as the product (see FIGURE 3). For purifications of labeled proteins, 300 μL BSA

chase solution was added to the column immediately before and after the product solution to minimize non-specific adsorption. As before, BSA chase solution was replaced with PBS for polymer purifications due to the heavy PEGylation of the polymer. For separation using the PD-10 columns, the manufacturer 'gravity protocol' was followed[1]. The only significant difference between the Disposaflex and PD-10 procedures was the total volumes for each step, which depended on the relative column volumes (see TABLE 1).

4.2.4 Characterization of Labeled Materials – Analytical Tools

Activity Measurement

For activity measurements of the gamma-emitting isotope, iodine-125, the final pooled product was measured on a Cobra II Auto Gamma counter (Perkin-Elmer/Packard, Waltham, MA). Five microliter samples were added to radioimmunoassay (RIA) tubes (VWR Scientific, Philadelphia, PA) tubes in triplicate and counting was performed for 5 min such that at least 1000 total events were counted. Total counts were often significantly (>100x) higher. The Cobra II, which was significantly more accurate than the QC2000 gamma counter, was used for all activity measurement unless otherwise specified.

Activity was also determined for polymer samples labeled with tritium, ^{3}H, by scintillation counting. Samples were combined with 3.5 mL of scintillation cocktail (Ultima Gold XR), vortexed, and measured on a Beckman Coulter LS6500 Multipurpose Scintillation Counter (Brea, CA). The measurement period was 5 min for each sample.

[1] Refer to 52-1308-00 BB 'PD-10 Desalting Columns, GE Healthcare

Mass Concentration Determination

Mass concentration of polymer samples was determined by absorbance measurements on a Hitachi Model U-3010 UV/vis spectrophotometer at a wavelength of 250 nm. Calibration curves were constructed for backbone polymer and polymer 027 (FIGURE 4.2A and B) by determining the absorbance of solutions of known concentrations of each polymer.

Mass concentration of free peptide was measured using the BCA (bicinchoninic acid) Protein Assay (Thermo Fisher) using a SpectraMax M2 microplate reader (Molecular Devices, Sunnydale, CA) according to the manufacturer protocol. The total product activity and mass concentration were used to calculate the specific activity of labeled polymer or labeled peptide samples.

Molecular Weight Measurement

Polymer molecular weight was measured using a Waters (Milford, MA) gel permeation chromatography (GPC) system, equipped with both UV/vis and refractive index detectors, with a bank of three Styragel® high resolution columns (HR1, HR3, HR4) and THF as the mobile phase. GPC methods were described in detail in the Polymerization Chapter. For material generated for GPC measurement, stable sodium iodide, $Na^{127}I$, was used as a substitute for radioiodine due to contamination and cost considerations. For GPC analysis, samples, all of which were aqueous, were freeze-dried because the mobile phase for the GPC system was THF. For the freeze drying procedure, samples were frozen (-80 °C) and water was removed using a freeze dryer (VirTis, Gardiner, NY) maintained at an absolute pressure of 10 μm Hg for at least 24 hr. The

samples were then dissolved in THF and the amount of THF added was recorded in each instance, varying from 1-5 mL.

Radio-High Performance Liquid Chromatography

Measurements were also performed using a radio-high performance liquid chromatography (radio-HPLC) system (Agilent, Santa Clara, CA) equipped with a UV/vis spectrophotometer and gamma detector. The column was a BioSep S2000 size exclusion column having the following dimensions: 75x7.5 mm (L x D, Phenomenex, Torrance, CA). The mobile phase was sodium chloride 0.9 wt % (w/v), 10 mM Tris buffer and the flow rate was 1.0 mL/min. At this method flow rate, there was one minute of elution time difference due to the length of tubing between the UV/vis and gamma detectors.

Evaluation of the Standard Reaction Protocol

A number of variations on the standard protocol, in combination with various analytical techniques, were used to evaluate the primary components of the standard protocol – the reaction and the purification. These experiments were designed to demonstrate that (1) radioiodine was covalently attached to the polymer and (2) that the labeled polymer product was effectively separated from unreacted, free iodine. The product was analyzed by a gamma counter, GPC, or radio-HPLC in different combinations depending on the desired goal of each experiment.

4.2.5 Confirmation of Covalent Attachment Using Sephadex

The components added to the standard reaction protocol were varied to determine whether iodine was covalently attached to the target polymer molecule. The elution profile of the product purification by G15 Sephadex was the primary result used to evaluate the different experimental conditions.

The first combination of components studied was (1) according to the complete standard protocol: Iodination bead, iodine-125 and polymer 027 (FIGURE 4.2B). The results for the Sephadex purification of the resulting reaction mixture were analyzed in the context of an ideal size exclusion activity elution profile (FIGURE 4.3). In group selection chromatography, a type of size exclusion chromatography, the media has a relatively uniform pore size. Material with a hydrodynamic diameter larger than the nominal pore size, such as our polymer molecules, travel in the voids between the resin beads eluting at a volume approximately equal to the void volume, while material much smaller than the exclusion limit, including unreacted iodide, completely enters the pores eluting at a volume equal to the total column volume.

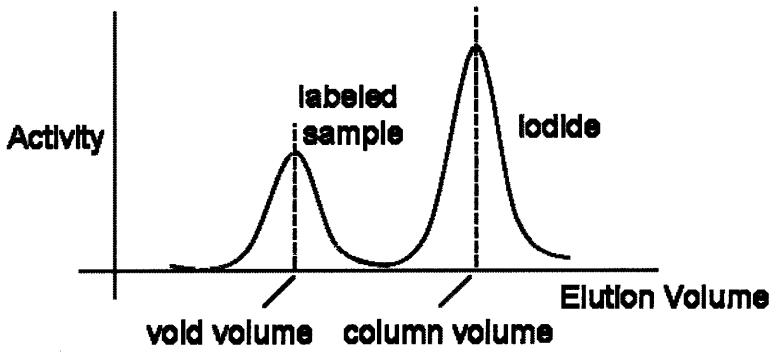

Figure 4.3. Schematic representation of an ideal size exclusion activity profile. The labeled sample, which is excluded from the pores of the size exclusion media, elutes at approximately the void volume.

The void volume and total column volume for both the Disposaflex and PD-10 columns packed with Sephadex size exclusion media are presented in TABLE 1. The

void volume was calculated assuming a void fraction in the packed bed of 0.30 according to specifications for the Sephadex media provided by the manufacturer (GE). Per the manufacturer recommendations for non-rigid gels, this void fraction was assumed for all Sephadex media used in this study. The total column volume was calculated according to the column dimensions. The Sephadex GXX resins are size exclusion media with molecular size exclusion limits designated as 1000 Da for Sephadex G10, 1500 Da for Sephadex G15, and so on. DEAE-Sephadex is an anion exchange media that can remove anionic species, such as iodide, from a sample by electrostatic interactions.

Table 4.1. Void and total column volumes for the Disposaflex and PD-10 columns packed with Sephadex size exclusion resins.

Column	Inner Diameter (cm)	Length (cm)	Void Volume (mL)	Total Volume (mL)
Disposaflex	0.8	20	3.0	10.1
PD-10	1.45	5.0	2.5	8.3

If the elution profile for the reaction with all three components resembled the ideal elution profile (FIGURE 4.3), it would indicate that the iodine was successfully attached during the reaction. However, it is also possible that the elution peak observed at the void volume would be due to either iodine associated with the polymer through non-covalent interactions such as adsorption or encapsulation or to free, unbound iodine. To address these possibilities, two additional combinations of components were studied: (2) iodine-125 and polymer 027 and (3) iodine-125 only. If no activity was observed in the void volume for the corresponding purifications, then that would indicate that a void volume elution peak observed for the standard protocol mixture of components would be due to covalently bound iodine-125.

4.2.6 Confirmation of Covalent Attachment Using Radio-High Performance Liquid Chromatography (HPLC)

Radio-HPLC was used as a second method to confirm covalent attachment of radioiodine to the polymer. All of these experiments were performed either by or under the supervision of Dr. Mikhail Papisov, Professor of Radiology, at the Harvard Medical School/Massachusetts General Hospital (HMS/MGH). The backbone polymer was investigated in this study.

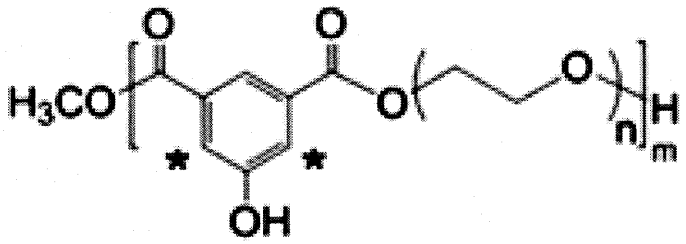

Figure 3.4. Structure of the polymer investigated by radio-HPLC. Backbone polymer was labeled and purified according to the standard protocol using iodine-124 and a PD-10 column.

The polymer was labeled and purified according to the standard protocol with the two following exceptions: (1) iodine-124 was used instead of iodine-125 and (2) purification was performed using a Phenomenex BioSep S-2000-equipped radio-HPLC system instead of Sephadex G25 or PD-10 columns. Fractions were pooled according to the results of the radio-HPLC, which simultaneously analyzed and purified the unpurified reaction product. In total, samples at three stages in the procedure were analyzed by radio-HPLC: (1) initial backbone polymer solution, (2) labeled, unpurified sample, and (3) purified product.

4.2.7 Effect of the Iodination on Chemical Structure

Studies were performed to determine if the labeling procedure adversely affected the chemical structure of the original polymer sample. Oxidative conditions are required to generate the reactive iodine species necessary to iodinate the target. Ethers and esters,

which are oxygen-containing functional groups present throughout the backbone polymer (FIGURE 4.2A), are susceptible to oxidative breakdown under particularly harsh conditions. Ethers and esters may also be present as linker groups between the backbone polymer and attached sidechains as was the case for polymer 027 (FIGURE 4.2B). The backbone polymer was chosen for this study to investigate the potential effect of oxidative conditions on the polymer since any decrease in molecular weight, as determined by GPC, would have to be due to degradation of the ether or ester bonds (or both) within the polymer chain.

The standard protocol was performed, substituting ^{125}I with stable ^{127}I to avoid equipment contamination with radioactivity. It was assumed that there would be no difference in the iodination behavior between the two isotopes. In order to obtain sufficient signal for GPC measurement, the initial polymer concentration in the reaction was increased to 10 mg/mL. The iodine concentration was increased proportionately to 58.8 μg/mL. (Note: only one iodination bead was used because this condition was still well within the oxidative capacity of a single bead [38]). Elution volumes from 0 to 8 mL (i.e. the entire elution) were collected and freeze-dried before being dissolved in 5 mL tetrahydrofuran (THF) for GPC analysis. The GPC chromatogram for the reaction product was compared to those for raw polymer dissolved in THF.

An additional experiment was designed to measure backbone polymer degradation at elevated oxidative conditions. To accomplish this, the concentration of iodine was increased from 5.88 μg/mL to 5.88 mg/mL, while the standard initial polymer concentration (1 mg/mL) was used. This significantly increased the number of oxidative species in solution relative to the oxidative targets within the polymer. ^{125}I was

substituted with ^{127}I and the entire elution (0 to 8 mL) was collected, freeze-dried, and dissolved in THF.

Evaluation of the Standard Protocol for Purification

4.2.8 GPC Analysis of Void Volume Fraction

The standard protocol for purification was followed (Disposaflex columns packed with Sephadex media) to generate fractions of material. The fraction collected near the void volume was analyzed by GPC to determine (1) if the polymer eluted near the void volume and (2) if the entire range of polymer molecular weights was present in the collected fraction surrounding the void volume. To accomplish this, 100 μL of polymer solution (1 mg/mL in PBS) was added to a Sephadex G15 column and a 2 mL fraction corresponding to elution volumes between 2 and 4 mL was collected. This fraction was selected based on the estimated void volume in the Disposaflex columns packed with Sephadex – 3 mL. The collected fraction was freeze dried, resuspended in THF, and analyzed by gel permeation chromatography.

4.2.9 Elution Profile of Free Iodine-125

Minimizing elution of free iodine during elution volumes over which labeled polymer is typically collected (i.e. elution volumes near the void volume) is one of the primary contributions to maximizing the purity of the radiolabeled polymer product. Therefore, it is desirable to choose a purification media that significantly delays the elution of free, unbound iodine. Elution profiles for five different purifications, Sephadex G10, G15, and G25, DEAE Sephadex, and PD-10 columns, were recorded to evaluate the

suitability of each purification media. With the exception of the PD-10 columns, the purifications were performed in Disposaflex columns.

In these experiments, the standard protocol for purification was followed; however, the reaction mixture was replaced by the following mixture: 10 μL of stock sodium [^{125}I]iodide solution, 100 μL Tris buffer, and 280 μL PBS. The volume of PBS was in place of the 100 μL of polymer solution, 120 μL of PBS wash, and 60 μL of sodium metabisulfite inactivation solution. Fractions were collected and analyzed using the QC2000 gamma counter. As before, this less accurate gamma counter was used due to safety considerations associated with handling of free radioiodine.

4.2.10 Elution Profile of Post-Reaction Mixtures Generated by the Standard Protocol

While it is important for a separation media to reduce the amount of residual free ^{125}I, it must do so without significantly affecting recovery of the labeled material. Three purification techniques were selected based on the results from the experiments measuring the elution profile of free iodine-125: G25 Sephadex, PD-10 columns, and DEAE-Sephadex. These media were investigated further by measuring elution profiles for unpurified post-reaction mixtures generated by the standard protocol. The results of these measurements were compared with the elution profiles for free iodine-125.

4.2.11 Fractional Recovery for the Purification Step with and without BSA

Bovine serum albumin (BSA) was often added to reduce non-specific adsorption of the target molecule and the corresponding loss in product recovery. Although the non-specific adsorption of PEGylated polymers is typically quite low, an experiment was performed to determine whether BSA was required to maximize product recovery.

To study fractional recovery, a 100-μL volume of polymer solution (1 mg/mL) was added to Disposaflex columns packed with Sephadex G25. Two different experimental conditions were examined: the standard protocol for column packing and purification was followed either with or without BSA chase solution. For experiments without BSA chase solution, equal volumes of PBS were used as a substitute. Elution volumes between 0 and approximately 5 mL were collected in a single fraction. For the experiments without BSA chase solution, concentrations were determined directly using the spectrophotometer calibration curve. For experiments with BSA solution, eluate was collected from a control column in which 100 μL of PBS was added as a blank in between addition of BSA chase solution as described by the standard protocol. The eluate absorbance measured for this blank column was used to adjust for absorbance due to BSA according to:

$$A_{p,cor} = A_p - A_{BSA} \tag{1}$$

where $A_{p,cor}$ is the corrected absorbance, which is the absorbance due to the presence of polymer, A_p is the absorbance measured experimentally for the columns with BSA added, which is due to both polymer and BSA, and A_{BSA} is the absorbance measured in the control experiment, which is due to BSA only. This calculation relies on the assumption that the absorbances measured in the polymer-BSA mixture are additive.

The fractional recovery of polymer across the column, R, was calculated by:

$$R = \frac{C_f V_f}{C_i V_i} \tag{2}$$

where C_i and C_f are the initial and final polymer concentration, respectively, and V_i and V_f are the load and collected fraction volume, respectively.

The fractional recovery across the column was also measured radiometrically by adding a solution of tritiated polymer at the top of the column. One milliliter fractions were collected for elution volumes from 0 to 5 mL (the fraction size was decreased to facilitate scintillation counting). In this radiometric experiment, the fractional recovery across the column, R, was calculated by:

$$R = \frac{\sum_j a_j}{a_i} \tag{3}$$

where a_j is the activity of the j^{th} fraction and a_i is the total initial activity added to the column (note: activity has units of cpm – counts per minute).

4.2.12 Labeling Yield

Reaction conditions, including reaction time and both polymer and radioiodine concentrations, were varied to measure their effect on overall fractional labeling yield, which is the fraction of the total initial ^{125}I added, a_i, that was covalently attached to the final product. The fractional labeling yield, Y, was calculated by:

$$Y = \frac{a_f}{a_i} \tag{4}$$

where a_f is the final activity of the labeled and purified product.

4.2.13 Radiolabel Stability

The stability of the covalent bond between iodine and the polymer was investigated using PD-10 columns. Labeled polymer samples were stored for different lengths of time and added, in their entirety, to the top of PD-10 columns. Elution fractions were collected and assayed for radioactivity according to the standard protocol for purification. The resulting elution profile was used to assess the stability of the iodine label. If the only activity detected during the elution was within fractions near the column

void volume, then all of the activity in the sample remained as iodine covalently bound to (or otherwise associated with) the polymer sample. Conversely, any activity that eluted near the total column volume would correspond to iodine that had become dissociated from the polymer over the storage period.

4.3 Results

Evaluation of the Standard Reaction Protocol

4.3.1 Confirmation of Covalent Attachment Using Sephadex

The polymer designated 027 (FIGURE 4.5) was used in the initial covalent attachment confirmation study. Sephadex G15 media was used for all experiments in this study.

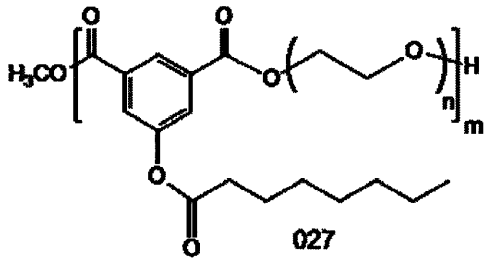

Figure 4.5. Chemical structure of polymer 027, which studied during the attempt to demonstrate covalent attachment of iodine.

The standard protocol was completed and the elution profile during the purification step was recorded (FIGURE 4.6). The reaction mixture for the standard protocol contains all of the standard components: the Iodination bead, ^{125}I, and polymer solution. The elution profile had a sharp, high-activity peak that occurred very shortly after the void volume, which was 3.0 mL for the Disposaflex column. High-activity elution immediately after the void volume is often accepted as sufficient proof of

covalent iodine attachment for peptide labeling applications. The second peak in (FIGURE 4.6) corresponds to the elution of free iodine that was not attached to the polymer during the reaction step. This peak was measured at an elution volume close to that of the total column volume (10 mL).

During a typical iodination, the elution profile is used to determine which fractions to pool to produce the purified labeled product. For the iodination of polymer 027 (FIGURE 4.6), the three fractions that were chosen for pooling are indicated by asterisks. Over the course of the iodinations performed for this work, the fractions pooled were the 2-3 highest activity fractions that eluted near the void volume. The small number of fractions is collected to minimize both dilution and contamination from unbound iodine. In the rare cases where no peak was observed in this range, no iodination product was retrieved and the procedure was repeated with fresh reagents.

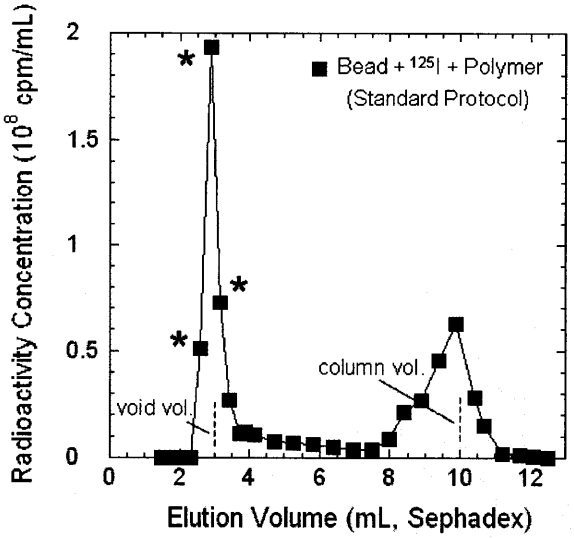

Figure 4.6. Elution profile for the labeling of polymer 027 according to the standard protocol. The void and total column volumes for this experiment, 3 and 10 mL, respectively, are indicated. Asterisks indicate fractions that were collected and pooled as the final labeled, purified product.

As described in the Methods, two more combinations of components were investigated in addition to that for the standard protocol. These additional reaction

mixtures were uncatalyzed, having no Iodination bead added, and consisted of ^{125}I and polymer 027, and ^{125}I only. The results for these reaction mixtures were compared to that for the standard protocol on semi-logarithmic coordinates to help determine whether or not the standard reaction protocol covalently attached radioiodine to our polymer. (FIGURE 4.7).

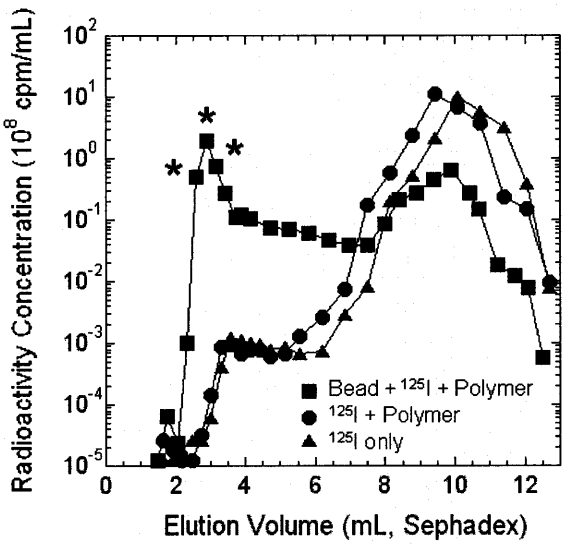

Figure 4.7. Elution profiles for the three different reaction mixtures studied: Iodination bead + ^{125}I + polymer 027, ^{125}I + polymer 027, and ^{125}I only. The results for the former, which represent the standard protocol, were reproduced from FIGURE 6. Asterisks indicate fractions that were collected and pooled as the final labeled, purified product.

The elution profiles for the two uncatalyzed reaction mixtures had much lower radioactivity concentrations than that for the standard protocol. In fact, at the elution volumes for the fractions that were pooled as the labeled polymer product (2.5-3.5 mL), the radioactivity concentration was 3-4 orders-of-magnitude higher for the standard protocol than for either of the uncatalyzed reaction mixtures. The significant difference in radioactivity concentration was a strong indication that the sharp, first high-activity elution peak for the standard protocol reaction was due to the covalent attachment of radioiodine to polymer 027 catalyzed by the Iodination bead.

The elution profiles for the uncatalyzed mixtures were quite similar over all elution volumes studied. Therefore, the two uncatalyzed mixtures, both with and without polymer 027 present, behaved similarly during purification, which implied that polymer 027 did not strongly adsorb or encapsulate ^{125}I. The elution profiles for the uncatalyzed reaction mixtures plateaued soon after 3 mL. The activity in this initial plateau remained at a constant and relatively low level until the majority of the activity eluted near the total column volume. Recall that, for the uncatalyzed reaction mixtures, the activity was added in the form of ^{125}I and should have been able to fully enter the pores of the resin.

The semi-logarithmic plot of the results for the standard protocol revealed that the radioactivity concentration did not return to the baseline after elution of the labeled product as might have been anticipated for an ideal purification (FIGURE 3).

4.3.2 Confirmation of Covalent Attachment Using Radio-High Performance Liquid Chromatography (HPLC)

Radio-HPLC was used as an additional tool to confirm the direct, covalent attachment of radioiodine to our polymer. These experiments were generously completed by Dr. Mikhail Papisov, Assistant Professor of Radiology at the Massachusetts General Hospital. Due to machine time limitations, only a few measurements were possible.

Unfortunately, due to a hard drive failure of the computer devoted to the radio-HPLC system, only scanned images of chromatogram printouts were available for data presentation (FIGURE 4.8). According to the manufacturer, the void volume in the Phenomenex BioSep S-2000 column was approximately 2.9 mL, which corresponds to a void time of 2.9 min. It is important to note that this relatively short and narrow size

exclusion column was primarily intended for preparative and not analytical applications, which may limit the interpretability of smaller chromatographic details.

The UV chromatogram for the initial sample provided a basis for comparison for the reaction and product samples. The backbone polymer eluted approximately thirty seconds after the void time (or volume) was reached. The wavelets in the absorbance profile were due to the effects of pressure fluctuations on the optical detection. Such fluctuations are common for low flow rates such as that used in this method.

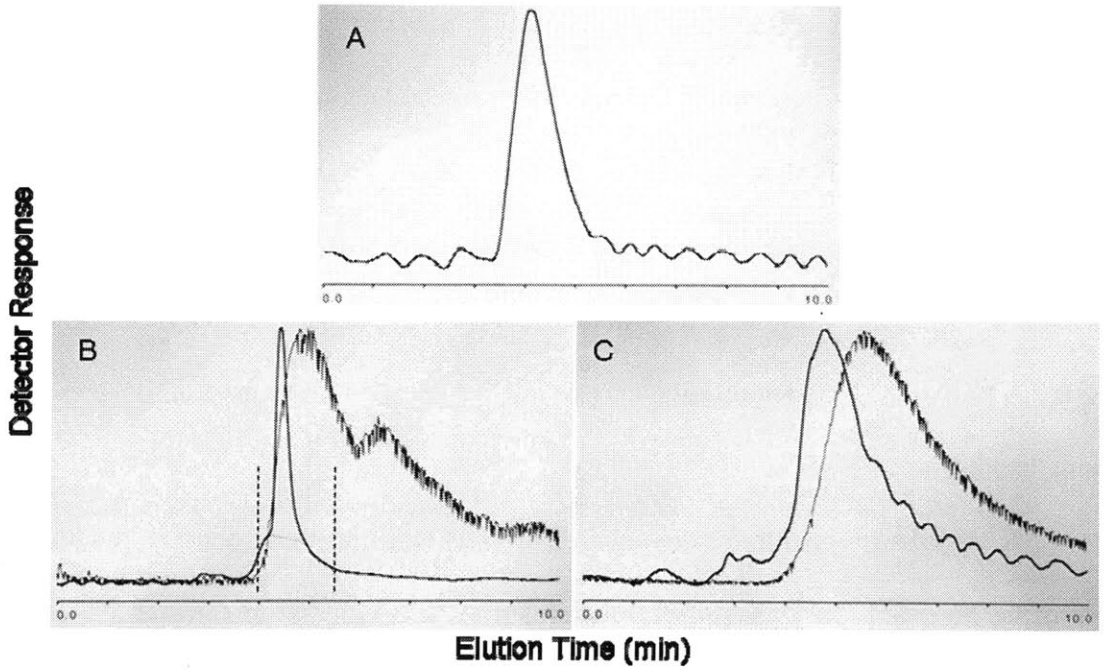

Figure 4.8. Radioactivity and absorbance (abs) detector response as a function of elution time measured by size-exclusion radio-HPLC with a 7.5x75 mm BioSep S-2000 column. (A) The initial solution, before labeling, was measured. (B) The backbone polymer was labeled with ^{124}I and analyzed. This radio-HPLC analysis was used to determine which fractions to collect and pool (indicated by the dashed lines). (C) The final, purified product was analyzed.

The activity profile for the labeled, unpurified product (FIGURE 4.8B) had two distinct peak. The first peak corresponded to labeled polymer while the second peak corresponded to unreacted, free iodine-124. In the purified product (8C), the labeled polymer peak persisted, while the free iodine peak was no longer present. As described in

the methods, there was a one minute delay for the activity measurements relative to the absorbance measurements due to the lines in between the detectors.

The absorbance profile for the labeled, unpurified product (8B) was similar in shape to the chromatogram measured for the unlabeled starting material. There were, however, two minor differences: (1) a slight shoulder on the leading edge of the absorbance elution peak and (2) a small, amorphous peak at an elution time of approximately 3 min. The should is most likely a peak abnormality related to the relatively low separation efficiency of the preparative size exclusion column, while the peak at 3 min may correspond to a small amount of impurities in the unpurified sample. This peak was more prominent in the final, purified sample (8C), suggesting that it was not an artifact of the original measurement. However, there was no radioactivity associated with this early elution time peak, which was encouraging. Finally, the elution peak at 1.5 min in the purified product was an artifact because it occurred before the void volume had been reached.

The absorbance profile for the purified product was much broader than the other two profiles recorded. This was most likely a result of the comparatively lower concentration of the polymer sample analyzed by the radio-HPLC. This peak broadening for low concentration samples is a commonly observed phenomenon in chromatography caused by diffusion within the lines comprising the post-column hold-up volume. The main peak absorbance and activity profiles for the labeled, purified product were similar in shape. This result suggested that the breadth of polymer molecular weights in the initial backbone polymer sample received radioiodine labels.

4.3.3 Effect of Iodination on Chemical Structure

Studies were performed to confirm that the labeling procedure did not adversely affect the chemical structure of the original polymer sample. The starting material for these studies was cold iodine-127 (in place of iodine-125) and backbone polymer dissolved in PBS. The molecular weight profile of the backbone polymer after undergoing the iodination procedure was the primary result. Therefore, the backbone polymer starting material was subjected to two different chromatography techniques: (1) the aqueous Sephadex column during the standard protocol and (2) the organic GPC system for molecular weight analysis.

In the first experiment, the initial polymer concentration in the reaction was increased to 10 mg/mL and the iodine concentration was increased proportionately to 58.8 μg/mL in order to obtain sufficient signal for GPC measurement. The reaction product was freeze-dried, resuspended in THF and the resulting GPC chromatogram for the reaction product was compared to that for raw polymer dissolved in THF (FIGURE 4.9). The raw polymer sample used for comparison was dissolved directly in THF from the solid form and was never dissolved in water or subjected to freeze-drying. Refer to APPENDIX D for greater detail concerning the calculation of fractional recovery and the manipulation of the chromatograms presented in this section.

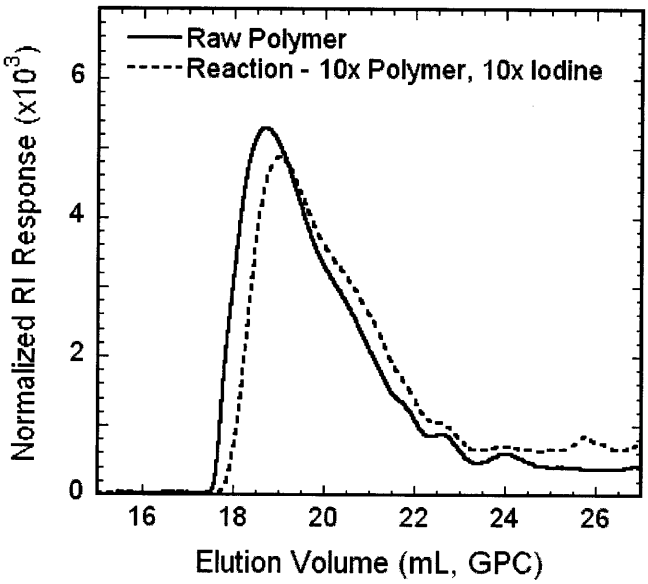

Figure 4.9. GPC chromatograms to determine the effect of the iodination on backbone polymer molecular weight. Data for backbone polymer labeled with cold iodine-127 (10 mg/mL polymer, 58.8 µg/mL iodine) compared to raw backbone polymer. The x-axis for these elution profiles refers to elution volume in the analytical GPC system (and not in Sephadex).

The chromatograms were qualitatively similar, which implied that the bulk molecular weight distribution of the recovered backbone polymer was largely unaffected by the standard protocol. There were, however, two noticeable differences in the shape of the chromatograms. There was an elevated refractive index response at GPC elution volumes greater than 23 mL for the iodination curve relative to the raw polymer curves. This was most likely a consequence of the freeze-drying procedure (see FIGURE 4.10). The major difference, however, was the slight shift of the peak to the right (i.e. lower molecular weights) and the slightly extended shoulder beginning at a GPC elution volume of 20 mL. The shift and shoulder were probably not caused by freeze drying and therefore may be considered to have been caused by the conditions of the standard protocol. The fractional recovery of the reaction product was estimated to be 0.88 (see APPENDIX for calculation details and associated discussion). Recovery at this level was deemed acceptable (see also Section 4.3.8: Fractional Recovery).

The weight-average molecular weights for the chromatograms presented in FIGURE 4.9 were calculated according to the empirical calibration described in detail during the Polymerization Chapter. The M_w for the 'reaction' polymer and the raw polymer were 5.1 and 5.3 kDa, respectively. Although differences were observed between the chromatograms, the bulk molecular weight properties of the polymer were minimally affected during the augmented reaction protocol in this experiment.

Experience with another sample, polymer 027, provided the basis for the interpretation of the elevated response at elution volumes greater than 23 mL. Specifically, beginning from the solid state, polymer 027 was dissolved in water, subjected to the freeze-drying procedure, resuspended in THF and analyzed by GPC. The resulting chromatogram was compared to that for polymer 027 dissolved directly into THF (FIGURE 4.10).

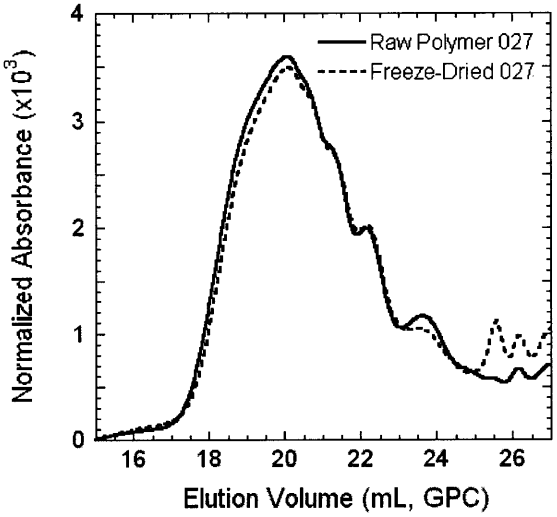

Figure 4.10. Comparison of two chromatograms for polymer 027. In one instance, the polymer was dissolved in water, freeze-dried and resuspended in THF. In the other, the polymer was dissolved directly in THF. The x-axis for these elution profiles refers to elution volume in the analytical GPC system (and not in Sephadex).

An additional experiment was performed to measure backbone polymer degradation at elevated oxidative conditions (FIGURE 4.11). This was accomplished by

increasing the initial amount of iodine-127 added to the reaction by 1000-fold while holding the concentration of backbone polymer constant at 1 mg/mL. As before, the raw polymer sample used for comparison was dissolved directly in THF from the solid form and was never dissolved in water or subjected to freeze-drying.

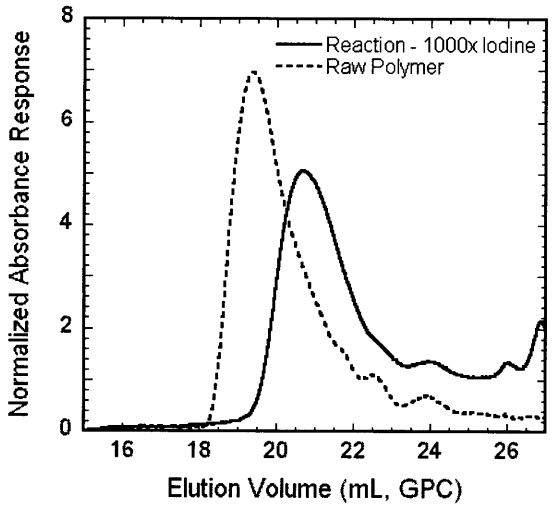

Figure 4.11. GPC chromatograms to determine the effect of elevated oxidative conditions on backbone polymer molecular weight. Data for backbone polymer labeled with cold iodine-127 (1 mg/mL polymer, 5.88 mg/mL iodine) were compared to raw backbone polymer. The x-axis for these elution profiles refers to elution volume in the GPC system (and not in Sephadex).

Absorbance response was chosen for these low concentration samples because of the comparatively lower sensitivity of the refractive index detector[2]. Comparing the reaction and raw polymer chromatograms, the major peak for the reaction polymer was shifted significantly to higher elution volumes. This increase in elution volume indicated a reduction in molecular weight caused by polymer degradation by the oxidative reaction conditions. As before, the presence of small peaks at GPC elution volumes greater than 25 mL may have been produced during freeze-drying. The estimated fractional recovery in this experiment was 0.36, considerably lower than that for the previous experiment (0.88). The low recovery was likely caused by the lower initial polymer mass and the

[2] Note: Refractive index response was preferred because PEG has very minimal absorbance at 250 nm.

disproportionate loss of material due to process recovery limitations or, more likely, losses within the phosphate buffer salts that were insoluble in THF.

The weight-average molecular weight was also calculated according to the calibration for these two chromatograms. The M_w for the 'reaction' polymer and the raw polymer were 3.2 and 5.3 kDa, respectively. Although the thousand-fold increase in iodine affected the molecular weight profile of the recovered polymer, the significant increase in reactive (oxidative) iodine species did not completely degrade the polymer.

4.3.4 Effect of the Iodination on Older Polymer Samples

While the backbone polymer used for the previously described experiments was synthesized and used within less than 6 mo (all but one experiment was conducted within 2 mo of synthesis), the preceding experiments were also completed using a backbone polymer sample that had been stored in the solid form under ambient conditions for more than one year after its synthesis ('old polymer'). A portion of this stored sample was dissolved in PBS and subjected to the augmented standard protocol (10 mg/mL polymer, 58.8 μg/mL $Na^{127}I$) and subsequently analyzed on the GPC system. Another portion of the stored sample was also dissolved directly in THF and the resulting chromatogram was measured as a basis for comparison (FIGURE 4.11).

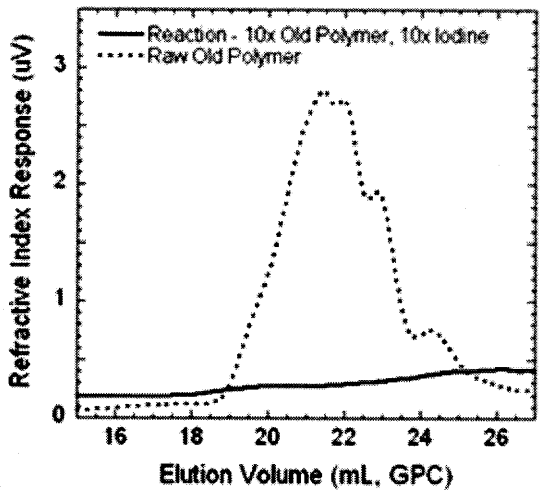

Figure 4.12. GPC chromatograms to determine the effect of iodination (augmented standard protocol) on old polymer molecular weight. The old backbone polymer was stored at ambient conditions for over one year. The x-axis for these elution profiles refers to elution volume in the GPC system (and not in Sephadex).

No discernible response was measured in the GPC analysis of the 'old polymer' that was subjected to the standard reaction protocol, freeze dried, and resuspended in THF. This result was repeated ($n > 5$) to confirm that experimental errors did not contribute to the observed phenomenon. The elevated chromatogram at GPC elution volumes greater than 23-24 mL implied that some lower molecular weight material was present in the sample. The iodination may have also produced material that was insoluble in THF or fragmented such that its elution would be indistinguishable from that of very low molecular weight contaminants, which include dissolved gases. These low molecular weight contaminants create an extremely noisy response, at GPC elution volumes greater than 30 mL that varies greatly between runs. For this reason, only elution volumes less than 27 mL were included in this and other GPC chromatograms.

Evaluation of the Standard Purification Protocol

4.3.5 GPC Analysis of Void Volume Fractions

The standard protocol for purification was followed with Sephadex G15 and polymer 027 and fraction collected near the void volume was analyzed by GPC to determine (1) if the polymer eluted near the void volume and (2) if the entire range of polymer molecular weights was present in the collected fraction surrounding the void volume. Therefore, for this experiment, the fraction collected from elution volumes between 2 and 4 mL from the Sephadex G15 column was analyzed using the analytical GPC system. The resulting elution profile (chromatogram) is the detector response as a function of elution volume in the GPC system (FIGURE 4.13).

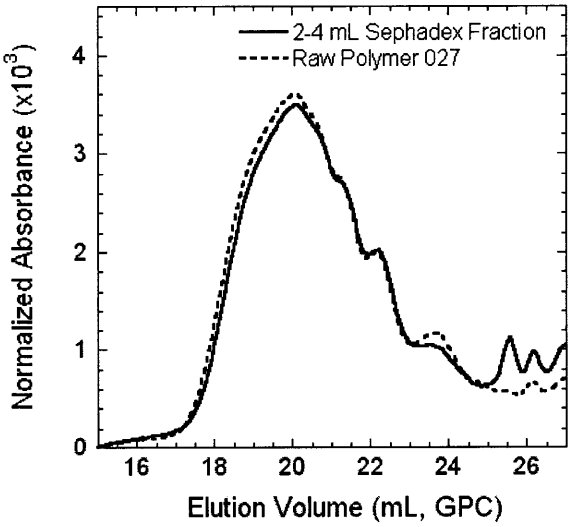

Figure 4.13. GPC chromatograms to confirm that the polymer co-elutes with the high activity elution peak. A fraction was collected from a Sephadex G15 column at elution volumes (EV) between 2-4 mL, freeze dried, and measured by GPC. The normalized absorbance (to adjust for differences in GPC sample sizes) was plotted as a function of GPC elution volume.

The chromatograms for the Sephadex 2-4 mL elution volumes and for the raw, unprocessed polymer 027 were compared. There was excellent agreement between the two chromatograms across the entire range of GPC elution volumes. Small peaks were observed at GPC elution volumes greater than 25 mL for the sample collected from the

Sephadex column. These peaks, which were not present in the raw polymer sample that was dissolved directly in THF, are indicative of small molecular weight species and were likely generated during freeze drying. It is highly unlikely that these peaks were caused by interactions with the inert Sephadex media.

4.3.6 Elution Profile of Free Iodine-125

Various Sephadex media were assessed for their ability to separate the labeled polymer product from the free, unlabeled radioiodide present in the post-reaction mixture. The relevant measurements, including the void and total column volumes, for both Disposaflex and PD-10 columns were summarized in TABLE 4.1.

The elution profiles for free iodide (^{125}I) were measured for the following Sephadex media: Sephadex G10, G15, and G25, DEAE Sephadex, and PD-10 columns (pre-packed with Sephadex G25). The radioactivity concentration in each fraction was plotted as a function of elution volume (FIGURE 14A). The cumulative fraction of the initial activity added was also plotted for each elution volume according to the following:

$$f_{k,cum} = \frac{\sum_{j=1}^{k} a_j}{a_i} \tag{4}$$

where $f_{k,cum}$ is the cumulative fraction of the initial activity added in the k^{th} fraction collected and a_i is the initial activity of ^{125}I added. The plots also include dashed lines indicating the void and total column volumes for the Sephadex-packed Disposaflex columns, 3 and 10 mL, respectively (the void volume for the PD-10 column was 2.5 mL).

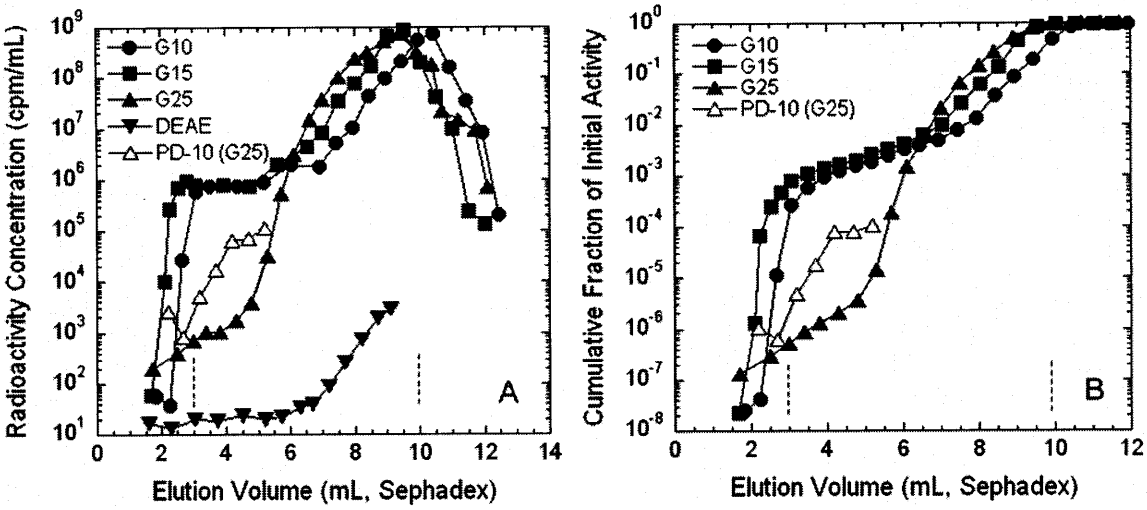

Figure 4.14. Elution profiles for free ^{125}I (1 mCi in µL PBS). Data are presented (A) radioactivity concentrations and (B) as the cumulative fraction of the initial activity added to each column. The approximate void and total column volumes for the Sephadex packed in Disposaflex columns (all but PD-10) are indicated by the dashed lines. The results for DEAE were not plotted in (B due to the extremely low activity in the collected fractions.

Elution volumes near the void volume comprised the region of greatest interest because they corresponded to fractions typically pooled as the labeled, purified polymer product. Consequently, the elution volumes from 2-4 mL were chosen as the focus for analysis of these results. The radioactivity concentration was the highest in the G10 and G15 Sephadex-packed columns, both of which reached a plateau before 3 mL at a radioactivity concentration of approximately $1x10^6$ cpm/mL. The two columns packed with G25 Sephadex were the next highest in activity; however, the radioactivity concentration measured in the 2-4 mL range was 2-4 orders-of-magnitude less than that for the G10 and G15 resins. The increased activity at early elution volumes (2-5 mL) in the G10 and G15 resin experiments would lead to an increased co-elution of free iodide together with labeled product in an actual separation, which would lead to decreased purity of the pooled fractions collected for these media. The radioactivity concentration for the size exclusion resins sharply increased as the elution volume approached the total column volume.

The radioactivity concentration for DEAE-Sephadex was extremely low for the elution volumes near the void volume. This nearly complete reduction in activity was caused by the ionic interactions between the positively charged DEAE functional groups and the negatively charged iodide ions. The gradual increase in activity as the elution volume approached the total column volume corresponded to flowthrough of iodide ions not trapped by the charged groups of the resin.

The elution profiles for free ^{125}I in various resins were also analyzed quantitatively by adding the activity collected during elution volumes from 2-4 mL (TABLE 4.2). The ^{125}I only results were presented along with that for the purification of the reaction mixture (Iodination bead, ^{125}I, and polymer 027, FIGURE 4.6). The results for the two sets of material added to the column were presented together to provide a rough order-of-magnitude comparison. The free iodide collected between 2-4 mL during the G10 and G15 purifications was between 2 and 3 orders-of-magnitude less than that collected for the post-reaction mixture for the labeling of polymer 027. The difference was even greater for the PD-10 and G25 purifications – 4 and 5 orders-of-magnitude, respectively. Although the difference was greatest for the DEAE media, it may not be an appropriate comparison since the polymer 027 reaction mixture was purified using a size exclusion media and not an ion exchange media (see next section for further detail).

Table 4.2. Comparison of activities collected between 2 and 4 mL elution volume from various Sephadex purifications. The results for the ^{125}I only experiments were determined from FIGURE 14, while those for the reaction mixture were calculated from FIGURE 6.

Material Added to Column	Resin	Activity in 2-4 mL (cpm)
Post-Reaction Mixture (^{125}I-027 and Unreacted ^{125}I)	G15	7.1×10^{3}
^{125}I only	G10	9.0×10^{5}
	G15	1.5×10^{6}
	G25	1.4×10^{3}
	PD-10 (G25)	1.3×10^{4}
	DEAE	2.1×10^{1}

4.3.7 Elution Profile of Post-Reaction Mixtures Generated by the Standard Protocol

Three methods were chosen based on the results for the free iodine elution profile experiments for further examination: G25 Sephadex, PD-10 columns (pre-packed with G25), and DEAE-Sephadex. These methods were investigated by measuring and comparing the elution profiles for unpurified post-reaction mixtures, which contain both labeled sample and unreacted ^{125}I, to those measured in the previous section for solutions of free ^{125}I only (FIGURE 4.15). The chemical structures of the polymer starting material used in the study are also included. Polymer with 100% of sidechains substituted with PEG3400 (067) was used for both the Sephadex G25 and DEAE-Sephadex experiments, while polymer substituted with 10% PEG3400 (068) was used for the PD-10 experiment.

The fractions that were pooled to form the labeled polymer product were labeled by asterisks. These fractions can be compared to the radioactivity concentrations in the free ^{125}I only elution profiles to estimate the amount of activity in the pooled fractions that was due to unbound radioiodine. Because the total amount of activity added to each column, 1 mCi, existed in both the bound and unbound forms, this type of analysis

provides an upper bound for the level of free iodine impurity. For the G25 Sephadex purifications, the radioactivity concentration in the pooled fractions of the reaction mixture was five orders-of-magnitude greater than that in the corresponding elution volumes for the ^{125}I only experiment. This implied that the pooled, labeled polymer product was 99.999% pure. This same difference for the experiments using PD-10 columns (pre-packed with Sephadex 25) was only approximately three orders-of-magnitude, which implied a product that was 99.9% pure.

For the DEAE-Sephadex column experiments, the difference in radioactivity concentration between the reaction mixture and iodine-125 only elution profiles at approximately 3 mL was the greatest observed – nearly six orders-of-magnitude. However, as indicated by the lack of asterisks in FIGURE 4.15C, no fractions were pooled due to the extremely low activity. The absolute magnitude of the activity for the DEAE-Sephadex purification of the reaction mixture was 10-50x less than that for the size exclusion purifications in FIGURE 4.15A and B. This was indicative of the polymer having become bound to the functional groups of the DEAE-Sephadex. If fractions were to have been pooled, the resulting labeled product would have represented an overall radioactive yield of less than 1%.

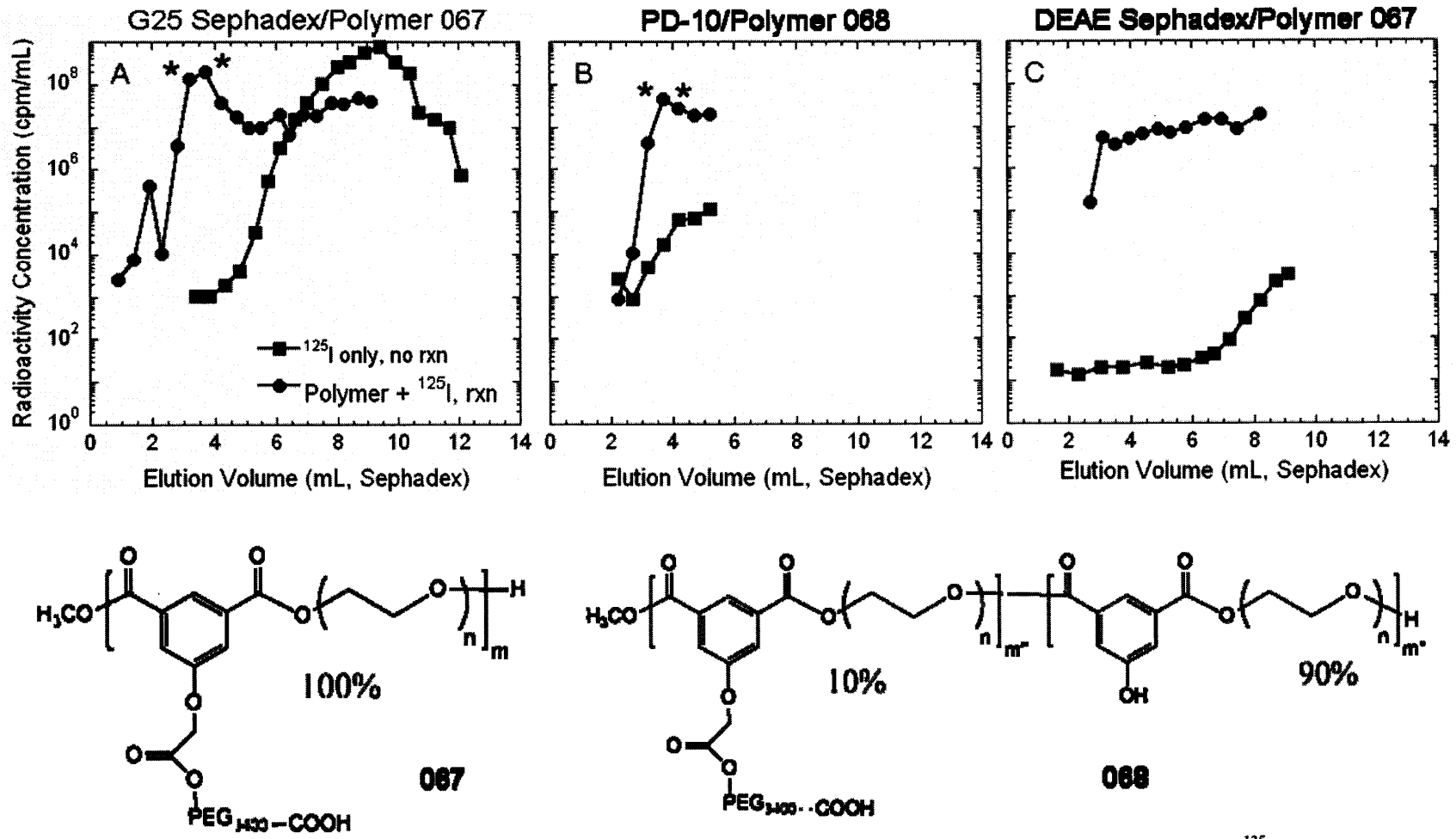

Figure 4.15. Elution profiles for (A) Sephadex G25, (B) PD-10 columns, and (C) DEAE-Sephadex for reaction mixtures and free ^{125}I only. Data are plotted semi-logarithmically as the radioactivity concentration as a function of elution volume. Polymer 067 was used in the G25 and DEAE-Sephadex experiments, while polymer 068 was used for PD-10. Asterisks indicate fractions that were pooled as the labeled polymer product (no pool was created for DEAE experiment due to low activity).

4.3.8 Fractional Recovery for the Purification Step with and without BSA

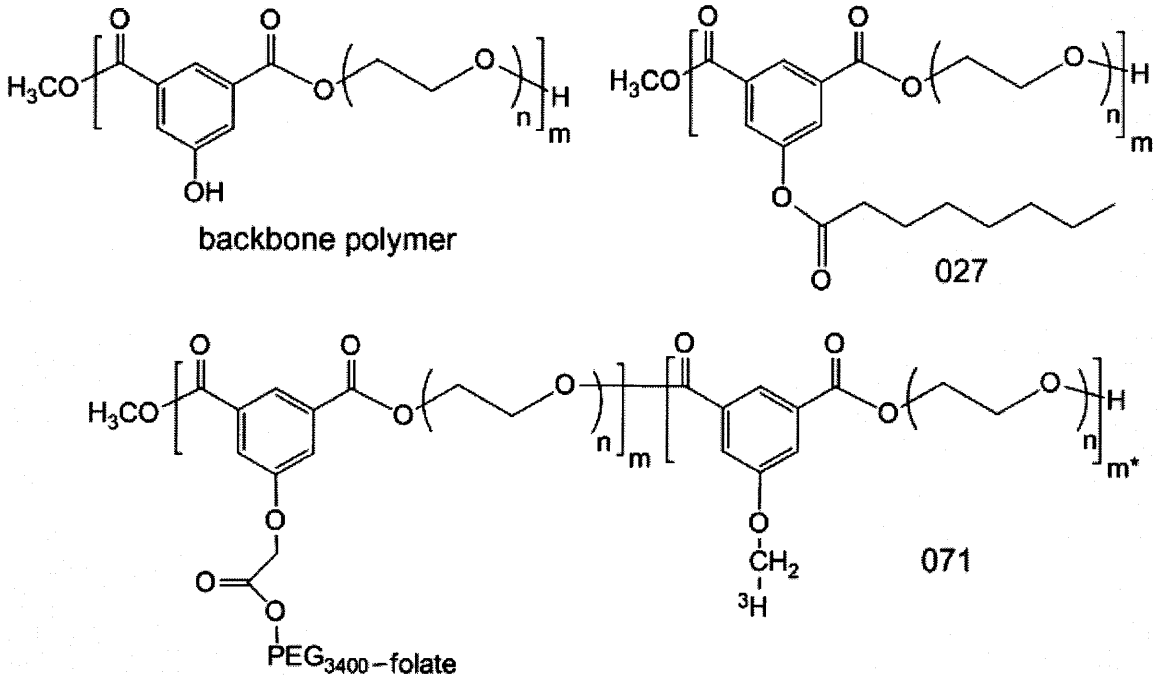

Figure 4.16. Structures of polymers investigated in percent recovery studies. Backbone polymer and Polymer 027 were measured spectrophotometrically, while Polymer 071, which contained a tritium label on substituted as approximately 2% of the side groups, was studied radiometrically.

The fractional recovery for the purification step was measured to determine whether the BSA chase solution was necessary in order to apply the standard protocol to our heavily PEGylated polymers. The fraction recovery was measured spectrophotometrically for Sephadex G15 and radiometrically for Sephadex G25 (TABLE 4.3) for three different polymers (FIGURE 4.16), both with and without BSA chase solution added as described in the Methods.

Table 4.3. Summary of results for percent recovery by mass experiments. Backbone polymer and 027 were run on Sephadex G15 and measured by UV/vis, while 071 was run on Sephadex G25 and measured by scintillation counting.

Polymer	BSA	R
Backbone	Y	0.94
	N	0.93
027	Y	0.93
	N	0.97
071	N	0.92

Under all measured conditions, the fractional recovery by mass of polymer, R, was greater than 90%. There was no difference in recovery between backbone polymer and polymer 027, which could form micelles. In previous work in our group, the critical micelle concentration (CMC) of polymer 027 was determined to be 0.07 mg/mL by surface tension measurements [39]. There was also no difference between experiments with and without the BSA chase solution added at the appropriate steps. Finally, the fractional recoveries determined according to the spectrophotometer and scintillation counting were similar.

4.3.9 Labeling Yield

The fractional labeling yield, as defined in EQUATION 4, was measured as a function of various experimental conditions, including reaction time, radioiodine concentration, and polymer concentration (TABLE 4.4). For these studies, polymer 027 was the starting material and Sephadex G15 was used throughout.

Table 4.4. Fractional labeling yield as a function of (A) reaction time, (B) polymer concentration, and (C) initial radioiodine activity. Experiments were performed using polymer 027. Data in italicized or underlined typeface indicate independent replicates of the same respective experimental conditions.

	Polymer Conc (mg/mL)	Init Activity (mCi)	Rxn Time (min)	Y
A	1	1	7.5	0.06
			15	*0.20*
			30	0.30
B	0.01	1	15	0.007
	0.1			0.02
	1			*0.23*
	5			<u>0.51</u>
C	5	0.1	15	0.43
		0.25		0.45
		1		<u>0.59</u>
		2		0.58

The greatest measured fractional yield, nearly 0.6, was for 5 mg/mL polymer labeled with either 1 or 2 mCi of initial radioiodine for 15 minutes. Variations in polymer concentration and reaction time had the greatest effect on reaction yield, while initial iodine activity, which is directly related to initial iodine concentration, had comparatively little effect on reaction yield for the measured conditions.

The fraction of linkers having radioiodine labels was calculated for the highest observed labeling yield, 0.59. Assuming a polymer with 5 repeat units and 1 mCi of initial iodine activity, it was estimated that only 1 in approximately 10,000 linker molecules have an iodine label. However, even at this low substitution, more than sufficient activity was present in the labeled product to support copious uptake measurements.

Kinetic modeling was performed to determine whether certain elementary reactions were applicable to the iodination system given the measured experimental yields. Theoretical yield relationships were derived for zeroth, first, and second order elementary reactions. The reaction was modeled as A + B → P, where A represented ^{125}I, B represented reactive sites, and P represented a labeled site within the polymer. The initial conditions were $C_A(0) = C_{Ao}$ and $C_P(0) = 0$. The model formulations for the three different reaction orders studied were solved to determine the corresponding analytical solution for theoretical yield, Y (FIGURE 4.17). The theoretical yield, Y, was determined for various reaction orders in iodine by deriving C_P as a function of time and dividing by C_{Ao}. The time-dependent concentration, $C_A(t)$, was derived where necessary.

Order	$-\frac{dC_A}{dt}$	$\frac{dC_P}{dt}$	Y
0th	0	kC_{B_0}	$\frac{kC_{B_0}t}{C_{A_0}}$
1st	$kC_AC_{B_0}$	$kC_{B_0}C_{A_0}e^{-kC_{B_0}t}$	$1-e^{-kC_{B_0}t}$
2nd	$kC_A{}^2C_{B_0}$	$kC_{B_0}\left[\frac{C_{A_0}}{kC_{A_0}C_{B_0}t+1}\right]^2$	$1-\frac{1}{kC_{A_0}C_{B_0}t+1}$

Figure 4.17. Model formulation and results for theoretical yield derivations based on zeroth, first, and second order elementary reactions proposed as potential representations of the iodination. In the model, A, B, and P corresponded to iodide, reactive sites on the polymer, and labeled sites, respectively. The initial conditions were $C_A(0) = C_{A0}$ and $C_P(0) = 0$, while C_B was assumed to be constant and equal to C_{B0} throughout.

As depicted in FIGURE 4.2, there are two reactive sites in each repeat unit of the backbone polymer at the position ortho to the aromatic hydroxyl. In all of the derivations the concentration of reactive sites, C_B, was assumed to be constant, C_{Bo}, because, with the exception of the 0.01 mg/mL polymer reaction, the number of reactive sites exceeded the total number of ^{125}I molecules in solution by seven times or greater for the experimental conditions studied. For example, assuming a backbone polymer molecular weight of 3 kDa, with 3 repeat units and 2 reaction sites per repeat unit, there would be 33 mmol of reactive sites in 100 μL of 1 mg/mL polymer solution. For comparison, there were 0.47 mmol of iodide molecules in 1 mCi of the radioiodine stock solution. Therefore, for 1 mCi iodine and 1 mg/mL polymer, there were 70 times more reactive sites than iodide molecules in solution. This ratio can be calculated proportionately for any of the other reaction conditions.

For the model that was first order with respect to A, no dependence on initial iodine concentration was predicted according to the derived result for the theoretical yield. This was reminiscent to the experimental results, which showed initial iodine concentration had a very weak influence on experimental yield. The theoretical yield for the second order model with respect to A predicted that initial iodine and reactive site concentration would have equal influence on the experimental yield. Such behavior was not observed in the experimental results. Finally, the 0^{th} order model with respect to A predicted a theoretical yield that decreased as the initial amount of iodide added was increased. This also was not observed experimentally. The theoretical yield for the 0^{th} order model was also increased monotonically and linearly in time, which would eventually lead to a physically unrealistic yield ($Y > 1$). This was a consequence of the assumption that the concentration of B remained constant.

The experimental data were used to estimate a rate constant for the iodination reaction based on the theoretical yield for the first order model in A, Y_1:

$$Y_1 = 1 - e^{-kC_{B_o}t} \tag{5}$$

EQUATION 5 was rearranged to:

$$1 - Y_1 = e^{-kC_{B_o}t} \tag{6}$$

and, according to EQUATION 6, the experimental yield data were plotted semi-logarithmically with $C_{B_o}t$ on the abscissa and (1-Y) on the logarithmic ordinate (FIGURE 4.18). The product $C_{B_o}t$ must be used because experimental yields were measured for different reaction times as well as different initial polymer concentrations. According to EQUATION 6, the slope of the data set plotted accordingly is equal to the opposite of the

effective forward rate constant for the iodination. The rate constant that resulted from the least-squares regression was 4.6×10^{-3} mL/(mg-min) with an R-squared value of 0.93.

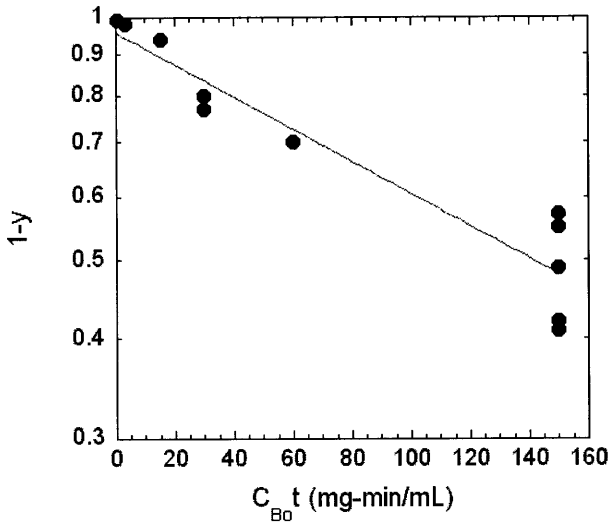

Figure 4.18. Experimental yield data plotted according to the theoretical yield derived for the first order model. The slope of the regression line for the semi-logarithmic plot is equal to the opposite of the iodination rate constant.

4.3.10 Labeling Yield for Ornamented Polymers

The yields reported to this point were the maximum observed. Many alterations were made to the basic structure of polymer 027 to include sidechains with targeting moieties such as peptides or the small molecule folate attached to the backbone by means of polyethylene glycol spacers of varying lengths. Based on the results of the labeling yield study for polymer 027, labeling of ornamented polymer formulations for the uptake and biodistribution studies described in Chapter 5 was performed using an initial polymer concentration of 5 mg/mL. During these labeling procedures, yields were typically observed between 0.05-0.50.

4.3.11 Radiolabel Stability

The radiolabel stability was investigated by applying labeled polymer 027 that was stored in PBS at 4°C for 6 mo to a PD-10 column (FIGURE 4.19). Equal volume, one milliliter fractions were collected and the activity in each fraction was normalized by the total pre-column activity added to the PD-10 column. In this experiment, any activity measured near the total column volume would indicate that radioiodine had dissociated from the polymer, most likely through cleavage of the carbon-iodine covalent bond. The PD-10 column, which was able to separate free, unbound iodine from labeled polymer in previous experiments (FIGURE 4.15), was chosen for convenience.

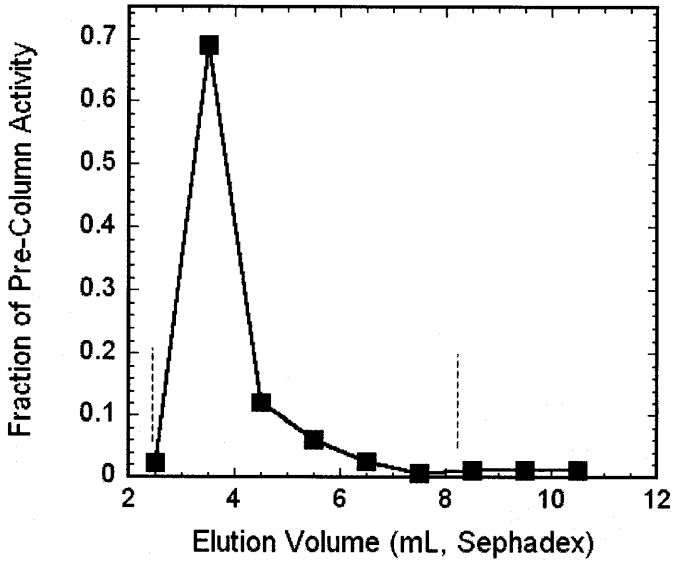

Figure 4.19. Elution profile of radiolabeled polymer 027 in PBS after storage for 6 months at 4°C. Data for each collected fraction are plotted as the fraction of the total activity initially added to the PD-10 column. The void and total column volumes for the PD-10 column are indicated by the dashed lines.

The majority of the activity eluted shortly after the elution volume reached the void volume (2.5 mL for the PD-10 column). There was a small tail from approximately 4.5 to 6.5 mL of elution. No activity peak was observed at the total column volume (8.5

mL for the PD-10). Together, these results demonstrated that iodine remained bound to the polymer 027 for the duration of the 6 mo storage period.

4.3.12 Considerations for Radiolabeling High Molecular Weight Backbone

Backbone polymer starting material with a number-average molecular weight of 3 kDa and polydispersity of 1.75 was used throughout the preceding studies. Although the basic chemical structure of the repeat unit does not vary as a function of molecular weight, decreased polymer solubility at increased molecular weight is a commonly observed phenomenon in polymer science (see also Polymerization Chapter). Consequently, the analyses performed for the lower molecular weight polymer, including those for labeling yield, stability, and purity would not necessarily be reproduced for higher molecular weight backbone polymer.

Labeling of higher molecular weight polymer was studied during the radioiodinations performed in support of the uptake and biodistribution studies described in Chapter 5. For these studies, polymers were synthesized using low polydispersity, high molecular weight backbone polymer (M_n = 12 kDa, PDI = 1.15) as the starting material (FIGURE 4.20).

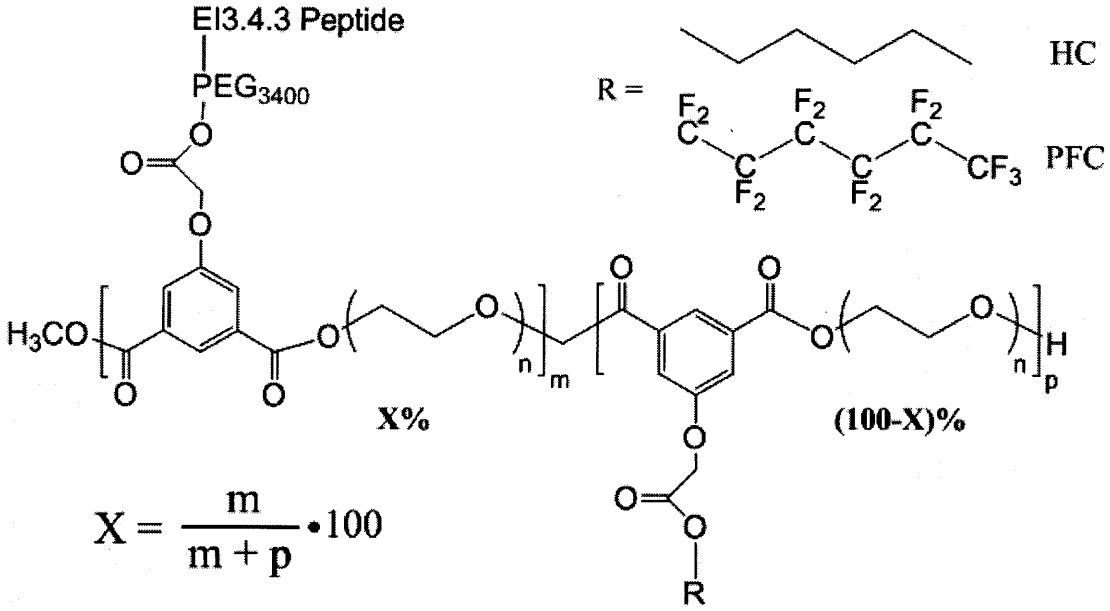

Figure 4.20. General structure of polymers synthesized using high molecular weight backbone polymer starting material (12 kDa, PDI = 1.15). Formulations varied X and R. Polymers without EI3.4.3 targeting peptide attached were also synthesized.

Polymers were labeled using the increased polymer concentration (5 mg/mL) and purified using either Sephadex G25 or PD-10 columns. Although labeling was performed identically to the successful iodinations completed for lower molecular weight polymer, the purity of the radioiodinated purified high molecular weight polymers was uncertain due to irregularities observed during *in vivo* measurements with the labeled high molecular weight material. In particular, significantly higher levels of activity were measured in the stomach during biodistribution studies with polymer synthesized from high molecular weight backbone polymer relative to that for lower molecular weight polymers. Increased activity in the stomach is a strong indicator of the presence free iodine *in vivo* (See Targeted Delivery Chapter for greater detail).

Labeled polymer solutions were tested for purity using PD-10 columns at different lengths of storage time after the original labeling and purification procedure. PD-10 columns were used for this study due to the large number of columns required in a short period of time. Activities of the collected elution fractions were measured and

analyzed according to the same method used for polymer 027 stored for 6 mo and data were plotted as the fraction of the total initial activity added to the PD-10 column (FIGURE 4.21).

Polymer substituted with 25% PEG3400-EI3.4.3 peptide and 75% perfluorocarbon (PFC) sidechains (see FIGURE 4.20 for structure) was labeled and purified and tested for purity 4 hr after the initial procedure (FIGURE 4.21a). The secondary peak at an elution volume of 9.5 mL, which was approximately equal to the total column volume, indicated the presence of free iodide in the labeled material. This finding confirmed the suspicion raised during the biodistribution studies concerning the purity of the labeled high molecular weight material.

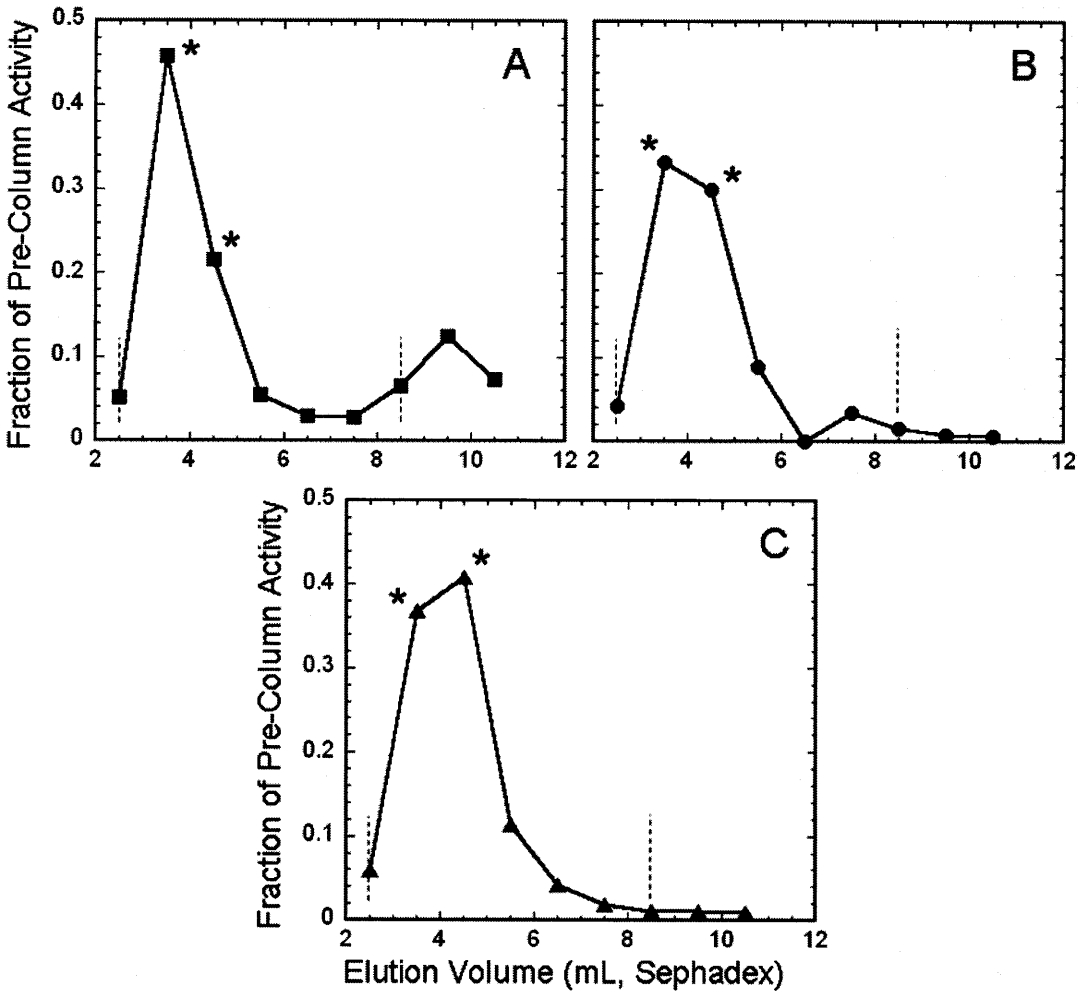

Figure 4.21. High molecular weight polymer substituted with 25% PEG3400-EI3.4.3 peptide and 75% PFC sidechains analyzed by a PD-10 column (A) 4hr, (B) 5 hr, and (C) 28 hr after initial labeling and purification (t=0). Asterisks indicate fractions that were pooled and either remeasured (A, B) or used in biological studies (C). The void and total column volumes for are indicated by dashed lines.

In addition to providing information about the purity, the PD-10 column also purified the sample. The high-activity fractions (indicated by asterisks) were collected and analyzed using a fresh PD-10 column one hour later, which was also 5 hr after completion of the initial procedure (FIGURE 4.20B). For this measurement, the secondary elution peak was significantly lower, but still present. The high-activity fractions, again indicated by asterisks, were collected and analyzed using a fresh PD-10 column 23 hr later, which was 28 hr after the initial procedure (FIGURE 4.20C). The

resulting elution profile had no significant late elution volume peak, which indicated that the sample added to the PD-10 column was radiochemically pure. To confirm this, the resulting sample was measured 3 days later and a similarly pure elution profile was observed (data not shown).

4.4 Discussion

Evaluation of the Standard Reaction Protocol

4.4.1 Confirmation of Covalent Attachment Using Sephadex

Polymer 027 was labeled and purified according to the standard protocol. Two distinct peaks were observed in the corresponding elution profile (FIGURE 6) near the void and total column volumes. The sharp elution peak for the labeled polymer indicated that the polymer was completely excluded from the pores of the resin. The peak corresponding to the free, unbound iodine which are small enough to enter the entirety of the porous resin, was comparatively diffuse. This is most likely due to dispersive effects that are commonly observed for materials traveling through porous media. Heterogeneities in the pore size could have also contributed to the observed diffuseness of the free iodine peak.

When plotted semi-logarithmically (FIGURE 4.7), it was apparent that the radioactivity did not return to the baseline after the primary elution peak of the labeled polymer 027 product. This tailing of the elution peak can be attributed to mixing occurring within the resin bed, which is usually a sign of loose packing. Loose packing may be a consequence of the gravity flow method used to pack the Disposaflex columns. Although it represents a deviation from the ideal profile presented qualitatively in

FIGURE 4.3, the observed tailing was relatively small when compared to the height of the elution peak.

For the uncatalyzed reaction mixtures in which no Iodination bead was added, a step change and subsequent plateau in radioactivity concentration was observed. This behavior may indicate a small degree of channeling or bypassing of the Sephadex G15 resin bed. The small proportion of activity bypassing the media remained constant until the major activity peak, which corresponded to free iodine, began eluting as the elution volume approached the total column volume. The consequence of this channeling or bypassing would be unbound iodine impurities in the pooled labeled polymer (indicated by asterisks).

Even though some channeling and tailing was observed, the disposable Sephadex G15 column packed and operated solely by the force of gravity yielded purified product. In fact, the observed 3-4 order-of-magnitude difference (FIGURE 4.7) was an initial indication that the purified labeled polymer had a radiochemical purity of at least 99%, if not higher. Subsequent experiments were performed to further improve the purification step.

4.4.2 Confirmation of Covalent Attachment Using Radio-High Performance Liquid Chromatography (HPLC)

The radio-HPLC experiments provided (FIGURE 4.8) additional evidence that radioiodine was covalently attached to the polymer, as well as evidence that the iodination reaction did not affect the bulk molecular weight characteristics of the polymer starting material. The fact that the radioiodine was spread throughout all polymer chain lengths in the starting mixture was important. This ensured that any activity measured for

a given sample would have equal contributions from all molecules in a given polymer sample. This result was achieved because the backbone was an alternating copolymer, with linker groups and their potential iodination sites in every repeat unit.

4.4.3 Effect of Iodination on Chemical Structure

Analytical GPC measurements of the backbone polymer molecular weight were performed to determine whether the iodination reaction had an effect on the chemical structure of the polymer (FIGURE 4.9). Any change in the molecular weight profile, whether gross or subtle, would be a direct result of the destruction of ester or ether bonds within the backbone of the polymer. Both of these oxygen-containing functional groups were considered the most likely targets of the oxidative conditions produced by the Iodination bead.

The standard reaction protocol, for initial concentrations of iodine and polymer elevated by a factor of ten, was shown to have a small, but measurable effect on the molecular weight profile of the backbone polymer. The slight shift toward longer elution volumes suggested a small decrease in the bulk molecular weight of the backbone polymer likely due to the conditions in the reaction. However, the shift was comparatively small and this fact, together with the sharp elution peak observed near the total column volume activity (FIGURE 4.6), provided strong evidence that the iodination reaction not only attached radioiodine to the polymer, but that it attached the radioiodine to intact polymer chains.

Unfortunately, these measurements were complicated by the requirement to freeze-dry the experimental samples for analysis in the organic mobile phase used in the available GPC system. This complication was evident by comparing the chromatograms

of freeze-dried polymer and raw polymer dissolved in THF (FIGURE 4.10). This experiment demonstrated that one of the liquid manipulation steps required for sample analysis produced the effect, albeit to a lesser extent, that was a potential outcome of the experiment. The effect of freeze-drying on the molecular weight profile did appear to be confined to the production of low molecular weight fragments at elution volumes greater than 23 mL.

In a second experiment, the oxidative conditions during the reaction were significantly elevated to determine whether conditions in the reaction could affect a significant change in the backbone polymer molecular weight (FIGURE 4.11). A one-thousand fold relative increase in oxidative species was achieved by increasing the concentration of cold iodine added to the reaction mixture with the backbone polymer and Iodination bead. A significant shift in the molecular weight profile was observed, which corresponded to a 60% reduction in weight-average molecular weight. This reduction in molecular weight could have been caused by degradation of the polymer backbone. However, it is also possible that the high concentration of iodine added to the polymer backbone may have affected the polymer retention by the GPC columns by changing the way in which the polymer interacted with the media.

4.4.4 Effect of the Iodination on Older Polymer Samples

Similar experiments were performed to assess the effect of the iodination on the chemical structure of older polymer samples (FIGURE 4.12). The resulting GPC measurements revealed complete degradation of the old backbone polymer upon exposure to the standard protocol with a tenfold increase in both polymer and iodine concentrations. These results suggested a potential mechanism for polymer breakdown. It

is well established that PEG oxidation occurs in humidified environments [40]. It is likely that the backbone polymer, which was stored for extended periods under ambient (i.e. humid) conditions, contained partially oxidized PEG subunits prior to use in this experiment (FIGURE 4.22). This partial oxidation could have made the backbone polymer more susceptible to the strong oxidative conditions of the iodination. Because the extent of this partial oxidation due to storage is related to the length, temperature, and moisture content of the exposure, polymer stability during iodination can be improved by storing polymer in a refrigerator and in the presence of a desiccant.

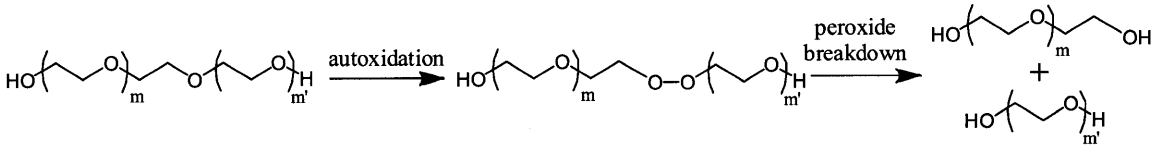

Figure 4.22. Chemical structure representation of the proposed mechanism for the degradation of the backbone polymer under oxidative conditions.

This proposed mechanism can be extended to the iodination reaction, wherein oxidative conditions enhance the degradation process, either by increasing the rate of peroxide formation or subsequent peroxide breakdown. Recall that each repeat unit in the backbone polymer is composed of the isophthalate linker and PEG900, the latter of which contains approximately 34 repeat units of ethylene oxide. The oxidative breakdown of just one of these many ether groups within the backbone will fracture the polymer chain.

Evaluation of the Standard Purification Protocol

4.4.5 GPC Analysis of Void Volume Fractions

The complete molecular weight profile of polymer 027 was recovered within elution volumes between 2-4 mL (FIGURE 4.13). This result implied that all lengths of backbone polymer in the sample added to the top of the column were excluded from the

pores of the Sephadex G15 media. The exclusion limit for this media was 1.5 kDa. As was observed for previous samples, small molecular weight fractions in the recovered, freeze-dried, and resuspended sample were likely generated during the freeze drying step. This experiment demonstrated that the activity measured in the standard protocol experiment (FIGURE 4.6) co-eluted with the breadth of the molecular weight profile measured for polymer 027. This fact was an additional piece of evidence indicating the successful attachment of radioiodine to the polymer.

4.4.6 Elution Profile of Free Iodine-125

The elution profile for free iodine-125 was measured in five different purification experiments, which covered 4 different media and 2 different column configurations (FIGURE 4.14). The results were used to evaluate the ability of each media to delay the elution of free, unbound iodine, which directly contributes to the radiochemical purity of the pooled labeled product. The significantly lower radioactivity concentration measured in the range between 2-4 mL made the Sephadex G25 (PD-10 and Disposaflex) and DEAE Sephadex columns most attractive for continued investigation. The promising results for the Sephadex G25 media experiments are consistent with the widespread use of PD-10 columns for purification of radioiodinated proteins found throughout the literature [1, 12, 13, 41, 42].

The sharp increase followed by a plateau in radioactivity concentration for the G10 and G15 experiments are an indication of some channeling or bypassing of the resin bed similar to that observed previously (FIGURE 4.7). The G10 and G15 exclusion limits (1 and 1.5 kDa, respectively) were the lowest (i.e. smaller pore sizes) of the media investigated. Although it does not seem likely that the lower exclusion limits themselves

can explain the observed bypassing behavior. One potential explanation may be incomplete swelling of the resin leading to small heterogeneities in the packed bed. While bypassing was observed to varying extents for all four experiments involving size exclusion media, the activity measured for the DEAE Sephadex was nearly at background levels until at least 6 mL of elution volume. This observation suggested that the charged groups of the DEAE media were able to compensate for any channeling or bypassing fluid dynamics through strong ionic interactions.

4.4.7 Elution Profile of Post-Reaction Mixtures Generated by the Standard Protocol

While a successful purification must delay the elution of free, unbound iodine-125, it must also allow for the recovery of the labeled product. The elution profiles for the post-reaction mixtures provided the information necessary to address this second requirement (FIGURE 4.15). For the G25 Sephadex, the five order-of-magnitude difference between the post-reaction mixture and free iodine elution profiles over the fractions pooled to yield the purified labeled sample (indicated by asterisks) were almost exclusively representative of iodine associated with the polymer and not unreacted, unpurified iodine. The PD-10, for which the labeled material was approximately three orders of magnitude greater than the free ^{125}I, also produced a product of >99.9% purity. Depending on the sensitivity of the end-use technique to free iodine impurities, this level of purity may be sufficient, which would make the PD-10 columns an attractive option because they arrive pre-packed with Sephadex G25 media.

Although DEAE-Sephadex yielded the labeled polymer with the greatest purity, the column conditions led to significant product loss during purification. Specifically, the buffer pH was not adjusted to (or beneath) the isoelectric point of the polymer. If the

polymer were to have been charge neutral or positively charged, the DEAE-Sephadex could have been operated in flow-through mode in which the labeled product would elute while the free, negatively charge iodide would bind to the DEAE. Because the iodination procedure is intended for a wide range of polymer formulations, one would likely have to determine the isoelectric point of each polymer formulation, of which there are many, and carefully control pH in order to maximize recovery of labeled material. There may also be stability issues at lower pH due to potential acid hydrolysis reactions of esters throughout the polymer.

Because the process was intended for use across a range of polymer formulations and it would be time-consuming to determine the pKa and appropriate buffer characteristics for each polymer formulation, it was determined that the Sephadex G25 in Disposaflex should be used as the universal media for the purification step due to its strong purity profile and general applicability. There may be opportunity to revisit the DEAE Sephadex either for applications that demand higher purity or once a small number of candidate polymer formulations are selected for intensive study.

4.4.8 Fractional Recovery

Although BSA is occasionally used in Sephadex purifications, particularly for high-adsorbing proteins, it did not appear to have any effect for our polymer system (TABLE 4.3). This result was not surprising due to the large amount of PEG in all of our polymer formulations. Finally, since the labeled polymer product solutions were frequently mixed with higher concentration, cold polymer solutions to produce the final labeled polymer for use in uptake or biodistribution studies, fractional recoveries greater than 0.90 were more than sufficient.

4.4.9 Labeling Yield

The results for the labeling yield experiments demonstrated that the initial polymer concentration added to the reaction mixture was the most significant factor in increasing yield (TABLE 4.4). There are some practical limitations associated with increasing the polymer concentration, including (1) limited solubility of heavily PEGylated polymers, especially those having higher molecular weights, (2) limitations in the availability of synthesized material, and (3) volume requirements in order to adequately submerge the Iodination bead in solution. These three limitations set the practical limit on initial polymer concentration at approximately 5-10 mg/mL.

The experimental labeling yield was also a function of total reaction time, although the effect appeared to be more asymptotic than that for polymer concentration. There were also practical limitations when considering an increase in reaction time, particularly with respect to degradation of the polymer by the oxidative conditions in the reaction. The longer reaction time increases the exposure of both the targeted sites on the aromatic ring and the functional groups susceptible to oxidative degradation to oxidizing species generated by the Iodination bead. In order to determine the proper reaction time, one would have to solve an optimization problem balancing yield and degradation requirements.

The insensitivity of yield to initial iodine activity was the primary reason that the particular kinetic model (first order in A, second order overall) was chosen as the appropriate description of the process yield (FIGURE 4.17). The R-squared value determined from the least-squared regression of the data, 0.93, indicated strong

agreement between the data and the theoretical model (FIGURE 4.18), which was particularly promising considering the relative simplicity of the model. Finally, the length of the activation period (currently 5 min in the standard protocol) is an additional variable that was not investigated.

4.4.10 Labeling Yield for Ornamented Polymers

The fractional labeling yield for ornamented polymers varied widely between 0.05-0.50. These were results compiled from production runs for a wide variety of polymer formulations. The data were examined to try and determine trends in the yield that corresponded to aspects of the chemical structure of the labeled polymers; other contributing factors complicated the picture. The most common issue was partial inactivation of the Iodination bead activity, which could only be determined after an iodination was completed. In all cases, the yield was more than sufficient to supply a breadth of *in vitro* update and *in vivo* biodistribution studies.

Although the optimum conditions may vary depending on the particular formulation, determining individually optimized conditions was infeasible due to the shear number of polymers investigated during the biological studies. A similar study would be advised before initiating any large-scale animal studies with a small number of lead candidate formulations.

4.4.11 Radiolabel Stability

The elution profile for polymer 027 stored for 6 mo at 4°C (FIGURE 4.19) demonstrated that the label on the polymer was stable over the duration of the storage period. Although one would probably not plan to store labeled material for extended time

periods due to activity losses associated with radioactive decay, this result provided information concerning the time-dependent reliability of the labeled polymer.

4.4.12 Considerations for Radiolabeling High Molecular Weight Backbone

The same radiolabel stability experimental procedure was performed on freshly labeled, high-molecular weight, ornamented polymer (FIGURE 4.20) that was synthesized for uptake and biodistribution studies. These measurements revealed that free, unbound iodine impurities were present in the sample 4 hr after the original reaction and purification. This could have been caused by experimental errors during purification of the original labeled product. This seems unlikely because this free iodine peak at t=4hr was observed for all of the polymer formulations in this high molecular weight series. From this it must be inferred that the effect is phenomenological and not procedural. To produce the effect, it is possible that some iodine had formed an association with the polymer that was strong enough to endure the purification but not strong enough to persist after 4 hr of storage.

The relatively higher molecular weight of the backbone polymer starting material (12 kDa vs. 3 kDa) was the primary difference in this sample in comparison to polymer 027, which did not exhibit this behavior. Recall that solubility decreases as molecular weight increases. Based on this, it was proposed that the strong association described in the previous explanation was somehow mitigated by local insolubilities in the higher molecular weight polymer.

For the second post-protocol purification (FIGURE 4.21B), the fact that the secondary peak was not observed at the total column volume, but slightly earlier, may suggest that the late elution volume activity was not caused by free iodine, but by

broadening or tailing of the labeled polymer peak. This would certainly be the case if the datum at elution volume of 6.5 mL was a low outlier that created a 'false positive' peak due to the discrete nature of the collected fractions.

Although the mechanistic explanation for the observed phenomenon was incomplete, the additional purifications of the high molecular weight polymer were ultimately able to produce radiochemically pure polymer to supply *in vitro* and *in vivo* studies. The additional purification steps reduced the overall process yield, the overall fractional labeling yields for the various high molecular weight polymers were approximately 0.05-0.10.

4.5 Conclusion

The preceding results represent the first demonstration that a nanoparticle-forming polymer that can be directly labeled with radioiodine using a standard protein-labeling technique without any additional chemical-alterations or intermediate reactions. The process has been characterized using a variety of chromatographic techniques, spectrophotometry, and radiometric measurements. These measurements have confirmed covalent, stable attachment of iodine isotopes, including ^{125}I, ^{124}I, and ^{127}I, to various polymer formulation.

A variety of purification media were investigated to assess their ability to retard the elution of free iodine while providing sufficient recovery of the labeled product for use in subsequent biological studies. Both G25 Sephadex and PD-10 columns provided excellent separation of labeled material from unreacted ^{125}I. The fact that PD-10 columns require comparatively little preparation makes them attractive for future use, particularly in non-research applications, such as in the clinic.

Reaction yields above 90% have been reported for many proteins [14] and small molecules [34] using various radioiodination methods. In this study, the tyrosine-like groups within polymer 027 are esterified, and further optimization is likely possible. Moreover, the specific activity of the labeled material, which is the key metric for diagnostic imaging applications such as PET or SPECT, can be increased as desired by increasing the initial activity of radioiodine added. Although this is not the most cost-effective method to achieve this aim, particularly considering the limited availability of isotopes like ^{124}I, the procedure as developed should provide radiochemical yields within an acceptable range.

The free iodine impurities observed in labeled and purified samples synthesized from high molecular weight backbone polymer was of concern. These results suggested that some molecular weight-related phenomenon created a subset of polymer-iodine associations that withstood the initial post-labeling purification only to dissociate less than four hours after the initial procedure. The exact mechanism for this behavior is unclear. Possibilities include high molecular weight-related adsorption of iodine by the polymer or increasing bond lability due to local insolubilities of the higher molecular weight polymer.

Overall, a broadly applicable process was developed to radiolabel a range of polymer formulations for use in biological studies, including *in vitro* cellular uptake, *in vivo* biodistribution, and live animal imaging by positron emission tomography (PET). Further polymer-specific improvements or condition adjustments may be necessary before cost-effectively translating the process to large-scale research or pre-clinical trials to improve product yield and related cost-effectiveness.

4.6 References

1. Moore, A., Medarova, Z., Potthast, A., Dai, G., *In vivo targeting of underglycosylated MUC-1 tumor antigen using a multimodal imaging probe.* Cancer Research, 2004. **64**(1821-1827).
2. Choi, H.S., Liu, W., Frangioni, J. V., *Renal clearance of quantum dots.* Nature Biotechnology, 2007. **25**(10): p. 1165-1170.
3. White, N.S., Errington, R. J., *Fluorescence techniques for drug delivery research: Theory and practice.* Adv Drug Delivery Rev, 2005. **57**: p. 17-42.
4. Benaron, D.A., *The future of cancer inaging.* Cancer and Metastasis Rev, 2002. **21**: p. 45-78.
5. Kukowska-Latallo, J.F., Candido, K. A., Cao, Z., Nigavekar, S. S., Majoros, I. J., Thomas, T. P., Balogh, L. P., Khan, M. K., Baker, Jr., J. R., *Nanoparticle targeting of anticancer drug improves therapeutic response in animal model of human epithelial cancer.* Cancer Research, 2005. **65**(12): p. 5317-5324.
6. Gu, F., Zhang, L., Teply, B. A., Mann, N., Wang, A., Radovic-Moreno, A. F., Langer, R., Farokhzad, O. C., *Precise engineering of targeted nanoparticles by using self-assembled biointegrated block copolymers.* PNAS, 2008. **105**(7): p. 2586-2591.
7. Rossin, R., Pan, D., Qi, K., Turner, J. L., Sun, X., Wooley, K. L., Welch, M. J., *64Cu-labeled folate-conjugated shell cross-linked nanoparticles for tumor imaging and radiotherapy: Synthesis, radiolabeling, and biologic evaluation.* J Nucl Med, 2005. **46**(7): p. 1210-1218.
8. Pirollo, K.F., Chang, E. H., *Does a targeting ligand influence nanoparticle tumor localization or uptake?* Trends in Biotechnology, 2008. **26**(10): p. 552-558.
9. Laverman, P., Dams, E. T. M., Oyen WJC., Storm, G., Koenders, E. B., Prevost, R., van der Meer, JWM., Corstens, FHM., Boerman, O. C., *A novel method to label liposomes with Tc-99m by the hydrazino nicotinyl derivative.* J Nucl Med, 1999. **40**(1): p. 192-197.
10. Lukyanov, A.N., Gao, Z., Mazzola, L., Torchilin, V. P., *Polyethylene glycol-diacyllipid micelles demonstrate increased accumulation in subcutaenous tumors in mice.* Pharmaceutical Res, 2002. **19**(10): p. 1424-1429.
11. Kojima, S., Andre, S., Korchagina, E. Y., Bovin, N. V., Gabius, H-J., *Tyramine-containing poly(4-nitrophenylacrylate) as iodinatable ligand carrier in biodistribution analysis.* Pharmaceutical Res, 1997. **14**(7): p. 879-886.
12. Dagdeviren, K., Unak, P., Bekis, R., Biber, F. Z., Akdurak, S., Ulker, O., Ergur, B., Ertay, T., Durak, H., *Radioiodinated magnetic targeted carriers (131I-MTC).* J Radioanalytical and Nucl Chem, 2007. **273**(3): p. 635-639.
13. Shokeen, M., Fettig, N. M., Rossin, R., *Synthesis, in vitro and in vivo evaluation of radiolabeled nanoparticles.* The Quarterly J Nucl Med and Molec Imaging, 2008. **52**(3): p. 267-277.
14. Adam, M.J., Wilbur, D. S., *Radiohalogens for imaging and therapy.* Chem Soc Rev, 2005. **34**: p. 153-163.
15. Serdons, K., Verbruggen, A., Bormans, G. M., *Developing new molecular imaging probes for PET.* Methods, 2009. **48**(2): p. 104-111.

16. Brands, B., Linden, O., Giammarile, F., Tennvall, J., Punt, C., *Clinical applications of newer radionuclide therapies.* European J Cancer, 2006. **42**(8): p. 994-1003.
17. Wadas, T.J., Wong, E. H., Weisman, G. R., Anderson, C. J., *Copper chelation chemistry and its role in copper radiopharmaceuticals.* Current Pharmaceutical Design, 2007. **13**(1): p. 3-16.
18. Shih, L.B., Thorpe, S. R., Griffiths, G. L., Diril, H., Ong, G. L., Hansen, H. J., Goldenberg, D. M., Mattes, M. J., *The processing and fate of antibodies and their radiolabels bound to the surface of tumor cells in vitro: A comparison of nine radiolabels.* J Nucl Med, 1994. **35**(5): p. 899-908.
19. Collingridge, D.R., Glaser, M., Osman, S., Barthel, H., Hutchinson, O. C., Luthra, S. K., Brady, F., Bouchier-Hayes, L., Martin, S. J., Workman, P., Price, P. Aboagye, E. O., *In vitro selectivity, in vivo biodistribution and tumour uptake of annexin V radiolabeled with a positron emitting radioisotope.* British J Cancer, 2003. **89**(7): p. 1327-1333.
20. Seevers, R.H., Counsell, R. E., *Radioiodination techniques for small organic molecules.* Chem Rev, 1982. **82**: p. 575-590.
21. Baldwin, R.M., *Chemistry of Radioiodine.* Appl Radiat Isot, 1986. **37**(8): p. 817-821.
22. Markwell, M.A.K., *A new solid-state reagent to iodinate proteins: conditions for the efficient labeling of antiserum.* Anal Biochem, 1982. **125**: p. 427-432.
23. Gillies, J.M., Prenant, C., Chimon, G. N., Smethurst, G. J., Perrie, W., Hamblett, I., Dekker, B., Zweit, J., *Microfluidic reactor for the radiosynthesis of PET radiotracers.* Appl Radiat Isot, 2006. **64**: p. 325-332.
24. Li, C., Yang, D. J., Kuang, L-R., Wallace, S., *Polyamino acid microspheres: Preparation, characterization and distribution after intravenous injection in rats.* Int J Pharmaceutics, 1993. **94**: p. 143-152.
25. Duncan, R., Kopeckova, P., Strohalm, J., Hume, I. C., Lloyd, J. B., Kopecek, J., *Anticancer agents coupled to N-(2-hydroxypropyl)methacrylamide copolymers.* British J Cancer, 1988. **57**: p. 147-156.
26. Pato, J., Mora, M., Naisbett, B., Woodley, J. F., Duncan, R., *Uptake and transport of poly(N-vinylpyrrolidone-co-maleic acid) by the adult-rat small-interstine cultured in vitro - Effect of chemical structure.* Int J Pharmaceutics, 1994. **104**(3): p. 227-237.
27. Macario, D.K., Entersz, I., Bolikal, D., Kohn, J., Nackman, G. B., *Iodine inhibits antiadhesive effect of PEG: Implications for tissue engineering.* J Biomed Mater Res, Part B, 2008. **86B**: p. 237-244.
28. Malik, N., Wiwattanapatapee, R., Klopsch, R., Lorenz, K., Frey, H., Weener, J. W., Meijer, E. W., Paulus, W., Duncan, R., *Dendrimers: Relationship between structure and biocompatibility in vitro, and preliminary studies on the biodistribtuion of 125I-labeled polyamidoamine dendrimers in vivo.* J Controlled Release, 2000. **65**: p. 133-148.
29. Deng, X., Yang, S., Nie, H., Wang, H., Liu, Y., *A generally adoptable radiotracing method for tracking carbon nanotubes in animals.* Nanotechnology, 2008. **19**: p. 075101.

30. Kumar, R., Shakil, N. A., Chen, M-H., Parmar, V. S., Samuelson, L. A., Kumar, J., Watterson, A. C., *Chemo-enzymatic synthesis and characterization of novel functionalized amphiphilic polymers.* J Macromolecular Science, 2002. **A39**(10): p. 1137-1149.
31. Kumar, R., Tyagi, R., Parmar, V. S., Samuelson, L. A., Watterson, A. C., Kumar, J., *Candida antarctica Lipase B catalyzed copolymerizations of non-proteinogenic amino acids and poly(ethylene glycol) to generate novel functionalized polyesters.* J Macromolecular Science, 2003. **A40**(12): p. 1283-1293.
32. Kumar, R., Chen, M-H., Parmar, V. S., Samuelson, L. A., Kumar, J., Nicolosi, R., Yoganathan, S., Watterson, A. C., *Supramolecular assemblies based on copolymers of PEG600 and functionalized aromatic diesters for drug delivery.* JACS, 2004. **126**: p. 10640-10644.
33. Zupan, M., Iskra, J., Stavber, S., *Room temperature regioselective iodination of aromatic ethers mediated by Selectfluor(TM) reagent F-TEDA-BF4.* Tetrahedron Letters, 1997. **38**(35): p. 6305-6306.
34. Yang, S.G., Kim, Y. H., *A practical iodination of aromatic compounds using tetrabutylammonium peroxydisulfate and iodine.* Tetrahedron Letters, 1999. **40**: p. 6051-6054.
35. Zhang, M.-R., Kumata, K., Maeda, J., Haradahira, T., Noguchi, J., Suhara, T., Halldin, C., Suzuki, K., *N-(5-fluoro-2-phenoxyphenyl)-N-(-[131I]iodi-5-methoxybenzyl)acetamide: A potent iodinated radioligand for the peripheral-type benzodiazepine receptor in brain.* J Med Chem, 2007. **50**: p. 848-855.
36. Hackel, B.J., *Fibronectin Domain Engineering*, in *Chemical Engineering*. 2009, M.I.T.
37. Hackel, B.J., Kapila, A., Wittrup, K. D., *Picomolar affinity fibronectin domains engineered utilizing loop length diversity, recursive mutagenesis, and loop shuffling.* J Molecular Biology, 2008. **281**(5): p. 1238-1252.
38. Scientific, T., *Instructions: Pierce Iodination Beads*. Received with Product, 2010.
39. Dawson, J.Z., *Physicochemical characterization of PEG-based comb-like amphiphilic copolymer structures for possible imaging and therapeutic applications*, in *Chemical Engineering*. 2008, MIT: Cambridge.
40. Kryuk, T.V., Mikhal'chuk, M., Petrenko, L. V., Nelepova, O. A., Nikolaevskii, *Promising inhibitors of poly(ethylene glycol) oxidation in aqueous solutions.* Pharmaceutical Chem J, 2002. **36**(1): p. 32-35.
41. Press, O.W., Shan, D., Howell-Clark J., et. al., *Comparative metabolism and retention of iodine-125, yttrium-90, and indium-111 radioimmunoconjugates by cancer cells.* Cancer Research, 1996. **56**: p. 2123-9.
42. Medarova, Z., Pham, W., Kim, Y., Dai, G., Moore, A., *In vivo imaging of tumor response to therapy using a dual-modality imaging strategy.* Int J Cancer, 2006. **118**: p. 2796-2802.

Physico-chemical and Biological Evaluation of EI3.4.3-Conjugated Polymers

5.1 Introduction

A number of circulating delivery systems have been developed in response to the need for efficient and selective drug transport to primary tumors and their metastases. Circulating delivery systems fall into three categories – liposomes, polymeric micelles, and dendrimers. These system are able to effectively circulate in the bloodstream by the addition of poly(ethylene glycol) (PEG) either by adsorption or chemical attachment. Addition of PEG to a delivery vehicle creates a dense 'conformational cloud' on the exterior conferring a level of stealth to the particle [1]. It is proposed that both the hydrophilic nature and the chain flexibility of PEG are necessary to avoid opsonization by plasma proteins and subsequent macrophage attack [2]. Interestingly, the PEG often serves a dual purpose in polymeric micelles, providing the hydrophilic 'head-group' necessary for micellization.

Liposomes are composed of phospholipids that form closed bilayer structures when in aqueous solution [3]. They are desirable as drug carriers due to their biocompatibility since they are typically constructed either using biological materials like phospholipids or made stealth via conjugation to PEG [4]. Moreover, liposomes can carry both hydrophobic and hydrophilic materials and be varied in size and surface properties by careful preparation. Liposomes are occasionally limited by issues of size; macrophage recognition and subsequent clearance occurs for particles above ~200 nm. Conjugation to PEG can slow macrophage detection, however this retarding effect decreases as liposome size increases [5]. Other issues include low stability, non-sterility, and poor encapsulation

efficiency [6]. Most recently, liposomes have found application in delivery of oligonucleotides for various therapeutic applications, including treatment of cancer [7].

Dendrimers are highly branched macromolecules synthesized by either divergent or convergent methods [8] yielding particles with a high number of surface units per area as well as an adaptable internal environment. An additional desirable property of dendrimers is their monodispersity [9]. Although dendrimeric drug delivery systems have achieved successes in *in vitro* studies [10], the synthesis is time-consuming, expensive, and poorly scalable. In spite of these constraints, the group of James Baker has published promising *in vivo* results using a PAMAM dendrimeric system targeted to the folic acid receptor overexpressed in the KB human cancer cell line. In this work, the chemotherapeutic methotrexate was delivered to mice bearing KB tumor xenografts. The dendrimers were covalently attached to both FITC and tritium for post-experiment histological assays. Their delivery system reduced methotrexate toxicity ten-fold and nearly doubled survival time in the methotrexate-treated group in comparison to controls. In their most recent work, the group of James Baker has begun using a new targeting ligand for the KB cell line, riboflavin [11, 12]. It is unclear why they have moved away from folic acid as a targeting ligand.

Additionally, current work in the Hammond lab in this department has focused on linear dendritic block copolymer micelles as targeted delivery systems. In this system, the linear block can be chosen to improve encapsulation, while the dendritic exterior provides many surface groups for addition of targeting capability. In recently published work and a current manuscript in preparation, dendritic block copolymers using folate as a targeted ligand and paclitaxel as the therapeutic agent have shown a significant increase

in efficacy relative to untargeted controls [13]. The synthesized particles were approximately 80 nm in diameter.

In addition to the circulating systems described above, a number of novel contrast agents have been developed, including superparamagnetic nanoparticles and quantum dots. Cross-linked iron oxide (CLIO) particles, which are powerful MRI contrast agents, are an example within the field of superparamagnetic nanoparticles for imaging [14]. The group of Anna Moore has used CLIO particles coated with dextran and targeted them to tumor cells demonstrating the utility of underglycosylated MUC1 as a target. They have also attached the fluorescent dye, Cy5.5, to CLIO particles to produce a multimodal system with capability for both MR and near infrared fluorescence imaging [15, 16]. Although these CLIO particles are not best suited for carrying therapeutic agents to tumors, a few methodologies converting iron oxide particles into simultaneous drug delivery and imaging vehicles have been reported [14]. Quantum dots are fluorescent nanocrystals that absorb a broad range of light while having a narrow and intense emission spectra tunable by altering the crystal size [17].

5.1.1 Polymeric micelles

Polymeric micelles [18-21] are amphiphilic colloids that spontaneously form aggregates composed of several amphiphilic molecules at concentrations and temperatures conducive for doing so. The critical micelle concentration (CMC) is the concentration above which micelle formation begins. Below the CMC, the amphiphilic sub-units remain solubilized. The resulting particles are typically of the order 5-100 nm in diameter and are usually spherical in morphology.

Polymeric micelles are composed of two major components. The interior, hydrophobic core is a hospitable environment for hydrophobic molecules, such as many contrast and therapeutic agents. The solubilization properties of this internal environment may be tailored to encapsulate these poorly soluble molecules. This encapsulation shelters the molecule from biological degradation while protecting healthy cells from the potentially cytotoxic agent. The second major component is the hydrophilic corona that surrounds the hydrophobic core. As previously described, this corona is often PEG, a molecule that gives a 'stealth' property to a circulating particle [19].

According to Torchilin, the ideal polymeric micelle system would have a diameter between 5 and 100 nm, demonstrate stability both *in vitro* and *in vivo* (low CMC and stability until reaching the desired destination), disintegrate into biocompatible materials after delivery, and encapsulate the desired agent in sufficient quantities [18]. The upper limit of the size recommendation is necessary in order to avoid clearance by the macrophages of the reticuloendothelial system (RES). The lower limit ensures that the delivery vehicle avoids rapid clearance by renal exclusion and that it takes advantage of the enhanced permeability and retention (EPR) effect where passive targeting is possible due to the 'leaky' vasculature often encountered in tumors [22-25]. It has been shown that non-targeted particles greater than 5-10 nm preferentially accumulate in primary tumors based on their size alone because of the EPR effect [23]. Acknowledging the tremendous advantages in size, stability, biocompatibility, and adaptability attributed to polymeric micelles, the next step is to then endeavor to construct delivery systems with the most ideal biodistribution and pharmacokinetic characteristics. Significant thought

has been devoted to the design of polymeric micelles since the seminal paper, including significant contributions from Omid Farokhzad [26] and Torchilin himself [27].

There has been a great deal of activity in the field of polymeric micelle drug delivery systems, particularly within the last 15-20 years. The following portrayal will both highlight the achievement thus far and introduce the breadth of investigation in this area of research.

The most extensive achievement in polymeric micelle delivery has been by the group of Kataoka in Japan. Their work began with poly(ethylene glycol)-poly(aspartic acid) block copolymers [PEG-PAsp] [28] and has since expanded to include other block copolymers (including PEG-poly(D,L-lactide) [PEG-PLA]), as well as polyion complex (PIC) micelles [20]. Most, if not all, of Kataoka's initial work does not include any targeting, instead relying on passive uptake via the EPR effect. The original PEG-PAsp system was chemically conjugated to the chemotherapeutic agent, doxorubicin, and this system is currently in clinical trials in Japan [29].

Work using paclitaxel-loaded poly(DL-lactide-co-glycolide) [PLGA] block copolymer nanoparticles targeted to the wheat germ agglutinin receptor have successfully increased tumor doubling time from 11 days in control animals to greater than 25 days for treated animals [30]. Poly(ethylene oxide)-block-poly(caprolactone) polymeric micelles have been used as siRNA delivery vehicles to successfully increase cellular susceptibility to the chemotherapeutic, doxorubicin [31]. Others have used polyester-based polymeric micelles to achieve increased cell death by increasing the cellular penetration of paclitaxel [32].

Most recently, Farokhzad and Langer have developed PLGA-b-PEG block copolymer nanoparticles encapsulating docetaxel [33] bioconjugated to an aptamer targeted to the prostate-specific membrane antigen. Aptamers are oligonucleotides that fold into conformations that bind to targets with high affinity and specificity [34]. In this study, the treatment group receiving the targeted, drug-loaded nanoparticles had 100% survival with 5/7 animals having complete tumor regression, whereas only 20% or less of control group mice survived during the 109 day experiment.

A number of shell cross-linked polymer micelle systems (SCKs) have been developed [35] in an attempt to improve micelle stability in the dilute conditions encountered upon injection *in vivo*. These SCKs are typically block copolymer micelles include polyion metal complex cores that may be chemically induced to form cross-links [36]. Moreover, these SCK systems have been used to try to alter the delivery pharmacokinetics. The group of Wooley has developed an extensive library of SCK micelles that may be used for controlled release via thermolytic cleavage of the cross-linking bonds [37-39]. Wooley and Wickline have collaborated to develop amphiphilic fluoropolymer SCKs for fluorine magnetic resonance imaging applications.

5.1.2 Targeted Delivery with the Alternating Amphiphilic Copolymer System

The initial work developing the *in vitro* methodologies to test the alternating amphiphilic copolymer system in targeted delivery applications was performed as part of the thesis of Dr. Michelle Miller in the Colton lab [40]. The thesis also investigated two different targeting pairs, both of which were discussed in the previous section: (1) EPPT/underglycosylated MUC-1, which was used in the work of Anna Moore, and (2) folate/folate receptor (FR).

Initial results with EPPT as targeting ligand showed an approximately two-fold increase in selective uptake of EPPT-containing polymer over polymer without EPPT in a receptor positive cell line. Focus shifted away from EPPT targeting ligand due to its exceedingly high cost of production. Folate was chosen a model system for its cost, affinity for its targeted receptor, and prevalence in the literature of the field. A library of polymers containing folate was synthesized by collaborators at UMass Lowell. A wide range of tests with these polymers were unable to show any increase in uptake due to the presence of folic acid targeting ligand. From these experiments, it was concluded that the measured uptake was due entirely to non-specific uptake. Dynamic light scattering measurements were performed to investigate the lack of specific uptake. The measurements revealed that the polymers, even those without hydrocarbon sidechains, were forming large aggregates of at least 200 nm (previous DLS measurements showed diameters ~10 nm). This aggregate formation was attributed to self-association of folate molecules, the consequence of which was a significant reduction in the exposed the targeting ligand. For these reasons, folate was abandoned as a targeting ligand.

5.1.3 The EI3.4.3 Peptide Targeting Ligand

After the disappointing results with folate as the targeting ligand, a new targeting ligand option was determined through collaboration with Dr. Benjamin Hackel from the laboratory of Professor K. Dane Wittrup in the Department of Chemical Engineering at MIT. In his thesis [41], Dr. Hackel developed protein engineering techniques to produce super-binding peptides for various targets. The tenth type III domain of the human fibronectin protein, which is a small, stable, single-domain, cysteine-free protein, was used as the scaffold for engineering.

The EI3.4.3 peptide was chosen from a library of super-binding peptide raised against the epidermal growth factor receptor (EGFR). The EI3.4.3 peptide was chosen from the available options due to its extremely low dissociation constant, K_D = 250 pM [42, 43], and its comparatively low number of tyrosine moieties in the binding domain, one.

5.2 Design of Targeted Polymers

In order to successfully design a polymer to maximize the uptake of targeted polymers into target-bearing tumors *in vivo*, it is imperative to understand how varying polymer components and resultant properties, including size, micellization, stability, and targeting ligand density, affects performance in four biological areas: (1) receptor binding, (2) access to the receptor, (3) time in circulation, and (4) the enhanced permeability and retention (EPR) effect.

One might propose an experimental design investigating targeted delivery building 'from the bottom-up.' The *in vivo* behavior of free EI3.4.3 peptide would be of primary interest after which the behavior of the peptide attached to a single PEG-linker repeat unit of the polymer would be studied. The next conceivable step in this bottom-up approach would be to synthesize a polymer that can form micelles, that is, a polymer having more than one repeat unit such that hydrophobic sidechains can be attached in addition to the peptide.

As the number of repeat units increase, the design choices, which include the polymer molecular weight, proportional substitution of the backbone with targeting and hydrophobic groups, the nature of the hydrophobic groups themselves, and the length of the spacer molecule connecting the peptide to the backbone, increase substantially and

the bottom-up design approach becomes less useful. Therefore, a systematic, conceptual evaluation of the various design parameters is needed in order to design a study that effectively assesses the performance of the targeted polymers.

5.2.1 Targeting Density and Molecular Weight

The density of targeting peptides within the polymer is unquestionably a variable of interest when designing a targeted delivery system. There are three interdependent variables that must be considered: (1) the number of linkers per chain (or the backbone polymer MW), (2) the number of peptides per chain, and (3) the percent of sidechains substituted with peptides. The interrelatedness of these three variables is illustrated in (FIGURE 5.1):

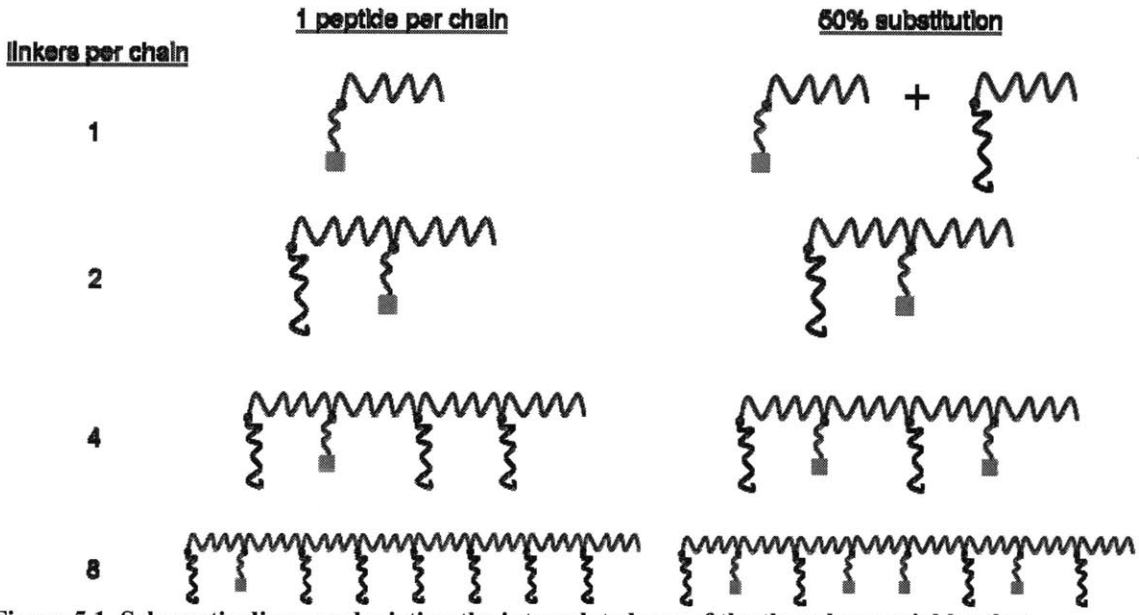

Figure 5.1. Schematic diagram depicting the interrelatedness of the three key variables that determine the targeting density: the number of linkers per chain, peptides per chain, and percent substitution. The linkers (circles) can only be substituted with so many peptides (squares) before the number of hydrophobic sidechains is reduced to the point where micelles can no longer form.

Holding the number of peptides per chain constant and increasing the linkers per chain (MW) decreases the percent substitution. Micelle formation creates an additional complicating factor because the number of peptides per micelle depends on the

aggregation number. If the aggregation number did not change, then the conversion would be straightforward. However, the micellization behavior could be a function of the polymer MW or the percent substitution of peptides, or both.

Changing the percent substitution of peptides also affects the hydrophobicity:hydrophilicity ratio of the polymer since greater percent peptide substitution means fewer sidechains can be hydrophobic. This may also have an affect on micellization behavior and therefore makes this ratio an additional potential variable since there is the capability of adding PEG groups of various lengths as sidechains, without targeting peptides. However, considering the already relatively low amount of hydrophobicity in the amphiphilic polymers as they are currently designed (as seen readily in the schematics above), one might instead consider varying the length of the hydrocarbon (or perfluorocarbon) sidechains to increase the relative hydrophobicity of the amphiphilic polymers.

There are many possible levels for the three dependent variables beyond what is depicted in the preceding figure. TABLE 5.1 provides the various options in a useful layout for experimental design. The highlighting and dotted lines on the table identify potential series for investigation. An investigation focusing on the effect of the backbone polymer MW would follow one (or more) of the vertical series. A study investigating the effect of the number of peptides per chain would follow one (or more) of the horizontal series. Finally, if the polymers within the selected horizontal and vertical series are chosen properly, the data from these experiments can be used to evaluate the effect of the third dependent variable, the percent of sidechains substituted as peptides.

Table 5.1. The potential design space for the investigation of the targeting ligand density on a polymer having variable molecular weight.

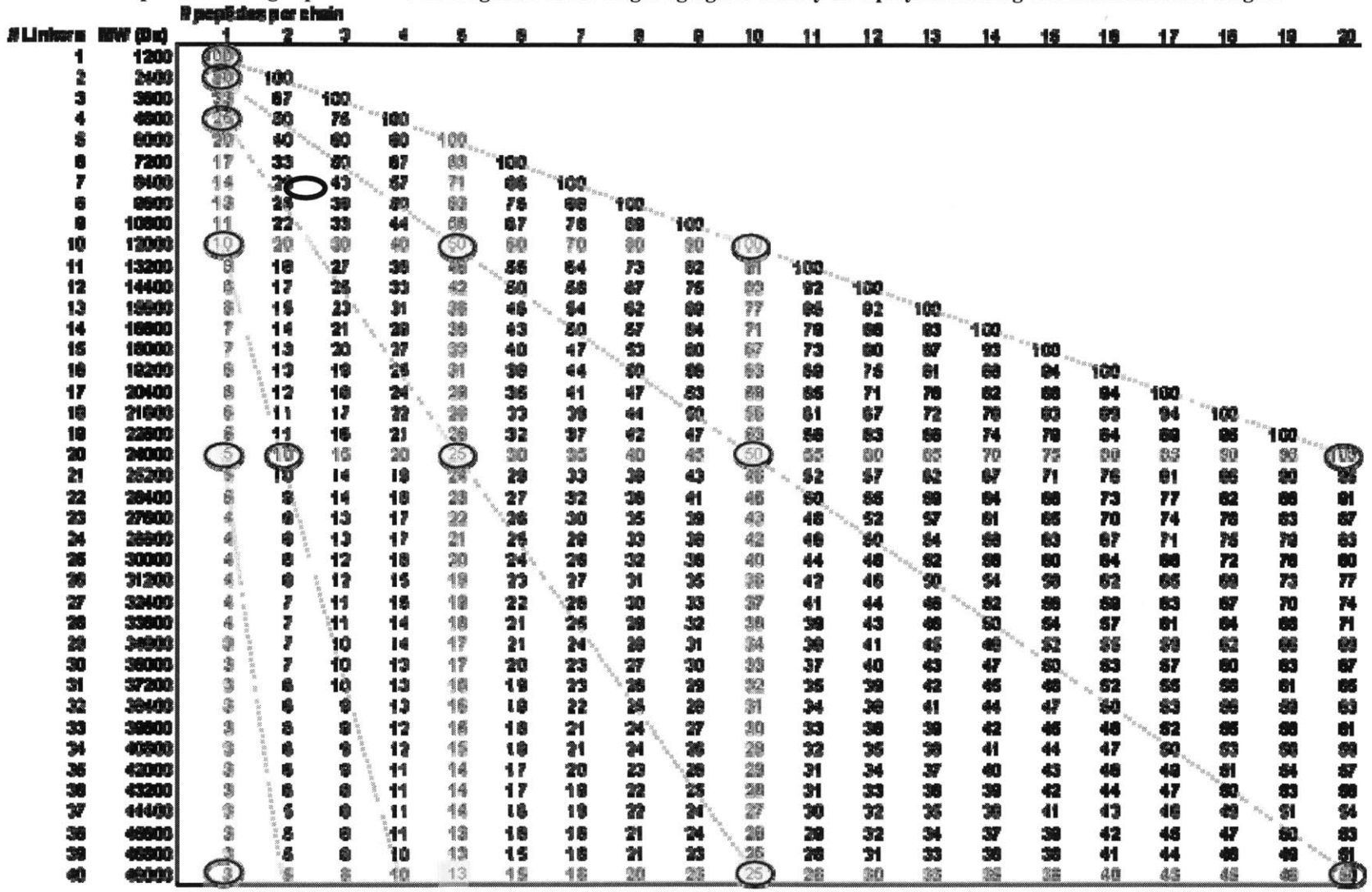

The circled values within the table represent a potential large study to comprehensively investigate the affect of polymer MW, peptides per chain, and percent substitution of peptide groups. In total, there are fourteen experimental levels circled. There is also the option to synthesize identical polymers without the targeting peptide attached as negative controls, which would immediately double the proposed polymer library to twenty-eight. Considering the fact that study of other potential variables, including sidechain identity and spacer length, are not included in reaching this value, it is clear that, although experiments studying the performance of polymers compassing all the circled levels would be ideal, significant reduction in scope is necessary. The other variables will also be considered in detail before doing so.

5.2.2 Hydrophobic Sidechain Identity

There are also a number of options for the identity of the sidechains on the remaining, unreacted linker hydroxyl groups. Hydrocarbon or perfluorocarbon chains can be added to impart amphiphilicity and the ability to form micelles. The linker hydroxyls can also remain unreacted (termed 'no sidechains'). Therefore, the identity of the remaining sidechains determines the physico-chemical properties of the synthesized polymer. Previous experiments by Jin Zhou Dawson revealed some trends. In particular, perfluorocarbon particles had critical micelle concentrations (CMC) about one order-of-magnitude lower than hydrocarbon particles. Additionally, particles with hydrocarbon sidechains were slightly larger than those with perfluorocarbons.

5.2.3 Spacer Length

The length of the PEG segment connecting the targeting peptide to the backbone polymer is another variable for consideration. Geometric modeling completed by Michelle Miller revealed the potential importance of spacer length, particularly for targeted particles. To summarize, the amount of area sampled by a targeted delivery system, for example one probing the cell surface for the targeted epitope, is directly related to both the particle size and spacer length. Using geometric arguments, it can be shown that for a given particle size, the number of targeting moieties available to participate in targeting events increases drastically with spacer length until a threshold is reached and strongly diminishing marginal returns persist.

5.2.4 Experimental Strategy

Before any of the previously described variables could be investigated, the first step was to test the EI3.4.3 peptide/EGFR targeting pair with our polymer system. Therefore, initial experiments were designed to determine whether the presence of the targeting ligand increased the uptake of our polymers *in vitro* relative to untargeted controls. Having achieved this, the ligand density and hydrophobic sidechain identity were selected as the variables of primary interest. PEG3400 was chosen as the spacer length since it was deemed suitably long to avoid any spacer length-related limitations.

In order to vary the ligand density (number of peptides per chain) over a wide range while still having sufficient linker hydroxyls available for substitution with hydrophobic groups, the molecular weight of the backbone polymer had to be increased. Using the backbone polymer produced in the Protherm (see Polymerization chapter), a high throughput, preparative gel permeation chromatography fractionation process was

developed to supply high molecular weight, low polydispersity backbone polymer for the EI3.4.3-conjugated polymer synthesis.

A library of EI3.4.3 polymers, together with their untargeted control polymer counterparts, was synthesized. These polymers were tested in a range of experiments, including dynamic light scattering to determine particle size distributions, *in vitro* uptake, and *in vivo* biodistribution and blood circulation studies.

5.3 Materials and Methods

5.3.1 Materials

All study polymers were synthesized as described in Chapter 2: Chemical Synthesis of Alternating Amphiphilic Copolymers. With the exception of backbone polymer synthesis, which was completed by the author, all chemical synthetic steps were performed in the laboratory of our collaborator, Dr. Arthur Watterson at the University of Massachusetts – Lowell. Unless otherwise noted, all polymers were weighed before dissolution in phosphate buffered saline (PBS, Mediatech, Inc.) to create concentrated stock solutions of 3-5 mg/mL. When the amount of polymer to be weighed was small, particularly for quantities less than 20 mg, a vial was weighed and deionized water was added. The polymer (typically about 10 mg) was dissolved into solution by pipetting up and down and removed from the vial. Any remaining solution not removed from the vial (typically a very small amount) was allowed to evaporate. The vial was weighed again and the difference between the initial and final weights was equal to the amount of polymer that had been dissolved in solution. Free peptide concentration was determined using the bicinchoninic acid (BCA) assay (Pierce Chemical) as described by the

manufacturer. Polymer radiolabeling was performed according to the protocol described in the Radioiodination chapter.

5.3.2 Backbone Polymer Fractionation by Preparative Size Exclusion Chromatography

High molecular weight backbone polymer was produced and isolated from reaction in the Protherm (500 rpm, molecular sieves) as described in the Polymerization chapter. The deionized water used as the chromatography mobile phase was also filtered using 0.2 μm 1L polyester sulfone (PES) filter units (Corning, Lowell, MA). The filtered water was degassed by applying vacuum while mixing and agitating with a magnetic stirring bar.

Polymer fractionation was performed using an AKTA Explorer preparative liquid chromatography system (GE Lifesciences, Piscataway, NJ) equipped with a high-prep Superdex 75 26/60 size exclusion column (also GE). These GPC/size exclusion experiments were performed on a different chromatography system with a different column than the GPC system used to analyze the backbone polymer molecular weight. The column and system pumps were much larger to increase throughput. This column is an off-the-shelf product pre-packed with Superdex size exclusion media. The 26/60 designation refers to a column having a 26 mm diameter and 60 cm bed height. These dimensions correspond to a total bed volume of 318.6 mL. The flow rate for all column operations was 1 mL/min. The AKTA Explorer system was monitored with a UV/vis detector (λ = 250 nm) and equipped with an automated fraction collector. The Superdex column was equilibrated with 3 column volumes (CV) of filtered, deionized water at the beginning of each run.

5.3.3 Evaluation of Preparative GPC for Backbone Polymer Fractionation

The Hi-prep Superdex column was studied for its potential use in fractionating the backbone polymer. The elution profile for backbone polymer was measured to evaluate the performance of this system. Because the preparative size exclusion column was packed with resin having variable pore sizes, polymer chains of different lengths would have different path lengths through the column. The goal, therefore, was to determine to what extent the Superdex column was able to spread the range of polymer molecular weights across a breadth of elution volumes.

In this experiment, high molecular weight backbone polymer produced in the Protherm (10 mg/mL in deionized water) was filtered using a 0.2 μm Acrodisc Supor® syringe filter units (Pall Corporation, Port Washington, NY). A total of one milliliter of this filtered sample was injected onto an equilibrated Superdex column via the injection valve on the AKTA Explorer. Fractions of varying elution volumes were collected, freeze dried, resuspended in tetrahydrofuran (THF), and analyzed using the Waters analytical GPC system described in the Polymerization chapter. Therefore, the analytical GPC was used to determine the molecular weight distribution of the fractions collected from the preparative GPC.

5.3.4 Development of a High-Throughput Fractionation Process

The fractionation process should also be capable of processing a large quantity of raw material into discrete fractions. To this end, the largest available column was purchased to maximize capacity and the flow rate was set to the highest value possible that also avoided the pressure limit for the column (1 mL/min). The remaining variables available for increased throughput were the concentration and total volume of the load

material and the scheduling of successive injections. The elution profile for the preparative GPC measured according to the previous section, together with the AKTA Unicorn method editor, was used to develop a method that minimized downtime between success injections. Also, for these experiments, the high molecular weight backbone polymer product was dissolved in deionized water at a concentration of 100 mg/mL and filtered using 0.2 μm Acrodisc Supor® syringe filter units. The developed method was used to perform a series of injections of high molecular weight Protherm-produced backbone polymer (3 mL/injection, 100 mg/mL). As was the case for the flow rate, the injection volume was set to the maximum possible without exceeding the pressure limit for the column. Each subsequent elution was fractionated by the fraction collector.

5.3.5 Dynamic Light Scattering

The particle size distributions of the various polymers studied were measured by dynamic light scattering (DLS). Stock polymer solutions were diluted to 0.5 mg/mL in phosphate buffered saline and filtered with 0.2 μm Acrodisc Supor® filters. The filtered solution was immediately transferred to BRAND disposable UV cuvettes (BrandTech, Essex, CT) and placed in a ZetaPALS (phase analysis light scattering) system (Brookhaven, Holtsville, NY). Samples were interrogated for one minute with at least 10 replicates for each polymer. Measurements were repeated, as many as 30 total times, until a steady response was achieved. Aside from the number and length of the measurement periods, the ZetaPALS system required only two additional parameters. (1) The system was instructed that the sample was aqueous, from which the appropriate fluid properties, including viscosity and refractive index, were determined from a database within the software. (2) The dust filter was turned off, which was possible because samples were

filtered directly into a clean cuvette immediately before measurement. Measurements performed with and without the dust filter showed no difference in particle size distribution, which confirmed the cleanness of the samples.

The accuracy of the ZetaPALS equipment was confirmed using dextran standards with known particle sizes of 20, 50, and 100 nm (Corpuscular, Cold Springs, NY).

5.3.6 Cell Culture, Lines and Media

All reagents were purchased from commercial sources. Dulbecco's minimum essential media (DMEM), fetal bovine serum (FBS), penicillin-streptomycin solution (pen-strep, 10,000 IU/mL), trypsin EDTA (1X, 0.25% trypsin/0.53 mM EDTA in HBSS), phosphate buffered saline (PBS, 1X), Hank's buffered salt solution (HBSS), and distilled deionized sterile water were purchased from Mediatech, Inc (Manassas, VA). Eagle's minimum essential media (EMEM) was purchased from American Type Culture Collection (ATCC, Manassas, VA). Guava Viacount assay kit was purchased from Guava Technologies/Millipore (Billerica, MA).

A431NS cells (epidermoid carcinoma, EGFR-positive) and MCF7 (breast adenocarcinoma, EGFR-negative) cells were purchased from ATCC and cultured in DMEM and EMEM, respectively. All cell growth media were supplemented with 10% (v/v) FBS and 1% (v/v) pen-strep. Cells were grown at 37 °C in a humidified atmosphere containing 5% CO_2.

5.3.7 Cellular Uptake Measurement with [^{125}I]*-polymer*

This procedure was originally developed and described in the thesis of Michelle Miller [40]. Cells were grown in their respective supplemented media, harvested with trypsin EDTA (1X, 0.25% trypsin/0.53 mM EDTA in HBSS) one day prior to

experimentation, and seeded in 96 well plates ($1x10^6$ cells/mL, 100 μL/well). All passage numbers were less than 20. Plating at this cell density resulted in wells that had just reached confluency upon initiation of each cellular uptake experiment.

Cells were incubated with either polymer (0.5 mg/mL) or various concentrations of free EI3.4.3 peptide (5-500 nM) that had been labeled with radioiodine[^{125}I] at 37 °C in a humidified atmosphere with 5% CO_2. Samples were taken after different lengths of incubation. The polymer or peptide was dissolved in the proper cell media for each respective cell line as required. Experiments were performed in triplicate wells whenever possible; however, material limitations for a small number of polymers required that only duplicate wells were used in these rare cases.

At designated times, the solution was removed by pipette and cells were washed three times with 100 μL PBS. Cells were harvested by adding 100 μL of trypsin EDTA (1X, 0.25% trypsin/0.53 mM EDTA in HBSS) to each well. After incubation at 37 °C for at least 15 min, the entire well volume was transferred to radioimmunoassay (RIA) tubes (VWR Scientific, Philadelphia, PA) and assayed for radioactivity on a Cobra II Auto Gamma counter (Perkin-Elmer/Packard, Waltham, MA). Samples were measured for 5 min each. The activity of each sample was measured in cpm and converted to mass using the individual polymer specific activity.

Polymers or free EI3.4.3 peptide were labeled according to the standard protocol as described in the Iodination chapter. In the iodinations performed to supply this study, the initial concentration of the polymer was 5 mg/mL while that for free EI3.4.3 peptide was 1 mg/mL. Between one and two millicuries of activity were added at the beginning of each labeling procedure. The remaining steps in the procedure were identical to those

described for the standard protocol. The specific activity of each labeled material was known (typically 0.1-1 mCi/mg).

Wells containing cells, but with no polymer added, were maintained to control for cell growth during the course of the experiment. At the designated times, these wells were also washed with PBS (3x), harvested with trypsin EDTA as above, and counted using the Guava Viacount method. For experiments with 4 hr durations, the amount of cell growth measured was very small, typically less than 2-3%. For the few experiments with 24 hr durations, the longest time frame investigated in this study, the total cells measured in the control wells increased by approximately 40%

The calculated polymer masses and cell count measurements were combined to determine the mass of polymer per cell. The procedure was identical for the EI3.4.3 peptide studies.

5.3.8 Cell Counting

Trypsinized cells were stained using Guava Viacount assay solution. Data were acquired on a Guava Personal Cell Analysis (PCA) flow cytometer. Each sample was run in triplicate and 1000 events were acquired using the Guava Viacount software. The dilution factor and initial volumes of each sample were used to calculate the total number of cells.

5.3.9 Biodistribution and Blood Circulation in a Mouse Model of Human Cancer

Female immunodeficient mice (*nu/nu*, <42 days) were purchased from Charles River Laboratories (Wilmington, MA). Mice received subcutaneous injections of A431NS tumor cells in their rear flank ($1x10^6$ cells/inj, 50 μL HBSS/injection). Once tumors grew to approximately 0.5 cm in diameter (estimated by eye), typically after 10-

14 days, mice were injected intravenously via the tail vein with ^{125}I-labeled polymer (2 mg/mL, 100 μL PBS/injection, specific activity: 0.1-1 mCi/mg) and sacrificed at designated time points. In addition to the excised tumor, the following organs were harvested and weighed immediately after sacrifice: liver, spleen, kidneys, stomach, colon, heart, lung, brain, and tail. Blood samples were taken from the thoracic cavity using a graduated, heparinized capillary tube (VWR Scientific, Philadelphia, PA).

The harvested samples were assayed for radioactivity on the COBRA II Auto-Gamma counter. Measurements of labeled polymer solutions of known concentration were also performed to control for sample-to-sample variations in specific activity. Based on these measurements, the percent injected dose in organ (*%ID*) and percent injected dose per gram of tissue (*%IDPG*) were calculated as follows:

$$\%\mathrm{ID} = \frac{a}{a^{*}_{tot}}(100\%) \tag{1}$$

$$\%\mathrm{IDPG} = \frac{\%\mathrm{ID}}{m} \tag{2}$$

where $_i$ is the mass of the organ or tissue, a is the activity measured in an organ and a_{tot}^{*} is the corrected total injected activity, which can be expressed as:

$$a^{*}_{tot} = a_{tot} - a_{tail} \tag{3}$$

where a_{tot} is the total activity in the syringe and a_{tail} is the activity measured in the tail. By subtracting the tail activity, the total initial injected activity in the circulation was corrected for dose remaining in the tissue interstitia of the tail. Blood circulation data were calculated only as %ID.

All animal experiments were performed in accordance with protocols approved by the Committee on Animal Care in the Department of Comparative Medicine at the

Massachusetts Institute of Technology. Additional animal studies were also performed in collaboration with former Colton group member, Dr. Michelle Miller. The results of these studies, which focused on other polymers and, in particular, other biomarker targets, were presented in Dr. Miller's thesis [40].

5.3.10 Comparison of in vivo Results to Semi-Empirical Model Predictions

Due to the complexity of the biological system, it is difficult to predict the behavior of a targeted circulating delivery agent *a priori*. To address this difficulty, Schmidt and Wittrup have developed a tumor targeting compartmental model [44]. In the model, which predicts the tumoral accumulation as a function of time post-injection in mice, only two physical characteristics of the targeted agent are required: the hydrodynamic radius and the binding affinity (K_D). This model was used as one tool to evaluate the *in vivo* biodistribution results for the alternating amphiphilic copolymer micelles relative to those found in the literature or estimated by current theoretical descriptions of tumor targeting.

The binding affinity contributes to the model by describing the active targeting contribution to tumoral uptake. The hydrodynamic radius is used to calculate a variety of mass transport parameters, including the permeability across the tumor capillary wall, diffusivity within the tumor, available volume fraction within the tumor for mass transport, and the plasma clearance rate [44]. Interestingly, while a small molecule may benefit from increased rates of mass transfer into and within the tumor, it also suffers from increased rate of clearance from the plasma by the renal system. Conversely, larger molecules or particles will have an increased circulation half-life due to a lower clearance

rate, but will also have a decreased rate of tumoral penetration because of their large effective diameter.

In their work, Schmidt and Wittrup used structural and empirical models to estimate the mass transfer parameters as a function of hydrodynamic radius. A two-pore representation of the tumor interstitial space was used to estimate the interstitial diffusivity, fluid volume fraction, and vascular permeability [45]. An empirical model was used to estimate the renal and non-renal clearance rates of circulating particles. The theoretical predictions according to the structural model were very comparable to experimental data compiled from the literature for multiple classes of molecules and particles (small peptides, PEG chains, and liposomes) covering a range of effective molecular weights (1-80 nm). The plots presented in Figure 1 of the cited paper were used to estimate the four mass transfer parameters for three different cases: (1) free EI3.4.3 peptide (MW = 12.5 kDa), and particles having hydrodynamic radii of (2) 5 nm and (3) 10 nm (TABLE 5.1).

Table 5.1. Size-dependent mass transfer parameters estimated according to the structural and empirical models of Schmidt and Wittrup. The pore diffusivity, D_{pore}, accessible void fraction, ε, capillary permeability, P_{pore}, and plasma clearance rate constant, k_{clear}, were estimated for three cases: free EI3.4.3 peptide and particles having hydrodynamic radii of 5 and 10 nm.

Case	D_{pore} (cm^2/s)	ε	P_{pore} (cm/s)	k_{clear} (1/hr)
Free Peptide	$7x10^{-7}$	0.34	$9.27x10^{-7}$	5.1
R = 5 nm	$2.4x10^{-7}$	0.23	$3.74x10^{-7}$	0.20
R = 10 nm	$3x10^{-8}$	0.075	$2.0x10^{-7}$	0.05

In addition to the size-dependent mass transfer parameters, experiment-related information is required to generate model predictions for direct comparison. These experimental parameters include the dose in μg, the surface concentration of the targeted antigen (EGFR in this case), the binding affinity of the circulating agent for the antigen,

the cellular internalization half-time, and the radiolabel catabolism and efflux half-time for ^{125}I. These figures, which were determined either according to experimental procedure or from cited literature, are summarized in TABLE 5.2.

Table 5.2. Size-independent parameters required by the tumor targeting compartmental model. The binding affinity was varied to higher values of K_D to account for potential steric effects or binding site occupation by ^{125}I.

Parameter	Value or Range	Source
Dose	200 μg	Exp.
Antigen Conc.	$2.5x10^6$ receptors/cell	[46]
Affinity	250 pM, 250 μM, 250 mM	[41]
Cellular Internalization Half-Time	1 hr	[41]
^{125}I Catabolism and Efflux Half-Time	2 hr	[47]

The parameters summarized in TABLES 5.1 and 2 were used as inputs in the tumor targeting compartment model. Schmidt and Wittrup have generously provided an online applet for the calculation of the model prediction (http://tumormodel.org/). This applet was used to generate model predictions for three different agent classes (free peptide, 5 nm radius, and 10 nm radius) and three different binding affinities (250 pM, 250 μM, 250 mM). The three cases were studied to account for some of the possible configurations present in our biodistribution studies, while the three binding affinities were studied to account for potential disruptions in binding due to steric effects or attachment of ^{125}I to the tyrosine in the binding domain.

5.4 Results

5.4.1 Polymer Naming Convention

A naming convention was developed to identify the polymers investigated in the targeted delivery studies. In general, the chemical structure of the polymers studied consisted of free hydroxyls on the backbone polymer linker group substituted with either a hydrophilic or hydrophobic sidechain to varying levels (FIGURE 5.2). The hydrophilic sidechain consisted of a hydrophilic spacer group (either PEG3400 or triethylene glycol, TEG) and, for targeting polymers, an EI3.4.3 at the chain terminus. The percentage of linker hydroxyls substituted with hydrophilic groups was defined as X%. The balance of the linker hydroxyls, (100-X)%, were substituted with either hydrocarbon or perfluorocarbon hydrophobic sidechains (R).

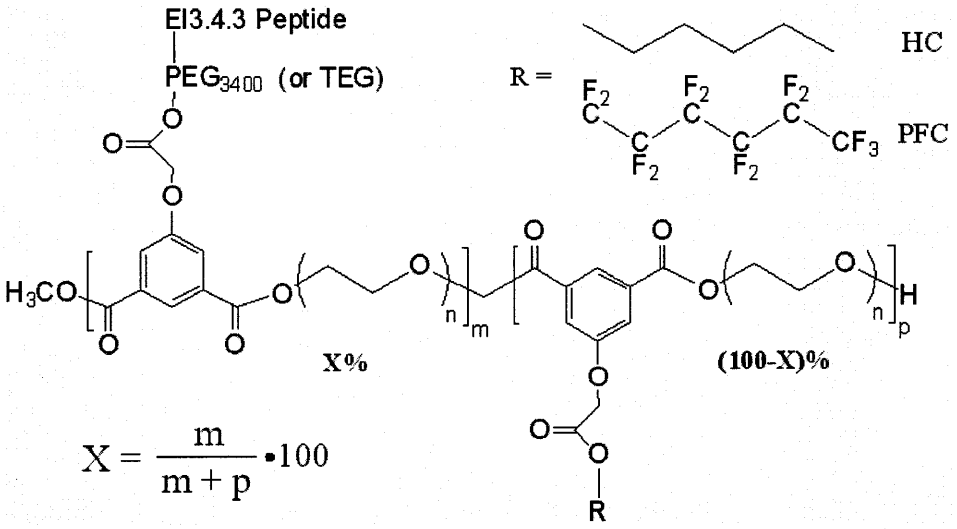

Figure 5.1. General chemical structure of the polymers investigated in the targeted delivery studies. The polymers were substituted X% with hydrophilic spacer groups (either PEG3400 or triethylene glycol, TEG). The remaining substituted groups are hydrophobic sidechains, R, in the form of hydrocarbons (HC) or perfluorocarbons (PFC).

The naming convention for EI3.4.3-conjugated polymers follows the form: X+, R, where X is the percent of sidechains substituted with hydrophilic spacer groups and R is the identity of the hydrophobic groups attached to the remaining (100-X)% linker

hydroxyls. The plus sign indicates that the polymer contains the EI3.4.3 peptide. For untargeted polymers, the plus sign is replaced with a minus sign ('-'). Finally, because all but two of the polymers studied contained PEG3400 as the hydrophilic spacer group, the identity of the spacer was not included in the polymer name. The two polymers with the triethylene glycol spacer (TEG) will be indicated as such. Therefore, a polymer designated X=10+, PFC would consist of 10% sidechains with EI3.4.3-conjugated PEG3400 spacers and 90% sidechains as perfluorocarbon chains.

5.4.2 In vitro Targeting with EI3.4.3-conjugated Polymers – Initial Study

As described in the Introduction to this chapter, the EI3.4.3/EGFR targeting pair was an attractive candidate for targeted delivery applications, particularly due to the very high binding affinity (low K_D) of the engineered targeting ligand. To evaluate whether this targeting pair would be viable for use with our polymer system, a small set of four polymers were synthesized and tested in *in vitro* uptake studies. If the targeted, EI3.4.3-containing polymers in this initial study showed increased, selective uptake relative to untargeted controls, then significant further study with this targeting pair would be justified.

Four polymers were synthesized with 10% of available sidechains substituted as PEG3400 or TEG spacers, either with or without EI3.4.3 peptide attached. The remaining linker hydroxyls (90%) in all four polymers were substituted with hydrocarbon sidechains, which imparted amphiphilicity to the molecules. The backbone polymer starting material, which was produced before the molecular weight increases were realized in the Protherm, was produced in a mechanically stirred flask with molecular sieves present and had the following molecular weight characteristics: $M_n = 5.2$, $M_w =$

7.2, PDI = 1.34. A summary of the polymers investigated in this initial study, including the molecular weight attributes, peptides per polymer chain, and hydrodynamic diameters as measured by dynamic light scattering, is presented in TABLE 3. Similar tables will be presented for subsequent sets of polymers studied. The polymer chain number-average molecular weights include the backbone, sidechains (PEG spacer and hydrophobic groups) and peptide, if present.

Table 4.3. Four polymers investigated during the initial study of the EI3.4.3/EGFR targeting pair with our polymer system. The polymer chain number average molecular weight, M_n, was calculated based on the components in the chemical structure. The number of peptides per chain was estimated assuming approximately five repeat units per backbone polymer chain based on a backbone polymer molecular weight of 5.2 kDa. The hydrodynamic diameter was determined by dynamic light scattering (see FIGURE 3).

Polymer	Spacer	Polymer Chain M_n (kDa)	Peptides per Chain	Hydrodynamic Diameter (nm)
X=10+, HC	PEG3400	15.0	0.5	4.5
X=10-, HC		8.7	0	4.5
X=10+, HC	TEG	11.7	0.5	8.0
X=10-, HC		5.5	0	10.0

The particle size distribution for the X = 10+, HC polymer with PEG3400 spacer at a concentration of 0.5 mg/mL in PBS was measured by dynamic light scattering (DLS) is presented in both bar graph (FIGURE 2A) and linear (2B) representations. The linear graph is a direct reproduction of the bar graph data in a different format, which allows for direct comparison of more than one particle size distribution at once. The particle size distributions for the polymers with PEG3400 (FIGURE 5.3A) and TEG (3B) spacers were also measured by DLS.

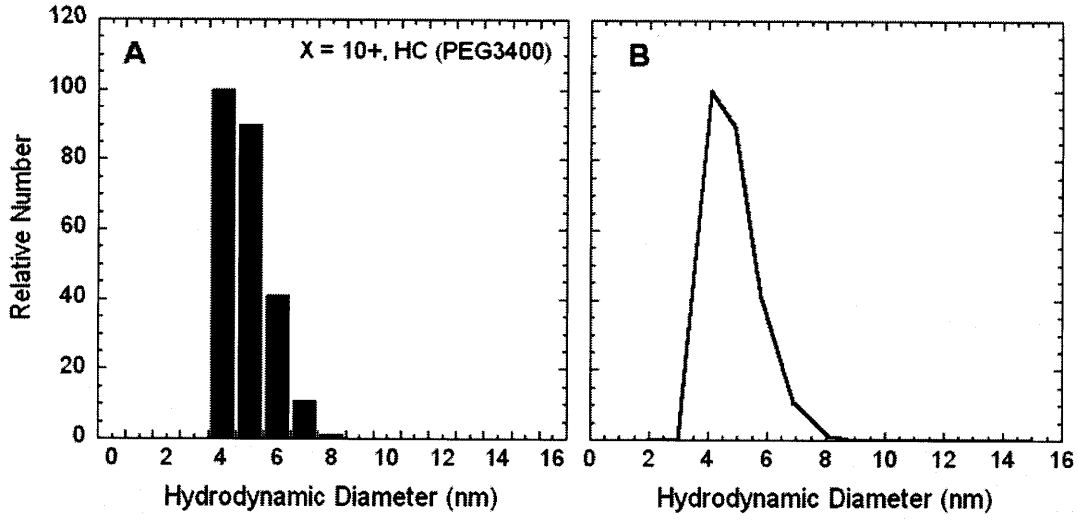

Figure 5.2. Particle size distribution of the X=10+, HC (PEG3400 spacer) polymer measured by dynamic light scattering. Data are presented in the (A) bar graph and (B) linear representations.

The hydrodynamic diameters for the X=10, HC polymers with PEG3400 spacers, both with and without EI3.4.3 peptide attached, were approximately 4-5 nm. Although there were approximately 0.5 EI3.4.3 peptides (12.5 kDa/peptide) per chain for the X=10+, HC polymers, the ultimate particle size distribution was nearly identical to that for the X=10-, HC polymer. Replacing the PEG3400 spacer with the shorter TEG spacer, the hydrodynamic diameters were determined to be 8.5 and 10 nm for polymers with and without EI3.4.3 attached, respectively. The size distributions for all four polymers were quite low in polydispersity.

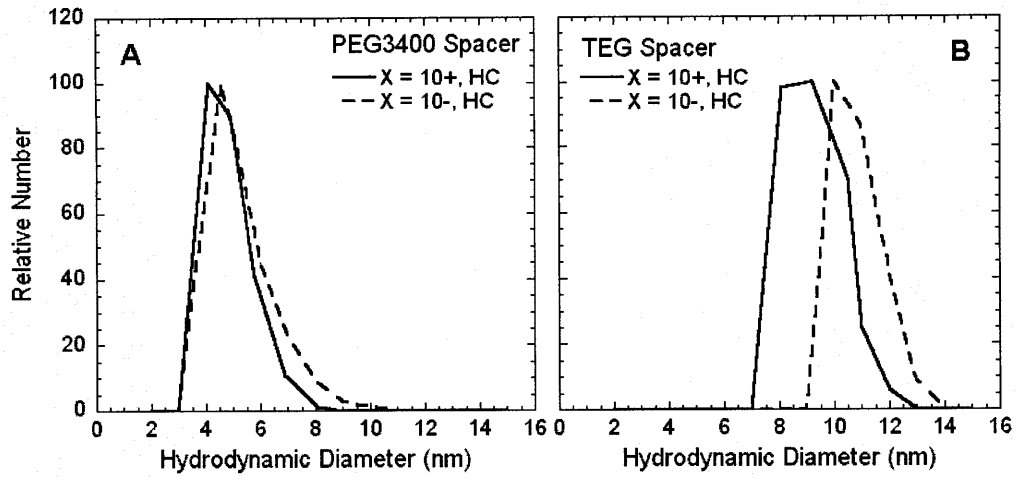

Figure 5.3. Particle size distributions measured by DLS for the X=10, HC polymers with either (A) PEG3400 or (B) triethylene glycol (TEG) hydrophilic spacers.

The four polymers were labeled with iodine-125 and purified according to the procedure described in the *Cellular Uptake Measurement with* [^{125}I]*-polymer* section of the Methods. The uptake of these four labeled polymers was measured in the EGFR-positive A431NS human cancer cell line (FIGURE 5.5). The uptake was calculated as the mass of polymer per cell. The mass of polymer was selected, as opposed to the number of polymer chains, because the individual chains self-assembled into nanoparticles. The uptake was normalized per cell to account for experiment-to-experiment and timpoint-to-timepoint variations in the number of cells in each well.

For both sets of polymers, those with PEG3400 and TEG spacers, the uptake was approximately 2-2.5x higher for polymers with EI3.4.3 peptide attached than for those without the targeting peptide present. The highest overall uptake measured was for the X=10+, HC polymer with the long, PEG3400 spacer. In both cases, the greatest selectivity, which was defined as the ratio of the uptake of the targeted polymers to that for the untargeted equivalents, was observed at the four hour time point.

The hydrodynamic diameter for this polymer was approximately half that of X=10+, HC polymer with the TEG spacer (FIGURE 5.3). The uptake of the untargeted

polymers (FIGURE 5.5, open circles) was quite similar for both the PEG3400 and TEG spacer polymers. This uptake corresponded to the non-specific uptake by the cells, likely due to pinocytosis of the highly PEGylated polymers.

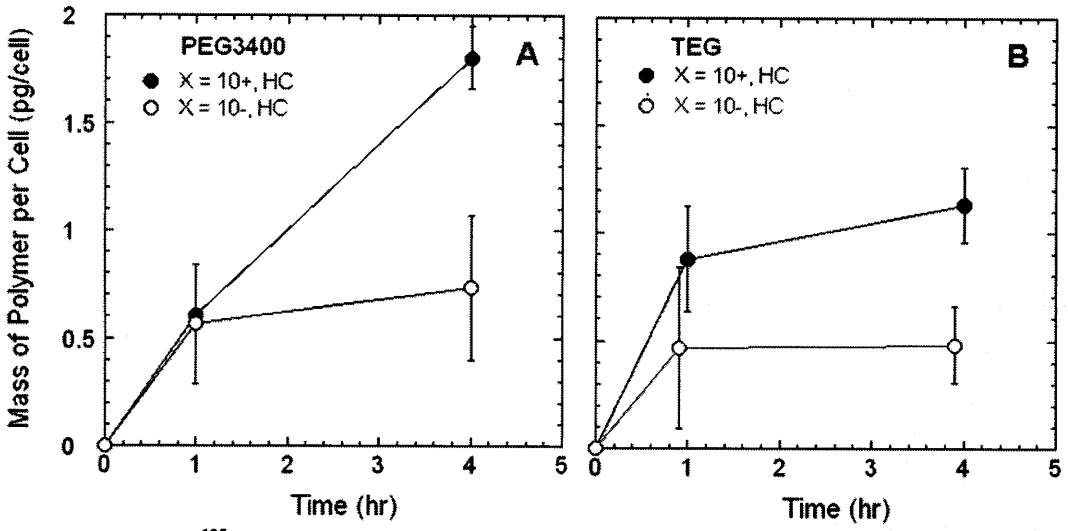

Figure 5.4. Uptake of ^{125}I-labeled polymer in the EGFR-positive human cancer cell line, A431NS. Polymers contained 10% substitution as PEG3400 or TEG spacer, either with or without EI3.4.3 peptide attached. The remaining sidechains were hydrocarbons.

5.4.3 Evaluation of Preparative GPC for Backbone Polymer Fractionation

The selectivity observed in the initial studies with the EI3.4.3 peptide and our polymer system demonstrated that further study of the EI3.4.3/EGFR targeting pair was warranted. As described during the Introduction, there were a number of variables that could be studied to improve the performance of the targeted polymer system, including the number of peptides per chain (polyvalency) and the backbone polymer molecular weight. To allow for full investigation of the former, the backbone polymer molecular weight had to be increased to increase the number of linker hydroxyls that could be substituted with targeting sidechains. Although the Protherm was able to substantially increase the weight-average molecular weight of the backbone polymer, one consequence of the increases realized for the condensation polymerization is increased polydispersity. Polymer fractionation by preparative GPC was used to reduce the polydispersity of the

backbone polymer in order to provide a clean, less polydisperse starting material for subsequent synthetic steps during which targeting and hydrophobic sidechains would be attached.

In order to determine whether the column was able to yield nearly monodisperse fractions of backbone polymer from the high molecular weight, high polydispersity Protherm product, one milliliter of raw backbone polymer (10 mg/mL) was injected and the elution profile for the Superdex 75 preparative gel permeation chromatography column was interpreted (FIGURE 5.6). Significant absorbance was measured over a 100 mL range in elution volume, even though the initial volume of the injected raw polymer sample was relatively small. The preparative GPC Superdex 75 column appeared to have effectively spread out the raw backbone polymer as desired.

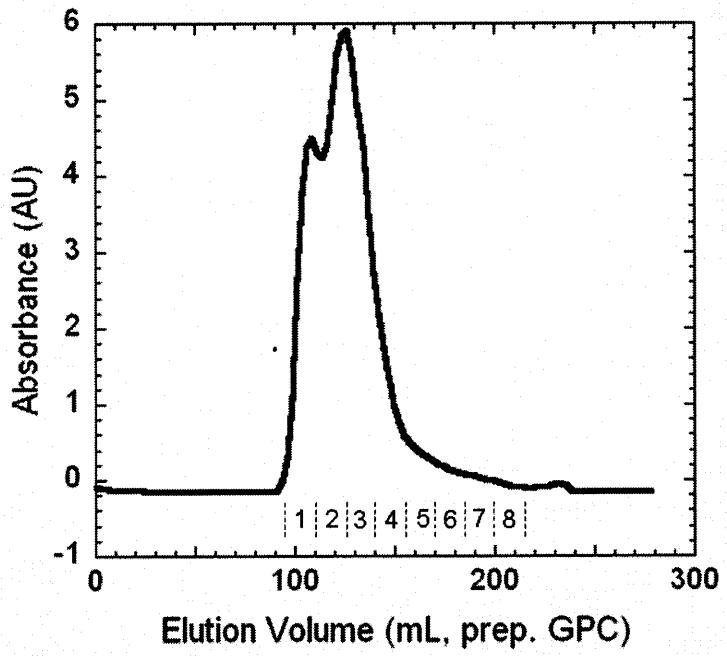

Figure 5.5. Preparative GPC chromatogram for a single injection of high molecular weight backbone polymer (10 mg/mL, 1 mL/injection) produced in the Protherm. The elution volumes for the x-axis are specific to the preparative and not the analytical GPC. Eight, 15 mL fractions were collected between elution volumes of 95 and 110 mL for subsequent analysis by analytical GPC.

Eight fifteen milliliter fractions were collected from the elution (indicated by vertical dashed lines), freeze dried and analyzed by GPC to determine the molecular weight characteristics of each collected fraction. These data would determine what fractions the preparative GPC had created by spreading the backbone polymer across the 100 mL elution volume. The results of these measurements, along with that for the unprocessed backbone polymer, are presented in TABLE 5.4.

Table 5.4. Summary of analytical GPC measurements, including M_n, M_w, and PDI, for the eight fractions collected from the preparative GPC (FIGURE 5). Results are compared to those for the raw Protherm (PT) backbone polymer for comparison. The elution volumes listed under the 'Sample' heading are specific to the preparative GPC elution volumes.

	Sample	M_n (kDa)	M_w (kDa)	PDI
	Raw PT Backbone Polymer	8.7	20.6	2.36
1	95-110 mL	14	17	1.15
2	110-125	12	14	1.17
3	125-140	9.0	10	1.16
4	140-155	6.6	7.2	1.11
5	155-170	4.5	5.3	1.15
6	170-185	3.3	3.7	1.13
7	185-200	2.3	2.6	1.14
8	200-215	1.7	1.9	1.12

The analytical GPC chromatograms were processed as described in APPENDIX A: Molecular Calculation by Breeze Software and Chromatogram Manipulation, to determine the relative number of polymer molecules at each respective molecular weight (FIGURE 5.7). The chromatograms for the second, third, and fourth polymer fractions (see TABLE 5.4) collected from the preparative GPC were compared to that for the raw backbone polymer.

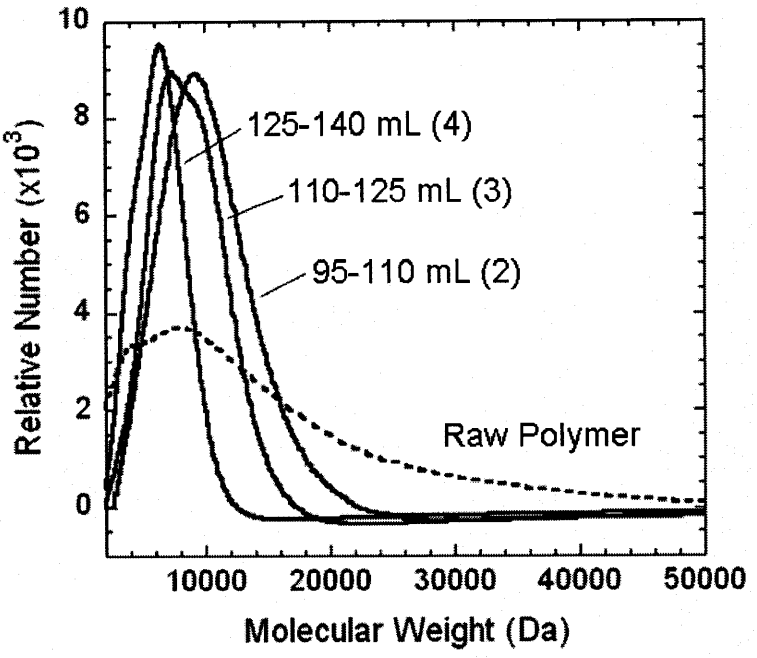

Figure 5.6. Relative number of backbone polymer molecules at each molecular weight for the second, third, and fourth fractions collected from the preparative GPC as analyzed by the analytical GPC. The chromatogram for the raw backbone polymer produced in the Protherm is also included.

The number-average molecular weight of the 8 fractions collected from the preparative GPC ranged from 1.7 to 14 kDa, while the polydispersity of each collected fraction was less than 1.17. This result demonstrated that the preparative GPC was able to create low polydispersity, comparatively high molecular weight fractions of backbone polymer. This is particularly true in comparison to the backbone polymer starting material used in the initial study of the EI3.4.3 peptide/EGFR targeting pair, which was produced by mechanical stirring in a flask with sieves added (but without fractionation) and had a number-average molecular weight and polydispersity of 5.2 kDa and 1.34, respectively.

The analytical GPC chromatograms in FIGURE 5.7, as well as the molecular weight data in TABLE 5.4, revealed that the entire range of polymer molecular weights present in the original raw backbone polymer sample was not recovered at the end of the preparative GPC column. Specifically, no backbone polymer oligomers with molecular

weights greater than 20-25 kDa were measured in the recovered fractions by analytical GPC, while oligomers as large as 40-50 kDa were measured in the unprocessed, raw backbone polymer produced in the Protherm.

Although each 15 mL fraction was low in polydispersity, the analytical GPC chromatograms for consecutive fractions (FIGURE 5.7) overlap one another to a significant extent. Because of dispersive effects commonly observed for processes in porous media, such as gel permeation chromatography, there is an inherent distribution of residence times even for a purely monodisperse starting material. This distribution was the primary contribution to the overlap between fractions 2 and 3, fractions 3 and 4, and so on. Variability in the porosity of the chromatography resin may also have contributed to the overlapping chromatograms observed by analytical GPC.

5.4.4 Development of a High-Throughput Fractionation Process

The preceding experiments demonstrated that, although the entire initial molecular weight range was not recovered, the preparative GPC was still able to create low polydispersity, high molecular weight fractions from the raw backbone polymer produced in the Protherm. In order to generate enough fractionated backbone polymer to supply the synthesis of polymers for the targeted delivery studies, the throughput of the fractionation process had to be increased significantly. The initial concentration of the backbone polymer load solution was increased from 10 to 100 mg/mL, while the total injection volume was increased from 1 to 3 mL.

Successive injections were scheduled every 300 mL of accumulated elution volume. This injection schedule ensured that material from consecutive injections did not overlap with one another in the column. This injection schedule also decreased the

downtime between successive injections while still maintaining a safety factor to avoid injection-to-injection overlap. Recall that the total column volume of the Superdex 75 preparative GPC column was 318 mL. The method that was developed and coded using the GE Unicorn software is included in APPENDIX E. Fractions were collected at the same post-injection preparative GPC elution volumes as those presented in TABLE 5.4, while the elution profile for a typical production run is presented in FIGURE 5.8.

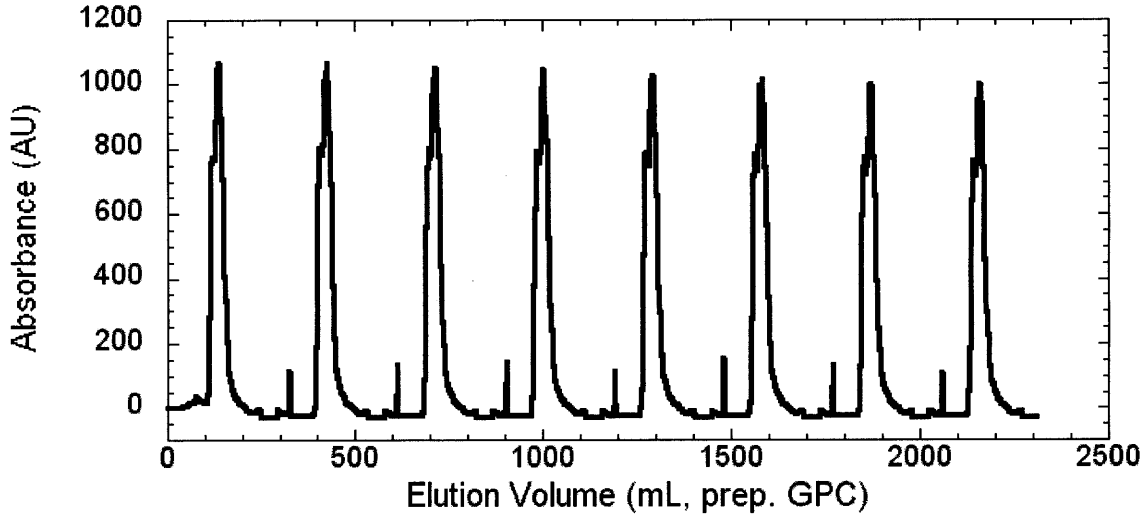

Figure 5.7. Chromatogram for an eight injection preparative GPC run to process and fractionate high molecular weight backbone polymer. Polymer was detected by an inline UV spectrophotometer (λ = 250 nm) and each elution was collected into eight 15 mL fractions for elution volumes between 95 and 215 mL post-injection.

The production run consisted of eight injections of the Protherm-produced backbone polymer. Each elution peak was fractionated into eight 15 mL fractions for elution volumes between 95 and 215 mL post each injection (dashed vertical lines not shown). Each successive elution peak was nearly identical with the only notable exception being the slight decrease in the peak maxima over the course of the eight injections and elutions. This decrease was likely due to fouling of the column pores. There was also an abrupt spike in the absorbance at the end of each elution peak. This spike corresponded directly to each 3 mL injection and was related to the significant

increase in pressure associated with the injection of the highly concentrated, highly viscous 100 mg/mL polymer solution.

The fractional recovery of backbone polymer was determined by weighing the polymer in each collected fraction and assuming that the initial mass added was 300 mg (3 mL of a 100 mg/mL solution). The calculated fractional recovery for each of the eight injections varied between 0.60 and 0.65, with the lowest recoveries occurring for the later injections. The pressure measured at the pump head in the AKTA Explorer system also increased steadily throughout the series of eight injections and elutions. While the pressure only increased from 0.20 to 0.25 MPa for the single injection and elution, a pressure increase from 0.20 to 0.50 MPa over the duration of the eight injection production run (FIGURE 5.8).

After each production run the column was cleaned with three column volumes of a 0.5 M sodium hydroxide solution (0.5 mL/min) and re-equilibrated with three column volumes of deionized water. After these two steps, the system pressure was restored to the original baseline of 0.20 MPa.

5.4.5 Size Measurements of EI3.4.3-Conjugated Polymer Synthesized from High Molecular Weight Backbone Polymer

High molecular weight backbone polymer was fractionated by FPLC and the 110-125 mL FPLC fraction (M_n = 12 kDa, PDI = 1.17, see TABLE 4) was used in the synthesis of various polymer candidates. Physico-chemical and biological assays were performed to evaluate their performance with different fractions of sidechain substitution, X, and with different identities of the hydrophobic sidechain (HC, PFC, or no added

sidechain). All polymers in the studies with the high molecular weight backbone polymer had PEG3400 spacers. The molecular weight attributes, peptides per polymer chain, and hydrodynamic diameters as measured by dynamic light scattering of two separately synthesized polymer batches are summarized in TABLE 5.5.

Table 5.5. Summary of the (A) first and (B) second batch of polymers synthesized for the investigation of the EI3.4.3/EGFR targeting pair with high molecular weight backbone polymer. The polymer chain M_n was calculated based on the components in the chemical structure. The number of peptides per chain was estimated assuming approximately ten repeat units per backbone polymer chain based on a backbone polymer molecular weight of 12 kDa. The hydrodynamic diameter was determined by dynamic light scattering (see FIGURES 8 and 9).

	Polymer	Polymer Chain M_n (kDa)	Peptides Per Chain	Hydrodynamic Diameter(s) (nm)
A	10+, PFC	30.8	1	7, 17
	25+, PFC	54.2	2.5	10, 15, 20
	25-, PFC	22.9	0	10, 21
	10+, HC	28.7	1	6
	25+, HC	52.4	2.5	17
	25-, HC	21.1	0	16, 22, 27
	50+, HC	92.0	5	23, 43, 61
	50+, NHS	91.5	5	30, 52, 72, 78
B	25+, PFC	54.2	2.5	16, 22, 26
	25-, PFC	22.9	0	14, 19
	50+, PFC	93.1	5	2, 19
	50-, PFC	30.6	0	2, 8, 29, 35, 43
	75+, PFC	132.1	7.5	10, 19, 40, 100
	75-, PFC	38.3	0	17, 24, 29, 61
	50+, HC	92.0	5	11, 24
	50-, HC	29.4	0	13, 33
	75+, HC	131.5	7.5	2, 7, 17, 34, 44
	75-, HC	37.9	0	13. 16, 25, 39, 52, 73

The molecular weight of each polymer formulation by adding the molecular weights of the individual components present in the polymer. Each backbone polymer chain was 12 kDa. The PEG spacer was 3400 Da and the EI3.4.3 peptide was 12.5 kDa. Due to the comparatively large size of the EI3.4.3 peptide (12.5 kDa) relative to the molecular weight of the backbone polymer starting material (12 kDa), the number of

peptides per chain most significantly affected the polymer chain molecular weight. The polymer molecular weight varied from approximately 20-130 kDa for the 18 synthesized polymers. Similarly substituted polymers either with or without the peptide attached varied in molecular weight by factors ranging from approximately two to four.

The particle size distributions for both batches synthesized from the low polydispersity, high molecular weight backbone polymer were measured by DLS (FIGURES 5.9 and 10). For the first batch, the X=10+, HC polymer had a hydrodynamic radius of 6 nm (FIGURE 9A). This result was quite similar to the size distribution measured for the X=10+, HC polymer synthesized from the lower molecular weight backbone (FIGURE 5.3). The size distribution for the X=10+, PFC polymer included two peaks, at diameters of 7 and 17 nm (9B). The X=25 polymers (9C and D) had hydrodynamic diameters between approximately 10 and 30 nm. The X=25+, HC distribution was essentially monodisperse at 17 nm, while the X=25-, HC distribution was broader and centered around 22 nm. The distributions for the X=25, PFC polymers were quite similar both with and without the EI3.4.3 peptide attached, with distinct peaks at diameters of approximately 10 and 20 nm.

From this first batch, the two X=50 were the primary outliers, having three distinct narrow particle size distributions that collectively ranged from 20 to 80 nm. Interestingly, particles were observed for the X=50+, no hydrophobic sidechains (NHS) polymer, even though there were no hydrophobic sidechains present on the 50% remaining free hydroxyls within the backbone polymer (9F).

For the second batch of polymers synthesized from the low polydispersity, high molecular weight backbone polymer, the hydrodynamic diameters for the X=25, PFC

polymers were between 10 and 25 nm (FIGURE 10A). This result was quite similar to the size distribution measured for the X=25, PFC polymers synthesized in the first batch (FIGURE 9D). The X=50+, HC polymer had two distinct peaks in the size distribution at diameters of 11 and 24 nm (10B). This result was different from the size distribution observed for the X=50+, HC polymer synthesized in the first batch (9E), which was broad and ranged from 20 to 60 nm.

Particles with hydrodynamic diameters of 2 nm were observed for a number of the more highly PEGylated polymers synthesized in the second batch, including the X=50, PFC and X=75, HC polymers. It is likely that the particles measured at this small size correspond to individual polymer chains or associations of a small number of chains.

Overall, the particle size distributions with the lowest polydispersity were those for the X=10 and the X=25 polymers. The diameters measured for these distributions were generally observed over a narrower range than for the other measured polymers. These polymers had a larger proportion of the sidechains devoted to hydrophobic sidechains, either in the form of hydrocarbons or perfluorocarbons. Conversely, the particle size distributions for the X=50 and X=75 polymers were generally more polydisperse, with less well-defined sizes. The notable exception to this generalization was the X=50, HC polymers from the second synthesis batch. Finally, the presence of the EI3.4.3 peptide targeting had varying effects on the ultimate particle size distribution.

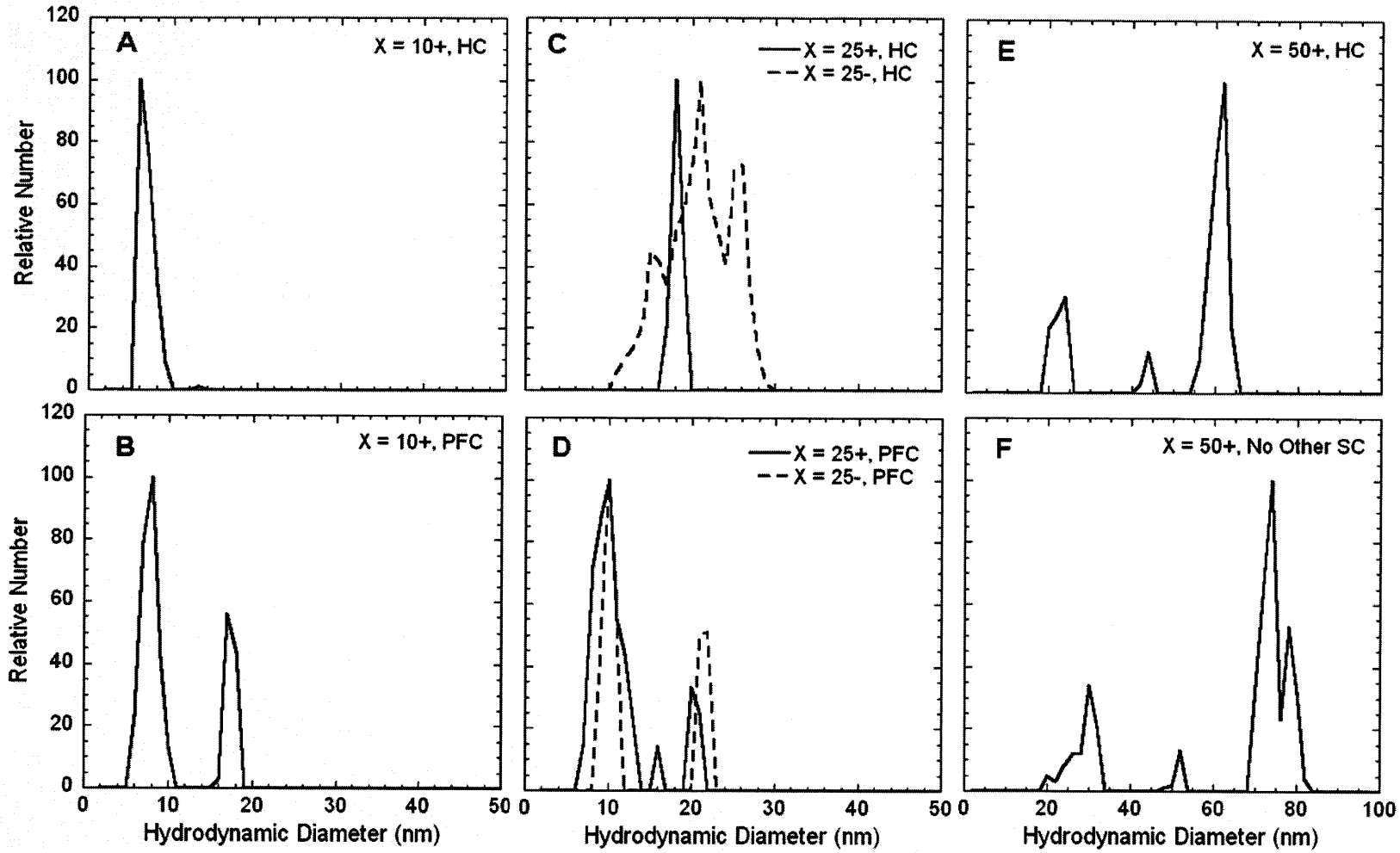

Figure 5.8. Particle size distributions of the first batch of polymers synthesized from high molecular weight backbone as measured by DLS. Solid lines indicate polymers with EI3.4.3 attached, while dotted lines indicate polymers without EI3.4.3. Note: The scale of the X-axis for the X=50 (E and F) polymers is twice that for the other data presented (A-D).

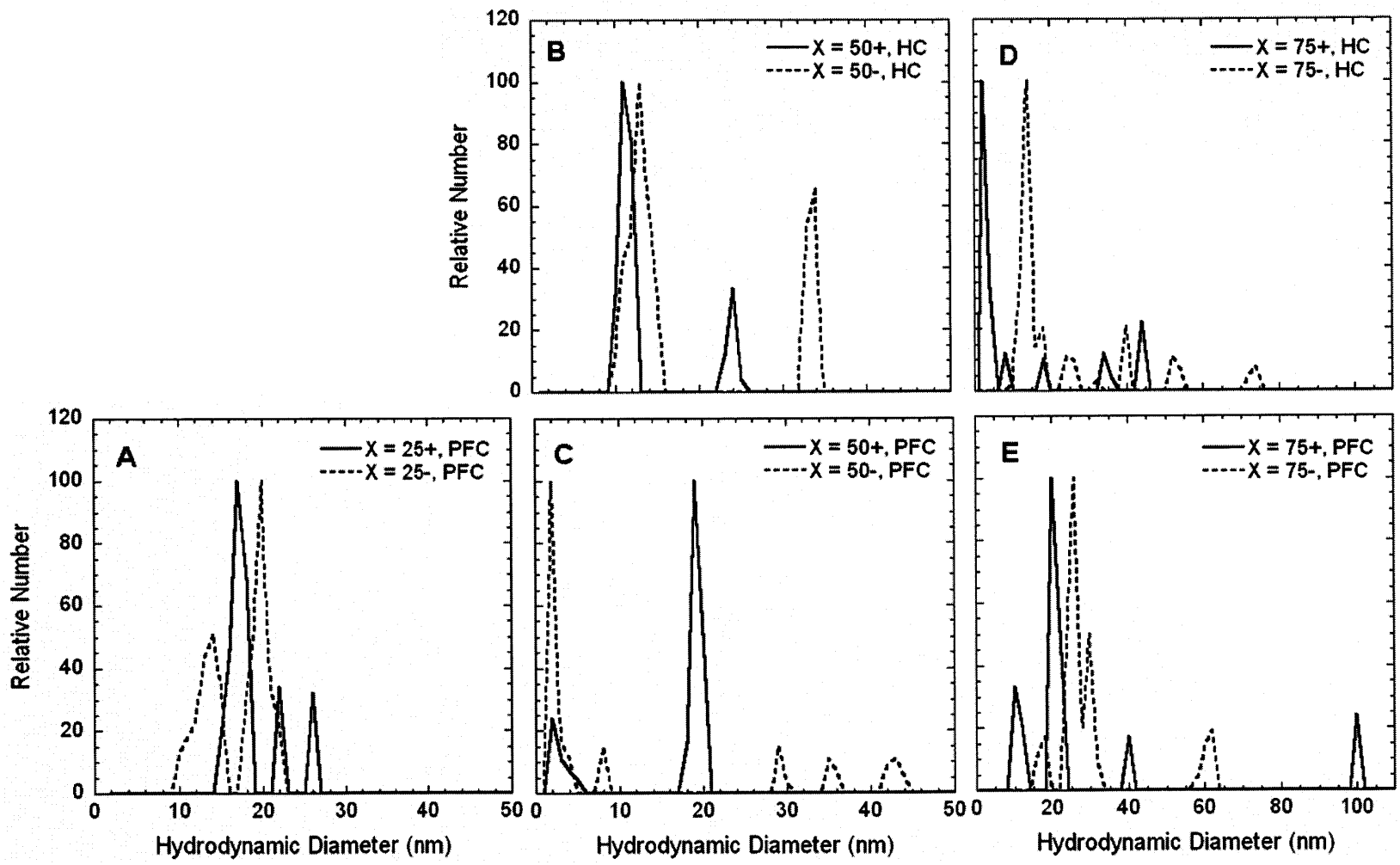

Figure 5.9. Particle size distributions as measured by DLS for the second batch of polymers synthesized from high molecular weight backbone. Solid lines indicate polymers with EI3.4.3 attached, while dotted lines indicate polymers without EI3.4.3. Note: The scale of the X-axis for the X=50 (D and E) polymers is twice that for the other data presented (A-C).The X=75, HC polymers were not studied further due to labor limitations and their relative similarity to the X=75, PFC polymers in composition.

5.4.6 In vitro Uptake of Free EI3.4.3 Peptide

The EI3.4.3 peptide was labeled with iodine-125 and the uptake of the labeled free peptide was measured at three different initial concentrations, 5, 50, and 500 nM (FIGURE 5.11). The uptake measurements were performed using the EGFR-positive cell line, A431NS.

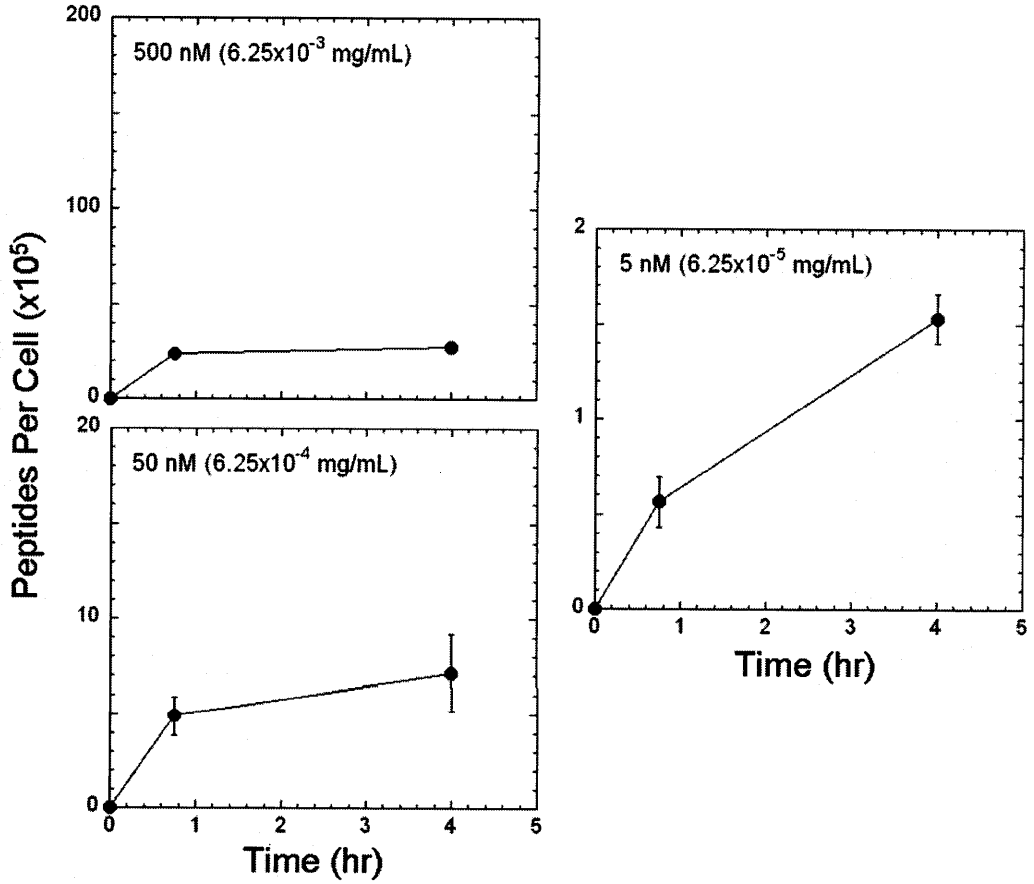

Figure 5.10. Uptake of free EI3.4.3 peptide by EGFR-positive A431NS cells at three different initial concentrations (in molar and mass units). The y-axes are scaled proportionately for the respective initial peptide concentrations.

At the highest concentration measured, 500 nM, the free EI3.4.3 peptide uptake leveled off at 1 hr (or earlier), while the uptake still appeared to be increasing at 4 hr for the 5 and 50 nM experiments. In addition, the amount of uptake was proportionately lower at the increased concentrations. This observation was aided by the proportionate scaling of the y-axes in FIGURE 5.11.

5.4.7 In vitro Uptake of EI3.4.3-Conjugated Polymer Synthesized from High Molecular Weight Backbone Polymer

The two batches of polymers synthesized from the low polydispersity, high molecular weight backbone polymer (TABLE 5.5) were labeled with ^{125}I and their uptake was measured in EGFR-positive A431NS cells at an initial polymer concentration of 0.5 mg/mL. Because the mass concentration was held constant for each polymer, the molar concentration differed from sample to sample, primarily as a function of percent PEG3400 substitution and presence of the peptide, according to the polymer chain molecular weights in TABLE 5.5. The results for the first and second synthesized batch are presented in FIGURES 5.12 AND 13, respectively. Due to material limitations, the uptake of the second batch of polymers was only measured in duplicate wells.

The most relevant basis for presentation of the uptake results was not clear, *a priori*, due to many complicating factors. Specifically, for polymers with and without the peptide attached, such as the X=25+, PFC and X=25-, PFC pair, the molecular weight of the individual polymer chains differs drastically depending on the presence of the comparatively high molecular weight EI3.4.3 peptide. This difference becomes more pronounced as the targeting ligand substitution increases. Differences in the specific activity of each polymer sample could also complicate analysis, particularly with respect to the distribution of labels to tyrosine groups on the EI3.4.3 peptide or the linker groups within the polymer backbone.

For succinctness, the mass of polymer per cell was chosen as the method of uptake data representation. Alternative strategies for representing the data were also

explored, including the number of polymer chains per cell and the fraction of initial activity per cell, and are presented in Appendix G.

For the first batch synthesized from high molecular weight backbone polymer, the highest uptake observed was for the X-25+, PFC polymer (12A). The mass of polymer per cell for this sample was two and four times higher than that its untargeted control polymer, X=25-, PFC, at the 0.75 and 4 hr time points, respectively. This fourfold increase in uptake relative to untargeted control was the greatest selectivity observed with our polymer system thus far. (Recall that a twofold increase was observed for the X=10+, HC polymer synthesized from the lower molecular weight backbone). Because the particle size distributions for the two X=25, PFC polymers were nearly identical (9D), the increase in uptake for the targeted polymer was attributable to the presence of the EI3.4.3 peptide. Also, while the uptake for the X=25-, PFC polymer appeared to be leveling off, that for the X=25+, PFC polymer had not leveled off by 4 hr, which suggested that further selectivity was achievable at longer incubation times. Finally, the uptake of the X=25+, PFC polymer was slightly higher than the uptake for the untargeted X=10-, PFC polymer.

The next highest uptake was observed for the X=50+, HC and the X=50+, NHS polymers (12B). For this batch, no control polymer counterparts without the EI3.4.3 peptide attached were synthesized for these two targeted polymers. This made it difficult to determine the selective uptake since there was no basis for comparison. If the uptake for the X=25-, HC polymer is used as a basis for comparison, the selectivity for the X=50+ polymers was a factor of approximately 4-6. The increased uptake of the X=50+ polymers occurred even though the particle sizes measured for these polymers were

generally much greater than those measured for the other polymers synthesized in this batch (9E and F).

The scale of the y-axis was decreased to facilitate further analysis of the results (12C). For the X=25, HC polymers, the uptake of the targeted polymer was approximately 50% higher at the 4 hr time point than that for the untargeted polymer. Although this increase was modest, the trend was still in the direction indicating selective uptake mitigated by the presence of the EI3.4.3 peptide. Overall, the variability in the data was significant, but not too large to obfuscate the data analysis. Using a two-tailed Student t-test, the p-values for all of the previous comparisons were less than 0.05.

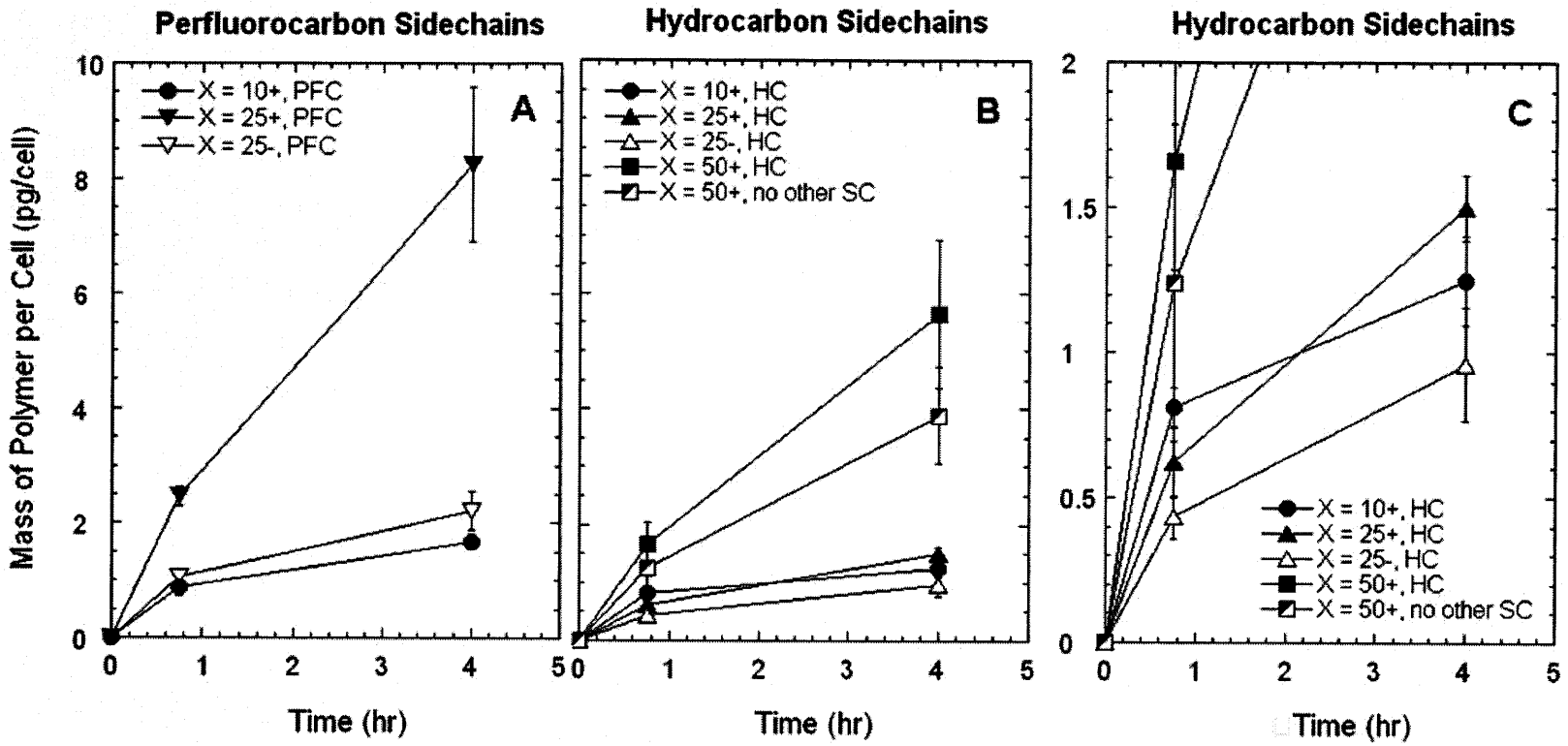

Figure 5.11. Uptake in EGFR-positive A431NS cells for the first batch of polymers synthesized from high molecular weight backbone polymer. The initial concentration was 0.5 mg/mL. Polymers were substituted with X% PEG3400 terminated either with or without EI3.4.3 peptide. The balance of the hydroxyl groups were substituted with perfluorocarbons, hydrocarbons, or no hydrophobic sidechains. The hydrocarbon sidechain data (B) were reproduced with a smaller y-axis (C).

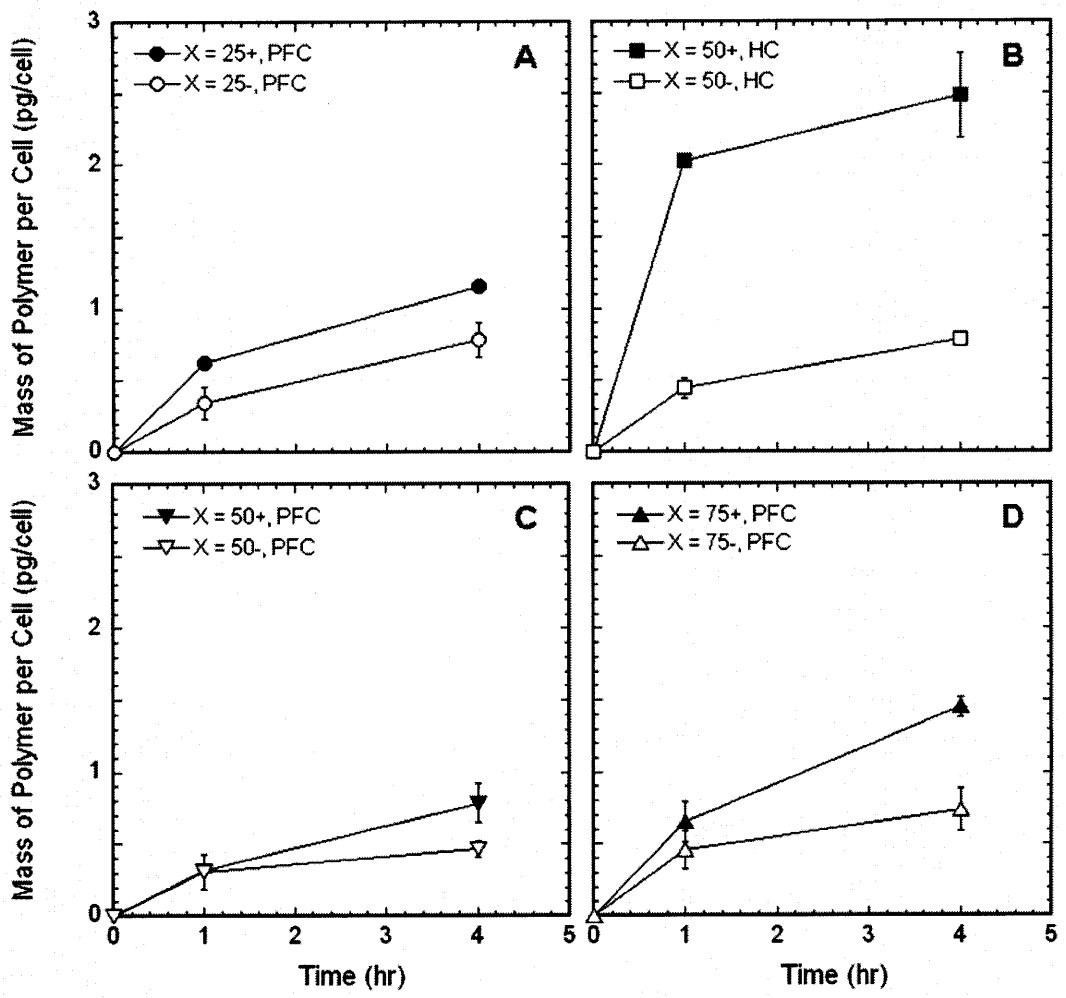

Figure 5.12. Uptake in EGFR-positive A431NS cells for the second batch of polymers synthesized from high molecular weight backbone polymer. The initial concentration was 0.5 mg/mL. Polymers were substituted with X% PEG3400 terminated either with or without EI3.4.3 peptide. The balance of the hydroxyl groups were substituted with perfluorocarbons or hydrocarbons. Note: The scale of the y-axes for these plots is 30% of those in FIGURE 11.

For the second batch of polymers synthesized from the high molecular weight backbone polymer, the highest overall uptake was observed for the X=50+, HC polymer (5.13B). The uptake for this polymer was approximately four times greater than that for the untargeted control polymer, X=50-, HC. This batch included the second synthesis of the X=25, PFC polymers. The results for the X=25, PFC polymers (12A) showed only a 25% increase in uptake due to the presence of the EI3.4.3 peptide, while a fourfold increase was observed for the uptake measurements of the first synthesis of this pair.

There was a significant difference in the absolute magnitude of the uptake results between the two batches. The highest uptake observed in the second batch of polymers (13B) was approximately 30% that observed for the first batch (12A). Aside from the fact that the polymers were synthesized in separate batches, including different productions of backbone polymer and EI3.4.3 peptide, the uptake experiments were also performed separately. This difference occurred despite the fact that the procedure was carefully reproduced, including labeling and purification, plating density, and time between plating and initiation of the experiment. Two different vials of A431NS that had been frozen from the same initial expansion were used for each experiment, having passage numbers of either 4 or 5.

There was, however, a difference in the total numbers of cells counted in the control wells for the two uptake experiments. For the first batch, there were approximately $1.5x10^5$ cells in each well at the start of the experiment, while for the second experiment, there were approximately $3.0x10^5$ cells in each well. It is possible that an error in cell counting or plating led to the increased cells for the second batch.

Increased uptake with the EI3.4.3 peptide attached (selectivity) was observed for all four pairs of polymers and was most pronounced at the longer, 4 hr time point. There was also minimal variability in the data, although it should be noted that the second batch polymers were only measured in duplicate.

5.4.8 Uptake Measurements in EGFR-positive and negative Cell Lines

Uptake was measured in the EGFR-negative MFC-7 human cancer line in addition to the EGFR-positive A431NS cells for the second synthesis batch. A difficulty arose in trying to compare the results between the two cell lines. Although the identical

number of cells was originally plated, the cell counts for the A431NS cell were four times higher than those for MCF-7 at the 1 and 4 time points. (As described in the methods, the uptake experiment was initiated on the day after cells were plated on 96 well plates. The time between plating and initiation of the experiment was approximately 18 hr.) Visualization of the two cell populations under the microscope confirmed that, although wells in both cases were confluent, there were many more A431NS cells per well due to their small size and extremely close packing.

To compare between the cell lines, the total mass of cell-associated polymer measured in each well was normalized by the cross-sectional area of a well. This choice was dependent on the anticipated basis for cellular internalization. Consider a limiting case in which a hypothetical negative control cell line was so large, that only 10 cells fit into a well at confluency. If the polymer uptake was mediated by the number of cells, then it would be appropriate to normalize the data by the cell number. However, it seemed likely that uptake would be mediated by some other mechanism, such as the total cell surface area available, particularly for untargeted internalization into the EGFR-negative cell line. For this reason, the uptake results in both the A431NS and MCF-7 cell lines were normalized by the area of a well in a 96-well plate (FIGURE 5.14). A plot of the total cell-associated mass in each experiment would have been an equivalent representation.

For these results, there were two variables studied, the presence of targeting ligand on the polymer and the presence of the target on the cell surface. Each of these variables had two levels, which led to four cases of interest. For three of the cases, the untargeted polymer and EGFR-positive cell line and both of the EGFR-negative cell line

cases, any cell-associated polymer measured should be due to non-specific uptake. Ideally, the uptake results for these three cases should be identical. This non-specific uptake can essentially be subtracted from the uptake observed for the targeted polymer and EGFR-positive cell line to yield the uptake that occurred due to the presence of the EI3.4.3 peptide, the specific uptake.

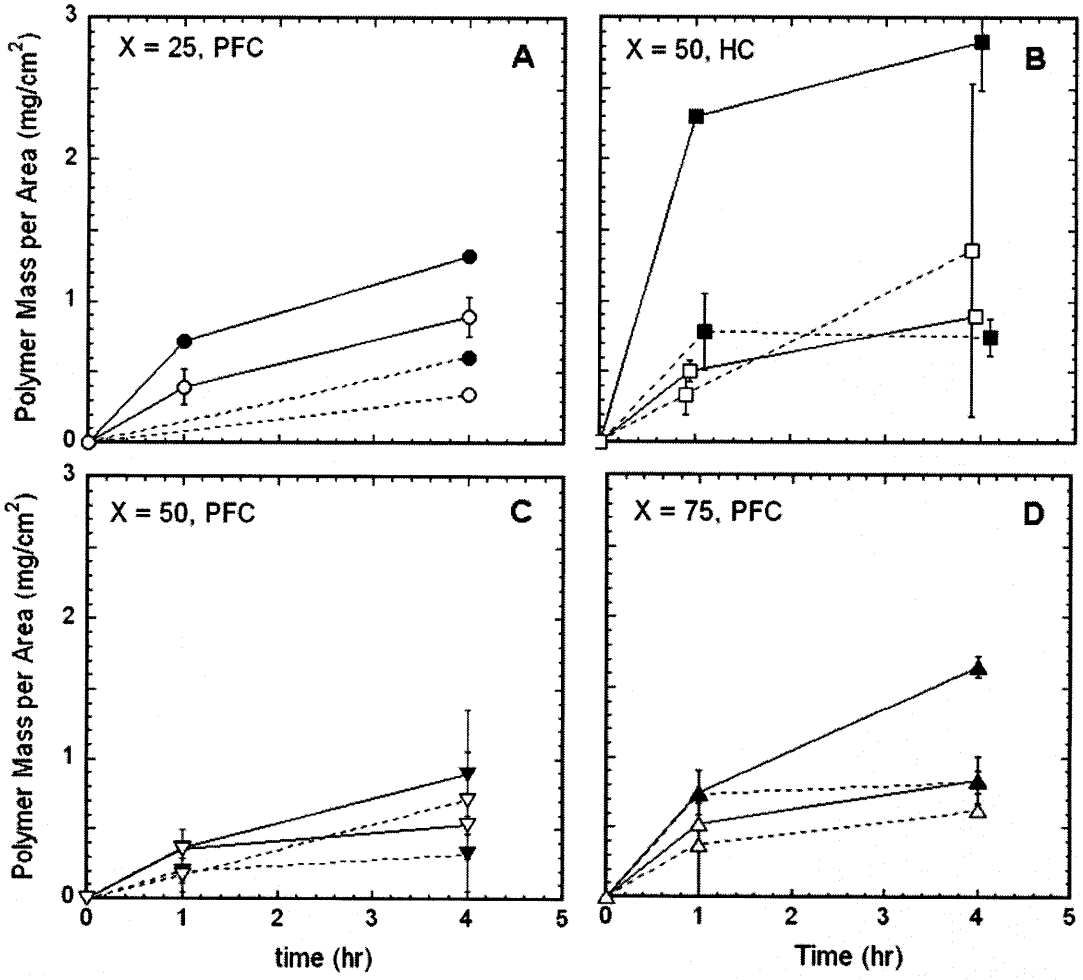

Figure 5.13. Uptake of batch 2 polymers in both EGFR-positive (A431NS, solid lines) and EGFR-negative (MCF-7, dashed lines) human cancer cell lines. Polymers both with (closed symbols) and without (open symbols) EI3.4.3 peptide attached were measured. Data were normalized by the cross-sectional area of a well in a 96-well plate. The, X=50, HC time points were purposefully offset to clarify the error bars.

The greatest difference between selective and non-specific uptake was observed for the X=50, HC polymers (14B). The uptake of the targeted polymer in the EGFR-

positive cell line was 2-3 times greater than that for the other three cases that represent non-specific uptake. The data for the three non-specific cases were essentially indistinguishable from one another. Interestingly, there was no observed difference in uptake for any of the four cases for the X=50, PFC polymer (14C). These two sets of X=50 polymers differed only in the nature of the hydrophobic sidechain. There was also minimal difference between the X=25+, PFC polymer and the three non-specific cases (14A). The 4 hr time point for the X=25-, PFC polymer in the EGFR-positive case was somewhat higher than the results for the EGFR-negative cell line. This may suggest that the X=25+, PFC, EGFR-positive results were an outlier or that some other, unknown effect contributed to the increased uptake.

There was also a significant difference in the uptake of the X=75+, PFC polymer in the EGFR-positive cell line relative to the three non-specific cases at 4 hr (14D). Overall, the results for the three non-specific uptake cases were not only similar to one another within each set of polymers, but also across all four pairs of polymers studied in two different human cancer cell lines.

5.4.9 Analysis of Uptake Normalized by Initial EI3.4.3 Peptide Concentration

The preceding data analysis focused on normalization of the uptake data by either the number of cells in or the surface area of an individual well. Because one of the primary variables evaluated was the number of targeting peptides per polymer chain, the initial EI3.4.3 peptide concentration at the beginning of each experiment was also used to normalize the uptake results. This normalization provided information about the targeting efficiency of the EI3.4.3-conjugated polymers, essentially the amount of material entering the cells per peptide attached.

To normalize the data, the initial concentration of EI3.4.3 peptide in solution was determined for the two synthesis batches and free EI3.4.3 peptide (FIGURES 5.11-13). For each EI3.4.3-conjugated polymer, the initial polymer concentration (0.5 mg/mL) was multiplied by the weight fraction of EI3.4.3 peptide in the particular polymer formulation. For example, according to the number of peptides per chain, the molecular weight of an individual chain and the molecular weight of the peptide (TABLE 5.5), the weight fraction of peptide in the X=10+, HC polymer was 0.41 (12.5 kDa/30.8 kDa) and the initial EI3.4.3 peptide concentration was 0.2 mg/mL. The initial peptide concentration for the free EI3.4.3 peptide data was straightforward. The experimental results normalized by initial peptide concentration are presented in FIGURE 5.15.

For the first batch of polymers, the greatest EI3.4.3-normalized uptake was observed for the X=25+, PFC polymer, while the second highest was for the X=10+, PFC polymer. Although the absolute uptake was considerable for the two X=50+ polymers in the first batch (12B), the efficiency of the uptake relative to the number of peptides in solution initially was minimal when the EI3.4.3-peptide normalization was applied. The EI3.4.3-normliazed uptake for the X=25+, PFC polymer was similar to that for the lowest free peptide concentration. The initial peptide concentrations for the X=25+, PFC and 5 nM experiments differed by four orders-of-magnitude (0.26 and 6.25×10^{-5} mg/mL, respectively). Although the free peptide uptake flattened out drastically with increased concentration (FIGURE 5.11), conjugation of the peptide to our polymer allowed for continued uptake beyond that predicted solely by the initial peptide concentration.

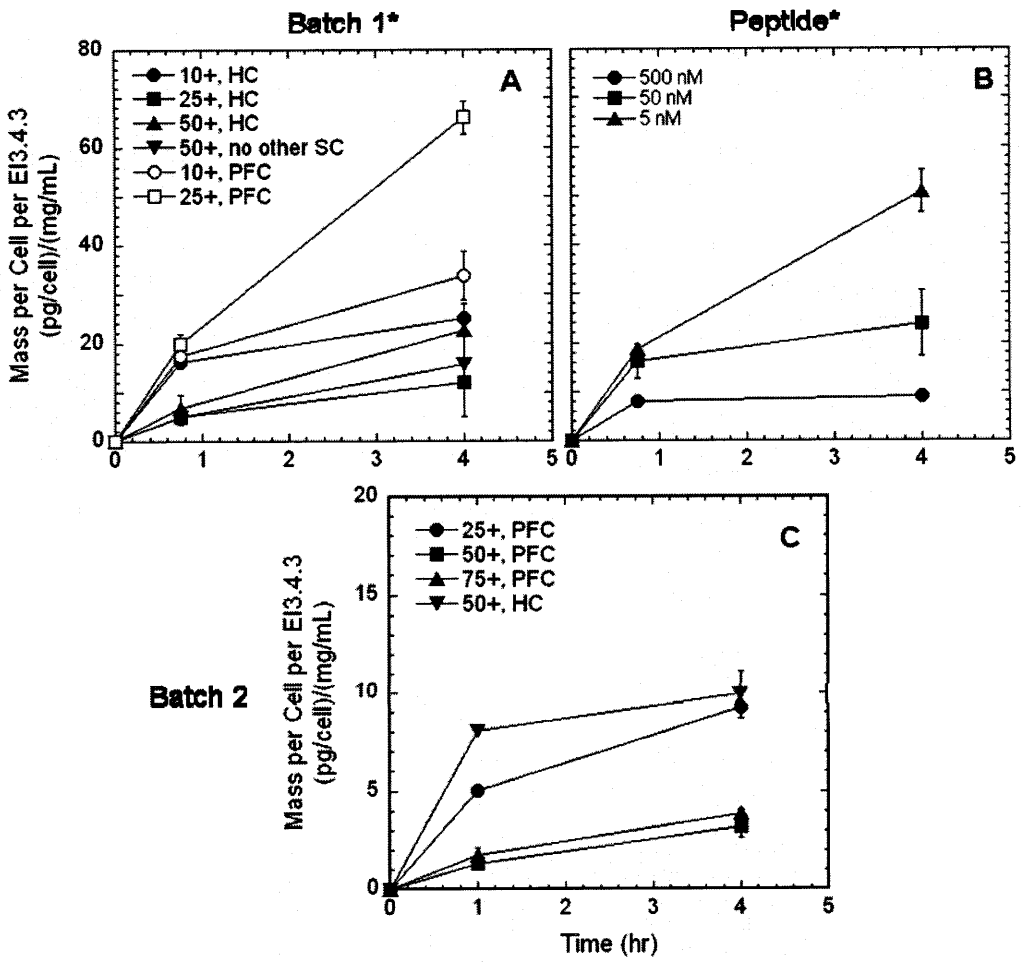

Figure 5.14. Uptake of EI3.4.3-conjugated polymer and free EI3.4.3 peptide normalized by the initial concentration of peptide in solution at t = 0. The asterisks indicate that the (A) batch 1 and (B) peptide experiments were performed in the same 96-well plates. The scale of the y-axis for the batch 2 (C) results is one-fourth that of the others. The original uptake results used to calculate the values in this figure were presented in FIGURES 5.11, 5.10, and 5.12, respectively.

The EI3.4.3-normlized uptake for the second batch was significantly lower than that for the first batch; this was due to the low absolute magnitude of the original uptake results. For this batch, the EI3.4.3-normalized uptake for the X=50+, HC polymer was equal to or greater than that for the X=25+, PFC polymer. This was the opposite of the trend observed in the first batch., which further emphasized the low uptake observed for the X=25+, PFC polymer in the second batch. The normalized uptake was much greater for the X=50+, HC polymer than the X=50+, PFC polymer because the weight fraction of peptide in the two polymers were very similar.

5.4.10 Biodistribution and Blood Circulation in a Mouse Model of Human Cancer

Candidates from both synthesis batches were investigated in *in vivo* biodistribution and blood circulation studies. For the first synthesis batch, polymers were selected according to which sample was synthesized in sufficient quantity to supply the experiment. For the second synthesis batch, all polymers were available in sufficient quantity. Together, this provided the opportunity to investigate a wide range of polymers in *in vivo* biodistribution experiments to (1) evaluate their performance in targeting the subcutaneous tumor and (2) to determine whether there was any correlation between *in vitro* selectivity and increased tumoral accumulation *in vivo.* In order to screen a wide range of polymers in *in vivo* studies, the time points studied and the number animals in each experimental group had to be reduced. The total number of animals for experimentation was somewhat restricted due to both labor and funding limitations. Animals were sacrificed at specified times and organs were harvested, weighed, and assayed for radioactivity to determine the accumulation.

The biodistribution for the first batch of polymers synthesized from the high molecular weight backbone polymer was measured at 1 and 6 hr (FIGURE 5.16). The uptake of the free EI3.4.3 peptide was also measured at these two time points. The highest tumoral accumulation was measured for the X=25+, PFC polymer at 1 hr, with a %IDPG of nearly 3%. This result was higher than that for the X=25-, PFC polymer, with a p value equal to 0.08. A p-value at this level, although not quite below 0.05, was encouraging considering the limited number of test animals in the group. There was also no difference in biodistribution between the two X=25, PFC polymers in all of the organs harvested or in the blood. This fact, together with the similar particle size distributions of

the two samples (9D), suggested that the increased accumulation in the tumor was due to the conjugation of the EI3.4.3 peptide. Additionally, the tumoral %IDPG for the X=25+, PFC polymer was 50% higher than that for the free EI3.4.3 peptide, but the difference was not statistically significant.

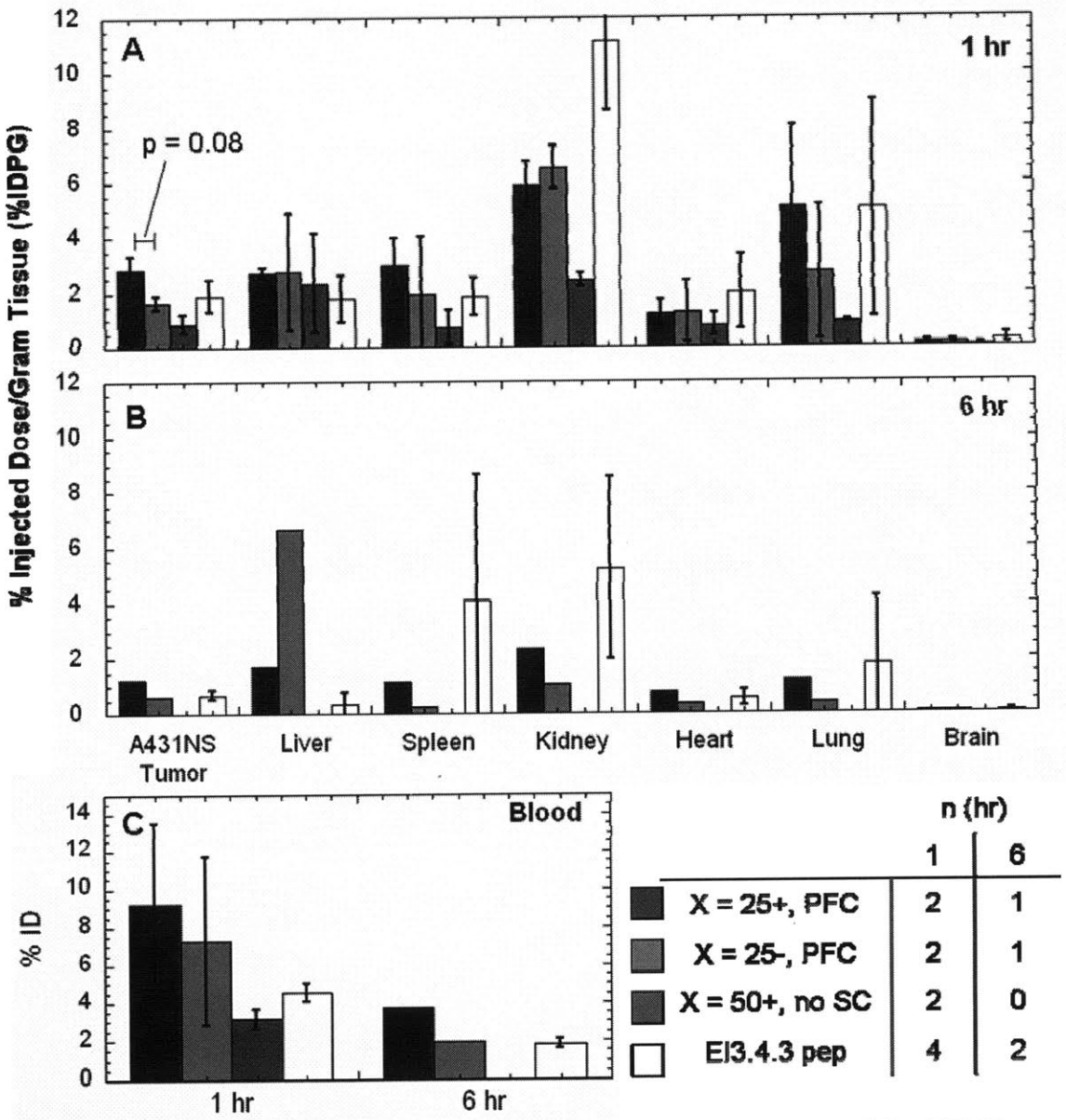

Figure 5.15. Biodistribution and blood circulation results for batch 1 polymers and free EI3.4.3 peptide (open bars). The number of animals, n, for each polymer at the 1 and 6 hr time points is tabulated.

Although there was significant *in vitro* uptake measured for the X=50+, NHS polymer (12B) with hydrodynamic diameters recorded between 20 and 80 nm (9F), the tumoral accumulation for this polymer was the lowest of all measured.

The highest overall %IDPGs were measured in the kidneys. Accumulation in the kidney would typically be observed before excretion in the urine. For the X=50+, NHS polymer, the low %IDPG in the kidney together with the low %ID in the blood indicate that the majority of the injected dose had been excreted before the 1 hr time point. The %ID for the X=50+, NHS was lower than that for the free peptide even though the polymer contained approximately 5 EI3.4.3 peptides attached to the high molecular weight polymer backbone by PEG3400 spacers. It is also possible that the EI3.4.3 peptides were associating with one another to lead to particle or aggregate formation and, in doing so, became inaccessible to EGFR.

Overall, there was accumulation measured in the other clearance organs, the liver and spleen, as well as some accumulation in the heart and, in particular, the lungs. It is possible that bleeding in the thoracic cavity during organ harvest contributed to the elevated activities measured in the lungs. Finally, there was no activity measured in the brain for any of the samples, which indicated that the injected material was unable to cross the blood-brain barrier. Based on this observation, the brain was not harvested in subsequent biodistribution measurements.

For the second synthesis batch, the stomach was also collected because the stomach as well as the thyroid, which was not recovered, can act as sinks for cleaved ^{125}I due to their iodide-specific ion channels [48]. For this second batch, the greatest tumoral %IDPG measured was for the X=50+, HC polymer (17B). This polymer also had the

greatest absolute uptake *in vitro* from this batch (13B). This %IDPG was over two times greater than that for the untargeted X=50-, HC polymer. The p-value for these two sets of data was 0.15.

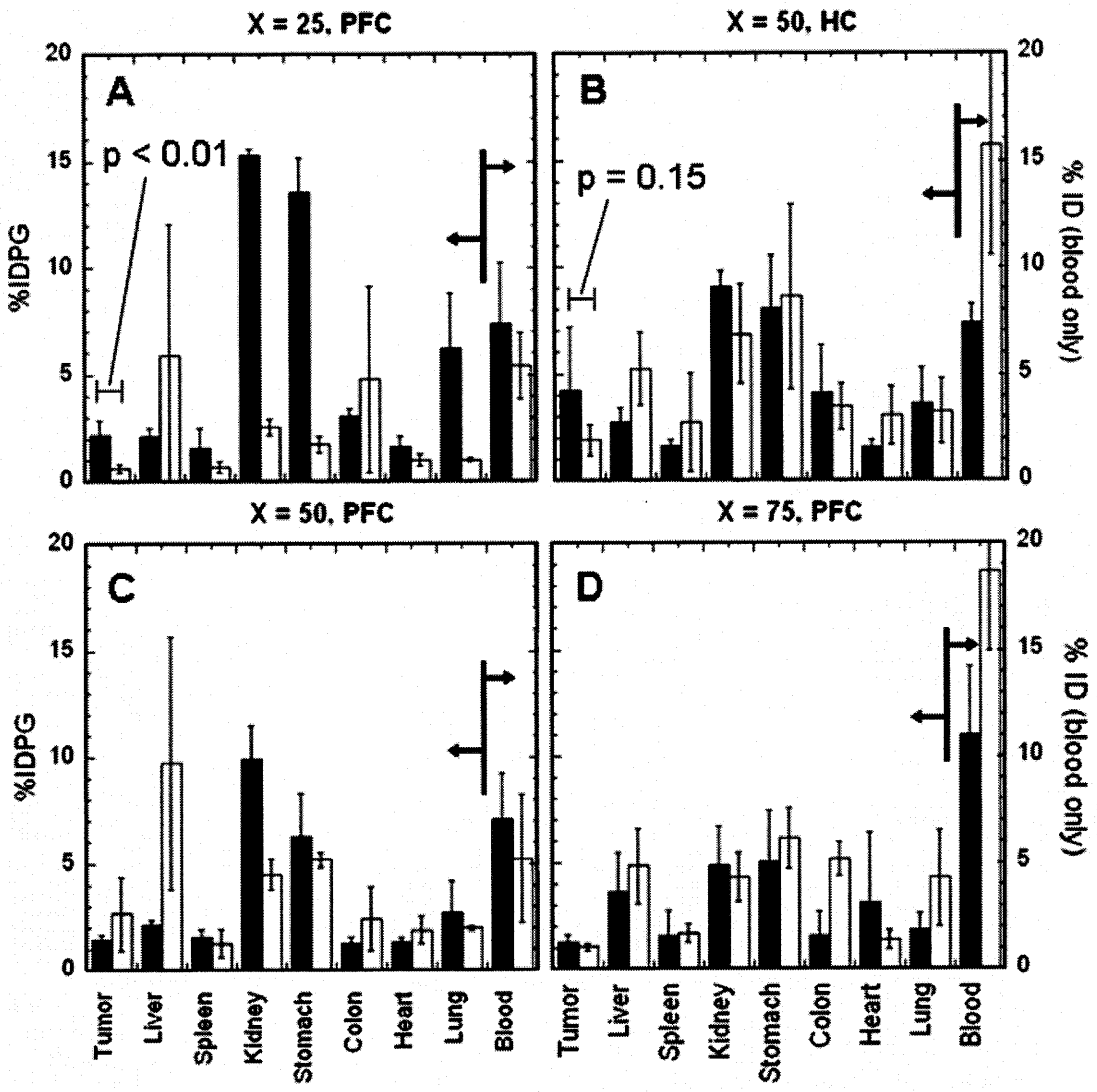

Figure 5.16. Biodistribution and blood circulation results for the second batch of polymers. All mice were sacrificed 1 hr post-injection. Blood data are presented as %ID (right axis), while the remaining data for the harvested organs are presented as %IDPG (left axis). There were three animals in each experimental group.

There was also significant selective tumor accumulation observed for the X=25, PFC polymer pair (17A). For this pair, the %IDPG for the targeted polymer was four times that of its untargeted counterpart. The accumulation for the X=25+, PFC was also

higher than that for X=25-, PFC in many of the organs harvested, most notably the kidney and the stomach. Although the %IDPG values were significantly higher in these organs, there was no statistical difference between the two X=25, PFC polymers for the %ID in the blood ($p = 0.64$). The selective accumulation of the EI3.4.3-conjugated polymer relative to the untargeted control was observed despite the fact that minimal selectivity was observed for this polymer *in vitro* (14A). The selective accumulation did, however, reproduce the biodistribution results for this same polymer formulation when it was synthesized in the first batch (16A). The %ID measured in the blood for the X=25, PFC polymers was also comparable between the two batches.

Finally, no selective accumulation was observed in the tumor for the X=50, PFC or X=75, PFC polymers.

5.4.11 Tumor Targeting Compartmental Model Predictions

The tumor targeting compartmental model of Schmidt and Wittrup was used to simulate the tumoral accumulation of three different targeted delivery agents: (1) the free EI3.4.3 peptide (12.5 kDa) and particles with hydrodynamic diameters of (2) 10 nm and (3) 20 nm. Larger particle sizes were not investigated because they would be out of range for the developed model. Each particle size was also simulated at three different dissociation constants: 250 pM, 250 μM, and 250 mM (FIGURE 5.18). The range of dissociation constants was selected because, although the native EI3.4.3 peptide had a K_D of 250 pM, steric effects or iodine-125 molecules in the binding site could reduce the effective binding constant of either the free peptide or peptide-conjugated particles.

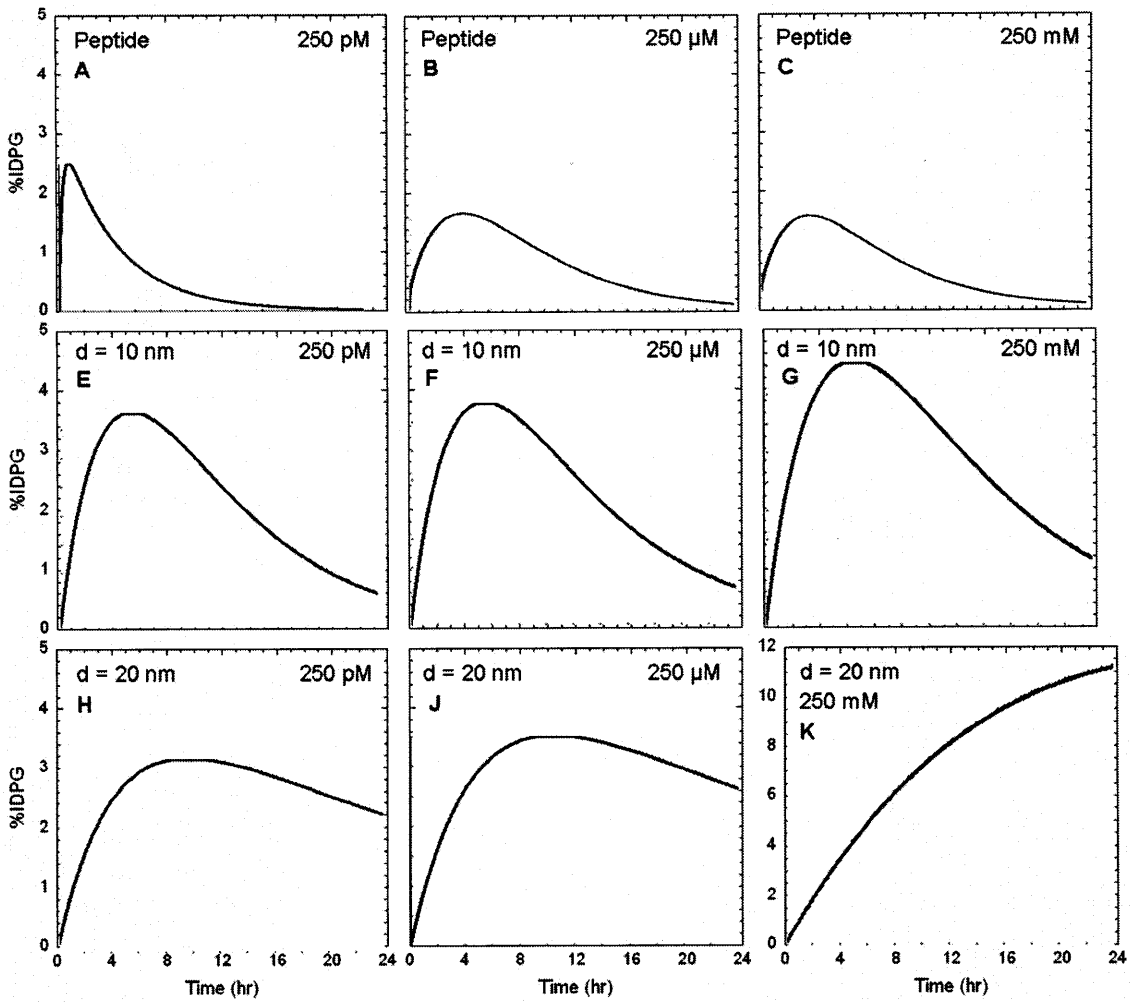

Figure 5.17. Simulation results using the tumor targeting compartmental model for three particle sizes (free 12.5 kDa EI3.4.3 peptide, and 10 and 20 nm diameter particles) at three binding dissociation constants (K_D). The results are presented as theoretical %IDPG in the tumor as a function of time. All y-axes are scaled identically with the exception of (K).

The general trend predicted by the model is an increase in accumulation in the tumor followed by a gradual decrease. The most rapid increase in %IDPG was predicted for the free peptide with a K_D of 250 pM (18A). This peptide would bind strongly to the receptors on the tumor while having comparatively minimal size-related mass transfer limitations. For the particles with a 10 nm diameter, the greatest predicted accumulation was actually for the particle having a K_D of 250 mM (18G). Because the renal clearance rate was identical for all of these equally sized particles, the decrease in predicted tumoral %IDPG would be entirely due to label catabolism and efflux.

The predicted %IDPG for the larger, 20 nm diameter particles increased more gradually than the smaller, 10 nm particles. This relatively slower increase was attributable to size-related limitations in the particle mass transfer. For the d = 20 nm, K_D = 250 mM simulation (18K), the predicted %IDPG increased monotonically over the entire simulated timeframe. This result suggested that the particle circulated freely with minimal renal clearance, but that it also bound and penetrated the tumor at a slow rate. This slow tumor penetration would also lead to a low rate of label catabolism and influx. It is also possible that the combination of these parameters led to a case that was outside the intended range of the model.

The model predictions were also compared to the experimental results. For the free EI3.4.3 peptide, the %IDPG was approximately 2 and 0.75% at 1 and 6 hr, respectively. These results compare favorably to the model predictions for the free peptide with a K_D of 250 pM, which were 2.4 and 0.6% for 1 and 6 hr, respectively. For the particles, the model predicted much lower accumulation in the tumor at 1 hr, between 0.5 and 1% IDPG depending on the simulated particle size and dissociation constant.

5.5 Discussion

5.5.1 In vitro Targeting with EI3.4.3-conjugated Polymers – Initial Study

The EI3.4.3 peptide was identified as a targeting ligand of interest due to its extremely high affinity for its target (K_D = 250 pM for EGFR), and its relatively straightforward and economical recombinant production in bacteria. The particle sizes for the four polymers synthesized for this initial study were consistent with polymers studied previously in our lab by Dr. Jin Zhou Dawson [49].

Both targeted polymers, with either the PEG3400 or TEG spacer, demonstrated an approximately twofold increase in selective uptake *in vitro* relative to untargeted controls after 4 hr. This difference was statistically significant with a p-value < 0.01. Interestingly, there was no selectivity at the 1 hr time point. This suggested that the binding and internalization required more than one hour to yield selective uptake. The demonstrated selectivity of the EI3.4.3-conjugated polymers *in vitro*, together with the economic advantages of EI3.4.3 production, strongly indicated the potential of the EI3.4.3-EGFR targeting pair for further study.

5.5.2 Evaluation of Preparative GPC for Backbone Polymer Fractionation

There was strong evidence in the literature [50-52], as well in previous work in our group [40], that polyvalency – increasing the multiplicity of targeting ligands on a particle or polymer chain – would be a key design variable for effective receptor targeting. Low molecular weight backbone polymer provided little opportunity to increase polyvalency due to the direct tradeoff between targeting and hydrophobic sidechains; increasing targeting inhibits particle formation.

Additionally, although the polymers synthesized from the lower molecular weight backbone polymer formed particles with diameters of 5-10 nm, particles of this size did not quite meet one of the key design constraints for circulating delivery vehicles. Glomerular clearance in the kidney leads to nearly complete first-pass clearance of particles with diameters less than 5 nm [2, 44, 53]. Blood circulation of particles with diameters between 5-10 nm may also be affected by kidney filtration. Consequently, the potential to form larger particles was a second benefit of increasing polymer molecular weight.

The preparative GPC was used effectively to produce monodisperse fractions of the backbone polymer with polydispersities between 1.12 and 1.17. These low PDIs were particularly encouraging considering the polydispersity of the backbone polymer sample loaded onto the preparative GPC column, 2.30. There is opportunity to create even more monodisperse fractions by decreasing the volume of the collected fraction; however, this leads to a tradeoff in the amount of mass in the particular fraction.

The highest molecular weight chains in the initial backbone polymer sample were not collected in any of the fractions. It is possible that these high molecular weight chains were not loaded onto the column in the first place, having been removed from the sample during syringe filtration performed to remove any particulates that may clog the lines. Removal during this initial filtration is possible considering the fact that high molecular weight PEGs have limited solubility in water. These insoluble or, more likely, poorly soluble high molecular weight backbone polymer chains could have been removed during the filtration. Other possible points of loss include the preparative GPC process and the freeze-drying of the recovered fractions. The increased system pressure during the course

of single- or multiple-injection preparative GPC runs may have been a result of high molecular weight chains exiting the solution and clogging the pores of the column; however, the pressure increase in the system would have been much more substantial had 30% of the loaded mass become effectively stuck in the column. Finally, although some polymer degradation was observed as a result of freeze drying, no degradation was observed that could account for the large loss of the highest molecular weight material.

The overall goal of the preparative GPC experiments was to develop a tool to isolate high molecular weight fractions from a raw, high molecular weight, polydisperse backbone polymer starting material. This meant that some questions that arose during these initial experiments were left unanswered. There is room for further improvement, particularly with respect to the recovery of the highest molecular weight fractions. To this end, different mobile phases for which the backbone polymer solubility is maximized would need to be investigated. Fortunately, the Superdex 75 column has a broad range of chemical compatibility.

Despite the unanswered questions, the developed high-through process was able to supply the starting material for the synthesis of the targeted and control polymers used in the biological studies.

5.5.3 In vitro Uptake of EI3.4.3-Conjugated Polymer Synthesized from High Molecular Weight Backbone Polymer

Having identified the EI3.4.3 and EGFR as a promising targeting pair, two primary variables of interest were studied: (1) the targeting ligand density, which is directly related to the percent of sidechains substituted with PEG3400 spacers, and (2) the identity of the hydrophobic sidechain (hydrocarbon, perfluorocarbon, or no added

sidechain). The polymer molecular weight was omitted as a variable to make the library more tractable and to minimize the number of synthetic steps. Results were separated by batch number to emphasize that each polymer was usually synthesized only once or, at most, twice.

The fourfold increase for the X=25+, PFC polymer was the greatest increase in selective uptake observed to this date with our polymer system. Unfortunately, it is difficult to draw comparisons of this result to the literature. The *in vitro* data in the literature typically relates to cell death caused by the delivery of a therapeutic agent or the silencing of some gene by delivery of siRNA, for example. This makes direct quantitative comparison tenuous. The fourfold difference in selectivity, however, is within the range observed for other polymeric micelle [31, 54] and dendrimeric [11] systems. It was also interesting that only minimal selective uptake was observed for the X=25+, HC polymer, which was identical to the X=25+, PFC with the exception of the hydrophobic sidechain. This result emphasized the importance of the sidechain identity as a key variable, as well.

The uptake for the X=50+, HC and X=50+, no other SC also appeared to be increased due to selectivity, but it was difficult to firmly conclude this because no negative control polymers were synthesized for either of these two formulations. Because of this, all polymers for the second batch were synthesized both with and without the EI3.4.3 peptide attached.

There was a significant difference in the absolute magnitudes of the polymer masses per cell between the two sets of data. This discrepancy was partially attributed to the total cell counts measured for the two uptake experiments, which differed by a factor

of two. However, the cell count variations did not account for the entire difference. There may have also been some unknown, systematic experimental error during the second batch uptake experiment. As previously discussed, the ability to perform repetitions was limited by both material limitations and the screening-oriented nature of the overall experimental plan.

5.5.4 Uptake Measurements in EGFR-positive and negative Cell Lines

It was quite difficult to select an EGFR-negative cancer cell line to try and measure passive, untargeted uptake. The MCF-7 cell line constitutively expresses EGFR at a low level, especially relative to A431NS cells ($3x10^3$ receptors per cell [46] versus more than $2x10^6$ [55]). The uptake data for A431NS and MCF-7 cells were compared after controlling for the significant difference in individual cell surface area. This adjustment relies on the assumption that both passive and active (i.e. targeted) cellular uptake were cell-surface area dependent processes. The results of this normalization by the area of a single well (i.e. the cell surface area in a confluent well) validated the choice to normalize by surface-area. The fact that the uptake per area for the untargeted polymer in the EGFR-positive cell line was nearly identical to that for the polymers in the EGFR-negative cell line confirmed that the MCF-7 cell line was a suitable choice as a receptor-negative cell line.

Although significant emphasis has been focused on increasing selectivity by increasing the uptake of the targeted polymers, selectivity can also be increased by decreasing the non-specific uptake. The fact that the uptake for the three non-specific cases is not only non-zero but the same order-of-magnitude as the specific uptake further emphasized this point. Strategies to reduce non-specific uptake exist in the literature,

most notably through the addition of negative charge to the particle surface. Such modifications would require additional synthetic development, but may prove extremely beneficial to increasing *in vitro* selectivity.

5.5.5 Analysis of Uptake Normalized by Initial EI3.4.3 Peptide Concentration

The uptake data were also processed to determine targeting efficiency as a function of peptide substitution. This analysis, which was independent of any size measurements, was performed to determine a potentially optimal level of substitution that maximizes targeting efficiency. In both batches, the X=25, PFC polymers exhibited highly efficient targeting relative to the other studied polymers, while the X=50, HC polymer was also highly efficient among the second batch polymers. Based on the results of this analysis, additional peptide substitution levels should be investigated between X=10 and X=50 to establish a greater continuum of substitutions.

5.5.6 Biodistribution and Blood Circulation in a Mouse Model of Human Cancer

Overall, the polymer accumulation in non-target organs, including the liver, spleen, and kidney, was relatively low. Significant accumulation in these organs usually indicates potential issues in toxicity studies. Comparing the %IDPG to comparable delivery systems in the literature ([54, 56], among others), which report %IDPG for liver and kidney greater than 10-20%, the general biodistribution profile for our system was encouraging. There was very little measurable signal in the brain, which implied that the polymers and free peptide were unable to cross the blood-brain barrier.

The greatest tumoral accumulation was observed for the X=25+, PFC polymer at 2.8% and the X=50+, HC polymer at 4.1%. This level of tumor accumulation compared quite favorably with the literature, in which %IDPG in the tumor typically ranged

between 1-4% [54, 56]. In their recent work, Poon and Hammond have successfully achieved %IDPG of greater than 10% in the tumor using their dendritic block copolymers. This result significantly outperforms other reports in the literature, including those in this work.

At this absolute magnitude of accumulation (2.8%) and selectivity relative to the untargeted control (twofold), the X=25+, PFC polymer labeled similarly with iodine-124, a positron emitting isotope, would be able to be visualized by positron emission tomography [57].

With respect to particle size and glomerular filtration, it is important to remember that the polymeric micelles experience significant dilution both upon injection and as particles are removed from the circulatory system. The rate of particle breakdown in the bloodstream depends on the stability of the micelle and the local concentration of the polymer. If rapid clearance was observed for a given polymer/particle, as was the case for the X=50+, NHS polymer, this would be an indication that the particles were rapidly dissociating in the bloodstream. There is also some evidence in the literature of PEG-mediated specific accumulation in the kidney [58], which may account for the substantially greater rate of clearance for the X=50+, NHS polymer relative to that for the free EI3.4.3 peptide. Overall, the increased circulation time, as evidenced by the measured %ID values, suggests that the majority of the particles were stable in the bloodstream at least to a certain extent.

For the second batch, biodistribution measurements were performed for four pairs of targeted and untargeted polymer having different particle size distributions as well as

various performances *in vitro*. The brain was not recovered during this study since there was no evidence in earlier studies that the polymer crossed the blood-brain barrier.

The second biodistribution experiment was able to repeat the selective accumulation of the X=25+, PFC polymer observed in the first study, with a %IDPG that was four times higher than that for the untargeted control, X=25-, PFC. It was also interesting that this selective accumulation was observed despite the fact that only minimal selectivity was observed *in vitro* for the second synthesis of the X=25, PFC polymer pair.

The elevated %IDPG values for the kidney and stomach were likely indicative of deiodination, an oxidase-mediated process that occurs upon internalization into cells [44, 47, 48, 59]. While the kidney accumulation was a function of its normal blood filtration, the stomach as well as the thyroid, which was not recovered, act as sinks for cleaved ^{125}I due to their iodide-specific ion channels [48]. Because tumors do not actively accumulate iodide, the measured tumoral activity was representative of radioiodine bound to either polymer or peptide. The elevated %IDPG in the stomach and kidney, especially compared to the untargeted control, may actually have been a 'symptom' of tumoral accumulation because increased cellular internalization of the X=25+, PFC polymer would lead to increased deiodination. (This label catabolism process was described while presenting the tumor compartmental model of Schmidt and Wittrup.)

The targeted X=50, HC polymer achieved the highest tumoral accumulation among the second batch with a %IDPG greater than 4. The experimental error was high enough that there was relatively poor statistical significance between the targeted and control polymers ($p = 0.18$). Selective accumulation of targeted polymer occurred even

though the blood concentration of untargeted polymer was statistically higher ($p<0.05$, $p=0.0495$) than the EI3.4.3-conjugated polymer.

The lack of selectivity observed for the remaining polymers in the second batch may be attributable to their inability to form well-behaved micelles. Their comparatively broad and disjointed particle size distributions suggested that the highly substituted polymers may have formed aggregates as opposed to micelles due to the high degree of PEGylation. Past work has suggested the aggregation phenomenon for highly PEGylated polymer is unstable and varies greatly with time [40].

It is also important to note that the experimental group sizes were small. Ideally, group sizes would have been preferably 5 or more animals. Nonetheless, there was moderate to high statistical significance observed for three different sets of polymers studied: the X=25+, PFC polymer in both batches and the X=50+, HC polymer in the second batch. Together, these were the first *in vivo* demonstrations of selectivity for our polymers.

5.5.7 Comparison to Theoretical Model Predictions

The tumor targeting compartmental model of Schmidt and Wittrup [44], which expanded upon the work of Thurber and Wittrup [60, 61], was solved for three different particle sizes and three different binding affinities.

Since the *in vivo* studies were designed to screen for the most promising formulation, the investigation of a multitude of time points was impractical; however the model predictions suggest that time course data would be valuable in evaluating the *in vivo* performance of a targeted polymer. For example, the time course data could be compared to the nine plots generated by the tumor compartmental model to estimate the

particle size and dissociation constant *in vivo*. Conclusions about the physical state of the particle (i.e. micelle versus individual chain) should be apparent from these comparisons.

Schmidt and Wittrup also compared their model predictions to data from the literature to assess the precision of their model. They found excellent agreement between the model and experiment for small peptides and antibody fragments and less precision for nanoparticles. Considering this, the differences between the model predictions and the experimental results described herein were reasonable.

5.6 Conclusion

A novel construct combining the high affinity binder, EI3.4.3, with amphiphilic alternating copolymers was investigated. Backbone polymer produced by the Protherm reactor was successfully fractionated into low polydispersity, high molecular weight starting material for use in subsequent synthetic steps. These high molecular weight fractions allowed for increased substitution of targeting sidechains while still allowing for attachment of the hydrophobic sidechains required to impart amphiphilicity to the molecule.

Initial studies demonstrated selective uptake of EI3.4.3-conjugated polymers into a target-bearing, EGFR-positive human cancer cell line relative to untargeted controls. Polymers synthesized from the fractionated backbone polymer achieved the greatest increase in selective uptake observed for this system (approximately 4-6X). Animal studies were performed to assess the biodistribution, blood circulation, and tumoral accumulation behavior of various polymer formulations. Selective tumor accretion was observed for two different targeted polymers, X=25, PFC and X=50, HC, including for

two separate syntheses of the former. A number of potential correlative relationships were considered, including the effect of particle size on blood circulation and the ability of *in vitro* experiments to predict selectivity *in vivo*.

The EI3.4.3-polymers have proven a rich platform for study. Their demonstrated ability to selectively accumulate in targeted tumors combined with their potential use in diagnostic and/or therapeutic clinical applications makes them an attractive option for intensified investigation.

5.7 References

1. Torchilin, V.P., Trubetskoy, V. S., *Which polymers can make nanoparticulate drug carries long-circulating?* Adv Drug Delivery Rev, 1995. **16**: p. 141-155.
2. Gref, R., Domb, A., Quellec, P., Blunk, T., Muller, R. H., Verbavatz, J. M., Langer, R., *The controlled intravenous delivery of drugs using PEG-coated sterically stabilized nanospheres.* Adv Drug Delivery Rev, 1995. **16**: p. 215-233.
3. Torchilin, V.P., *Recent advances with liposomes as pharmaceutical carriers.* Nature Reviews, 2005. **4**: p. 145-160.
4. Gabizon, A., Goren, D., Horowitz, A. T., Tzemach, D., Lossos, A., Siegal, T., *Long-circulating liposomes for drug delivery in cancer therapy: A review of biodistribution studies in tumor-bearing animals.* Adv Drug Delivery Rev, 1997. **24**(2-3): p. 337-344.
5. Klibanov, A.L., Maruyama, K., Beckerleg, A. M., Torchilin, V. P., Huang, L., *Acitivity of aphipathic poly(ethylene glycol) 5000 to prolong the circulation time of liposomes depnds on the liposome size and is unfavorable for immunoliposome binding to target.* Biochimica et Biophysica Acta, 1991. **1062**: p. 142-148.
6. Sharma, A., Sharma, U. S., *Liposomes in drug delivery: progress and limitations.* International J Pharmaceutics, 1997. **154**: p. 123-140.
7. De Rosa, G., De Stefano, D., Galeone, A., *Oligonucleotide delivery in cancer therapy.* Expert Opinion on Drug Delivery, 2010. **7**(11): p. 1263-1278.
8. Tomalia, D.A., Frechet, J. M., *Discovery of dendrimers and dendritic polymers: A brief historical perspective.* J Polymer Science: Part A: Polymer Chemistry, 2001. **40**: p. 2719-2728.
9. Ambabe, A.V., Savariar, E. N., Thayumanavan, S., *Dendrimeric micelles for controlled drug release and targeted delivery.* Molecular Pharmaceutics, 2005. **2**(4): p. 264-272.
10. Thomas, T.P., Patri, A. K., Myc, A., Myaing M. T., Ye, J. Y., Norris, T. B., Baker Jr., J. R., *In vitro targeting of synthesized antibody-conjugated dendrimer nanoparticles.* Biomacromolecules, 2004. **5**: p. 2269-2274.

11. Thomas, T.P., Choi, S. K., Li, M-H., Kotlyar, A., Baker Jr., J. R., *Design of riboflavin-presenting PAMAM dendrimers as a new nanoplatform for cancer-targeted delivery.* Bioorganic Med Chem Letters, 2010. **20**: p. 5191-5194.
12. Mullen, D.G., Borgmeier, E. L., Fang, M., McNerny, D. Q., Desai, A., Baker Jr., J. R., Orr, B. G., Holl, M. M. B., *Effect of mass transport in the synthesis of partially acetylated dendrimer: Implications for functional ligand-nanoparticle distributions.* Macromolecules, 2010. **43**: p. 6577-6587.
13. Poon, Z., Chen, S., Engler, A. C., Lee, H. I., Atas, E., von Maltzahn, G., Bhatia, S. N., Hammond, P. T., *Ligand-clustered patchy nanoparticles for modulated cellular uptake and in vivo tumor targeting.* Angewandte Chemie-International Edition, 2010. **49**(40): p. 7266-7270.
14. Neuberger, T., Schopf, B., Hofmann, H., Hofmann, M., von Rechenberg, B., *Superparamagnetic nanoparticles for biomedical applications: Possibilities and limitations of a new drug delivery system.* J Magnetism Magnetic Materials, 2005. **293**: p. 483-496.
15. Moore, A., Medarova, Z., Potthast, A., Dai, G., *In vivo targeting of underglycosylated MUC-1 tumor antigen using a multimodal imaging probe.* Cancer Research, 2004. **64**: p. 1821-1827.
16. Medarova, Z., Pham, W., Kim, Y., Dai, G., Moore, A., *In vivo imaging of tumor response to therapy using a dual-modality imaging strategy.* Int J Cancer, 2006. **118**: p. 2796-2802.
17. Voura, E.B., Jaiswal, J. K., Mattoussi, H., Simon, S. M., *Tracking metastatic tumor cell extravasation with quantum dot nanocrystals and fluorescence emission-scanning microscopy.* Nature Medicine, 2004. **10**(9): p. 993-998.
18. Torchilin, V.P., *Structure and design of polymeric surfactant-based drug delivery systems.* J Controlled Release, 2001. **73**: p. 137-172.
19. Allen, C., Maysinger, D., Eisenberg, A., *Nano-engineering block copoymer aggregates for drug delivery.* Colloids and Surfaces B: Biointerfaces, 1999. **16**: p. 3-27.
20. Kataoka, K., Harada, A., Nagasaki, Y., *Block copolymer micelles for drug delivery: design, characterization and biological significance.* Adv Drug Delivery Rev, 2001. **47**: p. 113-131.
21. Rosler, A., Vandermeulen, G. W. M., Klok, H-A., *Advanced drug delivery devices via self-assembly of amphiphilic block copolymers.* Adv Drug Delivery Rev, 2001. **53**: p. 95-108.
22. Maeda, H., Wu, J., Sawa, T., Matsumura, Y., Hori, K., *Tumor vascular permeability and the EPR effect in macromolecular therapeutics: a review.* J Controlled Release, 2000. **65**: p. 271-284.
23. Maeda, H., *The enhanced permeability and retention (EPR) effect in tumor vasculature: the key role of tumor-selective macromolecular drug targeting.* Advan Enzyme Regul, 2001. **41**: p. 189-207.
24. Noguchi, Y., Wu, J., Duncan, R., Strohalm, J., Ulbrich, K., Akaike, T., Maeda, H., *Early phase tumor accumulation of macromolecules: a great difference in clearance rate between tumor and normal tissues.* Jpn J Cancer Res, 1998. **89**: p. 307-314.

25. Hobbs, S.K., Monsky, W. L., Yuan, F., Roberts, W. G., Griffith, L., Torchilin, V. P., Jain, R. K., *Regulation of transport pathways in tumor vessels: Role of tumor type and microenvironment.* PNAS, 1998. **95**: p. 4607-4612.
26. Alexis, F., Pridgen, E., Molnar, L. K., Farokhzad, O. C., *Factors affecting the clearance and biodistribution of polymeric nanoparticles.* Molecular Pharmaceutics, 2008. **5**(4): p. 505-515.
27. Torchilin, V.P., *Tumor delivery of macromolecular drugs based on the EPR effect.* Adv Drug Delivery Rev, 2010. **In Press**.
28. Yokoyama, M., Lnoue, S., Kataoka, K., Yui, N., Sakurai, Y., *Preparation of adriamycin-conjugated poly(ethylene glycol)-poly(aspartic acid) block copolymer: A new type of plymeric anticancer agent.* Macromol Rapid Commun, 1987. **8**: p. 431-435.
29. Yokoyama, M., Fukushima, S., Uehara, R., Okamoto, K., Kataoka, K., Sakurai, Y., Okano, T., *Characterization of physical entrapment and chemical conjugation of adriamycin in polymeric micelles and their design for in vivo delivery to a solid tumor.* J Controlled Release, 1998. **50**: p. 79-92.
30. Mo, Y., Lim, L-Y., *Paclitaxel-loaded PLGA nanoparticles: Potentiation of anticancer activity by surface conjugation with wheat germ agglutinin.* J Controlled Release, 2005. **108**: p. 244-262.
31. Xiong, X.-B., Uludag, H., Lavasanifar, A., *Virus-mimetic polymeric micelles for targeted siRNA delivery.* Biomaterials, 2010. **31**: p. 5886-5893.
32. Gaucher, G., Marchessault, R. H., Leroux, J-C., *Polyester-based micelles and nanoparticles for the parenteral delivery of taxanes.* J Controlled Release, 2010. **143**: p. 2-12.
33. Farokhzad, O.C., Cheng, J., Teply, B. A., Sherifi, I., Jon, S., Kantoff, P. W., Richie, J. P., Langer, R., *Targeted nanoparticle-aptamer bioconjugates for cancer chemotherapy in vivo.* PNAS, 2006. **103**(16): p. 6315-6320.
34. Ellington, A.D., Szostak, J. W., *In vitro selection of RNA molecules that bind specific ligands.* Nature, 1990. **346**(6287): p. 818-822.
35. Liu, J., Zhang, Q., Remsen, E., Wooley, K., *Nanostructured materials designed for cell binding and transduction.* Biomacromolecules, 2001. **2**: p. 362-368.
36. Bronich, T.K., Keifer, P. A., Shlyakhtenko, L. S., Kabanov, A. V., *Polymer micelle with cross-linked ionic core.* JACS, 2005. **127**: p. 8236-8237.
37. Murthy, K.S., Ma, Q., Clark, Jr., C. G., Remsen, E. E., Wooley, K., L., *Fundamental design aspects of amphiphilic shell-crosslinked nanoparticles for controlled release applications.* Chem Commun, 2001: p. 773-774.
38. Du, W.J., Nystrom, A. M., Zhang, L., Powell, K. T., Li, Y. L., Cheng, C., Wickline, S. A., Wooley, K. L., *Amphiphilic hyperbranched fluoropolymers as nanoscopic F-19 magnetic resonance imaging agent assemblies.* Biomacromolecules, 2008. **9**(10): p. 2826-2833.
39. O'Reilly, R.K., Joralemon, M. J., Hawker, C. J., Wooley, K. L., *Preparation of orthogonally-functionalized core click cross-linked nanoparticels.* New Journal of Chemistry, 2007. **31**(5): p. 718-724.
40. Miller, M.T., *In vitro evaluation of cytotoxicity and cellular uptake of alternating copolymers for use as drug delivery vehicles*, in *Chemical Engineering*. 2009, MIT: Cambridge.

41. Hackel, B.J., *Fibronectin Domain Engineering*, in *Chemical Engineering*. 2009, M.I.T.
42. Hackel, B.J., Kapila, A., Wittrup, K. D., *Picomolar affinity fibronectin domains engineered utilizing loop length diversity, recursive mutagenesis, and loop shuffling.* J Molecular Biology, 2008. **281**(5): p. 1238-1252.
43. Hackel, B.J., Ackerman, M., Howland, S., Wittrup, K. D., *Stability and completementarity-determining region biases enrich binder functionality landscapes.* J Molecular Biology, 2010.
44. Schmidt, M.M., Wittrup, K. D., *A modeling analysis of the effects of molecular size and binding affinity on tumor targeting.* Molecular Cancer Therapeutics, 2009. **8**(10): p. 2861-2871.
45. Nugent, L.J., Jain, R. K., *Pore and fiber-matrix models for diffusive transport in normal and neoplastic tissues.* Microvasc Res, 1984. **28**: p. 270-274.
46. Imai, Y., Leung, C. K. H., Friesen, H. G., Shiu, R. P. C., *Epidermal growth factor receptors and effect of epidermal growth factor on growth of human breast cancer cells in long-term tissue culture.* Cancer Research, 1982. **42**: p. 4394-4398.
47. Press, O.W., Shan, D., Howell-Clark J., et. al., *Comparative metabolism and retention of iodine-125, yttrium-90, and indium-111 radioimmunoconjugates by cancer cells.* Cancer Research, 1996. **56**: p. 2123-9.
48. Shih, L.B., Thorpe, S. R., Griffiths, G. L., Diril, H., Ong, G. L., Hansen, H. J., Goldenberg, D. M., Mattes, M. J., *The processing and fate of antibodies and their radiolabels bound to the surface of tumor cells in vitro: A comparison of nine radiolabels.* J Nucl Med, 1994. **35**(5): p. 899-908.
49. Dawson, J.Z., *Physicochemical characterization of PEG-based comb-like amphiphilic copolymer structures for possible imaging and therapeutic applications*, in *Chemical Engineering*. 2008, MIT: Cambridge.
50. Rai, P., Padala, C., Poon, V., Saraph, A., Basha, S., Kate, S., Tao, K., Mogridge, J., Kane, R. S., *Statistical pattern matching facilitates the design of polyvalent inhibitors of anthrax and cholera toxins.* Nature Biotechnology, 2006. **24**(5): p. 582-586.
51. Hong, S., Leroueil, P. R., Majoros, I. J., Orr, B. G., Baker, Jr., J. R., Holl, M. M. B., *The binding avidity of a nanoparticle-based multivalent targeted drug delivery platform.* Chemistry & Biology, 2007. **14**: p. 107-115.
52. Gargano, J.M., Ngo, T., Kim, J. Y., Acheson, D. W. K., Lees, W. J., *Multivalent inhibition of AB5 toxins.* JACS, 2001. **123**: p. 12909-12910.
53. Caliceti, P., Veronese, F. M., *Pharmacokinetic and biodistribution properties of poly(ethylene glycol)-protein conjugates.* Adv Drug Delivery Rev, 2003. **55**: p. 1261-1277.
54. Gu, F., Zhang, L., Teply, B. A., Mann, N., Wang, A., Radovic-Moreno, A. F., Langer, R., Farokhzad, O. C., *Precise engineering of targeted nanoparticles by using self-assembled biointegrated block copolymers.* PNAS, 2008. **105**(7): p. 2586-2591.
55. Benveniste, M., Livneh, E., Schlessinger, J., Kam, Z., *Overexpression of epidermal growth factor receptor in NIH-3T3-transfected cells slows its lateral diffusion and rate of endocytosis.* J Cell Bio, 1988. **106**: p. 1903-1909.

56. Kukowska-Latallo, J.F., Candido, K. A., Cao, Z., Nigavekar, S. S., Majoros, I. J., Thomas, T. P., Balogh, L. P., Khan, M. K., Baker, Jr., J. R., *Nanoparticle targeting of anticancer drug improves therapeutic response in animal model of human epithelial cancer.* Cancer Research, 2005. **65**(12): p. 5317-5324.
57. Benaron, D.A., *The future of cancer inaging.* Cancer and Metastasis Rev, 2002. **21**: p. 45-78.
58. Torchilin, V.P., Narula, J., Halpern, E., Khaw, B. A., *Poly(ethylene glycol)-coated anti-cardiac myosin immunoliposomes: factors influencing targeted accumulation in the infarcted myocardium.* Biochimica et Biphysica Acta, 1996. **1279**: p. 75-83.
59. Collingridge, D.R., Glaser, M., Osman, S., Barthel, H., Hutchinson, O. C., Luthra, S. K., Brady, F., Bouchier-Hayes, L., Martin, S. J., Workman, P., Price, P. Aboagye, E. O., *In vitro selectivity, in vivo biodistribution and tumour uptake of annexin V radiolabeled with a positron emitting radioisotope.* British J Cancer, 2003. **89**(7): p. 1327-1333.
60. Thurber, G.M., Schmidt, M. M., Wittrup, K. D., *Factors determining antibody distribution in tumors.* Trends Pharmacol Sci, 2008. **29**(2): p. 57-61.
61. Thurber, G.M., Schmidt, M. M., Wittrup, K. D., *Antibody tumor penetration: Transport opposed by systemic and antigen-mediated clearnace.* Adv Drug Delivery Rev, 2008. **60**(12): p. 1421-1434.

Appendix A: Molecular Weight Calculation by Analytical GPC Breeze Software and Chromatogram Manipulation

The molecular weight was calculated using the Breeze software associated with the Waters GPC system. The PMMA calibration data (molecular weights and associated elution volumes) were entered into the software. To calculate the molecular weight for a given a chromatogram, a baseline was drawn and the 'Quantitate' button was pressed in the software to generate the number- and weight-average molecular weight, polydispersity index, and a number of other parameters according to the PMMA calibration.

In the screenshot (FIGURE A.1) as well as all other analyzed chromatograms, the baseline was drawn to include elution volumes between 15 and 27 mL. Any signal at elution volumes greater than the total volume of the column banks, 27 mL, was excluded from the analysis because any species eluting after this point, such as linker or water, could not be resolved from one another since they can fully enter the pores within the resin. The noisy signal at elution volumes greater than 29 mL is due to mobile phase impurities and small amounts of air dissolved in the sample.

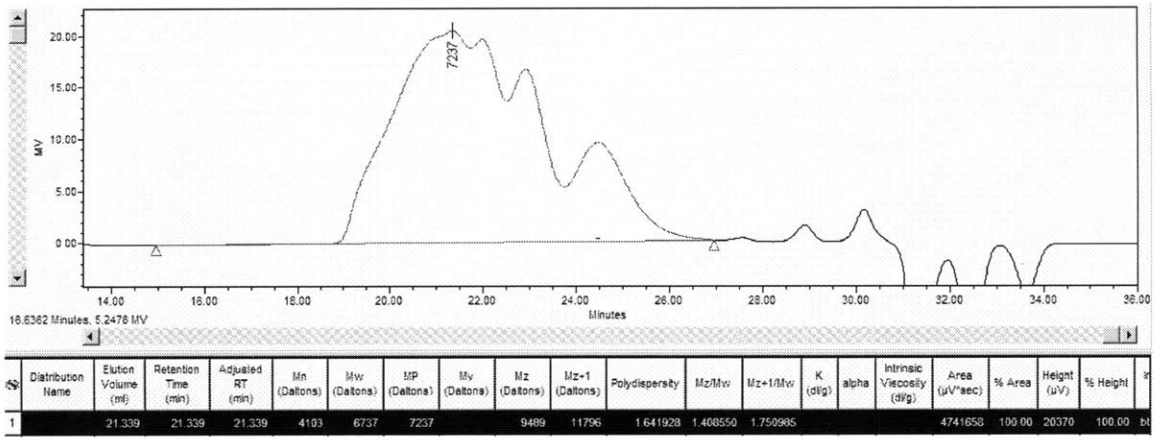

	Distribution Name	Elution Volume (ml)	Retention Time (min)	Adjusted RT (min)	Mn (Daltons)	Mw (Daltons)	MP (Daltons)	Mv (Daltons)	Mz (Daltons)	Mz+1 (Daltons)	Polydispersity	Mz/Mw	Mz+1/Mw	K (dl/g)	alpha	Intrinsic Viscosity (dl/g)	Area (µV*sec)	% Area	Height (µV)	% Height	
1		21.339	21.339	21.339	4103	6737	7237		9489	11796	1.641928	1.408550	1.750985				4741658	100.00	20376	100.00	

Figure A.1. Screenshot of Breeze GPC system software.

The accuracy of the Breeze molecular weight calculation algorithm was analyzed using a number of sample chromatograms. The chromatogram in FIGURE A.2, which relates refractive index (RI) response at various elution volumes, was chosen as a representative data set. As was the case in FIGURE A.1, only elution volumes between 15 and 27 mL were included in the analysis

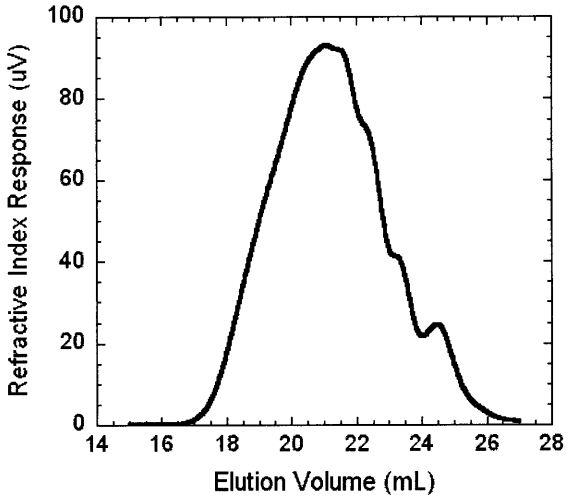

Figure A.2. Raw data output from the Breeze software. The polydisperse polymer sample exiting the column at various elution volumes is measured by a refractive index detector.

The instantaneous refractive index is recorded at equally spaced elution volume increments of 0.0166 mL. The frequency at which the data are recorded makes it appropriate to plot the chromatogram as a continuous line, as in FIGURE A.2. As described in the Polymerization Results, a standard kit containing samples of nearly monodisperse poly(methyl methacrylate) (PMMA) was used to calibrate the Styragel HR1, 3, and 4 column bank. The empirical relationship of Mori was used to convert the molecular weight according to PMMA into backbone polymer molecular weight. Using the calibration and empirical relationship, the x-axis can be transformed from elution volume to backbone polymer molecular weight (FIGURE A.3).

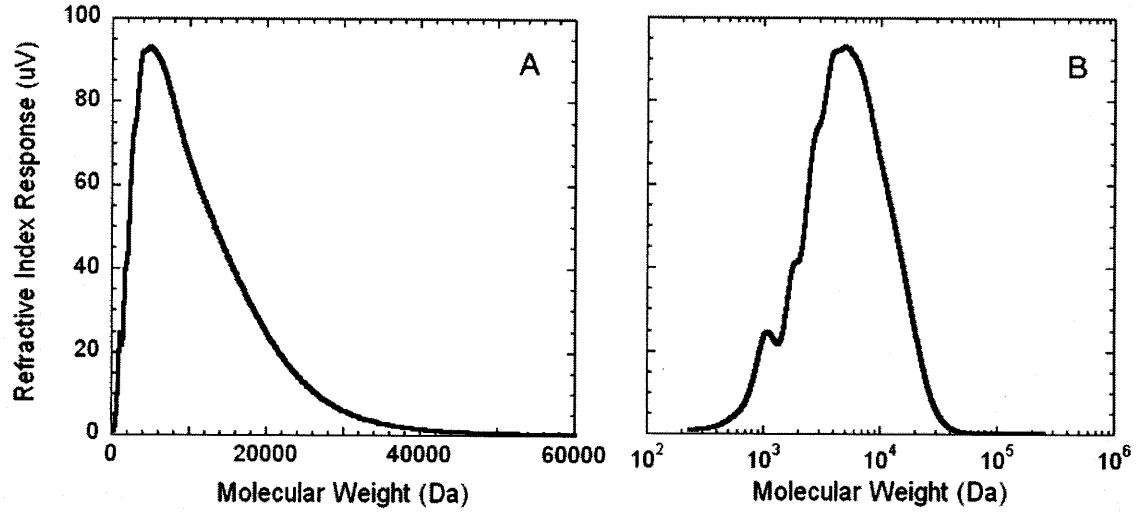

Figure A.3. Raw data refractive index response as a function of backbone polymer molecular weight on (A) rectangular and (B) semilogarithmic coordinates.

According to calculations performed within the Breeze software, this chromatogram had a number average molecular weight, M_n, of approximately 5.5 kDa. Upon inspection of the figure above, it may or may not be readily apparent whether or not this calculation is correct because the y-axis is the *RI response* for the species having various molecular weights and not the *number* of molecules at each molecular weight. Manipulations were performed to convert the y axis from RI response to number in order to better visualize the molecular weight distribution.

To convert RI response into number one must first understand the behavior of refractive index. Like other light-based phenomena, for example absorbance, which is governed by Beer's law, refractive index is proportional to the mass concentration of a species in solution. Therefore, a polymer having n repeat units will affect the refractive index of a solvent exactly the same way as n monomers in solution. Measurements of various molecules at various concentrations using the Waters RI detector have confirmed this (data not shown). The relationship between refractive index response, RI, and the mass concentration, C, can be written as follows:

$$RI = \alpha C \tag{1}$$

where α is a constant. The measurements shown in the preceding chromatograms are instantaneous representations of the refractive index made at regular intervals. Since the chamber through which the detector measures the RI never changes, the volume of eluent measured for each reading is identical. This allows the refractive index for the *i*th measurement, RI_i, to be directly related to the mass of material, m_i, associated with that reading:

$$RI_i = \left(\frac{\beta}{V_{cell}}\right) m_i \tag{2}$$

where V_{cell} is the volume of the cell in the RI detector. The mass present in the *i*th slice is related to the molecular weight of the *i*th slice, M_i. Therefore, the following relationship holds

$$m_i = \frac{N_i}{N_{Av}} M_i \tag{3}$$

where N_i is the number of molecules in the *i*th slice and N_{Av} is Avogadro's number. Combining EQUATIONS 2 and 3, yields an expression relating the number of molecules, N_i, having molecular weight, M_i, to the refractive index response:

$$N_i = \left(\frac{V_{cell} N_{Av}}{\beta}\right) \frac{RI_i}{M_i} \tag{4}$$

Using EQUATION 4, the y-axis from the chromatograms above (FIGURE A.3) can be converted from RI response to number by dividing by M_i. Since the pre-term is unknown, it was not included in the conversion and the y-axis becomes the relative number of molecules at a given molecular weight (FIGURE A.4). Knowledge of this pre-term is not required because it will be canceled out in subsequent steps in the derivation.

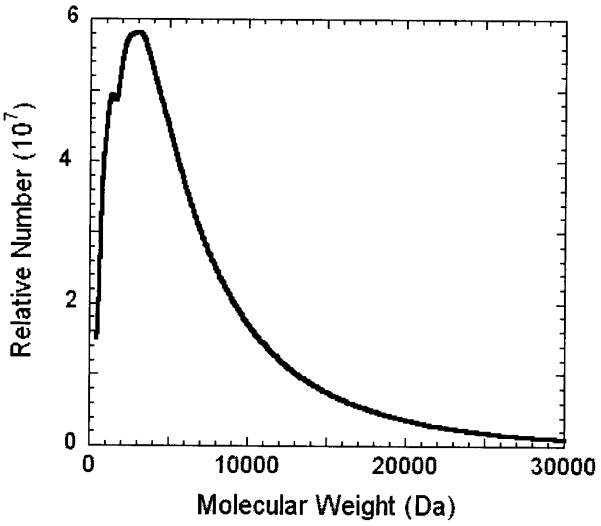

Figure A.4. Relative number of molecules at each backbone polymer MW for the sample chromatogram.

The number-average molecular weight can be calculated directly from the histogram in FIGURE 4 according to:

$$\bar{M}_n = \frac{\sum N_i M_i}{\sum N_i} \tag{5}$$

If it had been carried through, the unknown pre-factor in EQUATION 4 would cancel in EQUATION 5 and, consequently, does not need to be determined for this analysis. The number average molecular weight, M_n, calculated from FIGURE A.4 and EQUATION 5 is 5.5 kDa, which is identical to that determined by the Breeze software.

Appendix B: MATLAB Code for Kinetic and Mass transfer Modeling

The following program was used to simulate the weight-average molecular weight as a function of time for the homogeneous kinetic model. The program was also used to simulate the equilibrium molecular weight by setting 'tf' equal to $2x10^{10}$.

```
function [tmat,Mn] = polym_sim_water_Pn_test_Oct2010()

MA = 900;     % g/mol
MB = 210;
MM = 32;
M_0 = (MA + MB - 2*MM)/2;
M_eg = MM;

ti = 0;       % hour
tf = 20000;    % hour
tspan = [ti tf];

CA0 = 2;    % mol/L
CB0 = 2;

CL0 = 0;
CC0 = 0;
% CW0 = 1.5e-3;    % from KF drying experiments
CW0 = 0;
r = 1;

C0 = [CA0 CB0 CL0 CW0 CC0];

kf = 9.0e-3*60;    % L/mol-hr

Keq = 10;
kr = kf/Keq;

% set all other rate constants equal to kf for starters
kfh = kf;
krh = kf;
kfc = kf;
krc = kf;

% create a vector of methanol partial pressures and convert to
% concentration
PM = logspace(-4, 2, 4);    % mmHg
% PM = [50e-3,50e-3,50e-3,50e-3];
v_ave = 0.8;                  % L/mol
PM0 = 1900;                   % mmHg

for f=1:length(PM)
    CM(f) = PM(f)/(v_ave*PM0); %#ok<AGROW>
end

Clength = length(CM);
```

```
tamt = 150;
tmat = zeros(tamt,Clength);
Mn = zeros(tamt,Clength);

for Ci=1:Clength

[t,C] = ode15s(@fun, tspan, C0,[],kf,kr,CM(Ci),kfh,krh,kfc,krc);

tlength(Ci) = length(t);  %#ok<AGROW>

   for count=1:tlength(Ci)
       tmat(count,Ci) = t(count);
   end

fA = 1 - C(:,1)/CA0;    % fractional conversion of monomer A
fB = 1 - C(:,2)/CB0;

% calculate the degree of polymerization based on basic theory

for time=1:tlength(Ci)

    % call the function that calculates Pn
    Pn(time,Ci) = Pn_calc(fA(time),fB(time),r); %#ok<AGROW>

    % convert Pn to MW
    Mn(time,Ci) = Pn(time,Ci)*M_0 + M_eg;
    Mw(time,Ci) = M_0*(2*Pn(time,Ci)-1);  %#ok<AGROW>

end
end

% Clean up plot by making all indices that were left as zero equal to
the
% maximum
for Cj = 1:Clength
    tmax = tf;
    Mnmax = max(Mn(:,Cj));
    Mwmax = max(Mw(:,Cj));

    for Tj = (tlength(Cj)+1):tamt

        tmat(Tj,Cj) = tmax;
        Mn(Tj,Cj) = Mnmax;
        Mw(Tj,Cj) = Mwmax; %#ok<AGROW>

    end
end

loglog(tmat(:,1),Mw(:,1),'r',tmat(:,2),Mw(:,2),'b',tmat(:,3),Mw(:,3),'g
',...
    tmat(:,4),Mw(:,4),'m');

xlabel('time (hr)'); ylabel ('Mw (Da)');
```

```
xlswrite('poly_tmat_exp', tmat);
xlswrite('poly_Mnmat_exp', Mn);
xlswrite('poly_Mwmat_exp', Mw);

end

% System of differential equations describing the reaction kinetics
function dC = fun(t,C,kf,kr,CM,kfh,krh,kfc,krc) %#ok<INUSL>

R = kf*C(1)*C(2) - kr*C(3)*CM;
Rh = kfh*C(2)*C(4) - krh*C(5)*CM;
Rc = kfc*C(1)*C(5) - krc*C(3)*C(4);

dC = zeros(5,1);
dC(1) = -R - Rc;
dC(2) = -R - Rh;
dC(3) =  R + Rc;
dC(4) = -Rh + Rc;
dC(5) =  Rh - Rc;

end

% This function calculates the degree of polymerization based on
equations derived
% in both Odian and Prof Hammond's Polymer Synthesis course
function Pn = Pn_calc(fA,fB,r)

if r>=1
    f = fA;
else
    f = fB;
end

Pn = (1+r)/(1 - 2*f*r + r);

end
```

The following program was used to estimate the forward and reverse Damköhler numbers as well as the ratio of the bulk methanol concentration to that at the catalyst surface (θ_M). Similar programs were used to perform the calculations for the other proposed geometries or reactive species, substituting the relevant lines of code with the appropriate equations as specified in the main body of this text.

```
function Da_f = Da_calc_bead()

KS = 1.05e-10; % m4/mol-s
CM = 1e-11; % mol/m3
Keq = 1;
del_bead = 10e-4; % m
CA0 = 2e-3; % mol/m3
r = 1;

CA = linspace(0,CA0,5000);
CB = CA;

for i = 1:length(CA)
    CL(i) = CA0 - CA(i); %#ok<AGROW>
    fA(i) = 1 - CA(i)/CA0; %#ok<AGROW>
    fB(i) = 1 - CB(i)/CA0; %#ok<AGROW>

    Pn(i) = Pn_calc(fA(i),fB(i),r); %#ok<AGROW>
    Mn(i) = Mn_calc(Pn(i)); %#ok<AGROW>
    Mw(i) = Mw_calc(Pn(i)); %#ok<AGROW>
    muM(i) = visc_calc(Mn(i)); %#ok<AGROW>
    Dm(i) = Dm_calc(Mn(i)); %#ok<AGROW>

end

for k = 1:length(CA)

    Da_f(k) = (KS*del_bead)*(CA(k)*CB(k)/CM)/Dm(k); %#ok<AGROW>
    Da_r(k) = (KS*del_bead)*(CL(k))/(Dm(k)*Keq); %#ok<AGROW>
    C_ratio(k) = (3 + Da_f(k))/(3 + Da_r(k));  %#ok<AGROW>

end
figure;
semilogy(Mn,Da_f)
figure;
semilogy(Mn,Da_r)
figure;
semilogy(Mn,C_ratio)

xlswrite('Da_calc_bead_1e-11', [Mn',Mw',Da_f',Da_r',C_ratio']);
xlswrite('muM', [Mn',Mw',muM'])
xlswrite('C_mat',[Mn',CA',CL']);

end
```

```
% Diffusivity calculation function according to Wilke-Chang

function Dm = Dm_calc(MW)

VA = 0.416; % m3/kgmol
Mb = MW; % kg/kgmol
phi = 1;
T = 363; % K
mu = visc_calc(MW);

Dm = 1.173e-16*sqrt(phi*Mb)*T/(mu*(VA^0.6));

end

% Viscosity calculation function

function mu = visc_calc(MW)

ro = 1100; % kg/m3

if MW < 1000

    v_cSt = 0.0166*MW + 0.7149;

elseif MW < 3350
    v_cSt_low = 0.0166*(1000) + 0.7149;
    v_cSt_high = 58.81 + 3.980e-11*(3350)^3.4;
    Mvec = [1000,3350];
    viscvec = [v_cSt_low, v_cSt_high];

    fit = polyfit(Mvec,viscvec,1);

    v_cSt = polyval(fit,MW);

else
    v_cSt = 58.81 + 3.980e-11*MW^3.4;
end

v = v_cSt*1e-6;
mu = v*ro;

end

function Pn = Pn_calc(fA,fB,r)

if r>=1
    f = fA;
else
    f = fB;
end

Pn = (1+r)/(1 - 2*f*r + r);
```

```
end

function Mn = Mn_calc(Pn)

MA = 900;     % g/mol
MB = 210;
MM = 32;
M_0 = (MA + MB - 2*MM)/2;
M_eg = MM;

Mn = Pn*M_0 + M_eg;

end

function Mw = Mw_calc(Pn)

MA = 900;     % g/mol
MB = 210;
MM = 32;
M_0 = (MA + MB - 2*MM)/2;

Mw = M_0*(2*Pn-1);

end
```

Appendix C: Sample calculation of model parameters and model results

Calculation of the Intrinsic Rate Constant

The effective forward rate constant was estimated experimentally. Based on the geometry of the system in which the forward rate constant was estimated, the effective forward rate constant is related to the intrinsic forward rate constant according to (reproduced from EQUATION 29):

$$\kappa_f \sigma_{enz} = \frac{k_f V_{melt}}{A_{cat} N_{cat}}$$

The value for k_f was determined from the forward rate constant determination experiment, while the other parameters on the left hand side were known according to system- and geometry-specific parameters. The enzyme surface concentration was unknown. Fortunately, the product on the left hand side appeared as such in the effective rate constant equations for the other situations considered: single bead, stagnant melt, and Protherm (EQUATIONS 27, 28, and 39).

The terms on the right hand side used in the calculation are summarized below. SI units were used throughout the calculations for consistency.

Term	Value	SI Units
k_f	1.5×10^{-7}	$m^3/mol\text{-}s$
V_{melt}	8.33×10^{-6}	m^3
N_{bead}	3.8×10^{3}	dimensionless
A_{bead}	3.14×10^{-4}	m^2

These values were used to determine the product, $\kappa_f \sigma_{enz}$, which was 1.05×10^{-10} $m^4/mol\text{-}s$ according to EQUATION 29 (reproduced above).

Calculation of the Damköhler Numbers

The Damköhler numbers were calculated over a range of polymer molecular weights. These molecular weights were used to estimate polymer melt viscosity, which, in turn, was used to estimate the diffusivities. A single polymer molecular weight, 10 kDa, was chosen to demonstrate the calculation of the forward and reverse Damköhler numbers for the case of a single bead. The relevant parameters for each geometric case were summarized in TABLE 3.5. These values, together with the steps described above, can be used to verify any of the calculations for the single bead, stagnant film, and Protherm cases across the range of simulated weight-average molecular weights.

The methanol and PEG self-diffusivities in a polymer melt of 10 kDa are $2x10^{-11}$ and $4x10^{-14}$ m^2/s, respectively. These values were determined according to the results presented in FIGURE 3.28. The concentrations of the hydroxyl, linker ester, and ester linkage groups also vary as a function of molecular weight. An increase in molecular weight corresponds to a decrease in the concentration of the reactants A and B and a corresponding equimolar increase for the concentration of L. (Note: the bulk methanol concentration was assumed to be constant for all molecular weights.) The values for C_A, C_B, and C_L at a polymer *weight-average* molecular weight of 10 kDa were calculated according to EQUATIONS 18 and 21 and summarized below:

Term	Value	SI Units
C_A	$1.98x10^{-4}$	
C_B	$1.98x10^{-4}$	m^3/mol
C_L	$1.80x10^{-3}$	

The forward and reverse Damköhler numbers for the single bead case were presented in EQUATION 33:

$$Da_{f,M}^{bead} = \frac{k_f^{bead} R}{D_M}\left(\frac{C_A C_B}{C_M(R)}\right)$$

$$Da_{r,M}^{bead} = \frac{k_f^{bead} R}{D_M K_{eq}}\left(C_L\right)$$

where,

$$k_f^{bead} = \kappa_f \sigma_{enz}$$

The remaining terms required for the calculation were the bead radius, bulk methanol concentration, and the equilibrium constant. According to the manufacturer, the bead radius for the Novozym435 beads has a range of 1.55 to 5.0 mm. The bead radius was assumed to be $5x10^{-4}$ m (5 mm) for the Damköhler number calculations. The bulk methanol concentration, $1x10^{-7}$ mol/m^3, was determined assuming a Raoult's Law description of the vapor-liquid equilibrium. The equilibrium constant, K_{eq}, was assumed to be one.

The forward and reverse Damköhler numbers for the single bead case were calculated using the following combination of terms:

$$Da_{f,M}^{bead} = \frac{\left(1.05x10^{-10}\right)\left(5.0x10^{-4}\right)}{2.0x10^{-11}}\left(\frac{\left(1.98x10^{-4}\right)^2}{1.00x10^{-7}}\right) = 1.03x10^{-3}$$

$$Da_{r,M}^{bead} = \frac{\left(1.05x10^{-10}\right)\left(5.0x10^{-4}\right)}{\left(2.0x10^{-11}\right)(1)}\left(1.80x10^{-3}\right) = 4.73x10^{-6}$$

These results can be compared to the corresponding points on the plots in FIGURES 3.29 A and B.

Appendix D: Viscosity Measurements of PEG and Catalyst

Note: This appendix was adapted from a report prepared by Nathalie Pinkerton (NP). All experiments and data analysis were performed by NP during participation in the MIT Undergraduate Research Opportunity Program (UROP) under the guidance of the author and Clark K. Colton.

Overview

The viscosity of the polymer melt can significantly affect the backbone polymerization. Specifically, the diffusivities of the species within the melt, including the methanol byproduct and monomer or oligomer reactive endgroups, are inversely related to polymer viscosity. Viscosity increases as the reaction proceeds and higher MW backbone polymer is achieved. Viscosity can also be affected by the addition of solids into the melt, such as the support upon which the catalyst is immobilized, or by addition of solvent, such as the PEG250 dimethyl ether. As a result, a study was performed to develop a quantitative understanding of the viscosity of the backbone polymer melt as a function of MW, catalyst loading, and solvent wt% (w/w).

Materials and Methods

The effect of the aforementioned on viscosity was investigated by adding solvent to samples of PEG4600, PEG8000 and PEG12000 with and without catalyst beads. These relatively low polydispersity (PDI < 1.15) PEGs were assumed to be representative of backbone polymer of comparable MWs. An AR-G2 plate-plate rheometer (TA Instruments, New Castle, DE) was used to perform the viscometry measurements. Measurements were performed at 90°C across a range of shear rates. Samples were dried before viscosity measurement to remove water.

Results

Addition of Solvent

Solvent was added to PEG12000 in wt% (w/w) between 5 and 25% without catalyst beads present (FIGURE 1). Solvent addition significantly reduced the viscosity across all measured shear rates. In particular, the average viscosity was reduced from 4.26 Pa-s to 1.33 Pa-s with the addition of 25 wt% PEG250 dimethyl ether. Interestingly, the independence of viscosity with respect to shear rate implied that the polymer exhibited Newtonian behavior over the range of shear rates investigated.

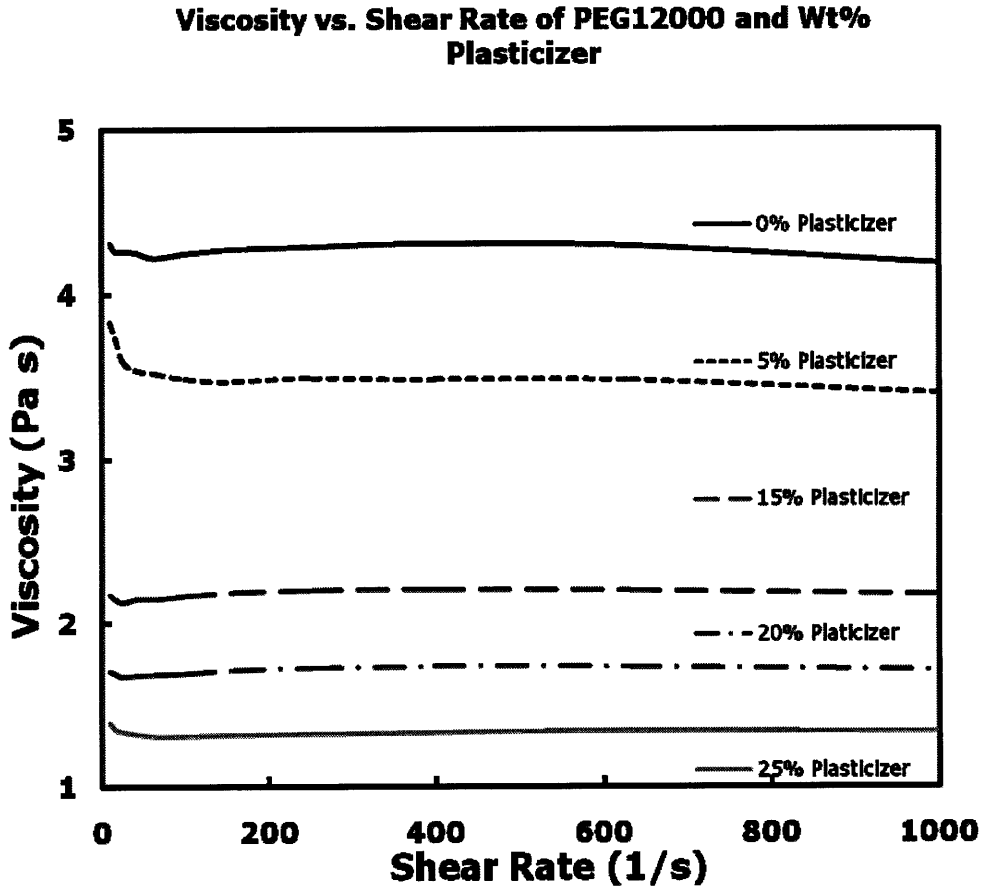

Figure 1: PEG12000 viscosity measurements with different wt% of solvent added as measured across a range of shear

Addition of Catalyst Support

Polymer melts with catalyst beads (10 wt%, w/w) suspended were also measured in order to assess the effect of such a solids addition. Solvent was also added at 5 and 25 wt% (w/w). The shear rate range was decreased for these measurements because of technical issues – the catalyst bead polymer suspension was ejected from between the plates at shear rates greater than 100 s^{-1}. The gap size was increased from 1000μm to 2000μm to accommodate the beads.

The results for PEG4600, 8000 and 12,000 exhibited similar trends (FIGURES 2-4). As anticipated, the presence of the catalyst support greatly increased the melt viscosity, with a corresponding decrease in viscosity upon addition of solvent. In fact, addition of solvent at 25 wt% (w/w) was able to restore the viscosity to a level below that of the original, pure PEG sample. The addition of 5 wt% (w/w) solvent actually increased the viscosity for both PEG4600 and 12,000. This result may have been an artifact of the increase in the gap between the rheometer plates.

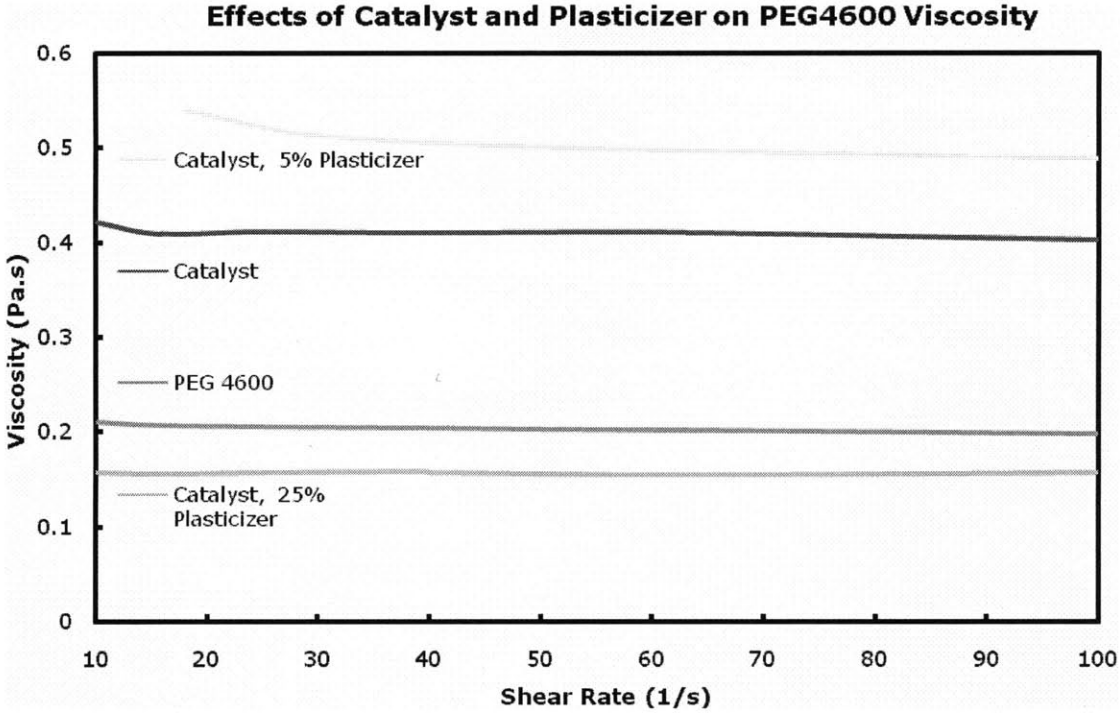

Figure 2: Viscosity measurements of PEG4600 at various solvent wt%, both with and without the catalyst beads added (10 wt%, w/w).

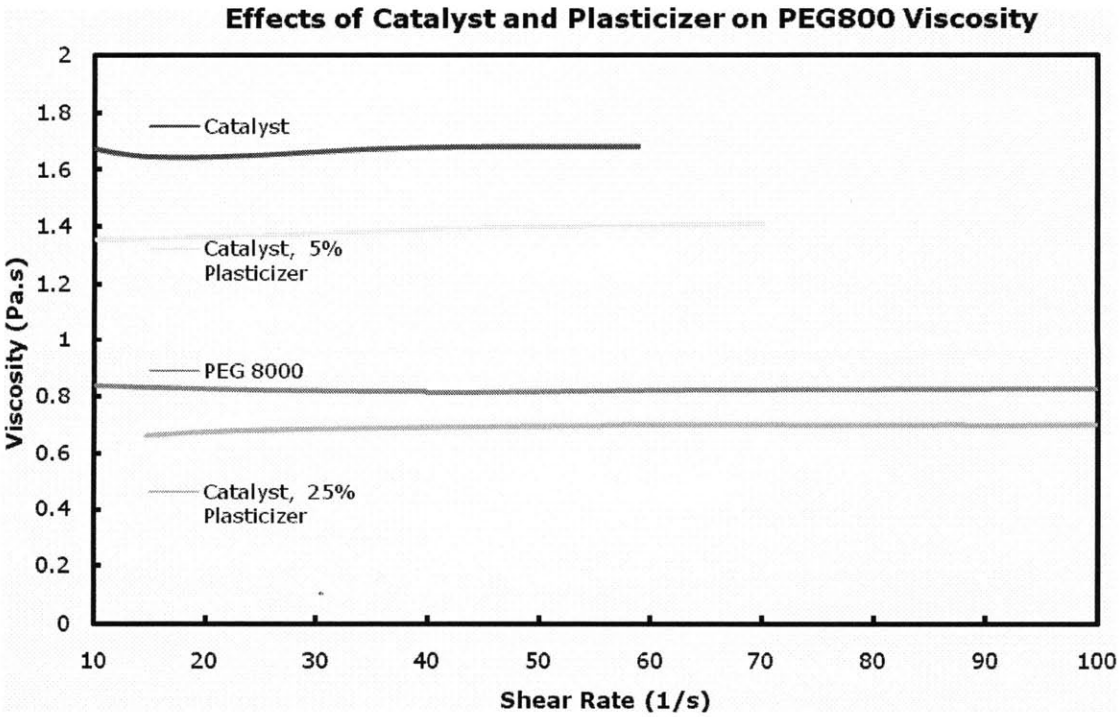

Figure 3: Viscosity measurements of PEG8000 at various solvent wt%, both with and without the catalyst beads added (10 wt%, w/w).

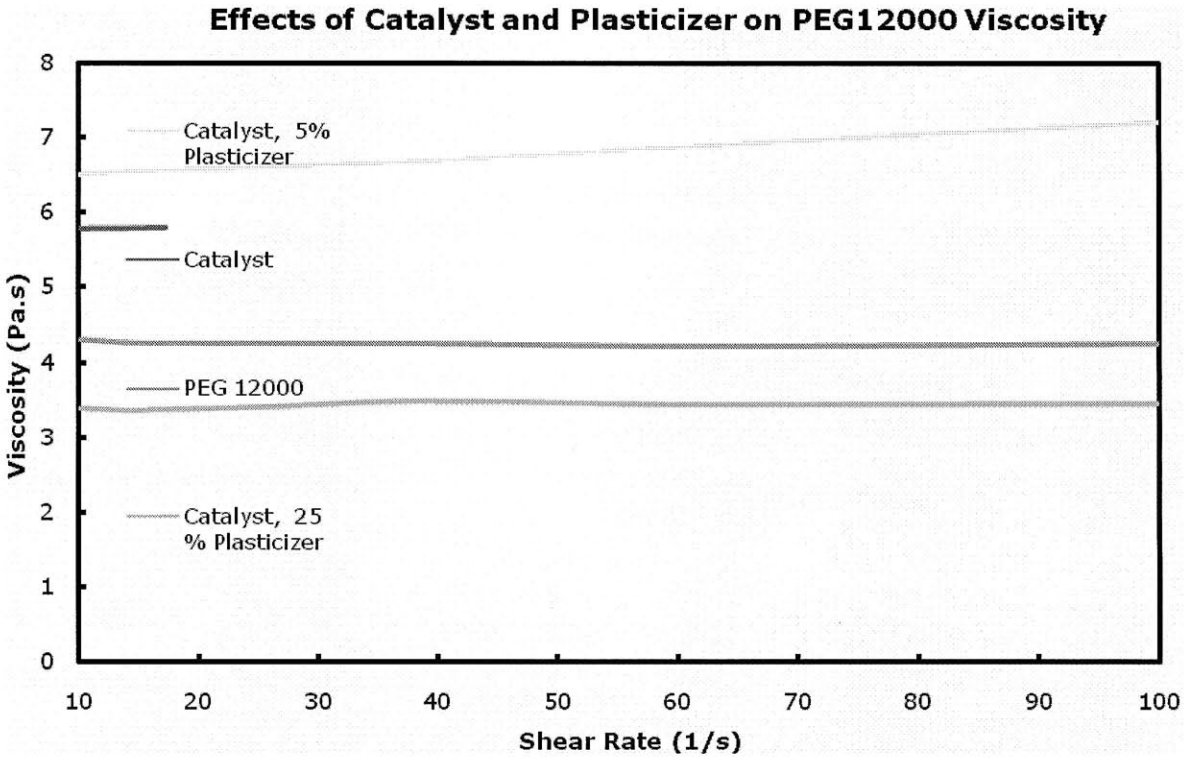

Figure 4: Viscosity measurements of PEG12000 at various solvent wt%, both with and without the catalyst beads added (10 wt%, w/w).

Appendix E: Effect of Iodination on Molecular Weight: Recovery Calculation and Chromatogram Adjustments

In order to compare the chromatograms, the sample analyzed by the GPC system had to be representative of that which was recovered at the end of the purification step. However, in order to perform the GPC analysis, water had to be removed from the sample before resuspension in the organic mobile phase solvent, THF. There were two procedural difficulties that may have affected the quality of the sample during this transition from water to THF. First, some polymer degradation had been observed due to the freeze-drying process itself (FIGURE 4.10). Secondly, it was difficult to dissolve the freeze dried product in THF due to the presence of crystallized salts from the phosphate buffer solution. To maximize recovery, the vial containing the freeze dried product was washed and resuspended in a known volume THF.

The overall recovery of polymer for the entire experiment, which included the iodination with cold, ^{127}I, freeze-drying, and resuspension in THF, was calculated according to the peak area of the resulting GPC chromatogram. This calculation was performed using a calibration curve constructed by analyzing samples of backbone polymer dissolved in THF at a broad range of concentrations.

The calculation was performed according to the following steps: (1) the initial mass of polymer at the beginning of the experiment was 1 mg (100 μL of 10 mg/mL solution). This was the denominator for the fractional recovery calculation. (2) The concentration of backbone polymer in the unknown sample was determined according to the peak area calibration curve. (3) The total mass in the resuspended sample was determined by multiplying the concentration by the total volume of THF used to wash

and resuspend the freeze-dried sample. (4) The fractional recovery was determined by dividing the final mass by the initial mass.

To construct the peak area calibration curve described above, chromatograms were generated for a wide range of backbone polymer concentrations. The result with the peak area most closely resembling each of the two cold iodination sample chromatograms was selected from this library of chromatograms. Using this strategy, the library chromatogram for the first cold iodination was that for backbone polymer dissolved in THF at 0.25 mg/mL, while the concentration of the library sample for comparison to the second cold iodination was 0.0625 mg/mL. Each pair of chromatograms, which included that for each cold iodination sample and its corresponding library chromatogram for comparison, were normalized by their total peak area. The resulting y-axis for the normalized chromatograms was the normalized absorbance response.

Appendix F: Unicorn Method Code for Polymer Fractionation

The following method was used to perform the polymer fractionation described in Chapter 5. The code includes a loop command with the loop number set to 8.

```
Method: C:\UNICORN\Local\Fil\default\Method\Kevin Prep Run 5xw.m01

Main method:
¤ (Main)
  0.00 Base Volume 318.557 {ml}
(HiLoad_26/60_Superdex_75_prep_grade)#Column
¤ 0.00 Block Start_with_PumpWash_Purifier
   (Start_with_PumpWash_Purifier)
   0.00 Base SameAsMain
   0.00 PumpWashBasic On On
   0.00 End_Block
¤ 0.00 Block Flow_Rate
   (Flow_Rate)
   0.00 Base SameAsMain
   0.00 Flow (0.800)#Flow_Rate {ml/min}
   0.00 End_block
¤ 0.00 Block Column_Pressure_Limit
   (Column_Pressure_Limit)
   0.00 Base SameAsMain
   0.00 Alarm_Pressure Enabled (1.00)#Column_PressureLimit {MPa} 0.02 {MPa}
   0.00 End_Block
¤ 0.00 Block Start_Instructions
   (Start_Instructions)
   0.00 Base SameAsMain
   0.00 AveragingTimeUV (10.00)#Averaging_Time_UV
   0.00 End_block
¤ 0.00 Block Eluent_A_Inlet
   (Eluent_A_Inlet)
   0.00 Base SameAsMain
   0.00 BufferValveA1 A11
   0.00 End_block
¤ 0.00 Block Eluent_B_Inlet
   (Eluent_B_Inlet)
   0.00 Base SameAsMain
   0.00 End_block
¤ 0.00 Block Start_Conc_B
   (Start_Conc_B)
   0.00 Base SameAsMain
   0.00 Gradient (0)#Start_ConcB {%B} 0.00 {base}
   0.00 End_block
¤ 0.00 Block Column_Valve
   (Column_Valve)
   0.00 Base SameAsMain
   0.00 ColumnPosition (Position7)#Column_Position
   0.00 End_Block
```

```
¤ 0.00 Block Column_Equilibration
  (Column_Equilibration)
  0.00 Base SameAsMain
  (325.00)#Equilibrate_with End_Block
¤ 0.00 Block AutoZero_UV
  (AutoZero_UV)
  0.00 Base SameAsMain
  0.00 Watch_Off UV
  0.00 AutoZeroUV
  0.00 End_Block
 0.00 Loop 8
¤ 0.00 Block Sample_Run
  (Sample_Run)
  0.00 Base SameAsMain
  0.00 Gradient 100 {%B} 0.5 {base}
  4.00 Gradient 0 {%B} 0.5 {base}
  95.00 ;
  214.00 ;
  245.00 ColumnPosition Position1Bypass
  245.10 ;
  246.00 Flow 10 {ml/min}
  286.00 Flow 0.800 {ml/min}
  288.00 Alarm_Pressure Enabled 1.00 {MPa} 0.02 {MPa}
  288.40 ColumnPosition Position7
  289.00 End_Block
 0.00 Loop_End
¤ 0.00 Block Isocratic_Elution
  (Isocratic_Elution)
  0.00 Base SameAsMain
¤  0.00 Block Length_of_Elution
   (Length_of_Elution)
   0.00 Base SameAsMain
   (320.00)#Length_of_Elution End_Block
  0.00 End_Block
```

Appendix G: Additional Representations of the Cellular Uptake Results

The uptake results in FIGURE 5.11 were also calculated according to the number of polymer chains per cell. To manipulate the data, the mass per cell results were divided by the molecular weights presented in TABLE 5.5 and multiplied by Avogadro's number.

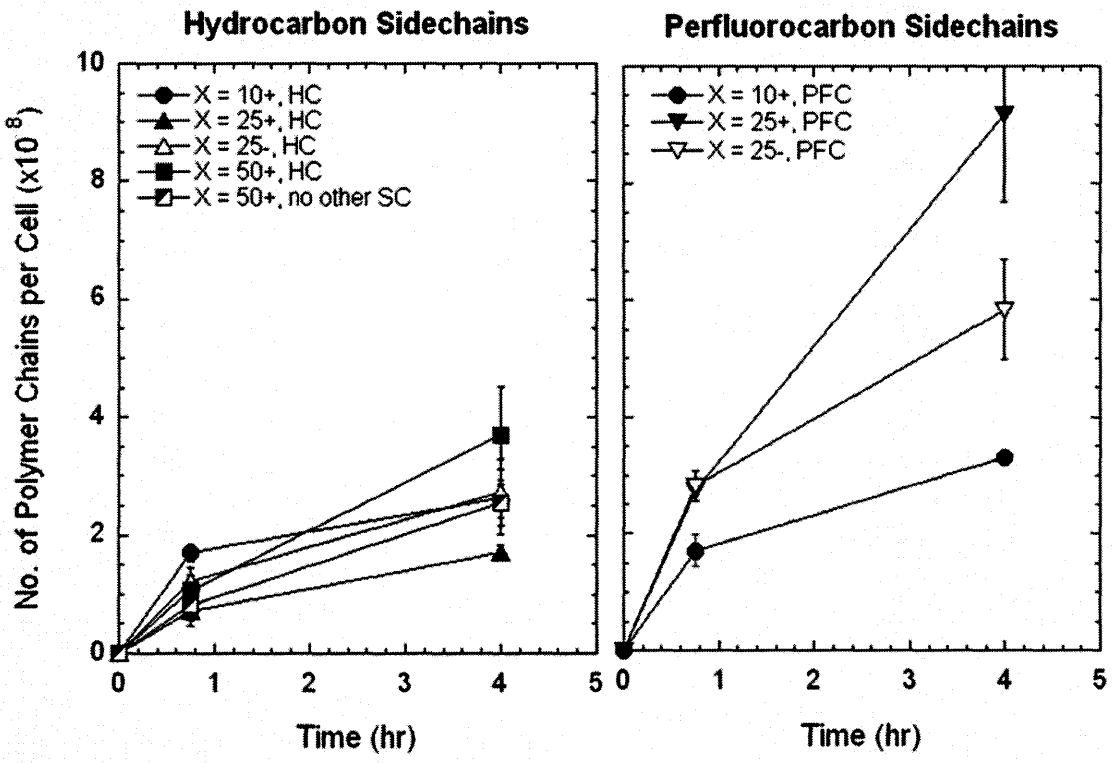

Based on these manipulations, the greatest uptake observed was for the X=25+, PFC polymer, which still exhibited selective uptake relative to its untargeted, X=25-, PFC counterpart, albeit to a lesser extent than that observed for the polymer mass per cell method of data presentation.

The uptake results for the second synthesis batch were also subjected to the same manipulations to yield the number of polymer chains per cell.

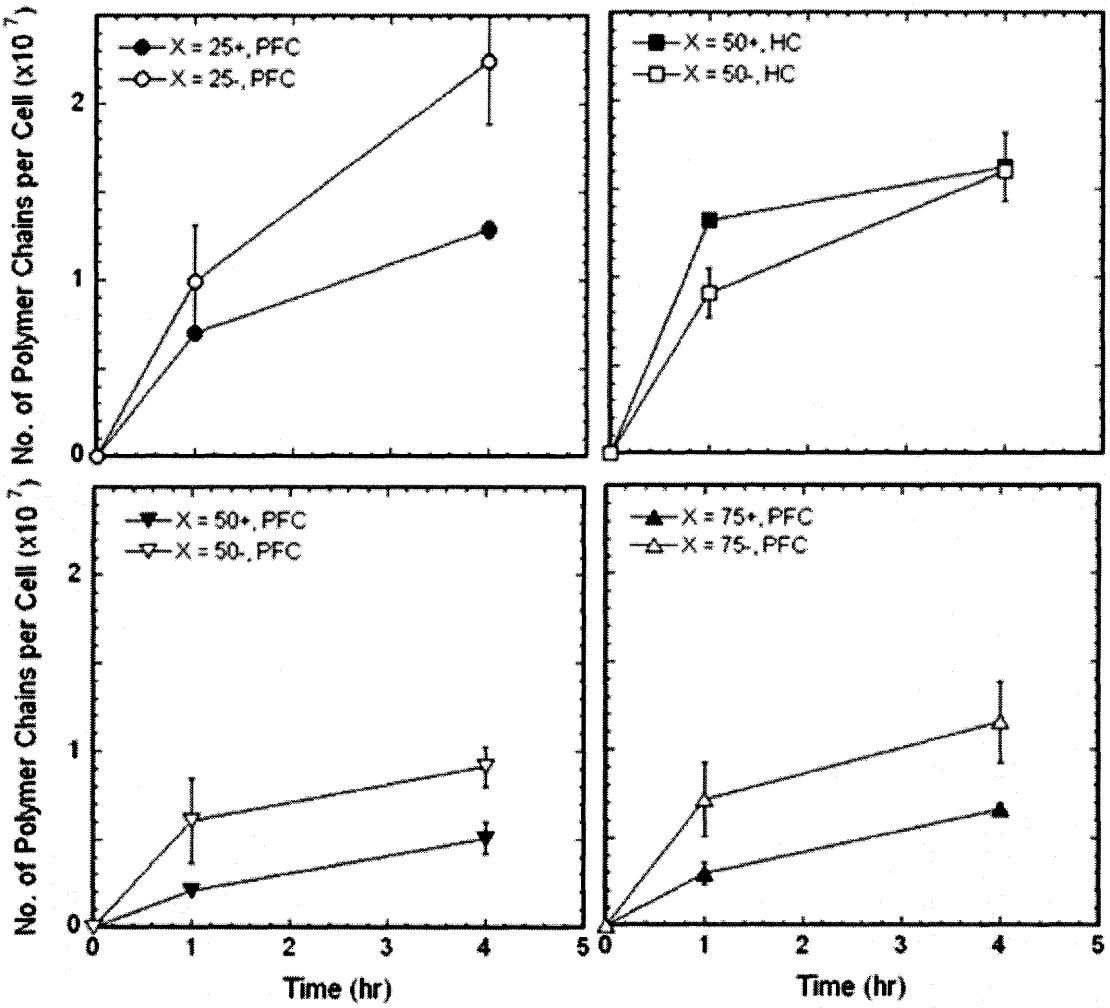

For the second batch, no selectivity was observed based on the chains per cell representation. In fact, the uptake for the untargeted polymers was higher than that for the targeted polymers for three of the polymer pairs.

The data were also manipulated to determine the fraction of the initial activity added to each well that was internalized or bound to the cell at given time point. These results were also normalized by the number of cells in each well. The polymer mass and bound radioactivity (as ^{125}I) are related by:

$$a = A_{spec}m$$

where a is the activity, A_{spec} is the specific activity of a radiolabeled polymer (units of activity per mass), and m is the mass. The specific activity can be used to convert mass to total activity. It can also be used to convert the initial mass added to the initial activity added. When calculating the fraction of activity per cell at a given time point, the specific activity of the polymer in question cancels. Therefore, the uptake results for the fraction of initial activity per cell will be qualitatively identical to those for the polymer mass per cell representation. This is a consequence of the choice to maintain the initial mass of polymer in each experiment constant.

Appendix H: Positron Emission Tomography (PET) of ^{124}I-labeled polymers

A collaboration was established with Dr. Mikhail Papisov, Professor of Radiology, Harvard-MGH. The polymer labeling and PET imaging weree graciously completed by or under the supervision of Dr. Papisov. Image reconstructions and much of the data interpretation described in this Appendix were also performed by Dr. Papisov.

The backbone polymer and polymer 027 (see FIGURE 4.2A and B) were labeled with iodine-124 according to the standard protocol and purified using the radio-HPLC techniques described in Chapter 4. The labeled polymers were injected into non-tumor-bearing rats as a proof-of-principle for the use of the amphiphilic alternating copolymers as a diagnostic tool. The PET imaging of these polymers provided real-time, non-invasive pharmacokinetic data. Images after 20 min for both the backbone polymer and polymer 027 were similar; the image for polymer 027 is presented below as a representative result.

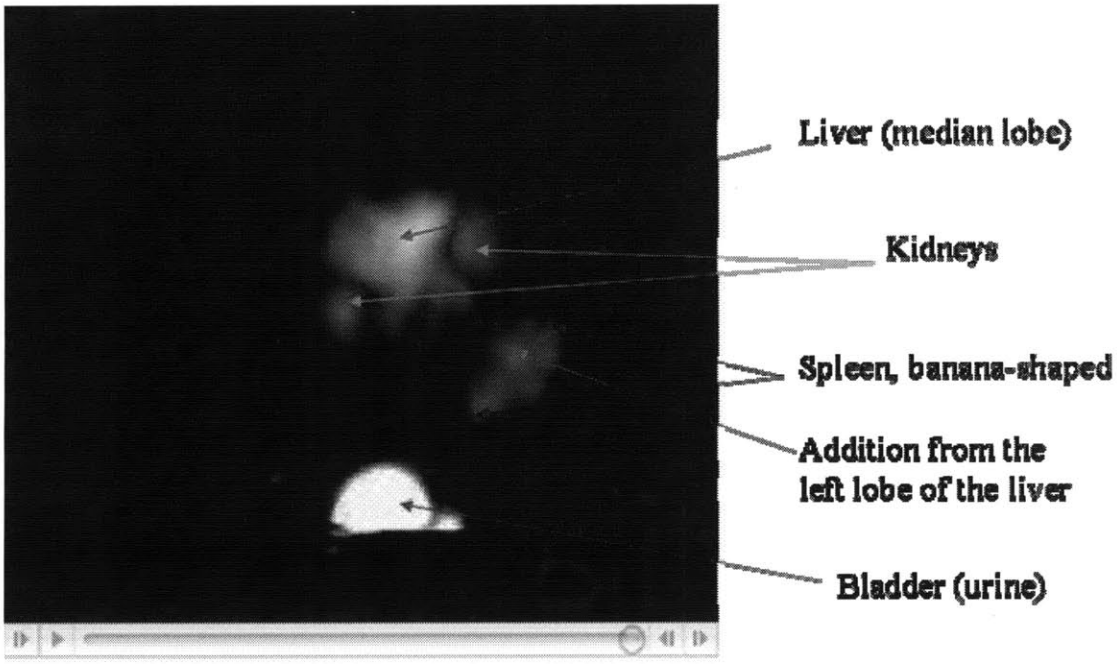

The greatest signal was observed in the bladder, which indicated that the majority of the activity exiting the animal was due to excretion in the urine. This result was

consistent with observations during the biodistribution experiments in which the greatest activity within each experimental cage was measured in the urine accumulated by the bedding. The other organs observed in the image, the liver, kidneys, and spleen, are all heavily vascularized. The signal measured in these organs indicated that the labeled polymer was present in the bloodstream at 20 min.

The best candidates from the uptake and biodistribution studies described in Chapter 5 were also studied in the laboratory of Dr. Papisov. The goal of these experiments was to replicate the selective uptake observed during the biodistribution studies in a live animal. EGFR-positive tumors were grown subcutaneously on *nu/nu* mice, while three different polymer formulations were chosen for labeling with iodine-124 and subsequent injection into the animals. The polymer formulations were: X=25+, PFC, X=25-, PFC, and X=50+, HC.

The radio-HPLC result for the X=25-, PFC polymer is presented below. Absorbance measurements for four different proteins and one small molecule were also measured and plotted with the results for the X=25-, PFC polymer. The radio-HPLC results, which include both the UV and gamma-detector response, are presented below.

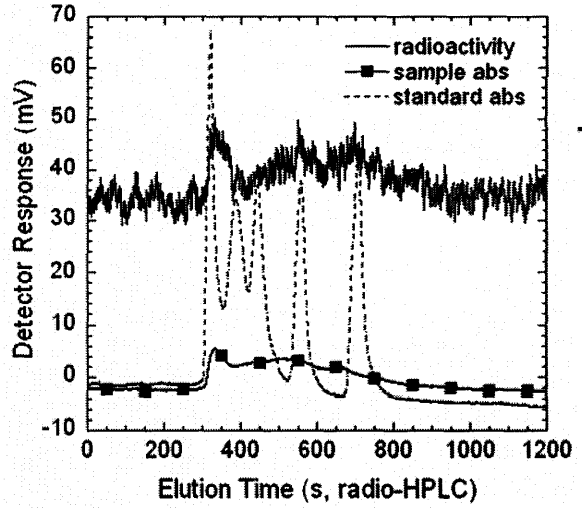

Sample	MW (kDa)
thyroglobulin	670
g-globulin	158
ovalbumin	44
myoglobin	17
Vitamin B-12	1.35

The UV absorbance profile was broad, ranging from approximately 300 to 800 seconds in elution time. According to the protein and small molecule 'standards,' these elution times corresponded to a breadth of molecular weights, from 670 kDa to 1.35 kDa. This suggested that the X=25-, PFC polymers existed in both micelle and individual polymer states under the analytical conditions. The radioactivity measurements corresponded strongly with the absorbance measurements, which indicated that the polymer was labeled uniformly throughout the polymer chains in the sample.

The radio-HPLC results for all three polymers after the labeling experiments are presented below.

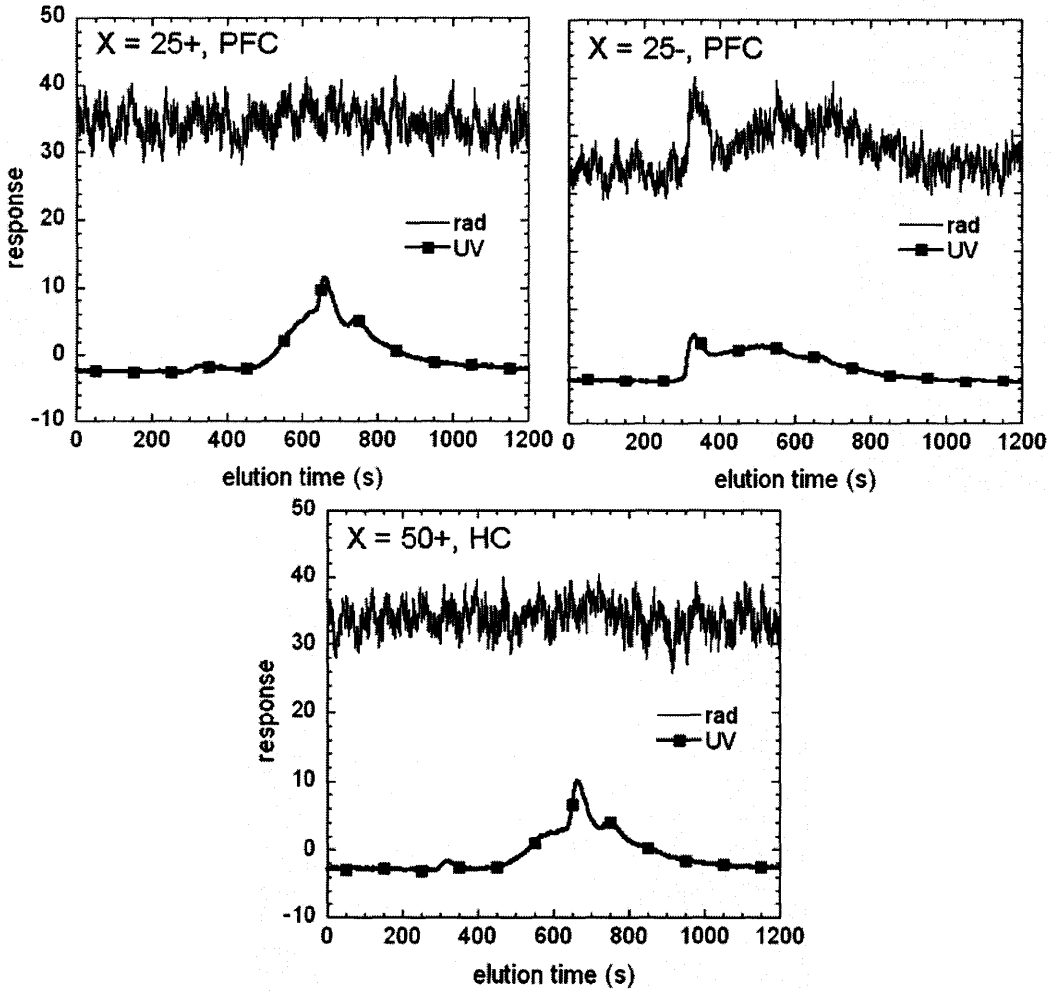

The absorbance profiles for both of the EI3.4.3-conjugated polymers were drastically different from that for the X=25-, PFC polymer. In both of these profiles, there was a small peak near approximately 300 s, which likely corresponded to a particle. The remaining absorbance was recorded at much longer elution times (lower molecular weights). This result could indicate the formation of smaller particles or associations of a small number of chains with one another, such as dimers or trimers, during the analytical testing procedure.

The activity profiles for both EI3.4.3-conjugated polymers did not have a strong correlation to the absorbance profiles. In fact, there was little activity signal at all in the purified label polymer samples. The labeling yields for the EI3.4.3-conjugated polymers were extremely low (<1%). This result was unexpected because labeling yields of the same polymers performed at MIT, albeit with iodine-125, were approximately 5-10%. The result was also particularly interesting considering the fact that, although the absorbance detector indicated the presence of significant material in the sample, material which is known to have potentially iodination sites both within the linkers of the polymer backbone and the tyrosines in the EI3.4.3 peptide, minimal labeling was achieved. This suggested that the iodination sites may had somehow become inaccessible to the iodination procedure or that the iodination sites were inactivated.

The increased molecular weight of the polymer backbone (12 kDa) and the associated decrease in solubility of the individual polymer chains was one proposed explanation for the observed phenomenon. Additionally, due to significant restrictions in the scheduling of PET machine time, the samples for all three polymers were refrigerated for approximately 8 weeks. This refrigeration period occurred after the polymers were

studied at MIT in uptake and biodistribution experiments. The stability of the polymers and, in particular, the conjugation of the EI3.4.3 peptide to the polymer backbone, was unknown and not studied.

Unfortunately, due to the low labeling yield, no PET imaging was performed for the EI3.4.3-conjugated polymers because sufficient signal would not have been achieved. Improvements in labeling yield are absolutely necessary for any viable PET studies due to the high cost of iodine-124. It is recommended that future experiments minimize the time polymers exist in solution before labeling and imaging and that additional labeling yield and stability studies are performed on polymers synthesized from high molecular weight, low polydispersity backbone polymer.